

Predictive Modeling of Partitioned Systems: Implementation and Applications.

Zur Erlangung des akademischen Grades

Doktor der Ingenieurwissenschaften

der Fakultät für Maschinenbau

Karlsruher Institut für Technologie (KIT)

genehmigte

Dissertation

von

Dipl.-Ing. Christine Latten

Tag der mündlichen Prüfung: 14.07.2014

Hauptreferent: o. Prof. Dr. rer. nat. Dr. h. c. mult. D. G. Cacuci

Korreferent: Prof. Dr. X. Cheng

Acknowledgements

I sincerely thank Professor D. G. Cacuci for proposing the topic, his guidance and continuous support throughout this work. Also, I am very grateful to Professor X. Cheng for his support and accepting to co-supervise my thesis.

Many thanks to all co-workers at the University of South Carolina for the good atmosphere and cooperation; especially to Dr. Proctor for valuable suggestions, indispensable lunch breaks and manifold help throughout this work.

Abstract

In the present work a general mathematical methodology for predictive modeling of coupled multi-physics systems, formulated by [10], is implemented. The new formulation is denoted here as partitioned data assimilation (DA). In this work the method of [10] has been applied without change to an illustrative heat conduction example and reactor physics benchmarks. Application of the partitioned DA yields optimal values of system parameters and responses, while simultaneously reducing the corresponding uncertainties in parameters and responses. This methodology also provides quantitative indicators constructed from sensitivity and covariance matrices for determining the consistency among the a priori computational and experimental data. Standard formulations of DA methods treat all of the available computational and experimental information simultaneously. In case of very large systems, this simultaneous approach can become computationally expensive. In particular, the memory requirement can exceed available computational resources. The new partitioned data assimilation is constructed in a way that an implementation can consider parts of the available information sequentially rather than all information simultaneously, while preserving exactly the same results. The maximal required memory is significantly smaller with the new partitioned DA.

The applicability of data assimilation to neutron transport benchmarks in the non-partitioned formulation of [9] has already been demonstrated in [27]. His work in conjunction with [14] established a chain of computational tools to obtain best-estimate system parameters and responses as well as reduced uncertainties of parameters and responses for large-scale reactor physics benchmarks. These existing tools are the basis of implementing the partitioned data assimilation for coupled neutron transport applications. The development of an algorithm that puts the partitioned data assimilation formulas into practice represents a novelty. The main focus of this research project is to thoroughly test this new algorithm by means of synthetic data and highlight major features with the help of reactor physics benchmarks.

The first application is an illustrative heat conduction example with synthetic data. 1-dimensional time-dependent heat conduction in an infinite medium has an analytic solution, which makes sensitivity coefficients readily available. Various sets of synthetic data are used to demonstrate that partitioned and non-partitioned data assimilation yield exactly the same results, while the partitioned data assimilation requires considerably less memory. However, further analysis of the performance of the algorithm also shows that the minimal memory requirement comes at a high cost of execution time. In addition, the heat conduction problem based on synthetic data is also used to feature a new consistency evaluation procedure,

which indicates the agreement between computed and experimentally measured responses. This new procedure is a modification of the established method of [36] designed to obtain a sequence of most to least discrepant responses with less computational effort. Discrepancy in a data set is usually caused by only a few blatantly discrepant responses and the new consistency evaluation procedure identifies the same responses, which are most discrepant, than the standard method. However, the two methods are not mathematically equivalent and a deviation between the two methods has been observed in case marginally discrepant responses of a system that already complies with a chosen confidence criterion are identified.

Several neutron transport benchmarks of the International Handbook of Evaluated Criticality Safety Benchmark Experiments [19] are considered as applications. The benchmarks' parameters include individual cross sections for each material, nuclide, reaction type and energy-group, fission spectra and average number of prompt neutrons emitted per fission, while the responses include the respective benchmarks' effective multiplication constants, various fission rate ratios and various radiative capture rate ratios. The deterministic neutron transport code Denovo developed at Oak Ridge National Laboratory (ORNL) is used for the numerical computations in the present work.

Jezebel-239 and Jezebel-240 are plutonium spheres that are coupled to each other via shared isotopes. Partitioned data assimilation is applied to each benchmark individually as well as to the two Jezebel benchmarks considered as a coupled system. The new method yields in both cases calibrated response and parameter values with reduced calibrated uncertainties. The interdependence is stronger for *similar* responses, which were measured in both benchmarks, than for *dissimilar* responses, which were measured merely in Jezebel-239. Considering both benchmarks jointly leads to more accurate calibrated values for responses and parameters, because the more a priori consistent information is available the larger is the reduction in uncertainty.

Godiva is a uranium sphere that demonstrates the application of the consistency evaluation procedure to a neutron transport benchmark. This system includes initially discrepant responses and the new procedure facilitates the decision, which responses need to be excluded in order to obtain a consistent system. In case of Godiva two sets of responses, which comply with user-defined criteria of consistency, are identified and compared. One of the sets of consistent responses is also calibrated jointly with Jezebel-239 and Jezebel-240. The partitioned data assimilation provides an efficient way to couple an additional system like Godiva to an already calibrated system like to two Jezebel benchmarks.

The Zero Power Reactor 6 assembly 7 is with over one hundred thousand parameters and twenty-five responses the largest application in the present work. A detailed as-built model of Loading 41 is created, which is used as input deck for the Monte Carlo code MAVRIC and the deterministic Denovo included in ORNL's SCALE6.1 code package. The as-built model yields better, more detailed computational results than the homogenized, cylindrical model that comes with the benchmark description in [\[19\]](#). The capabilities of Denovo as well as the availability of computer resources limit the simulations to a coarse energy-group structure and coarse spatial mesh.

The present work presents an implementation of the partitioned data assimilation of [\[10\]](#) for the first time. The performance, applicability and major features of this new algorithm have been demonstrated based on synthetic data as well as neutron transport benchmarks. The results of this work can readily be modified and adapted for future work in the field of coupled large-scale multi-physics data assimilation.

Zusammenfassung

Die vorliegende Arbeit setzt eine umfassende mathematische Methode, welche in [\[10\]](#) hergeleitet ist, für prädiktive Modellkalibrierung gekoppelter multiphysikalischer Systeme um. Diese neue mathematische Formulierung wird hier als Datenanpassung (DA) bezeichnet. Die Methode aus [\[10\]](#) wird in der vorliegenden Arbeit unverändert auf ein Beispiel der Wärmeleitung, welches zur Veranschaulichung dient, und auf Experimente aus der Reaktorphysik angewendet. Die partitionierte DA liefert optimale Werte für Systemparameter und –antworten bei gleichzeitiger Reduktion der Unsicherheiten in Systemparametern und -antworten. Quantitative Indikatoren, welche sich aus Sensitivitäten und Kovarianzen zusammensetzen, werden ebenfalls von dieser Methode bereitgestellt. Diese quantitativen Indikatoren helfen dabei die Übereinstimmung zwischen a priori berechneten und experimentell gemessenen Daten zu bewerten. Übliche Formulierungen der verschiedenen Methoden für DA verarbeiten alle berechneten und experimentellen Informationen, welche zur Verfügung stehen, gleichzeitig. Diese Herangehensweise kann im Fall von sehr großen Systemen mit hohen Kosten für die Berechnung einhergehen. Insbesondere der Bedarf an Arbeitsspeicher kann die vorhandenen Ressourcen erschöpfen. Die neue, partitionierte DA aus [\[10\]](#) ist daher auf eine Weise konstruiert, dass der maximal benötigte Arbeitsspeicher deutlich reduziert werden kann. Die neue Implementierung ermöglicht es, dass Teile der vorhandenen Informationen nacheinander anstatt gleichzeitig verwertet werden

Die Formulierung für eine nicht-partitionierte DA wurde in [\[9\]](#) streng mathematisch hergeleitet und die Eignung dieser speziellen DA wurde für Benchmarks des Neutronentransports in [\[27\]](#) belegt. Seine Arbeit stellt zusammen mit [\[14\]](#) eine rechengestützte Werkzeugkette bereit, welche die Berechnung bestmöglicher Systemparameter und –antworten mit jeweils reduzierten Unsicherheiten für großmaßstäbliche Experimente der Reaktorphysik ermöglicht. Diese bereits entwickelten Werkzeuge bilden die Grundlage der Implementierung der partitionierten Datenanpassung für gekoppelte Neutronentransportanwendungen. Die Entwicklung eines Algorithmus, welcher die mathematischen Gleichungen der partitionierten DA in die Praxis umsetzt, stellt eine Neuheit dar. Schwerpunkt der vorliegenden Forschungsarbeit ist es, sowohl diesen neuen Algorithmus gründlich zu testen, als auch seine wesentlichen Eigenschaften hervorzuheben. Alle Tests erfolgen mittels synthetisch generierter Daten, während die Eigenschaften anhand von Experimenten aus der Reaktorphysik aufgezeigt werden.

Der erste Anwendungsfall ist ein Beispiel aus der Wärmeübertragung, welches zur Veranschaulichung dient und auf synthetischen Daten basiert. Für den Fall der 1-dimensionalen, zeitabhängigen Wärmeleitung in einem unbegrenzten Medium existiert eine

analytische Lösung, wodurch Sensitivitätskoeffizienten direkt berechnet werden können. Unterschiedliche, synthetische Datensätze werden verwendet um zu zeigen, dass die partitionierte und die nicht-partitionierte Datenanpassung jeweils identische Ergebnisse liefern bei gleichzeitigem deutlich geringerem Arbeitsspeicherbedarf der partitionierten DA. Bei näherer Betrachtung der Leistung des Algorithmus zeigt sich jedoch auch, dass der geringere Bedarf an Arbeitsspeicher zu Lasten der benötigten Rechenzeit geht. Am Beispiel der Wärmeleitung angewandt auf synthetische Daten wird weiterhin eine neue Vorgehensweise für die Auswertung der Übereinstimmung von berechneten und experimentell gemessenen Systemantworten vorgestellt. Diese neue Vorgehensweise ist eine Abwandlung der bereits etablierten Methodik aus [36] und definiert mit geringem Rechenaufwand eine Reihenfolge der Systemantworten im Hinblick auf Konsistenz. Die Diskrepanz in einem Datensatz wird üblicherweise durch einige wenige Systemantworten, welche offensichtlich widersprüchlich sind, verursacht. Wie die Standardmethode identifiziert die neue Vorgehensweise für die Auswertung der Konsistenz die Systemantworten, welche die geringste Übereinstimmung zwischen berechneten und experimentell gemessenen Werten aufweist. Allerdings ist die neue Vorgehensweise mit der Standardmethode nicht mathematisch äquivalent. Es kann zu abweichenden Ergebnisse zwischen beiden Methoden kommen. Dieser Fall tritt insbesondere ein wenn Systemantworten, welche nur geringfügig widersprüchlich sind, identifiziert werden sollen, während das System bereits eine gewählte statistische Sicherheit erfüllt.

Mehrere Benchmarks aus dem Bereich des Neutronentransports, welche im International Handbook of Evaluated Criticality Safety Benchmark Experiments [19] beschrieben sind, dienen als Anwendungsbeispiele. Der Parameterraum dieser Experimente umfasst separate Wirkungsquerschnitte der Neutronen für jedes Material, Nuklid, Reaktionsart und Energiegruppe, das Energiespektrum der bei der Kernspaltung freigesetzten Neutronen und die durchschnittliche Anzahl der prompten Neutronen pro Kernspaltung. Die Systemantworten beinhalten den jeweiligen effektiven Multiplikationsfaktor des entsprechenden Benchmarks sowie verschiedene Reaktionsraten der Kernspaltung und des Neutroneneinfangs. Zur numerischen Berechnung der Benchmarks wird in der vorliegenden Arbeit der deterministische Neutronentransport Code namens Denovo, welcher am Oak Ridge National Laboratory (ORNL) entwickelt wurde, verwendet.

Die Bezeichnung Jezebel-239 und Jezebel-240 stehen jeweils für ein Benchmark, welches aus einer Plutoniumkugel in kritischer Anordnung besteht. Beide Experimente sind über gemeinsame Isotope miteinander gekoppelt. Jedes der beiden Benchmarks wird sowohl einzeln als auch gekoppelt mittels der partitionierten Datenanpassung betrachtet. Die neue Methodik stellt in beiden Fällen kalibrierte Werte der Systemparameter und –antworten mit

entsprechend reduzierten Unsicherheiten bereit. *Ähnliche* Systemantworten, welche in beiden Experimenten gemessen wurden, weisen eine stärkere Wechselbeziehung auf als *unähnliche* Systemantworten, welche ausschließlich in Jezebel-239 gemessen wurden. Werden beide Experimente gemeinsam betrachtet führt dies zu genaueren, kalibrierten Werten für Systemantworten wie auch –parametern, da die Unsicherheit im System aufgrund mehr a priori zur Verfügung stehenden konsistenten Informationen stärker reduziert wird.

Das Experiment Godiva ist eine Urankugel, welche als Anwendungsfall für die neue Vorgehensweise für die Auswertung der Übereinstimmung von berechneten und experimentell gemessenen Systemantworten dient. Der Datensatz für Godiva weist zunächst widersprüchliche Systemantworten auf. Mittels der neuen Vorgehensweise kann eine Auswahl getroffen werden, welche Systemantworten ausgeschlossen werden müssen um ein konsistentes System zu erhalten. Dazu wird zunächst ein Kriterium festgelegt, welches einen vom Anwender als ausreichend eingestuften Konsistenzgrad wiedergibt. Für Godiva werden zwei konsistente Datensätze identifiziert und verglichen. Zusätzlich wird einer der konsistenten Datensätze noch gemeinsam mit Jezebel-239 und Jezebel-240 kalibriert. Die partitionierte Datenanpassung ermöglicht es somit auch ein zusätzliches System, beispielsweise hier Godiva, mit bereits kalibrierten Systemen, beispielsweise hier die beiden Jezebel Benchmarks, auf effiziente Weise zu koppeln.

Das Experiment Zero Power Reactor 6 Anordnung 7 stellt mit über einhunderttausend Systemparametern und fünfundzwanzig Systemantworten das größte Anwendungsbeispiel der vorliegenden Arbeit dar. Zur Berechnung dieses Experiments mit dem Monte Carlo Code namens MAVRIC und dem deterministischen Code Denovo, welche beide im Softwarepaket SCALE6.1 des ORNL enthalten sind, wird ein detailliertes Modell für den Beladungsfall 41 erstellt. Dieses detaillierte Modell liefert besser numerische Resultate mit größerer Detailschärfe als das homogenisierte, zylindrische Modell, welches bei der Beschreibung des Benchmarks in [\[19\]](#) inbegriffen ist. Die Möglichkeiten von Denovo wie auch die verfügbaren Computerressourcen begrenzen die durchgeführten Simulationen auf ein grobes geometrisches Gitter und wenige Energiegruppen.

Die vorliegende Arbeit präsentiert eine Implementierung der partitionierten Datenanpassung aus [\[10\]](#). Diese Umsetzung stellt eine Neuheit dar, welche bis heute in dieser Form nicht durchgeführt worden ist. Die Leistung, Anwendbarkeit und wesentliche Eigenschaften dieses neuen Algorithmus werden sowohl mit synthetischen Datensätzen als auch mit Experimenten des Neutronentransports demonstriert. Die Ergebnisse der vorliegenden Arbeit können leicht modifiziert und angepasst werden um zukünftige Forschungsvorhaben im Bereich der gekoppelten, großmaßstäblichen und multiphysikalischen Datenanpassung zu ermöglichen.

Contents

Acknowledgements	iii
Abstract	v
Zusammenfassung	ix
Contents	xiii
Figures	xv
Tables	xxi
1. Introduction	1
1.1 Motivation and Objectives	2
1.2 Outline of the Present Work	3
2. Mathematical Framework for Data Assimilation	5
2.1 Non-partitioned DA	5
2.2 Subsystem II and Coupling Terms	8
2.3 Consistency Indicator χ^2	16
2.4 Summary of Partitioned DA Equations	18
3. Application to 1-dimensional Heat Conduction as Illustrative Example	21
3.1 1-D time-dependent Heat Conduction in Infinite Medium	21
3.2 Non-partitioned DA	25
3.3 Partitioned DA.....	26
3.4 Implementation of partitioned DA	28
3.5 Evaluation Procedure to Identify least consistent Responses.....	33
4. Application to Neutron Transport Benchmarks	44
4.1 Neutron Transport.....	44
4.2 Data Assimilation on Jezebel-239 and Jezebel-240	49
4.3 Data Assimilation on Godiva	73
4.4 Data Assimilation on ZPR	92
5. Summary and Conclusion	107
Appendix	112
A Derivation of Eqs. (2.10) and (2.34)	113
B Derivation of Optimal Predicted Values	114
C Synthetic Data	119
D Implementation of partitioned DA	122
E Optimal Results for Godiva	137

F KENOVI Input Listings for as-built Model.....	139
Bibliography	141
Eigenständigkeitserklärung.....	145
Lebenslauf	146

Figures

Figure 1: Initial temperature distribution with 10 and 100 randomly sampled Fourier coefficients23

Figure 2: Synthetic measured and computed responses with one standard deviation for 1-D heat conduction. Measured values are shifted to the right for ease of visualization.24

Figure 3: Measured, computed and best-estimate responses with one standard deviation normalized to the nominal measured value for the heat conduction example with synthetic data26

Figure 4: Average maximum in allocated memory of four different partitions for 2 sets of synthetic data32

Figure 5: Measured and computed responses with one standard deviation normalized to the measured nominal value.36

Figure 6: Normalized χ^2 of the remaining 9 responses computed with the standard and the new procedure.....37

Figure 7: Normalized χ^2 for progressively excluded discrepant responses38

Figure 8: Normalized measured, computed and best-estimate responses with one standard deviation for the complete system with ten responses and a selected, reduced system with eight responses.40

Figure 9: Measured and computed responses for synthetic data set with $N_r = 100$ 41

Figure 10: Normalized χ^2 for progressively excluded discrepant responses in case of the synthetic data set with $N_r = 100$ 41

Figure 11: Average time on 1 CPU to identify the 20 least consistent responses using the new partitioned DA method compared to the standard method for several data sets42

Figure 12: Relative change in best-estimate fission spectrum of ^{235}U prior (blue) and after (red) renormalization of the fission spectrum covariance data for Godiva.48

Figure 13: Spectrum of the neutron flux for Jezebel-239 and Jezebel-24051

Figure 14: Sensitivity profile of k_{eff} to selected parameters for Jezebel-239.....	53
Figure 15: Sensitivity profile of k_{eff} to selected parameters for Jezebel-240.....	54
Figure 16: Sensitivity profile of $r_2 = \frac{\sigma_f(^{238}U)}{\sigma_f(^{235}U)}$ to selected parameters for Jezebel-239	54
Figure 17: Sensitivity profile of $r_8 = \frac{\sigma_\gamma(^{63}Cu)}{\sigma_f(^{235}U)}$ to selected parameters for Jezebel-239	55
Figure 18: Non-zero elements in the covariance matrix C_p indicating parameters that are present in both Jezebel systems. $C_{\alpha\alpha}$ refers to Jezebel-239, $C_{\beta\beta}$ refers to Jezebel-240 and $C_{\alpha\beta}$ contains the cross-terms, which indicate the coupling between the two benchmarks. ...	59
Figure 19: Jezebel-239 and Jezebel-240 – Measured, computed and best-estimate (single model) k_{eff} as well as optimal k_{eff} (coupled model) with one standard deviation normalized to the nominal measured value.....	61
Figure 20: Jezebel-239 and Jezebel-240 – <i>Similar</i> measured, computed and best-estimate responses (single model) as well as optimal responses (coupled model) with one standard deviation normalized to the nominal measured value	63
Figure 21: Jezebel-239 measured, computed and best-estimate responses (single model) as well as optimal responses (coupled model) for <i>dissimilar</i> reaction rate ratios with one standard deviation normalized to the nominal measured value.....	64
Figure 22: Relative change in individually and jointly adjusted elastic scattering cross section in ^{239}Pu for Jezebel-239 and Jezebel-240	68
Figure 23: Nominal, individually and jointly adjusted relative standard deviation of the elastic scattering cross section in ^{239}Pu for Jezebel-239 and Jezebel-240	68
Figure 24: Relative change in individually and jointly adjusted inelastic scattering cross section in ^{239}Pu for Jezebel-239 and Jezebel-240	69
Figure 25: Nominal, individually and jointly adjusted relative standard deviation of the inelastic scattering cross section in ^{239}Pu for Jezebel-239 and Jezebel-240.....	69

Figure 26: Nominal, individually and jointly adjusted fission cross section in ^{237}Np for Jezebel-239 and Jezebel-240.....	70
Figure 27: Relative change in individually and jointly adjusted fission cross section in ^{237}Np for Jezebel-239 and Jezebel-240	71
Figure 28: Nominal, individually and jointly adjusted relative standard deviation of the radiative capture cross section in ^{93}Nb for Jezebel-239	71
Figure 29: Relative change in individually and jointly adjusted radiative capture cross section in ^{93}Nb for Jezebel-239.....	72
Figure 30: Spectrum of the neutron flux for Godiva and Jezebel configurations.....	75
Figure 31: Sensitivity profile of k_{eff} to selected parameters for Godiva.....	76
Figure 32: Sensitivity profile of $r_2 = \frac{\sigma_f(^{238}\text{U})}{\sigma_f(^{235}\text{U})}$ to selected parameters for Godiva	77
Figure 33: Sensitivity profile of $r_6 = \frac{\sigma_\gamma(^{55}\text{Mn})}{\sigma_f(^{235}\text{U})}$ to parameters for Godiva	77
Figure 34: Measured (green), computed (blue) and optimal (red) values for all 17 responses of benchmark Godiva. Error bars correspond to one standard deviation. All values are normalized to the experimental value. Note that the computational value of response r_{12} , r_{16} and r_{17} scales according to the right hand side y-axis.....	79
Figure 35: Normalized χ^2 for each excluded response at the first iteration	81
Figure 36: Normalized χ^2 for progressively excluded discrepant responses for Godiva	81
Figure 37: Measured, computed and optimal values for $N_r = 10$ responses with one standard deviation normalized to the nominal measured value.....	84
Figure 38: Measured, computed and optimal values for $N_r = 11$ responses with one standard deviation normalized to the nominal measured value.....	84

Figure 39: Relative change in the adjusted elastic scattering cross section of ^{235}U for particular sets of responses for Godiva	86
Figure 40: Nominal and adjusted relative standard deviation of the elastic scattering cross section of ^{235}U for particular sets of responses for Godiva.....	86
Figure 41: Relative change in the adjusted inelastic scattering cross section of ^{235}U for particular sets of responses for Godiva	87
Figure 42: Nominal and adjusted relative standard deviation of the inelastic scattering cross section of ^{235}U for particular sets of responses for Godiva.....	88
Figure 43: Relative change in the adjusted radiative capture cross section of ^{55}Mn for particular sets of responses for Godiva	88
Figure 44: Nominal and adjusted relative standard deviation of the radiative capture cross section of ^{235}U for particular sets of responses for Godiva.....	89
Figure 45: Non-zero elements in the covariance matrix \mathbf{C}_p of parameters. $\mathbf{C}_{\alpha\alpha}$ refers to the combined Jezebel systems, $\mathbf{C}_{\beta\beta}$ refers to Godiva and $\mathbf{C}_{\alpha\beta}$ contains the cross-terms, which indicate the coupling between the benchmarks.	90
Figure 46: Measured, computed and adjusted values for k_{eff} and one standard deviation for individual benchmarks (“be”), couple Jezebel benchmarks (“opt,1”) and coupled Jezebel benchmarks and Godiva (“opt,2”)	91
Figure 47: Measured, computed and adjusted values for <i>similar</i> responses and one standard deviation for individual benchmarks (“be”), couple Jezebel benchmarks (“opt,1”) and coupled Jezebel benchmarks and Godiva (“opt,2”).....	92
Figure 48: XY view of benchmark model for ZPR-6/7 Loading 41, [19]......	95
Figure 49: Axial dimensions in cm for the ZPR-6/7 Loading 41 benchmark R-Z model, [19].	95
Figure 50: KENOVI results for several ENDF/B libraries computed with both the R-Z model and the benchmark-model of the ZPR-6/7 assembly Loadings 12 and 41.	97

Figure 51: Denovo computations of the spectrum of the neutron flux for ZPR-6/7 Loading 41	98
Figure 52: Fast scalar flux of ZPR-6/7 at Z=0cm. Left half is computed with the R-Z model, right half is computed with the as-built model. Matrix positions which contain measurement foils are highlighted (not to scale).	99
Figure 53: Measured and computed (Denovo) k_{eff} and spectral indices at S-23/23 Z=0-2in. Error bars represent one standard deviation.....	100
Figure 54: Sensitivity profile of k_{eff} to selected parameters for ZPR-6/7 based on the R-Z model	102
Figure 55: Sensitivity profile of k_{eff} to selected parameters for ZPR-6/7 based on the as-built model	102
Figure 56: ZPR-6/7 measured, computed and best-estimate k_{eff} and spectral indices at location S-23/23 Z=0-2in. Error bars correspond with one standard deviation.	104
Figure 57: ZPR-6/7 measured, computed and best-estimate responses at location S-23/23 Z=28-30in. Error bars correspond with one standard deviation.....	105
Figure 58: ZPR-6/7 measured, computed and best-estimate responses at location S-23/37 Z=0-2in. Error bars correspond with one standard deviation.....	105
Figure 59: ZPR-6/7 measured, computed and best-estimate responses at location S-23/37 Z=28-30in. Error bars correspond with one standard deviation.....	106

Tables

Table 1: Material properties taken from [7] and assumed uncertainty of soil	22
Table 2: Synthetic data for heat conduction example with 10 Fourier coefficients at $t = 10s$.	24
Table 3: Measure and computed system response with relative standard deviation as well as best-estimate responses with their respective relative standard deviation	26
Table 4: Deviation between updated results according to non-partitioned (“be”) and partitioned (“opt”) data assimilation.....	28
Table 5: Pseudo-Code of block-wise inversion, excerpt of Appendix D	29
Table 6: Cases for block-matrix partitioning of data set A and B.....	31
Table 7: Parameter and response space of benchmarks	46
Table 8: Unity constraint for the best-estimate fission spectrum of selected fissionable nuclides prior and after renormalization of the covariance data	49
Table 9: Composition of the Plutonium in Jezebel-239 and Jezebel-240, [19].....	50
Table 10: Atom densities for the Jezebel-239 and Jezebel-240 benchmark, [19]	50
Table 11: Uncertainty contribution from Eq. (4.11) in k_{eff} and $r_2 = \frac{\sigma_f(^{238}U)}{\sigma_f(^{235}U)}$ for Jezebel-239	56
Table 12: Uncertainty contribution from Eq. (4.11) in k_{eff} and $r_2 = \frac{\sigma_f(^{238}U)}{\sigma_f(^{235}U)}$ for Jezebel-240	57
Table 13: Comparison of consistency indicator χ^2 for benchmarks Jezebel-239 and Jezebel-240 regarded as single models separately and coupled models.....	60
Table 14: Jezebel-239 and Jezebel-240 measured and computed (Denovo) response values, as well as best-estimate and optimal values (based on partitioned DA) for k_{eff}	62

Table 15: Jezebel-239 and Jezebel-240 measured and computed (Denovo) response values, as well as optimal values (based on partitioned DA) for <i>similar</i> reaction rate ratios.	63
Table 16: Measured and computed (Denovo) response values as well as best-estimate and optimal values (based on partitioned DA) for <i>dissimilar</i> reaction rate ratios of Jezebel-239. .	65
Table 17: Performance for partitioned DA algorithm compared to non-partitioned DA. Results shown are average values over 10 individual runs on 1 CPU.	73
Table 18: Atom densities for the Godiva benchmark, [19]	74
Table 19: Uncertainty contribution from Eq. (4.11) in k_{eff} and $r_2 = \frac{\sigma_f(^{238}U)}{\sigma_f(^{235}U)}$ of Godiva.....	78
Table 20: Godiva responses r_i and corresponding label	79
Table 21: Measured, computed and optimal values for 10 and 11 selected responses of Godiva.....	83
Table 22: k_{eff} for the homogeneous R-Z benchmark model as well as the as-built model computed using SCALE6.1 KENOVI with 650 generations, 100 000 particles per generation and the first 50 generations skipped	97

1. Introduction

Understanding and predicting the behavior of a system can be based on measurements or on numerical models. In many applications however neither of these approaches alone is able to provide an accurate picture of the behavior of the system. Despite best efforts, experiments contain errors and uncertainties in the measurements and generally provide an incomplete description of the system. Sources of uncertainty include, for example, operator errors, sampling population errors, and/or instrument errors. While some residual uncertainty in experimental data is unavoidable, quantifying this error is essential to data analysis. On the other hand, any numerical model is a simplification of the real world and contains uncertainties in model parameters, such as material properties, boundary conditions, and/or initial conditions. Due to these uncertainties, even a hypothetically perfect model would yield results that are different from the respective experimental observations. However, both sources of information – experiments and physically based mathematical models – are valuable and often complementary. Data assimilation (DA) is a methodology that integrates information from both measurements and computational results to obtain best-estimate values of the state of the system and thus improves the predictions. There exists a multitude of DA approaches, based either on deterministic or statistical concepts; see for example [8], [21] and [25]. An overview of the field is complicated by the fact that the same methodologies can be named interchangeably data assimilation as well as data adjustment, [37]. Furthermore, data assimilation is closely related to inverse theory problems which in turn come with their own specific terminology, [33]. Despite the various names most of these methods share an almost identical mathematical formulation and yield similar best-estimate results, [30]. In this work the mathematically rigorous formulation of [9] is used. The formulation referred to in [9] as predictive modeling is labeled throughout this work as data assimilation. A special feature of this particular methodology is the inclusion of a priori uncertainty information for correlations between responses and parameters. This information is rarely available in practice and based on the maximum entropy principle the a priori correlation matrix is assumed to be zero in this case. Even though the a priori elements of the correlation matrix are zero, the particular DA methodology of [9] yields best-estimate results for the a posteriori correlation between responses and parameters that are non-zero. The suitability of this particular DA formulation to various applications in nuclear engineering has been demonstrated in [2], [3], [6], [26], [5] and [27].

Any flavor of data assimilation relies on sensitivity analysis. This analysis yields coefficients that represent the change in some system response due to a change in an input parameter. The magnitude of change in a response is an indicator how important a particular parameter

is to the physical process. One of the first systematic sensitivity theories is usually attributed to the Russian scientist Usachev in the 1960s. Since then sensitivity analysis has undergone a series of theoretical developments and extensions to become the well-established method it is in nuclear analysis today, [28]. In general, sensitivity coefficients can be obtained deterministically with two different techniques, called direct or forward method and adjoint method. The direct method computes sensitivity coefficients by means of differences between two independent calculations basically calculating the forward finite difference of a small perturbation in a parameter. This method is especially computationally expensive if the system has few responses and many parameters. For such systems the adjoint sensitivity analysis is advantageous since the adjoint equations can be solved independently of the forward equations as long as the considered system is linear in the state variables. The assumption of linearity in the state variable is true for all applications considered in the present work. Once sensitivity coefficients are available they can be utilized for uncertainty estimation and parameter adjustment.

The mathematical framework of data assimilation is quite general and can be used for a wide variety of applications. General drawbacks of this method include the strong dependence of available a priori information, e.g. covariance data for parameters as well as responses. The quality of best-estimate predictions is limited by the quality of the data used as input. In case of nuclear data, great efforts have been made to compile a comprehensive covariance data library, but even this library is far from complete and has entries of varying fidelity, [31]. In case of experiments a loss of information regarding the experimental description and a lack of uncertainty information between similar experiments pose major problems.

1.1 Motivation and Objectives

Despite safety concerns in Germany, there has been a revival of interest in nuclear power as emission free source of energy worldwide. As new reactor concepts are emerging, the need for high-fidelity predictive computer simulations is increasing. Accompanied by the continuing computer technology progress this leads to a new development and application of multi-physics, multi-scale coupled methodologies for reactor analysis. This necessitates a data assimilation framework that can match these developments. Such a new method was presented in [10] and a first illustrative application of this new theory was shown in [22]. Based on these references, the objectives of the present work were set as the following:

- Implement the partitioned data assimilation theory in MATLAB. MATLAB is commercial mathematical software produced by Math Works Inc., [23], which

is used to develop mathematical algorithms, data visualization and data analysis. It is a convenient tool, which has high efficiency with matrix operations and uses simple scripting language. All this facilitates a fast way to gauge the computational considerations of an algorithm for a serial environment.

- Compare the computational cost with special regard to memory requirements of the new partitioned DA to the existing non-partitioned DA
- Identify suitable applications to demonstrate the validity and benefits of the partitioned data assimilation
- Model and compute the chosen benchmarks using the computational tools SCALE6.1 and Denovo of Oak Ridge National Laboratory (ORNL)
- Apply sensitivity analysis and uncertainty quantification to the chosen applications. Compare the updated values yielded by partitioned and non-partitioned data assimilation respectively

1.2 Outline of the Present Work

Chapter 2 presents the mathematical framework for data assimilation and simultaneous calibration of model parameters and responses for a time-independent physical system based on the formulation of [9]. The framework for partitioned data assimilation applicable to coupled multi-physics systems developed by D.G. Cacuci in [10] follows. Both methodologies include a quantitative indicator for determining the degree of consistency between measured and computed responses. Chapter 2 closes with a summary of essential equations necessary for implementing the partitioned DA in an algorithm.

Chapter 3 and 4 compare applications for both DA methods. 1-dimensional heat conduction with synthetic data is chosen as illustrative application to highlight major features of the partitioned DA in chapter 3. Synthetic data is advantageous because on the one hand systems tailored to specific problems can be created and on the other hand a wider variety of systems can be analyzed than is available as real-world benchmarks. The chapter begins with a small set of data which is adjusted via both the non-partitioned and partitioned DA to demonstrate that both methods yield identical results to numerical precision. This has already been shown in theory in [10]. Furthermore, the proposed computational benefit for the partitioned DA regarding memory requirements is analyzed with a large set of data. Lastly, this chapter presents deliberately discrepant sets of data as starting point for a consistency evaluation procedure. Again, a small set of data is considered first as detailed introduction to

the suggested consistency evaluation procedure. And finally the computational benefit of this procedure compared to the existing one is analyzed with large sets of data.

Chapter 4 applies the DA methods to well-known neutron transport benchmarks, namely the bare uranium sphere Godiva, the bare plutonium spheres Jezebel-239 and Jezebel-240 as well as the cylindrical assembly ZPR-6/7 which uses mixed plutonium-uranium-oxide as fuel and which has a thick depleted uranium reflector. The two different types of integral system response considered for the neutron transport applications in the present work are the effective multiplication factor k_{eff} and spectral indices. Input parameters of deterministic neutron transport models are usually comprised of microscopic multi-group neutron cross section data of major reaction types, the average prompt fission neutron multiplicity $\bar{\nu}$ and fission spectrum information. Special characteristics of utilizing fission spectrum information as parameter in data assimilation are also explained.

A brief description of each benchmark is given, followed by selected results of the sensitivity analysis and uncertainty quantification. Best-estimate values for the responses with reduced uncertainties as well as best-estimate values for selected parameters with reduced uncertainties are presented as well. Furthermore, each benchmark or combination of several benchmarks was chosen to demonstrate a particular feature of the partitioned DA. The two Jezebel benchmarks have been selected for the effect of strong coupling between systems. Next, the Godiva benchmark illustrates the consistency evaluation procedure in the presence of discrepant responses. The same benchmark in combination with the Jezebel benchmarks also shows the effect of weak coupling between uranium and plutonium systems. Finally the ZPR configuration demonstrates data assimilation on a large scale benchmark. Lastly, a summary of results and concluding remarks can be found in chapter 5.

2. Mathematical Framework for Data Assimilation

One particular data assimilation formulation for combining computational results with experiments to obtain best-estimate predictions of models was presented in [9]. Its mathematical framework is restated here for completeness. Completely analogous, the mathematical framework for the partitioned data assimilation recently developed by D. G. Cacuci in [10] is restated next. The reader is referred to these publications for a detailed theoretical derivation, here only a brief summary of each method is provided.

A time-independent physical system with N_α parameters and N_r distinct responses is initially analyzed. For instance, parameters can be material properties like density, thermal conductivity or neutron cross sections and responses can be measured quantities like temperature or neutron flux. Let $\mathbf{r}_m = \{r_i \mid i = 1, \dots, N_r\}$ denote the experimentally measured responses of the initial system and let $\boldsymbol{\alpha} = \{\alpha_n \mid n = 1, \dots, N_\alpha\}$ denote the parameters defining the model used to simulate theoretically these responses yielding the associated calculated values $\mathbf{r}_c = \{r_i \mid i = 1, \dots, N_r\}$. After the analysis of this initial system is completed, the partitioned DA method permits additional parameters and/or responses to be introduced. This could be useful in case additional information, e.g. previously unknown physics, becomes available or additional responses are desired. Also, in context of large multi-physics systems, this method enables the combination of single-physics subsystems that have been treated separately initially. Let the number of additional parameters and responses be denoted as N_β and N_q respectively. Next, let $\mathbf{q}_m = \{q_j \mid j = 1, \dots, N_q\}$ denote the experimentally measured responses of the additional system and let $\boldsymbol{\beta} = \{\beta_m \mid m = 1, \dots, N_\beta\}$ denote the parameters defining the model used to simulate theoretically these responses yielding the associated calculated values $\mathbf{q}_c = \{q_j \mid j = 1, \dots, N_q\}$.

2.1 Non-partitioned DA

Initially one system is considered separately, yielding the non-partitioned data assimilation formulation of [9]. The system parameters are considered to be variates with the nominal value $\boldsymbol{\alpha}^0$ for the parameters and a standard deviation of $\boldsymbol{\sigma}_\alpha$. The general form to describe the covariance between any two of the parameters α_i and α_j is the symmetric variance-covariance matrix

$$\mathbf{C}_{\alpha\alpha}^{(N_\alpha \times N_\alpha)} \equiv \left\langle (\boldsymbol{\alpha} - \boldsymbol{\alpha}^0)(\boldsymbol{\alpha} - \boldsymbol{\alpha}^0)^\dagger \right\rangle \quad (2.1)$$

with dimensions $(N_\alpha \times N_\alpha)$. For introduction purposes only, a notation that displays directly the dimension of each matrix is chosen. Later on, this notation is simplified to ease readability. The respective elements of this covariance matrix of the model parameters are

$$\text{cov}(\alpha_i, \alpha_j) \equiv E\left((\alpha_i - \alpha_i^0)(\alpha_j - \alpha_j^0)\right) = \langle \delta\alpha_i \delta\alpha_j \rangle. \quad (2.2)$$

where $\langle x \rangle$ denotes the expected value of x . The measured responses can be characterized in a similar way with nominal values \mathbf{r}_m and the symmetric covariance matrix

$$\mathbf{C}_{rr}^{(N_r \times N_r)} \equiv \left\langle (\mathbf{r} - \mathbf{r}_m)(\mathbf{r} - \mathbf{r}_m)^\dagger \right\rangle = \langle \delta\mathbf{r} \delta\mathbf{r}^\dagger \rangle. \quad (2.3)$$

The computed response \mathbf{r}_c is linearized by way of a Taylor-series expansion around the nominal values $\mathbf{r}_c = \mathbf{r}_c(\boldsymbol{\alpha}^0)$, such that the system can be written as

$$\mathbf{r} = \mathbf{r}_c(\boldsymbol{\alpha}^0) + \mathbf{S}_{r\alpha}(\boldsymbol{\alpha}^0)(\boldsymbol{\alpha} - \boldsymbol{\alpha}^0) + \text{higher-order terms}. \quad (2.4)$$

where $\mathbf{S}_{r\alpha}$ denotes the matrix of sensitivity coefficients. This sensitivity matrix contains the first derivatives of the computed responses \mathbf{r} with respect to the parameters $\boldsymbol{\alpha}$

$$\mathbf{S}_{r\alpha}^{(N_r \times N_\alpha)}(\boldsymbol{\alpha}^0) \equiv \begin{bmatrix} \frac{\partial r_1}{\partial \alpha_1} & \dots & \frac{\partial r_1}{\partial \alpha_{N_\alpha}} \\ \vdots & \frac{\partial r_i}{\partial \alpha_n} & \vdots \\ \frac{\partial r_{N_r}}{\partial \alpha_1} & \dots & \frac{\partial r_{N_r}}{\partial \alpha_{N_\alpha}} \end{bmatrix}. \quad (2.5)$$

Applying the propagation of uncertainty method results in the (first-order) expectation value $\langle \mathbf{r} \rangle = \mathbf{r}_c(\boldsymbol{\alpha}^0)$ and the covariance matrix of the computed responses

$$\mathbf{C}_{rc}^{(N_r \times N_r)}(\boldsymbol{\alpha}^0) = \left\langle \mathbf{S}_{r\alpha}(\boldsymbol{\alpha}^0)(\boldsymbol{\alpha} - \boldsymbol{\alpha}^0)(\boldsymbol{\alpha} - \boldsymbol{\alpha}^0)^\dagger \mathbf{S}_{r\alpha}(\boldsymbol{\alpha}^0)^\dagger \right\rangle = \mathbf{S}_{r\alpha}(\boldsymbol{\alpha}^0) \mathbf{C}_{\alpha\alpha} \mathbf{S}_{r\alpha}^\dagger(\boldsymbol{\alpha}^0). \quad (2.6)$$

Identifying a probability distribution that corresponds with the a priori available computational and experimental information as described above can be formulated as a moment-constrained maximum entropy problem, see [1], [9] and [33]. The most objective solution to the multidimensional 2-moment problem, as it is posed here, is the multivariate Gaussian of the form

$$P(\mathbf{z}|\mathbf{C})d\mathbf{z} = \frac{\exp\left[-\frac{1}{2}Q(\mathbf{z})\right]}{\sqrt{\det(2\pi\mathbf{C})}}d\mathbf{z}, \quad Q(\mathbf{z}) \equiv \mathbf{z}^\dagger \mathbf{C}^{-1} \mathbf{z}, \quad -\infty < z_j < \infty \quad (2.7)$$

with the vector \mathbf{z} combining parameters and responses

$$\mathbf{z} \equiv \begin{bmatrix} \boldsymbol{\alpha} - \boldsymbol{\alpha}^0 \\ \mathbf{r} - \mathbf{r}_m \end{bmatrix} \quad (2.8)$$

and the matrix \mathbf{C} combining all available uncertainty information

$$\mathbf{C} \equiv \begin{bmatrix} \mathbf{C}_{\alpha\alpha} & \mathbf{C}_{r\alpha}^\dagger \\ \mathbf{C}_{r\alpha} & \mathbf{C}_{rr} \end{bmatrix}. \quad (2.9)$$

Assuming quadratic loss, the best-estimate quantities can be computed as solutions to a constrained minimization problem. A suitable form for the later on minimization is

$$\text{Non-partitioned DA: } [\mathbf{S}_{r\alpha} \quad -\mathbf{I}]\mathbf{z} + \mathbf{r}_d = \mathbf{Z}(\boldsymbol{\alpha}^0)\mathbf{z} + \mathbf{r}_d = 0, \quad (2.10)$$

where \mathbf{I} denotes the identity matrix and \mathbf{r}_d describes the discrepancies between the nominal computed responses \mathbf{r}_c and the nominal measured responses \mathbf{r}_m . Appendix A provides the derivation of Eq. (2.10). It is this equation that now acts as the constraint for minimizing $Q(\mathbf{z})$ of Eq. (2.7). Let $\boldsymbol{\lambda}$ be a vector of Lagrange multipliers, then the augmented Lagrangian functional $P(\mathbf{z}, \boldsymbol{\lambda})$ follows with

$$P(\mathbf{z}, \boldsymbol{\lambda}) \equiv Q(\mathbf{z}) + 2\boldsymbol{\lambda}^\dagger [\mathbf{Z}(\boldsymbol{\alpha}^0)\mathbf{z} + \mathbf{r}_d] = \min, \quad \text{at } \mathbf{z} = \mathbf{z}^{be} \equiv \begin{bmatrix} \boldsymbol{\alpha}^{be} - \boldsymbol{\alpha}^0 \\ \mathbf{r}^{be} - \mathbf{r}_m \end{bmatrix}. \quad (2.11)$$

The solution to this constrained minimization problem is detailed in the Appendix of [9]. Here, only the final results for best-estimate parameters, responses and covariance matrices are listed in their time-independent form.

The best-estimate predicted nominal values \mathbf{a}^{be} for parameters are

$$\mathbf{a}^{be} = \mathbf{a}^0 + (\mathbf{C}_{ra} - \mathbf{C}_{\alpha\alpha} \cdot \mathbf{S}_{ra}^\dagger) \cdot \mathbf{C}_d^{-1} \cdot \mathbf{r}_d \quad (2.12)$$

where \mathbf{C}_d is the uncertainty matrix for the deviation vector \mathbf{r}_d

$$\begin{aligned} \mathbf{C}_d &\equiv \langle \mathbf{r}_d \cdot \mathbf{r}_d^\dagger \rangle \\ &= \mathbf{C}_{rc} - \mathbf{C}_{ra} \cdot \mathbf{S}_{ra}^\dagger - \mathbf{S}_{ra} \cdot \mathbf{C}_{ra}^\dagger + \mathbf{C}_{rr}. \end{aligned} \quad (2.13)$$

The best-estimate predicted nominal values \mathbf{r}^{be} for responses are

$$\mathbf{r}^{be} = \mathbf{r}_m + (\mathbf{C}_{rr} - \mathbf{C}_{ra} \cdot \mathbf{S}_{ra}^\dagger) \cdot \mathbf{C}_d^{-1} \cdot \mathbf{r}_d. \quad (2.14)$$

Finally, the best-estimate predicted covariance matrices $\mathbf{C}_{\alpha\alpha}^{be}$ for parameters and \mathbf{C}_{rr}^{be} for responses as well as the best-estimate predicted uncertainty correlation matrix \mathbf{C}_{ra}^{be} :

$$\mathbf{C}_{\alpha\alpha}^{be} = \mathbf{C}_{\alpha\alpha} - (\mathbf{C}_{ra}^\dagger - \mathbf{C}_{\alpha\alpha} \cdot \mathbf{S}_{ra}^\dagger) \cdot \mathbf{C}_d^{-1} \cdot (\mathbf{C}_{ra}^\dagger - \mathbf{C}_{\alpha\alpha} \cdot \mathbf{S}_{ra}^\dagger)^\dagger, \quad (2.15)$$

$$\mathbf{C}_{rr}^{be} = \mathbf{C}_{rr} - (\mathbf{C}_{rr} - \mathbf{C}_{ra} \cdot \mathbf{S}_{ra}^\dagger) \cdot \mathbf{C}_d^{-1} \cdot (\mathbf{C}_{rr} - \mathbf{C}_{ra} \cdot \mathbf{S}_{ra}^\dagger)^\dagger, \quad (2.16)$$

$$\mathbf{C}_{ra}^{be} = \mathbf{C}_{ra} - (\mathbf{C}_{rr} - \mathbf{C}_{ra} \cdot \mathbf{S}_{ra}^\dagger) \cdot \mathbf{C}_d^{-1} \cdot (\mathbf{C}_{ra}^\dagger - \mathbf{C}_{\alpha\alpha} \cdot \mathbf{S}_{ra}^\dagger)^\dagger. \quad (2.17)$$

This concludes the non-partitioned data assimilation for a single system as derived in [9].

2.2 Subsystem II and Coupling Terms

Here an additional system is introduced and combined with the existing system – now referred to as subsystem I – as introduced in the previous section. Completely analogous to subsystem I the parameters of the additional system are variates with mean values $\boldsymbol{\beta}^0$ and a

standard deviation of σ_β . Parallel to Eq. (2.1) the symmetric variance-covariance matrix between any two of the parameters β_i and β_j is defined as

$$\mathbf{C}_{\beta\beta}^{(N_\beta \times N_\beta)} \equiv \left\langle (\boldsymbol{\beta} - \boldsymbol{\beta}^0)(\boldsymbol{\beta} - \boldsymbol{\beta}^0)^\dagger \right\rangle \quad (2.18)$$

and the respective elements of this covariance matrix of the additional parameters are analogous to Eq. (2.2)

$$\text{cov}(\beta_i, \beta_j) \equiv \left\langle (\beta_i - \beta_i^0)(\beta_j - \beta_j^0) \right\rangle = \left\langle \delta\beta_i \delta\beta_j \right\rangle. \quad (2.19)$$

In addition to the covariance matrix $\mathbf{C}_{\beta\beta}$ for additional parameters $\boldsymbol{\beta}$ of subsystem II only, the uncertainty between one particular parameter α_i of subsystem I and one particular parameter β_j of subsystem II is contained in the correlation matrix $\mathbf{C}_{\alpha\beta}$

$$\begin{aligned} \mathbf{C}_{\alpha\beta}^{(N_\alpha \times N_\beta)} &\equiv \left\langle (\boldsymbol{\alpha} - \boldsymbol{\alpha}^0)(\boldsymbol{\beta} - \boldsymbol{\beta}^0)^\dagger \right\rangle \\ &= \left[\mathbf{C}_{\beta\alpha}^{(N_\beta \times N_\alpha)} \right]^\dagger \end{aligned} \quad (2.20)$$

$$\text{cov}(\alpha_i, \beta_j) \equiv \left\langle (\alpha_i - \alpha_i^0)(\beta_j - \beta_j^0) \right\rangle. \quad (2.21)$$

Depending on the number of parameters in each subsystem this correlation matrix may or may not be square. In fact, it would only be square in the rare case when the number of parameters in both systems match, i.e. $N_\alpha = N_\beta$.

The additionally measured responses can be characterized in a way similar to Eq. (2.3) with mean values of responses \mathbf{q}_m of subsystem 2 the variance-covariance matrix is

$$\mathbf{C}_{qq}^{(N_q \times N_q)} \equiv \left\langle (\mathbf{q} - \mathbf{q}_m)(\mathbf{q} - \mathbf{q}_m)^\dagger \right\rangle. \quad (2.22)$$

Furthermore, responses of subsystem I and II can be correlated. This uncertainty information is expressed via a correlation matrix \mathbf{C}_{rq}

$$\begin{aligned}\mathbf{C}_{rq}^{(N_r \times N_q)} &\equiv \left\langle (\mathbf{r} - \mathbf{r}_m)(\mathbf{q} - \mathbf{q}_m)^\dagger \right\rangle \\ &= \left[\mathbf{C}_{qr}^{(N_q \times N_r)} \right]^\dagger\end{aligned}\quad (2.23)$$

$$\text{cov}(r_i, q_j) \equiv \left\langle (r_i - r_i^m)(q_j - q_j^m) \right\rangle. \quad (2.24)$$

This covariance matrix is only square in case the number responses for each subsystem match exactly, i.e. $N_r = N_q$.

So far, individual matrices for each subsystem or coupling terms between the subsystems have been introduced. The next step is to think of these matrices as blocks of a super-matrix combining the information of both subsystems.

The variance-covariance information between all parameters, both initial $\boldsymbol{\alpha}$ and additional $\boldsymbol{\beta}$, takes the form of a block matrix combining Eqs. (2.1), (2.18) and (2.20).

$$\mathbf{C}_p^{(N_\alpha + N_\beta) \times (N_\alpha + N_\beta)} = \begin{bmatrix} \mathbf{C}_{\alpha\alpha}^{(N_\alpha \times N_\alpha)} & \mathbf{C}_{\alpha\beta}^{(N_\alpha \times N_\beta)} \\ \mathbf{C}_{\beta\alpha}^{(N_\beta \times N_\alpha)} & \mathbf{C}_{\beta\beta}^{(N_\beta \times N_\beta)} \end{bmatrix} = \begin{bmatrix} \mathbf{C}_{\alpha\alpha}^{(N_\alpha \times N_\alpha)} & \mathbf{C}_{\alpha\beta}^{(N_\alpha \times N_\beta)} \\ \mathbf{C}_{\alpha\beta}^\dagger & \mathbf{C}_{\beta\beta}^{(N_\beta \times N_\beta)} \end{bmatrix} \quad (2.25)$$

This resulting variance-covariance block matrix \mathbf{C}_p is now symmetric for all cases and contains all a priori available uncertainty information for parameters. In a similar way, the variance-covariance matrix for all measured responses, again including both the initial responses \mathbf{r}_m and the additional ones \mathbf{q}_m , can be combined into a block matrix based on Eqs. (2.3), (2.22) and (2.23).

$$\mathbf{C}_m^{(N_r + N_q) \times (N_r + N_q)} = \begin{bmatrix} \mathbf{C}_{rr}^{(N_r \times N_r)} & \mathbf{C}_{rq}^{(N_r \times N_q)} \\ \mathbf{C}_{qr}^{(N_q \times N_r)} & \mathbf{C}_{qq}^{(N_q \times N_q)} \end{bmatrix} = \begin{bmatrix} \mathbf{C}_{rr}^{(N_r \times N_r)} & \mathbf{C}_{rq}^{(N_r \times N_q)} \\ \mathbf{C}_{rq}^\dagger & \mathbf{C}_{qq}^{(N_q \times N_q)} \end{bmatrix} \quad (2.26)$$

The resulting variance-covariance matrix is again symmetric and contains all a priori available uncertainty information for measured responses. Additionally, the uncertainty between the responses \mathbf{r} of subsystem I and any additional parameters $\boldsymbol{\beta}$ as well as the uncertainty between additional responses \mathbf{q} of subsystem II and parameters $\boldsymbol{\alpha}$ are included using the block matrix \mathbf{C}_{pm} ,

$$\begin{aligned}
 \mathbf{C}_{pm}^{(N_\alpha+N_\beta) \times (N_r+N_q)} &\equiv \left\langle \left(\begin{array}{c} \boldsymbol{\alpha} - \boldsymbol{\alpha}^0 \\ \boldsymbol{\beta} - \boldsymbol{\beta}^0 \end{array} \right) \left((\mathbf{r} - \mathbf{r}_m)^\dagger (\mathbf{q} - \mathbf{q}_m)^\dagger \right) \right\rangle \\
 &= \begin{pmatrix} \langle \delta \boldsymbol{\alpha} \delta \mathbf{r}^\dagger \rangle & \langle \delta \boldsymbol{\alpha} \delta \mathbf{q}^\dagger \rangle \\ \langle \delta \boldsymbol{\beta} \delta \mathbf{r}^\dagger \rangle & \langle \delta \boldsymbol{\beta} \delta \mathbf{q}^\dagger \rangle \end{pmatrix} \\
 &= \begin{bmatrix} \mathbf{C}_{ar}^{(N_\alpha \times N_r)} & \mathbf{C}_{aq}^{(N_\alpha \times N_q)} \\ \mathbf{C}_{br}^{(N_\beta \times N_r)} & \mathbf{C}_{bq}^{(N_\beta \times N_q)} \end{bmatrix}.
 \end{aligned} \tag{2.27}$$

Equivalent to the procedure applied to subsystem I by itself in chapter 2.1, the responses of the combined system $\mathbf{r}_A = \begin{bmatrix} \mathbf{r} \\ \mathbf{q} \end{bmatrix}$ is linearized via a Taylor-series expansion around the nominal values $\mathbf{r}_{A,c}^0$ of the computed responses. The system can therefore be written analogous to Eq. (2.4)

$$\mathbf{r}_A = \mathbf{r}_{A,c}(\boldsymbol{\alpha}^0, \boldsymbol{\beta}^0) + \mathbf{S}(\boldsymbol{\alpha}^0, \boldsymbol{\beta}^0) (\boldsymbol{\alpha} - \boldsymbol{\alpha}^0, \boldsymbol{\beta} - \boldsymbol{\beta}^0)^\dagger + \text{higher-order terms}. \tag{2.28}$$

with the sensitivity matrix $\mathbf{S}^{(N_r+N_q) \times (N_\alpha+N_\beta)}$ now dependent on both initial and additional parameters, $\boldsymbol{\alpha}$ and $\boldsymbol{\beta}$ respectively. Written out in detail and accounting for the additional sensitivity coefficients Eq. (2.28) is

$$\mathbf{r}_A - \mathbf{r}_{A,c}(\boldsymbol{\alpha}^0) = \begin{bmatrix} \frac{\partial r_1}{\partial \alpha_1} & \dots & \frac{\partial r_1}{\partial \alpha_{N_\alpha}} & \frac{\partial r_1}{\partial \beta_1} & \dots & \frac{\partial r_1}{\partial \beta_{N_\beta}} \\ \vdots & \ddots & \vdots & \vdots & \ddots & \vdots \\ \frac{\partial r_{N_\alpha}}{\partial \alpha_1} & \dots & \frac{\partial r_{N_\alpha}}{\partial \alpha_{N_\alpha}} & \frac{\partial r_{N_\alpha}}{\partial \beta_1} & \dots & \frac{\partial r_{N_\alpha}}{\partial \beta_{N_\beta}} \\ \frac{\partial q_1}{\partial \alpha_1} & \dots & \frac{\partial q_1}{\partial \alpha_{N_\alpha}} & \frac{\partial q_1}{\partial \beta_1} & \dots & \frac{\partial q_1}{\partial \beta_{N_\beta}} \\ \vdots & \ddots & \vdots & \vdots & \ddots & \vdots \\ \frac{\partial q_{N_q}}{\partial \alpha_1} & \dots & \frac{\partial q_{N_q}}{\partial \alpha_{N_\alpha}} & \frac{\partial q_{N_q}}{\partial \beta_1} & \dots & \frac{\partial q_{N_q}}{\partial \beta_{N_\beta}} \end{bmatrix} \begin{bmatrix} \alpha_1 - \alpha_1^0 \\ \vdots \\ \alpha_{N_\alpha} - \alpha_{N_\alpha}^0 \\ \beta_1 - \beta_1^0 \\ \vdots \\ \beta_{N_\beta} - \beta_{N_\beta}^0 \end{bmatrix}$$

$$\mathbf{r}_A - \mathbf{r}_{A,c}(\boldsymbol{\alpha}^0) = \underbrace{\begin{bmatrix} \mathbf{S}_{r\alpha}^{(N_r \times N_\alpha)} & \mathbf{S}_{r\beta}^{(N_r \times N_\beta)} \\ \mathbf{S}_{q\alpha}^{(N_q \times N_\alpha)} & \mathbf{S}_{q\beta}^{(N_q \times N_\beta)} \end{bmatrix}}_{\mathbf{S}} \begin{bmatrix} \boldsymbol{\alpha} - \boldsymbol{\alpha}^0 \\ \boldsymbol{\beta} - \boldsymbol{\beta}^0 \end{bmatrix}. \quad (2.29)$$

For instance, the particular block $\mathbf{S}_{r\alpha}^{(N_r \times N_\alpha)}$ stems from the subsystem I and is equivalent to Eq. (2.5) of the non-partitioned DA. The covariance matrix for the computed, augmented responses is

$$\mathbf{C}_c^{(N_r+N_q) \times (N_r+N_q)} = \underbrace{\begin{bmatrix} \mathbf{S}_{r\alpha} & \mathbf{S}_{r\beta} \\ \mathbf{S}_{q\alpha} & \mathbf{S}_{q\beta} \end{bmatrix}}_{\mathbf{S}} \underbrace{\begin{bmatrix} \mathbf{C}_{\alpha\alpha} & \mathbf{C}_{\alpha\beta} \\ \mathbf{C}_{\alpha\beta}^\dagger & \mathbf{C}_{\beta\beta} \end{bmatrix}}_{\mathbf{C}_p} \underbrace{\begin{bmatrix} \mathbf{S}_{r\alpha}^\dagger & \mathbf{S}_{r\beta}^\dagger \\ \mathbf{S}_{q\alpha}^\dagger & \mathbf{S}_{q\beta}^\dagger \end{bmatrix}}_{\mathbf{S}^\dagger}. \quad (2.30)$$

Eq. (2.30) is thus the equivalent for a partitioned system to Eq. (2.6) for a non-partitioned system. Analogous to Eq. (2.7) application of the maximum entropy algorithm to the combined system of subsystem I and II yields a multivariate Gaussian of the form

$$P(\mathbf{z}_A | \mathbf{C}_A) d\mathbf{z}_A = \frac{\exp\left[-\frac{1}{2} \mathbf{z}_A^\dagger \mathbf{C}_A^{-1} \mathbf{z}_A\right]}{\sqrt{\det(2\pi \mathbf{C}_A)}} d\mathbf{z}_A, \quad Q(\mathbf{z}_A) \equiv \mathbf{z}_A^\dagger \mathbf{C}_A^{-1} \mathbf{z}_A, \quad -\infty < z_j < \infty \quad (2.31)$$

with the vector \mathbf{z}_A now combining parameters and responses of both subsystems

$$\mathbf{z}_A \equiv \begin{bmatrix} \boldsymbol{\alpha} - \boldsymbol{\alpha}^0 \\ \boldsymbol{\beta} - \boldsymbol{\beta}^0 \\ \mathbf{r} - \mathbf{r}_m \\ \mathbf{q} - \mathbf{q}_m \end{bmatrix} \quad (2.32)$$

and the matrix

$$\mathbf{C}_A \equiv \begin{bmatrix} \mathbf{C}_{\alpha\alpha} & \mathbf{C}_{\alpha\beta} & \mathbf{C}_{\alpha r} & \mathbf{C}_{\alpha q} \\ \mathbf{C}_{\beta\alpha} & \mathbf{C}_{\beta\beta} & \mathbf{C}_{\beta r} & \mathbf{C}_{\beta q} \\ \mathbf{C}_{r\alpha} & \mathbf{C}_{r\beta} & \mathbf{C}_{rr} & \mathbf{C}_{rq} \\ \mathbf{C}_{q\alpha} & \mathbf{C}_{q\beta} & \mathbf{C}_{qr} & \mathbf{C}_{qq} \end{bmatrix} = \begin{bmatrix} \mathbf{C}_p & \mathbf{C}_{rp}^\dagger \\ \mathbf{C}_{rp} & \mathbf{C}_m \end{bmatrix} \quad (2.33)$$

This symmetric block matrix contains all the available uncertainty information and results from a combination of Eqs. (2.25), (2.26) and (2.27). Assuming quadratic loss, the best-

estimate quantities can be computed as solutions to a constrained minimization problem. A suitable form, derived in Appendix A, for the later on minimization is

$$\text{partitioned DA: } [\mathbf{S} \quad -\mathbf{I}] \mathbf{z}_A + \begin{bmatrix} \mathbf{r}_d \\ \mathbf{q}_d \end{bmatrix} = 0. \quad (2.34)$$

Eq. (2.33) is the equivalent of Eq. (2.10) for partitioned systems. In addition to the deviation vector \mathbf{r}_d for responses of subsystem I there exists now a deviation vector \mathbf{q}_d for responses of subsystem II,

$$\mathbf{r}_d \equiv \mathbf{r}_c(\boldsymbol{\alpha}^0, \boldsymbol{\beta}^0) - \mathbf{r}_m \quad \text{and} \quad \mathbf{q}_d \equiv \mathbf{q}_c(\boldsymbol{\alpha}^0, \boldsymbol{\beta}^0) - \mathbf{q}_m. \quad (2.35)$$

Again, using the method of Lagrange multipliers the functional $P(\boldsymbol{\alpha}, \boldsymbol{\beta}, \mathbf{r}, \mathbf{q}, \boldsymbol{\lambda}_r, \boldsymbol{\lambda}_q)$ for the constraint minimization becomes

$$P(\mathbf{z}_A, \boldsymbol{\lambda}) = \underbrace{\begin{bmatrix} \boldsymbol{\alpha}^{opt} - \boldsymbol{\alpha}^0 \\ \boldsymbol{\beta}^{opt} - \boldsymbol{\beta}^0 \\ \mathbf{r}^{opt} - \mathbf{r}_m \\ \mathbf{q}^{opt} - \mathbf{q}_m \end{bmatrix}}_{\mathbf{z}_A^\dagger} \mathbf{C}_A^{-1} \underbrace{\begin{bmatrix} \boldsymbol{\alpha}^{opt} - \boldsymbol{\alpha}^0 \\ \boldsymbol{\beta}^{opt} - \boldsymbol{\beta}^0 \\ \mathbf{r}^{opt} - \mathbf{r}_m \\ \mathbf{q}^{opt} - \mathbf{q}_m \end{bmatrix}}_{\mathbf{z}_A} + 2 \left[\begin{bmatrix} \boldsymbol{\lambda}_r^\dagger \\ \boldsymbol{\lambda}_q^\dagger \end{bmatrix} \mathbf{S}(\boldsymbol{\alpha}^0, \boldsymbol{\beta}^0) - \begin{bmatrix} \boldsymbol{\lambda}_r^\dagger \\ \boldsymbol{\lambda}_q^\dagger \end{bmatrix} \right] \underbrace{\begin{bmatrix} \boldsymbol{\alpha}^{opt} - \boldsymbol{\alpha}^0 \\ \boldsymbol{\beta}^{opt} - \boldsymbol{\beta}^0 \\ \mathbf{r}^{opt} - \mathbf{r}_m \\ \mathbf{q}^{opt} - \mathbf{q}_m \end{bmatrix}}_{\mathbf{z}_A} + 2 \begin{bmatrix} \boldsymbol{\lambda}_r^\dagger \\ \boldsymbol{\lambda}_q^\dagger \end{bmatrix} \begin{bmatrix} \mathbf{r}_d \\ \mathbf{q}_d \end{bmatrix}. \quad (2.36)$$

Eq. (2.36) is the equivalent of Eq. (2.11) for partitioned systems at the minimum. Note that the updated values for the partitioned DA are denoted as ‘‘optimal’’. This label is introduced to keep the calibrated values of the partitioned DA apart from the best-estimate values of the non-partitioned DA. A detailed derivation of the optimal predicted values for the partitioned data assimilation can be found in Appendix B based on [10]. Here, only the final results are reported.

2.2.1 Optimal Predicted Values for Parameters

$$\boldsymbol{\alpha}^{opt} = \boldsymbol{\alpha}^0 - \left[\underbrace{\mathbf{C}_{\alpha\alpha} \mathbf{S}_{r\alpha}^\dagger + \mathbf{C}_{\alpha\beta} \mathbf{S}_{r\beta}^\dagger - \mathbf{C}_{\alpha r}}_{\mathbf{X}_\alpha}, \underbrace{\mathbf{C}_{\alpha\alpha} \mathbf{S}_{q\alpha}^\dagger + \mathbf{C}_{\alpha\beta} \mathbf{S}_{q\beta}^\dagger - \mathbf{C}_{\alpha q}}_{\mathbf{Y}_\alpha} \right] \mathbf{D}^{-1} \begin{bmatrix} \mathbf{r}_c - \mathbf{r}_m \\ \mathbf{q}_c - \mathbf{q}_m \end{bmatrix} \quad (2.37)$$

$$\boldsymbol{\beta}^{opt} = \boldsymbol{\beta}^0 - \left[\underbrace{\mathbf{C}_{\alpha\beta}^\dagger \mathbf{S}_{r\alpha}^\dagger + \mathbf{C}_{\beta\beta}^\dagger \mathbf{S}_{r\beta}^\dagger - \mathbf{C}_{\beta r}^\dagger}_{\mathbf{X}_\beta}, \underbrace{\mathbf{C}_{\alpha\beta}^\dagger \mathbf{S}_{q\alpha}^\dagger + \mathbf{C}_{\beta\beta}^\dagger \mathbf{S}_{q\beta}^\dagger - \mathbf{C}_{\beta q}^\dagger}_{\mathbf{Y}_\beta} \right] \mathbf{D}^{-1} \begin{bmatrix} \mathbf{r}_c - \mathbf{r}_m \\ \mathbf{q}_c - \mathbf{q}_m \end{bmatrix} \quad (2.38)$$

where \mathbf{D} is a block matrix for the uncertainty of the deviation vector $\begin{bmatrix} \mathbf{r}_d & \mathbf{q}_d \end{bmatrix}^\dagger$,

$$\begin{aligned} \mathbf{D} &= \begin{bmatrix} \mathbf{D}_{rr} & \mathbf{D}_{rq} \\ \mathbf{D}_{rq}^\dagger & \mathbf{D}_{qq} \end{bmatrix} = \left\langle \begin{bmatrix} \mathbf{r}_c - \mathbf{r}_m \\ \mathbf{q}_c - \mathbf{q}_m \end{bmatrix} \begin{bmatrix} \mathbf{r}_c - \mathbf{r}_m \\ \mathbf{q}_c - \mathbf{q}_m \end{bmatrix}^\dagger \right\rangle \\ &= \left\langle \begin{bmatrix} \mathbf{r}_d \\ \mathbf{q}_d \end{bmatrix} \begin{bmatrix} \mathbf{r}_d^\dagger & \mathbf{q}_d^\dagger \end{bmatrix} \right\rangle = \begin{pmatrix} \langle \mathbf{r}_d \cdot \mathbf{r}_d^\dagger \rangle & \langle \mathbf{q}_d \cdot \mathbf{r}_d^\dagger \rangle \\ \langle \mathbf{r}_d \cdot \mathbf{q}_d^\dagger \rangle & \langle \mathbf{q}_d \cdot \mathbf{q}_d^\dagger \rangle \end{pmatrix}. \end{aligned} \quad (2.39)$$

The individual blocks are defined as

$$\mathbf{D}_{rr} = \mathbf{S}_{r\alpha} \mathbf{X}_\alpha + \mathbf{S}_{r\beta} \mathbf{X}_\beta - \mathbf{X}_r, \quad (2.40)$$

$$\mathbf{D}_{qq} = \mathbf{S}_{q\alpha} \mathbf{Y}_\alpha + \mathbf{S}_{q\beta} \mathbf{Y}_\beta - \mathbf{Y}_q, \quad (2.41)$$

$$\mathbf{D}_{rq} = \mathbf{S}_{r\alpha} \mathbf{Y}_\alpha + \mathbf{S}_{r\beta} \mathbf{Y}_\beta - \mathbf{Y}_r. \quad (2.42)$$

The matrices \mathbf{X}_r , \mathbf{Y}_r , \mathbf{X}_q and \mathbf{Y}_q are defined in section 2.2.2 immediately below.

Computing the inverse of the block matrix \mathbf{D} is discussed in chapter 3.4 for the implementation as algorithm.

2.2.2 Optimal Predicted Values for Responses

$$\mathbf{r}^{opt} = \mathbf{r}_m - \left[\underbrace{\mathbf{C}_{\alpha r}^\dagger \mathbf{S}_{r\alpha}^\dagger + \mathbf{C}_{\beta r}^\dagger \mathbf{S}_{r\beta}^\dagger - \mathbf{C}_{rr}^\dagger}_{\mathbf{X}_r}, \underbrace{\mathbf{C}_{\alpha r}^\dagger \mathbf{S}_{q\alpha}^\dagger + \mathbf{C}_{\beta r}^\dagger \mathbf{S}_{q\beta}^\dagger - \mathbf{C}_{rq}^\dagger}_{\mathbf{Y}_r} \right] \mathbf{D}^{-1} \begin{bmatrix} \mathbf{r}_c - \mathbf{r}_m \\ \mathbf{q}_c - \mathbf{q}_m \end{bmatrix} \quad (2.43)$$

$$\mathbf{q}^{opt} = \mathbf{q}_m - \left[\underbrace{\mathbf{C}_{\alpha q}^\dagger \mathbf{S}_{r\alpha}^\dagger + \mathbf{C}_{\beta q}^\dagger \mathbf{S}_{r\beta}^\dagger - \mathbf{C}_{rq}^\dagger}_{\mathbf{X}_q}, \underbrace{\mathbf{C}_{\alpha q}^\dagger \mathbf{S}_{q\alpha}^\dagger + \mathbf{C}_{\beta q}^\dagger \mathbf{S}_{q\beta}^\dagger - \mathbf{C}_{qq}^\dagger}_{\mathbf{Y}_q} \right] \mathbf{D}^{-1} \begin{bmatrix} \mathbf{r}_c - \mathbf{r}_m \\ \mathbf{q}_c - \mathbf{q}_m \end{bmatrix} \quad (2.44)$$

2.2.3 Optimal Predicted Variance-Covariance Matrices for Parameters

$$\begin{aligned}
 \mathbf{C}_{\alpha\alpha}^{opt} &\equiv \left\langle (\boldsymbol{\alpha} - \boldsymbol{\alpha}^{opt})(\boldsymbol{\alpha} - \boldsymbol{\alpha}^{opt})^\dagger \right\rangle \\
 &= \mathbf{C}_{\alpha\alpha} - [\mathbf{X}_\alpha, \mathbf{Y}_\alpha] \mathbf{D}^{-1} \begin{bmatrix} \mathbf{X}_\alpha^\dagger \\ \mathbf{Y}_\alpha^\dagger \end{bmatrix} \\
 &= \mathbf{C}_{\alpha\alpha} - \left((\mathbf{X}_\alpha \mathbf{D}_{11} + \mathbf{Y}_\alpha \mathbf{D}_{12}^\dagger) \mathbf{X}_\alpha^\dagger + (\mathbf{X}_\alpha \mathbf{D}_{12} + \mathbf{Y}_\alpha \mathbf{D}_{22}) \mathbf{Y}_\alpha^\dagger \right)
 \end{aligned} \tag{2.45}$$

$$\begin{aligned}
 \mathbf{C}_{\beta\beta}^{opt} &\equiv \left\langle (\boldsymbol{\beta} - \boldsymbol{\beta}^{opt})(\boldsymbol{\beta} - \boldsymbol{\beta}^{opt})^\dagger \right\rangle \\
 &= \mathbf{C}_{\beta\beta} - [\mathbf{X}_\beta, \mathbf{Y}_\beta] \mathbf{D}^{-1} \begin{bmatrix} \mathbf{X}_\beta^\dagger \\ \mathbf{Y}_\beta^\dagger \end{bmatrix} \\
 &= \mathbf{C}_{\beta\beta} - \left((\mathbf{X}_\beta \mathbf{D}_{11} + \mathbf{Y}_\beta \mathbf{D}_{12}^\dagger) \mathbf{X}_\beta^\dagger + (\mathbf{X}_\beta \mathbf{D}_{12} + \mathbf{Y}_\beta \mathbf{D}_{22}) \mathbf{Y}_\beta^\dagger \right).
 \end{aligned} \tag{2.46}$$

$$\begin{aligned}
 \mathbf{C}_{\alpha\beta}^{opt} &\equiv \left\langle (\boldsymbol{\alpha} - \boldsymbol{\alpha}^{opt})(\boldsymbol{\beta} - \boldsymbol{\beta}^{opt})^\dagger \right\rangle \\
 &= \mathbf{C}_{\alpha\beta} - [\mathbf{X}_\alpha, \mathbf{Y}_\alpha] \mathbf{D}^{-1} \begin{bmatrix} \mathbf{X}_\beta^\dagger \\ \mathbf{Y}_\beta^\dagger \end{bmatrix} \\
 &= \mathbf{C}_{\alpha\beta} - \left((\mathbf{X}_\alpha \mathbf{D}_{11} + \mathbf{Y}_\alpha \mathbf{D}_{12}^\dagger) \mathbf{X}_\beta^\dagger + (\mathbf{X}_\alpha \mathbf{D}_{12} + \mathbf{Y}_\alpha \mathbf{D}_{22}) \mathbf{Y}_\beta^\dagger \right).
 \end{aligned} \tag{2.47}$$

The individual blocks of the inverse of \mathbf{D} can be computed via block-wise inversion, [\[11\]](#)

$$\mathbf{D}^{-1} = \begin{bmatrix} \mathbf{D}_{11} & \mathbf{D}_{12} \\ \mathbf{D}_{12}^\dagger & \mathbf{D}_{22} \end{bmatrix} = \begin{bmatrix} \mathbf{D}_{rr}^{-1} + \mathbf{D}_{rr}^{-1} \mathbf{D}_{rq} \mathbf{D}_{22} \mathbf{D}_{rq}^\dagger \mathbf{D}_{rr}^{-1} & -\mathbf{D}_{rr}^{-1} \mathbf{D}_{rq} \mathbf{D}_{22} \\ -\mathbf{D}_{22} \mathbf{D}_{rq}^\dagger \mathbf{D}_{rr}^{-1} & (\mathbf{D}_{22} - \mathbf{D}_{rq}^\dagger \mathbf{D}_{rr}^{-1} \mathbf{D}_{rq})^{-1} \end{bmatrix}. \tag{2.48}$$

2.2.4 Optimal Predicted Variance-Covariance Matrices for Responses

$$\begin{aligned}
 \mathbf{C}_{rr}^{opt} &\equiv \left\langle (\mathbf{r} - \mathbf{r}^{opt})(\mathbf{r} - \mathbf{r}^{opt})^\dagger \right\rangle \\
 &= \mathbf{C}_{rr} - [\mathbf{X}_r, \mathbf{Y}_r] \mathbf{D}^{-1} \begin{bmatrix} \mathbf{X}_r^\dagger \\ \mathbf{Y}_r^\dagger \end{bmatrix} \\
 &= \mathbf{C}_{rr} - \left((\mathbf{X}_r \mathbf{D}_{11} + \mathbf{Y}_r \mathbf{D}_{12}^\dagger) \mathbf{X}_r^\dagger + (\mathbf{X}_r \mathbf{D}_{12} + \mathbf{Y}_r \mathbf{D}_{22}) \mathbf{Y}_r^\dagger \right),
 \end{aligned} \tag{2.49}$$

$$\begin{aligned}
 \mathbf{C}_{qq}^{opt} &\equiv \left\langle (\mathbf{q} - \mathbf{q}^{opt})(\mathbf{q} - \mathbf{q}^{opt})^\dagger \right\rangle \\
 &= \mathbf{C}_{qq} - [\mathbf{X}_q, \mathbf{Y}_q] \mathbf{D}^{-1} \begin{bmatrix} \mathbf{X}_q^\dagger \\ \mathbf{Y}_q^\dagger \end{bmatrix} \\
 &= \mathbf{C}_{qq} - \left((\mathbf{X}_q \mathbf{D}_{11} + \mathbf{Y}_q \mathbf{D}_{12}^\dagger) \mathbf{X}_q^\dagger + (\mathbf{X}_q \mathbf{D}_{12} + \mathbf{Y}_q \mathbf{D}_{22}) \mathbf{Y}_q^\dagger \right),
 \end{aligned} \tag{2.50}$$

$$\begin{aligned}
 \mathbf{C}_{rq}^{opt} &\equiv \left\langle (\mathbf{r} - \mathbf{r}^{opt})(\mathbf{q} - \mathbf{q}^{opt})^\dagger \right\rangle & (2.51) \\
 &= \mathbf{C}_{rq} - [\mathbf{X}_r, \mathbf{Y}_r] \mathbf{D}^{-1} \begin{bmatrix} \mathbf{X}_q^\dagger \\ \mathbf{Y}_q^\dagger \end{bmatrix} \\
 &= \mathbf{C}_{rq} - \left((\mathbf{X}_r \mathbf{D}_{11} + \mathbf{Y}_r \mathbf{D}_{12}^\dagger) \mathbf{X}_q^\dagger + (\mathbf{X}_r \mathbf{D}_{12} + \mathbf{Y}_r \mathbf{D}_{22}) \mathbf{Y}_q^\dagger \right).
 \end{aligned}$$

2.2.5 Optimal Predicted Correlation Matrices for Responses and Parameters

$$\begin{aligned}
 \mathbf{C}_{ar}^{opt} &\equiv \left\langle (\boldsymbol{\alpha} - \boldsymbol{\alpha}^{opt})(\mathbf{r} - \mathbf{r}^{opt})^\dagger \right\rangle \\
 &= \mathbf{C}_{ar} - [\mathbf{X}_\alpha, \mathbf{Y}_\alpha] \mathbf{D}^{-1} \begin{bmatrix} \mathbf{X}_r^\dagger \\ \mathbf{Y}_r^\dagger \end{bmatrix} & (2.52) \\
 &= \mathbf{C}_{ar} - \left((\mathbf{X}_\alpha \mathbf{D}_{11} + \mathbf{Y}_\alpha \mathbf{D}_{12}^\dagger) \mathbf{X}_r^\dagger + (\mathbf{X}_\alpha \mathbf{D}_{12} + \mathbf{Y}_\alpha \mathbf{D}_{22}) \mathbf{Y}_r^\dagger \right),
 \end{aligned}$$

$$\begin{aligned}
 \mathbf{C}_{\alpha q}^{opt} &\equiv \left\langle (\boldsymbol{\alpha} - \boldsymbol{\alpha}^{opt})(\mathbf{q} - \mathbf{q}^{opt})^\dagger \right\rangle & (2.53) \\
 &= \mathbf{C}_{\alpha q} - [\mathbf{X}_\alpha, \mathbf{Y}_\alpha] \mathbf{D}^{-1} \begin{bmatrix} \mathbf{X}_q^\dagger \\ \mathbf{Y}_q^\dagger \end{bmatrix} \\
 &= \mathbf{C}_{\alpha q} - \left((\mathbf{X}_\alpha \mathbf{D}_{11} + \mathbf{Y}_\alpha \mathbf{D}_{12}^\dagger) \mathbf{X}_q^\dagger + (\mathbf{X}_\alpha \mathbf{D}_{12} + \mathbf{Y}_\alpha \mathbf{D}_{22}) \mathbf{Y}_q^\dagger \right),
 \end{aligned}$$

$$\begin{aligned}
 \mathbf{C}_{\beta r}^{opt} &\equiv \left\langle (\boldsymbol{\beta} - \boldsymbol{\beta}^{opt})(\mathbf{r} - \mathbf{r}^{opt})^\dagger \right\rangle & (2.54) \\
 &= \mathbf{C}_{\beta r} - [\mathbf{X}_\beta, \mathbf{Y}_\beta] \mathbf{D}^{-1} \begin{bmatrix} \mathbf{X}_r^\dagger \\ \mathbf{Y}_r^\dagger \end{bmatrix} \\
 &= \mathbf{C}_{\beta r} - \left((\mathbf{X}_\beta \mathbf{D}_{11} + \mathbf{Y}_\beta \mathbf{D}_{12}^\dagger) \mathbf{X}_r^\dagger + (\mathbf{X}_\beta \mathbf{D}_{12} + \mathbf{Y}_\beta \mathbf{D}_{22}) \mathbf{Y}_r^\dagger \right),
 \end{aligned}$$

$$\begin{aligned}
 \mathbf{C}_{\beta q}^{opt} &\equiv \left\langle (\boldsymbol{\beta} - \boldsymbol{\beta}^{opt})(\mathbf{q} - \mathbf{q}^{opt})^\dagger \right\rangle & (2.55) \\
 &= \mathbf{C}_{\beta q} - [\mathbf{X}_\beta, \mathbf{Y}_\beta] \mathbf{D}^{-1} \begin{bmatrix} \mathbf{X}_q^\dagger \\ \mathbf{Y}_q^\dagger \end{bmatrix} \\
 &= \mathbf{C}_{\beta q} - \left((\mathbf{X}_\beta \mathbf{D}_{11} + \mathbf{Y}_\beta \mathbf{D}_{12}^\dagger) \mathbf{X}_q^\dagger + (\mathbf{X}_\beta \mathbf{D}_{12} + \mathbf{Y}_\beta \mathbf{D}_{22}) \mathbf{Y}_q^\dagger \right).
 \end{aligned}$$

2.3 Consistency Indicator χ^2

A quantitative indicator to measure the consistency of the available experimental and computational information is constructed in this chapter. Based on Eq. (2.7) for the non-

partitioned DA and Eq. (2.31) for the partitioned DA the extremum of the functional $P(\boldsymbol{\alpha}, \mathbf{r})$ or $P(\boldsymbol{\alpha}, \boldsymbol{\beta}, \mathbf{r}, \mathbf{q})$ respectively becomes

$$\text{Non-partitioned DA: } P^{\min} = \begin{bmatrix} \boldsymbol{\alpha}^{be} - \boldsymbol{\alpha}^0 \\ \mathbf{r}^{be} - \mathbf{r}_m \end{bmatrix}^\dagger \mathbf{C}^{-1} \begin{bmatrix} \boldsymbol{\alpha}^{be} - \boldsymbol{\alpha}^0 \\ \mathbf{r}^{be} - \mathbf{r}_m \end{bmatrix} \quad (2.56)$$

$$\text{partitioned DA: } P^{\min} = \begin{bmatrix} \boldsymbol{\alpha}^{opt} - \boldsymbol{\alpha}^0 \\ \boldsymbol{\beta}^{opt} - \boldsymbol{\beta}^0 \\ \mathbf{r}^{opt} - \mathbf{r}_m \\ \mathbf{q}^{opt} - \mathbf{q}_m \end{bmatrix}^\dagger \mathbf{C}_A^{-1} \begin{bmatrix} \boldsymbol{\alpha}^{opt} - \boldsymbol{\alpha}^0 \\ \boldsymbol{\beta}^{opt} - \boldsymbol{\beta}^0 \\ \mathbf{r}^{opt} - \mathbf{r}_m \\ \mathbf{q}^{opt} - \mathbf{q}_m \end{bmatrix}. \quad (2.57)$$

Replacing the calibrated values above, i.e. “be” or “opt” values, with their respective first-order Taylor expansion around the calibrated value yields the quadratic form

$$\text{Non-partitioned DA: } P^{\min} \equiv \chi^2 = \mathbf{r}_d^\dagger \cdot \mathbf{C}_d^{-1} \cdot \mathbf{r}_d \quad (2.58)$$

$$\text{partitioned DA: } P^{\min} \equiv \chi_A^2 = \begin{bmatrix} \mathbf{r}_d^\dagger & \mathbf{q}_d^\dagger \end{bmatrix} \mathbf{D}^{-1} \begin{bmatrix} \mathbf{r}_d \\ \mathbf{q}_d \end{bmatrix}. \quad (2.59)$$

As already indicated in Eq. (2.58) and Eq. (2.59) the quadratic form obeys a χ^2 -distribution with as many degrees of freedom as there are experimental responses. Written out in detail, the consistency indicator for the partitioned data assimilation follows as

$$\begin{aligned} \chi_A^2 &\equiv \begin{bmatrix} (\mathbf{r}_c - \mathbf{r}_m)^\dagger & (\mathbf{q}_c - \mathbf{q}_m)^\dagger \end{bmatrix} \begin{bmatrix} \mathbf{D}_{11} & \mathbf{D}_{12} \\ \mathbf{D}_{12}^\dagger & \mathbf{D}_{22} \end{bmatrix} \begin{bmatrix} \mathbf{r}_c - \mathbf{r}_m \\ \mathbf{q}_c - \mathbf{q}_m \end{bmatrix} \\ &= (\mathbf{r}_c - \mathbf{r}_m)^\dagger \mathbf{D}_{11} (\mathbf{r}_c - \mathbf{r}_m) + (\mathbf{r}_c - \mathbf{r}_m)^\dagger \mathbf{D}_{12} (\mathbf{q}_c - \mathbf{q}_m) + \\ &\quad + (\mathbf{q}_c - \mathbf{q}_m)^\dagger \mathbf{D}_{12}^\dagger (\mathbf{r}_c - \mathbf{r}_m) + (\mathbf{q}_c - \mathbf{q}_m)^\dagger \mathbf{D}_{22} (\mathbf{q}_c - \mathbf{q}_m) \\ &= \chi_{rr}^2 + \chi_{rq}^2 + \chi_{qq}^2 \end{aligned} \quad (2.60)$$

The consistency indicator χ_A^2 above can thus be split into three respective parts – one containing primarily information for the initial subsystem I with quantities $(\mathbf{r}, \boldsymbol{\alpha})$, one containing primarily information for the additional subsystem II with quantities $(\mathbf{q}, \boldsymbol{\beta})$, and the last part containing cross-terms that represent the coupling between both subsystems.

$$\chi_{rr}^2 = \mathbf{r}_d^\dagger \cdot \mathbf{D}_{11} \cdot \mathbf{r}_d \quad (2.61)$$

$$\chi_{qq}^2 = \mathbf{q}_d^\dagger \cdot \mathbf{D}_{22} \cdot \mathbf{q}_d \quad (2.62)$$

$$\chi_{rq}^2 = 2 \cdot \mathbf{r}_d^\dagger \cdot \mathbf{D}_{12} \cdot \mathbf{q}_d \quad (2.63)$$

Eqs. (2.60) to (2.63) are utilized in chapter 3.5 to develop a consistency evaluation procedure that is computationally beneficial.

2.4 Summary of Partitioned DA Equations

For convenience the final results are repeated here to give a compact summary of all the essential equations for the partitioned data assimilation. All numerical results presented in later chapters of this work are implemented in the scripting language MATLAB based on this summary.

$$\mathbf{D}^{-1} = \begin{bmatrix} \mathbf{D}_{11} & \mathbf{D}_{12} \\ \mathbf{D}_{12}^\dagger & \mathbf{D}_{22} \end{bmatrix} = \begin{bmatrix} \mathbf{D}_{rr}^{-1} + \mathbf{D}_{rr}^{-1} \mathbf{D}_{rq} \mathbf{D}_{22} \mathbf{D}_{rq}^\dagger \mathbf{D}_{rr}^{-1} & -\mathbf{D}_{rr}^{-1} \mathbf{D}_{rq} \mathbf{D}_{22} \\ -\mathbf{D}_{22} \mathbf{D}_{rq}^\dagger \mathbf{D}_{rr}^{-1} & (\mathbf{D}_{qq} - \mathbf{D}_{rq}^\dagger \mathbf{D}_{rr}^{-1} \mathbf{D}_{rq})^{-1} \end{bmatrix}$$

$$\mathbf{D}_{rr} = \mathbf{S}_{r\alpha} \mathbf{X}_\alpha + \mathbf{S}_{r\beta} \mathbf{X}_\beta - \mathbf{X}_r$$

$$\mathbf{D}_{rq} = \mathbf{S}_{r\alpha} \mathbf{Y}_\alpha + \mathbf{S}_{r\beta} \mathbf{Y}_\beta - \mathbf{Y}_r$$

$$\mathbf{D}_{qq} = \mathbf{S}_{q\alpha} \mathbf{Y}_\alpha + \mathbf{S}_{q\beta} \mathbf{Y}_\beta - \mathbf{Y}_q$$

$$\mathbf{C}_{rc,11} = \mathbf{S}_{r\alpha} \cdot \mathbf{C}_{\alpha\alpha} \cdot \mathbf{S}_{r\alpha}^\dagger + 2 \cdot \mathbf{S}_{r\alpha} \cdot \mathbf{C}_{\alpha\beta} \cdot \mathbf{S}_{r\beta}^\dagger + \mathbf{S}_{r\beta} \cdot \mathbf{C}_{\beta\beta} \cdot \mathbf{S}_{r\beta}^\dagger$$

$$\mathbf{C}_{qc,22} = \mathbf{S}_{q\alpha} \cdot \mathbf{C}_{\alpha\alpha} \cdot \mathbf{S}_{q\alpha}^\dagger + 2 \cdot \mathbf{S}_{q\alpha} \cdot \mathbf{C}_{\alpha\beta} \cdot \mathbf{S}_{q\beta}^\dagger + \mathbf{S}_{q\beta} \cdot \mathbf{C}_{\beta\beta} \cdot \mathbf{S}_{q\beta}^\dagger$$

$$\boldsymbol{\alpha}^{opt} = \boldsymbol{\alpha}^0 - (\mathbf{X}_\alpha \mathbf{D}_{11} + \mathbf{Y}_\alpha \mathbf{D}_{12}^\dagger)(\mathbf{r}^c - \mathbf{r}^m) - (\mathbf{X}_\alpha \mathbf{D}_{12} + \mathbf{Y}_\alpha \mathbf{D}_{22})(\mathbf{q}^c - \mathbf{q}^m)$$

$$\boldsymbol{\beta}^{opt} = \boldsymbol{\beta}^0 - (\mathbf{X}_\beta \mathbf{D}_{11} + \mathbf{Y}_\beta \mathbf{D}_{12}^\dagger)(\mathbf{r}^c - \mathbf{r}^m) - (\mathbf{X}_\beta \mathbf{D}_{12} + \mathbf{Y}_\beta \mathbf{D}_{22})(\mathbf{q}^c - \mathbf{q}^m)$$

$$\mathbf{r}^{opt} = \mathbf{r}^m - (\mathbf{X}_r \mathbf{D}_{11} + \mathbf{Y}_r \mathbf{D}_{12}^\dagger)(\mathbf{r}^c - \mathbf{r}^m) - (\mathbf{X}_r \mathbf{D}_{12} + \mathbf{Y}_r \mathbf{D}_{22})(\mathbf{q}^c - \mathbf{q}^m)$$

$$\mathbf{q}^{opt} = \mathbf{q}^m - (\mathbf{X}_q \mathbf{D}_{11} + \mathbf{Y}_q \mathbf{D}_{12}^\dagger)(\mathbf{r}^c - \mathbf{r}^m) - (\mathbf{X}_q \mathbf{D}_{12} + \mathbf{Y}_q \mathbf{D}_{22})(\mathbf{q}^c - \mathbf{q}^m)$$

$$\begin{aligned}\chi_A^2 &= \left[(\mathbf{r}^c - \mathbf{r}^m)^\dagger, (\mathbf{q}^c - \mathbf{q}^m)^\dagger \right] \begin{bmatrix} \mathbf{D}_{rr} & \mathbf{D}_{rq} \\ \mathbf{D}_{rq}^\dagger & \mathbf{D}_{qq} \end{bmatrix}^{-1} \begin{bmatrix} \mathbf{r}^c - \mathbf{r}^m \\ \mathbf{q}^c - \mathbf{q}^m \end{bmatrix} \\ &= \chi_{rr}^2 + \chi_{rq}^2 + \chi_{qq}^2\end{aligned}$$

$$\chi_{rr}^2 = (\mathbf{r}^c - \mathbf{r}^m)^\dagger \mathbf{D}_{11} (\mathbf{r}^c - \mathbf{r}^m)$$

$$\chi_{qq}^2 = (\mathbf{q}^c - \mathbf{q}^m)^\dagger \mathbf{D}_{22} (\mathbf{q}^c - \mathbf{q}^m)$$

$$\chi_{rq}^2 = 2(\mathbf{r}^c - \mathbf{r}^m)^\dagger \mathbf{D}_{12} (\mathbf{q}^c - \mathbf{q}^m)$$

$$\mathbf{C}_{\alpha\alpha}^{opt} = \mathbf{C}_{\alpha\alpha} - \left((\mathbf{X}_\alpha \mathbf{D}_{11} + \mathbf{Y}_\alpha \mathbf{D}_{12}^\dagger) \mathbf{X}_\alpha^\dagger + (\mathbf{X}_\alpha \mathbf{D}_{12} + \mathbf{Y}_\alpha \mathbf{D}_{22}) \mathbf{Y}_\alpha^\dagger \right)$$

$$\mathbf{C}_{\beta\beta}^{opt} = \mathbf{C}_{\beta\beta} - \left((\mathbf{X}_\beta \mathbf{D}_{11} + \mathbf{Y}_\beta \mathbf{D}_{12}^\dagger) \mathbf{X}_\beta^\dagger + (\mathbf{X}_\beta \mathbf{D}_{12} + \mathbf{Y}_\beta \mathbf{D}_{22}) \mathbf{Y}_\beta^\dagger \right)$$

$$\mathbf{C}_{\alpha\beta}^{opt} = \mathbf{C}_{\alpha\beta} - \left((\mathbf{X}_\alpha \mathbf{D}_{11} + \mathbf{Y}_\alpha \mathbf{D}_{12}^\dagger) \mathbf{X}_\beta^\dagger + (\mathbf{X}_\alpha \mathbf{D}_{12} + \mathbf{Y}_\alpha \mathbf{D}_{22}) \mathbf{Y}_\beta^\dagger \right)$$

$$\mathbf{C}_{rr}^{opt} = \mathbf{C}_{rr} - \left((\mathbf{X}_r \mathbf{D}_{11} + \mathbf{Y}_r \mathbf{D}_{12}^\dagger) \mathbf{X}_r^\dagger + (\mathbf{X}_r \mathbf{D}_{12} + \mathbf{Y}_r \mathbf{D}_{22}) \mathbf{Y}_r^\dagger \right)$$

$$\mathbf{C}_{qq}^{opt} = \mathbf{C}_{qq} - \left((\mathbf{X}_q \mathbf{D}_{11} + \mathbf{Y}_q \mathbf{D}_{12}^\dagger) \mathbf{X}_q^\dagger + (\mathbf{X}_q \mathbf{D}_{12} + \mathbf{Y}_q \mathbf{D}_{22}) \mathbf{Y}_q^\dagger \right)$$

$$\mathbf{C}_{rq}^{opt} = \mathbf{C}_{rq} - \left((\mathbf{X}_r \mathbf{D}_{11} + \mathbf{Y}_r \mathbf{D}_{12}^\dagger) \mathbf{X}_q^\dagger + (\mathbf{X}_r \mathbf{D}_{12} + \mathbf{Y}_r \mathbf{D}_{22}) \mathbf{Y}_q^\dagger \right)$$

$$\mathbf{C}_{ar}^{opt} = \mathbf{C}_{ar} - \left((\mathbf{X}_\alpha \mathbf{D}_{11} + \mathbf{Y}_\alpha \mathbf{D}_{12}^\dagger) \mathbf{X}_r^\dagger + (\mathbf{X}_\alpha \mathbf{D}_{12} + \mathbf{Y}_\alpha \mathbf{D}_{22}) \mathbf{Y}_r^\dagger \right)$$

$$\mathbf{C}_{\alpha q}^{opt} = \mathbf{C}_{\alpha q} - \left((\mathbf{X}_\alpha \mathbf{D}_{11} + \mathbf{Y}_\alpha \mathbf{D}_{12}^\dagger) \mathbf{X}_q^\dagger + (\mathbf{X}_\alpha \mathbf{D}_{12} + \mathbf{Y}_\alpha \mathbf{D}_{22}) \mathbf{Y}_q^\dagger \right)$$

$$\mathbf{C}_{\beta r}^{opt} = \mathbf{C}_{\beta r} - \left((\mathbf{X}_\beta \mathbf{D}_{11} + \mathbf{Y}_\beta \mathbf{D}_{12}^\dagger) \mathbf{X}_r^\dagger + (\mathbf{X}_\beta \mathbf{D}_{12} + \mathbf{Y}_\beta \mathbf{D}_{22}) \mathbf{Y}_r^\dagger \right)$$

$$\mathbf{C}_{\beta q}^{opt} = \mathbf{C}_{\beta q} - \left((\mathbf{X}_\beta \mathbf{D}_{11} + \mathbf{Y}_\beta \mathbf{D}_{12}^\dagger) \mathbf{X}_q^\dagger + (\mathbf{X}_\beta \mathbf{D}_{12} + \mathbf{Y}_\beta \mathbf{D}_{22}) \mathbf{Y}_q^\dagger \right)$$

Also for convenience the shorthand applied above follows here written out in detail,

$$\mathbf{X}_\alpha = \mathbf{C}_{\alpha\alpha} \mathbf{S}_{r\alpha}^\dagger + \mathbf{C}_{\alpha\beta} \mathbf{S}_{r\beta}^\dagger - \mathbf{C}_{\alpha r}$$

$$\mathbf{Y}_\alpha = \mathbf{C}_{\alpha\alpha} \mathbf{S}_{q\alpha}^\dagger + \mathbf{C}_{\alpha\beta} \mathbf{S}_{q\beta}^\dagger - \mathbf{C}_{\alpha q}$$

$$\mathbf{X}_\beta = \mathbf{C}_{\alpha\beta}^\dagger \mathbf{S}_{r\alpha}^\dagger + \mathbf{C}_{\beta\beta} \mathbf{S}_{r\beta}^\dagger - \mathbf{C}_{\beta r}$$

$$\mathbf{Y}_\beta = \mathbf{C}_{\alpha\beta}^\dagger \mathbf{S}_{q\alpha}^\dagger + \mathbf{C}_{\beta\beta} \mathbf{S}_{q\beta}^\dagger - \mathbf{C}_{\beta q}$$

$$\mathbf{X}_r = \mathbf{C}_{\alpha r}^\dagger \mathbf{S}_{r\alpha}^\dagger + \mathbf{C}_{\beta r}^\dagger \mathbf{S}_{r\beta}^\dagger - \mathbf{C}_{rr}$$

$$\mathbf{Y}_r = \mathbf{C}_{\alpha r}^\dagger \mathbf{S}_{q\alpha}^\dagger + \mathbf{C}_{\beta r}^\dagger \mathbf{S}_{q\beta}^\dagger - \mathbf{C}_{rq}$$

$$\mathbf{X}_q = \mathbf{C}_{\alpha q}^\dagger \mathbf{S}_{r\alpha}^\dagger + \mathbf{C}_{\beta q}^\dagger \mathbf{S}_{r\beta}^\dagger - \mathbf{C}_{rq}^\dagger$$

$$\mathbf{Y}_q = \mathbf{C}_{\alpha q}^\dagger \mathbf{S}_{q\alpha}^\dagger + \mathbf{C}_{\beta q}^\dagger \mathbf{S}_{q\beta}^\dagger - \mathbf{C}_{q q}$$

3. Application to 1-dimensional Heat Conduction as Illustrative Example

The fundamental functionality of the partitioned data assimilation as proposed in [10] has already been demonstrated in [22]. This chapter exercises both the non-partitioned and partitioned DA on synthetic data to familiarize the reader with the basic concepts. The evaluated results of the non-partitioned DA are referred to as “best-estimate” (be) while the corresponding results of the partitioned DA are referred to as “optimal” (opt) to more easily distinguish between the two approaches. Furthermore, the actual algorithm of the partitioned DA optimized towards minimum memory requirements is discussed.

While the framework of the partitioned DA was originally created to handle multi-physics applications in a new, more efficient way, the method is here used on one single-physics system that can be split into individual subsystems. This is done in practice by partitioning the underlying matrices as introduced in chapter 2 into individual matrix blocks. The goal is then to make use of these block-partitions in a serial algorithm. The algorithm was implemented in the scripting language MATLAB as an easy and fast way to develop the basic structure of the algorithm. A discussion and outlook towards parallelization and program languages concludes the chapter.

3.1 1-D time-dependent Heat Conduction in Infinite Medium

The equation for time-dependent heat conduction in the direction x without internal heat generation is

$$\frac{\partial^2 T(x,t)}{\partial x^2} = \frac{1}{\alpha} \frac{\partial T(x,t)}{\partial t} \quad (3.1)$$

where α is the thermal diffusivity defined as $\alpha = \frac{k}{\rho \cdot c_p} \left[\frac{m^2}{s} \right]$. Please note that the scalar material property α is completely unrelated to the vector of parameters $\mathbf{\alpha}$ and matrix index α used excessively throughout chapter 2. The medium for the heat conduction is assumed to be infinite, i.e. $-\infty < x < \infty$, and the material is chosen as soil with properties listed in Table 1.

Table 1: Material properties taken from [7] and assumed uncertainty of soil

$k \left[\frac{W}{m K} \right]$	$\rho \left[\frac{kg}{m^3} \right]$	$c_p \left[\frac{J}{kg K} \right]$
$0.59 \pm 2.95 \cdot 10^{-2} (\pm 5\%)$	$2040 \pm 204 (\pm 10\%)$	$1.84 \cdot 10^3 \pm 36.8 (\pm 2\%)$

Let the initial temperature distribution be a Fourier series

$$T(x, t = 0) = F(x) = \sum_{n=1}^N (a_n \cos(nx) + b_n \sin(nx)). \quad (3.2)$$

This choice of the initial condition allows not only having any shape of initial temperature distribution but also enables systems with large numbers of parameters. The system response is the temperature at a given point in time and space $T(x_i, t_j)$. The parameters are the thermal conductivity k , soil density ρ , specific heat capacity c_p , time t_j and location x_i as well as all Fourier coefficients, i.e. a_n and b_n , of the initial temperature distribution. To facilitate any given combination of coefficients without encountering unphysical temperatures, the initial temperature distribution is defined as the temperature difference to the far-field temperature in Kelvin. The coefficients a_n and b_n are sampled randomly from the interval $[0, 1]$. Figure 1 shows two examples of initial temperature distributions with 10 and 100 coefficients respectively.

The temperature distribution $T(x, t)$ can be determined analytically by combining Eqs (3.1) and (3.2),

$$T(x, t) = \frac{1}{\sqrt{4\pi\alpha t}} \int_{-\infty}^{\infty} F(x') e^{-\frac{(x-x')^2}{4\alpha t}} dx' \quad (3.3)$$

which finally yields

$$T(x, t) = \sum_{n=1}^N (a_n \cdot e^{-n^2\alpha t} \cdot \cos(nx) + b_n \cdot e^{-n^2\alpha t} \cdot \sin(nx)). \quad (3.4)$$

With the analytic solution readily available the sensitivities can be derived as the partial derivatives of Eq. (3.4), namely $\frac{\partial T}{\partial k}$, $\frac{\partial T}{\partial \rho}$, $\frac{\partial T}{\partial c_p}$, $\frac{\partial T}{\partial t_j}$, $\frac{\partial T}{\partial x_i}$, $\frac{\partial T}{\partial a_n}$ and $\frac{\partial T}{\partial b_n}$. In general, analytic

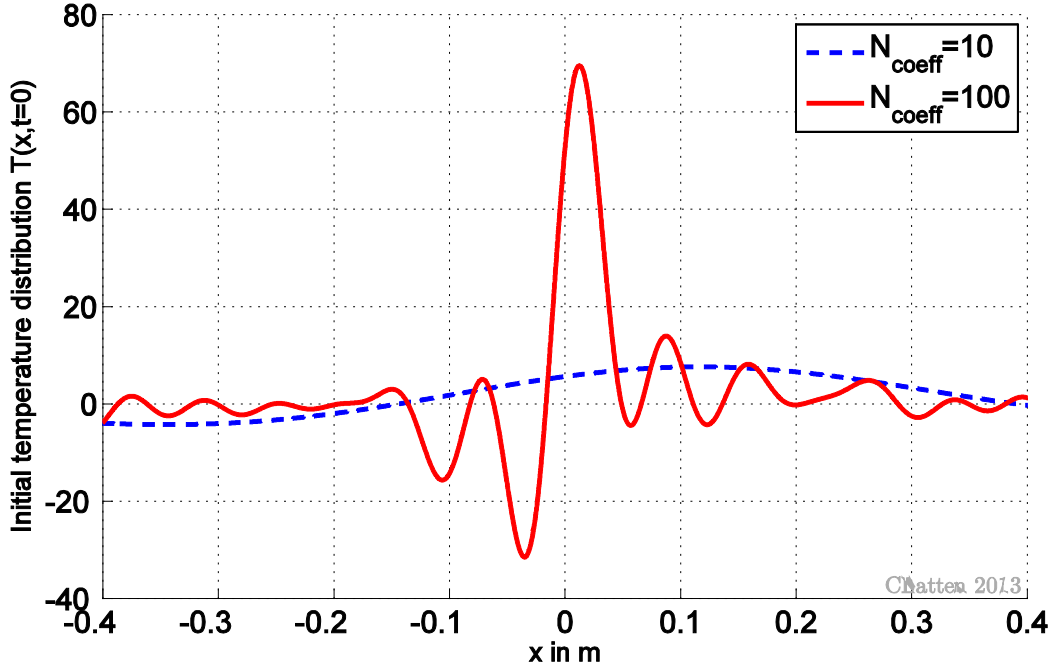


Figure 1: Initial temperature distribution with 10 and 100 randomly sampled Fourier coefficients

solutions are unavailable and computing sensitivity coefficients requires special techniques like the forward sensitivity analysis procedure or adjoint methods.

For an illustrative example let the number of responses be $N_r = 10$ and let the time t_j be $t = 10s$. Each response $T(x_i, t_j)$ is then defined by its location x_i . Ten locations are sampled randomly from the interval $[-0.4, 0.4]$ and the particular values are listed in Table 2. The nominal value of the computed responses $T_c(x_i, t_j)$ is based on the analytic temperature distribution as defined in Eq. (3.4). The nominal value of the measured responses $T_m(x_i, t_j)$ is created synthetically by adding a random offset to the nominal computed response. As it is the case for many experiments, it is assumed that only variance data for the measured responses is available, i.e. the variance-covariance matrix C_{rr} for the measured responses has only non-zero elements on the diagonal. Again, this information is created synthetically by sampling values for the standard deviation of each measured response from a normal distribution. The standard deviation for the remaining parameters t_j , x_i , a_n and b_n are created in the same way. All parameters are assumed to be independent and the resulting variance-covariance matrix $C_{\alpha\alpha}$ for the parameters is thus diagonal.

This completes the information required for data assimilation. A summary of the locations and both measured and computed responses is listed in Table 2. Figure 2 shows the analytic

solution as a dotted line on the interval $[-0.4, 0.4]$, which was selected for this example. Computed responses are shown in blue and measured (synthetic) responses are shown in green. The error bars in this figure indicate one standard deviation. The values of the synthetic measured data have a slight off-set in the x-direction for ease of visualization. The complete input data can be found in Appendix C.

Table 2: Synthetic data for heat conduction example with 10 Fourier coefficients at $t = 10s$

#	Location x_i	$r_c \pm \sigma_c^{rel} [\%]$		$r_m \pm \sigma_m^{rel} [\%]$	
		(analytic solution)		(synthetic data)	
1	-0.3955	-2.5785	± 18.616	-2.9206	± 6.032
2	-0.2907	-2.8506	± 12.018	-3.4484	± 7.753
3	-0.2701	-2.6932	± 16.205	-2.2743	± 16.056
4	-0.2401	-2.3190	± 18.503	-3.0087	± 15.451
5	0.0344	5.2739	± 10.436	5.9451	± 16.655
6	0.0859	6.0092	± 10.493	6.1601	± 12.529
7	0.1439	6.0589	± 10.649	5.0676	± 11.382
8	0.2118	5.0995	± 16.130	5.9364	± 14.169
9	0.2172	4.9846	± 17.323	5.4591	± 17.837
10	0.2867	3.1601	± 36.403	4.4123	± 15.062

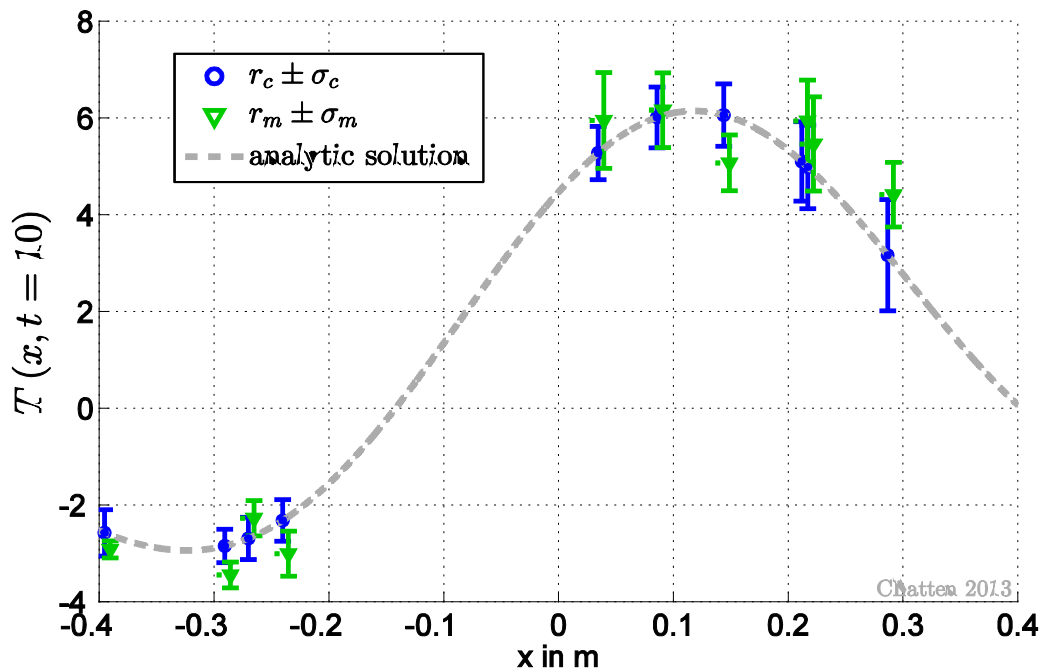


Figure 2: Synthetic measured and computed responses with on standard deviation for 1-D heat conduction. Measured values are shifted to the right for ease of visualization.

3.2 Non-partitioned DA

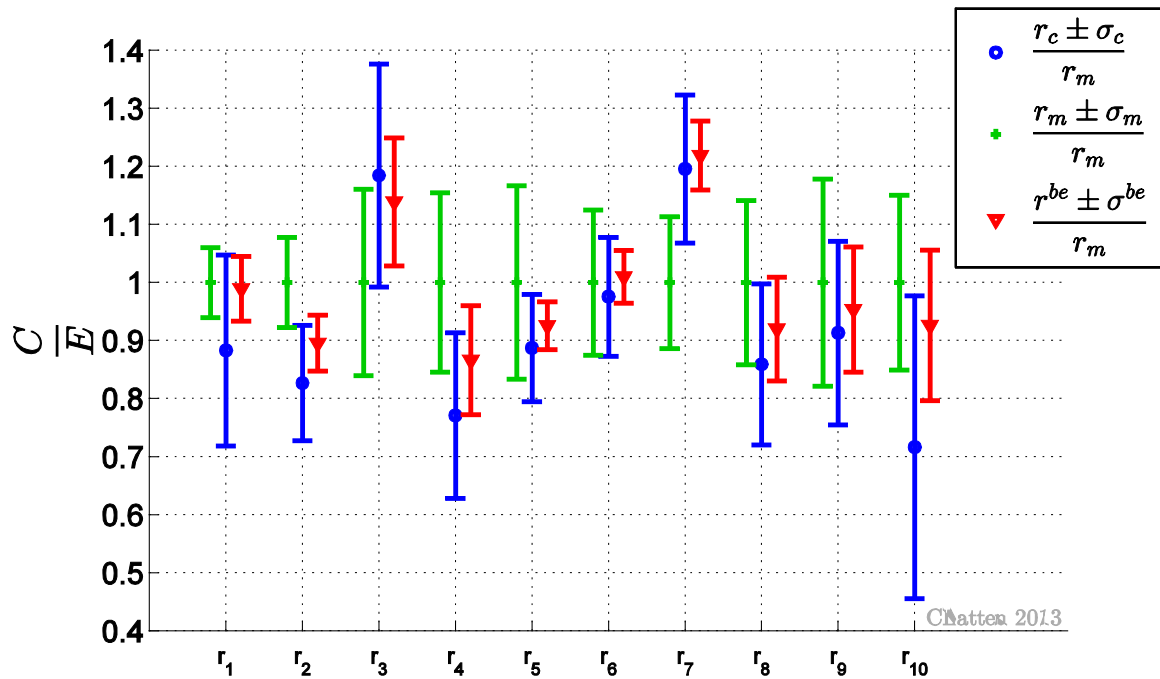
Applying data assimilation to the complete system with $N_r = 10$ and $N_\alpha = 34$ as introduced above yields best-estimate values for all system responses and parameters including best-estimate uncertainties. In this chapter the non-partitioned formulation is used, whereas the partitioned formulation is applied in the subsequent chapter. Table 3 and Figure 3 present the measured, computed and best-estimate values for $T(x_i, t_j)$, along with (\pm) one standard deviation, all normalized to the nominal measured value. Normalization of all (computed) values with respect to experimentally measured values is also referred to as C/E values. In both table and figure, \mathbf{r}_c and σ_c denote the mean value and corresponding standard deviation for a computed response, \mathbf{r}_m and σ_m denote the mean value and corresponding standard deviation for a measured response and lastly \mathbf{r}^{be} and σ^{be} denote the mean value and corresponding standard deviation for a best-estimate response resulting from the application of the non-partitioned data assimilation formulation. All data, which was used here, is created synthetically and whether a particular measured nominal value is larger than the computed nominal value is random. Several important features of the predictive modeling procedure are illustrated in Figure 3. The non-partitioned DA calibrates all responses to updated best-estimate values which fall in between the measured and the computed ones, while reducing the respective best-estimate standard deviations. The relative values of the measured and computed standard deviations for response r_1 , for example, indicate that the experimental nominal value is more accurately known than the computed one. The DA methodology shifts in this case the best-estimate mean value r_1^{be} closer to the measured nominal value $r_{m,1}$ and reduces its accompanying best-estimate standard deviation σ_1^{be} to a value that is actually smaller than the corresponding measured standard deviation. This inherent reduction of uncertainty is explained in detail in [9] for the non-partitioned data assimilation procedure. Table 3 below shows that the relative standard deviation of the best-estimate responses is indeed for all responses less than the smaller standard deviation of either the computed or measured response, $\sigma_i^{be} < \min\{\sigma_{m,i}, \sigma_{c,i}\}$. The consistency indicator

χ^2 per degrees of freedom is $\frac{\chi^2}{N_r} = \frac{10.8369}{10} = 1.0837$. This value falls within the 90% central

confidence range of a χ^2 distribution (0.3940, 1.8307), which indicates that all data used here is consistent.

Table 3: Measure and computed system response with relative standard deviation as well as best-estimate responses with their respective relative standard deviation

#	Location x_i	$r_c \pm \sigma_c$ [%]		$r_m \pm \sigma_m$ [%]		$r^{be} \pm \sigma^{be}$ [%]	
		(analytic solution)		(synthetic data)			
1	-3.9548e-001	-2.5785	± 18.616	-2.9206	± 6.032	-2.8893	± 5.6436
2	-2.9068e-001	-2.8506	± 12.018	-3.4484	± 7.753	-3.0883	± 5.3917
3	-2.7014e-001	-2.6932	± 16.205	-2.2743	± 16.056	-2.5905	± 9.6875
4	-2.4013e-001	-2.3190	± 18.503	-3.0087	± 15.451	-2.6067	± 10.843
5	3.4436e-002	5.2739	± 10.436	5.9451	± 16.655	5.5028	± 4.4361
6	8.5872e-002	6.0092	± 10.493	6.1601	± 12.529	6.2207	± 4.5195
7	1.4390e-001	6.0589	± 10.649	5.0676	± 11.382	6.1771	± 4.8768
8	2.1183e-001	5.0995	± 16.130	5.9364	± 14.169	5.4619	± 9.7078
9	2.1719e-001	4.9846	± 17.323	5.4591	± 17.837	5.2068	± 11.297
10	2.8672e-001	3.1601	± 36.403	4.4123	± 15.062	4.0865	± 13.982


Figure 3: Measured, computed and best-estimate responses with one standard deviation normalized to the nominal measured value for the heat conduction example with synthetic data

3.3 Partitioned DA

The synthetic data of the previous section is now fed into the new partitioned DA algorithm. A comparison of results is done to demonstrate that both methods yield the same updated values. The benefits of the new partitioned DA are explained and illustrated in detail in consecutive sections.

The complete system with $N_r = 10$ is partitioned evenly into subsystem I and subsystem II such that,

$$\begin{aligned} \mathbf{r}^{pDA} &= \{r_1 \ r_2 \ r_3 \ r_4 \ r_5\}^\dagger \\ \mathbf{q}^{pDA} &= \{r_6 \ r_7 \ r_8 \ r_9 \ r_{10}\}^\dagger \\ &\equiv \{q_1 \ q_2 \ q_3 \ q_4 \ q_5\}^\dagger. \end{aligned} \quad (3.5)$$

Subsystem I has now $N_\alpha^{pDA} = 29$ parameters, namely

$$\boldsymbol{\alpha}^{pDA} = \{k \ \rho \ c_p \ t_j \ x_1 \ \cdots \ x_5 \ a_1 \ \cdots \ a_{10} \ b_1 \ \cdots \ b_{10}\}^\dagger. \quad (3.6)$$

$N_\beta^{pDA} = 5$ parameters are exclusive to subsystem II, namely

$$\boldsymbol{\beta}^{pDA} = \{x_6 \ x_7 \ x_8 \ x_9 \ x_{10}\}^\dagger. \quad (3.7)$$

This is the most general case of the partitioned data assimilation where a system with additional responses and additional parameters is added to an already existing system. The method has cross-terms that allow for the coupling of parameters and responses between the two subsystems. Here, the material properties are for instance assigned as parameters to subsystem I. However, the matrix block $\mathbf{S}_{q\alpha}$ represents the sensitivity of the additional responses \mathbf{q} to a change in the material properties in $\boldsymbol{\beta}$. This guarantees that all the available information is used.

Applying the partitioned DA on the synthetic data of the heat conduction example yields updated optimal values. As expected these optimal values match the best-estimate results of the non-partitioned DA, which have been presented in the previous chapter, precisely. Those numeric values are not repeated here. Instead, the maximum norm of the difference between the best-estimate results of the non-partitioned DA and the optimal results of the partitioned DA is computed as deviation metric. The deviation is of the order of numeric precision as shown in Table 4. This demonstrates that both methods, if applied correctly, yield indeed the same results.

The partitioned DA supplies a consistency indicator for each subsystem and an additional consistency indicator for the cross-term. The sum of all three terms yields the same numeric value as the non-partitioned DA on the same data set,

$$\frac{\chi^2}{N_r^{pDA} + N_q^{pDA}} = \frac{\chi_{rr}^2 + \chi_{rq}^2 + \chi_{qq}^2}{10} = \frac{5.503 + 0.866 + 4.468}{10} = 1.0837. \quad (3.8)$$

Yet, only the partitioned DA allows quantifying the consistency of each subsystem individually without the need to isolate and recomputed each subsystem by itself. This benefit of the partitioned DA is described in detail and illustrated with an example in chapter 3.5.

Table 4: Deviation between updated results according to non-partitioned (“be”) and partitioned (“opt”) data assimilation

$$\left\| \mathbf{r}^{be} - \begin{bmatrix} \mathbf{r}^{opt} \\ \mathbf{q}^{opt} \end{bmatrix} \right\|_{\infty} = 4.4409 \cdot 10^{-16}$$

$$\left\| \mathbf{C}^{be} - \begin{bmatrix} \mathbf{C}_{rr}^{opt} & \mathbf{C}_{rq}^{opt} \\ (\mathbf{C}_{rq}^{opt})^{\dagger} & \mathbf{C}_{qq}^{opt} \end{bmatrix} \right\|_{\infty} = 1.1102 \cdot 10^{-16}$$

$$\left\| \boldsymbol{\alpha}^{be} - \begin{bmatrix} \boldsymbol{\alpha}^{opt} \\ \boldsymbol{\beta}^{opt} \end{bmatrix} \right\|_{\infty} = 2.2737 \cdot 10^{-13}$$

$$\left\| \mathbf{C}_{\alpha\alpha}^{be} - \begin{bmatrix} \mathbf{C}_{\alpha\alpha}^{opt} & \mathbf{C}_{\alpha\beta}^{opt} \\ \mathbf{C}_{\beta\alpha}^{opt} & \mathbf{C}_{\beta\beta}^{opt} \end{bmatrix} \right\|_{\infty} = 3.4694 \cdot 10^{-18}$$

$$\left\| \mathbf{C}_{ra}^{be} - \begin{bmatrix} \mathbf{C}_{ra}^{opt} & \mathbf{C}_{r\beta}^{opt} \\ \mathbf{C}_{qa}^{opt} & \mathbf{C}_{q\beta}^{opt} \end{bmatrix} \right\|_{\infty} = 1.0408 \cdot 10^{-17}$$

3.4 Implementation of partitioned DA

Developing algorithms is an extremely involved process balancing opposing goals like performance, stability, range of use, complexity of the implementation etc. Finding and thoroughly testing a close to optimal implementation is outside the scope of this work. The task was set to find an implementation of the partitioned DA that uses the least memory in a serial environment disregarding any trade-offs with regard to execution time. Memory is here defined as the physical RAM that is occupied with variables during the run time of the partitioned DA script. In practice the workspace requirements of the scripting language MATLAB was measured and compared to the theoretical memory requirements as explained in detail later. The overhead of the MATLAB environment is quite considerable and causes the memory requirements in practice to be larger than the theoretical value. Any application of well-known high-performance linear algebra libraries that make use of parallelization and distributed memory would further improve the overall performance of the algorithm implementation presented here, [\[12\]](#).

At the core of the partitioned DA formulation lays the block-wise matrix inversion. This inversion strategy is a standard method in numerical linear algebra,

$$\mathbf{D}^{-1} = \begin{bmatrix} \mathbf{D}_{11} & \mathbf{D}_{12} \\ \mathbf{D}_{12}^\dagger & \mathbf{D}_{22} \end{bmatrix} = \begin{bmatrix} \mathbf{D}_{rr}^{-1} + \mathbf{D}_{rr}^{-1} \mathbf{D}_{rq} \mathbf{D}_{22} \mathbf{D}_{rq}^\dagger \mathbf{D}_{rr}^{-1} & -\mathbf{D}_{rr}^{-1} \mathbf{D}_{rq} \mathbf{D}_{22} \\ -\mathbf{D}_{22} \mathbf{D}_{rq}^\dagger \mathbf{D}_{rr}^{-1} & (\mathbf{D}_{qq} - \mathbf{D}_{rq}^\dagger \mathbf{D}_{rr}^{-1} \mathbf{D}_{rq})^{-1} \end{bmatrix}, \quad (3.9)$$

assuming only that the blocks \mathbf{D}_{rr} and \mathbf{D}_{qq} are square and that \mathbf{D}_{rr} and its Schur complement $(\mathbf{D}_{qq} - \mathbf{D}_{rq}^\dagger \mathbf{D}_{rr}^{-1} \mathbf{D}_{rq})$ are non-singular. The usual implementation starts by building all three sub-matrices \mathbf{D}_{rr} , \mathbf{D}_{qq} and \mathbf{D}_{rq} to then proceed to building the inverse of dimensions $(N_r + N_q) \times (N_r + N_q)$ by inverting only the matrices $(N_r \times N_r)$, $(N_q \times N_q)$ and four matrix multiplications of dimensions $(N_r \times N_r)$ or $(N_q \times N_q)$, [111]. This standard method can be applied to any symmetric positive-definite matrix \mathbf{D} and reduces the number of arithmetic operations thus increasing performance. The benefit of this strategy with regard to time has already been demonstrated in [22]. In the present work, the memory requirements are of principal interest and to this end no more than three matrices or vectors are kept in memory at any single time during the script is executed. The complete implementation can be found in Appendix D as pseudo-code. To illustrate the basic idea an excerpt is listed below in Table 5. While the benefit of the reduced arithmetic operations is in principle conserved (see e.g. line 126 137 and 141) the considerably increased input/output (I/O) operations cause a loss of performance with respect to time. Depending on the number of responses and parameters I/O can consume a substantial percentage of the execution time of the script.

Table 5: Pseudo-Code of block-wise inversion, excerpt of Appendix D

<pre> %++++Build the Schur complement D22 123 Read from file $(\mathbf{D}_{rr})^{-1}$ 124 $\mathbf{D}_{temp} = (\mathbf{D}_{rr})^{-1} \cdot \mathbf{D}_{rq}$ %build temporary variable 125 Write \mathbf{D}_{temp} to file 126 $\mathbf{D}_{22} = \mathbf{D}_{temp}$ %build D22 step 1) 127 Delete \mathbf{D}_{temp} $(\mathbf{D}_{rr})^{-1}$ 128 $\mathbf{D}_{22} = \mathbf{D}_{rq}^\dagger \cdot \mathbf{D}_{22}$ %build D22 step 2*) 129 *allocation mismatch if $N_r \neq N_q$ causes temporary memory requirement of </pre>	<pre> In memory $N_r \cdot N_q + N_r \cdot N_r$ $2 \cdot N_r \cdot N_q + N_r \cdot N_r$ $2 \cdot N_r \cdot N_q + N_r \cdot N_r$ $2 \cdot N_r \cdot N_q + N_r \cdot N_r$ $2 \cdot N_r \cdot N_q$ $N_r \cdot N_q + N_q \cdot N_q$ $2 \cdot N_r \cdot N_q + N_q \cdot N_q$ </pre>
---	---

130	Delete \mathbf{D}_{rq}	$N_q \cdot N_q$
131	Read \mathbf{D}_{qq} from file	$2 \cdot N_q \cdot N_q$
132	$\mathbf{D}_{22} = \mathbf{D}_{qq} - \mathbf{D}_{22}$ %build D22 step 3)	$2 \cdot N_q \cdot N_q$
133	Delete \mathbf{D}_{qq}	$N_q \cdot N_q$
134	Compute Inverse of \mathbf{D}_{22} %build D22 step 4) (complete)	$N_q \cdot N_q$
135	Write \mathbf{D}_{22} to file %+++++Build D12	$N_q \cdot N_q$
136	Read \mathbf{D}_{temp} from file	$N_q \cdot N_q + N_r \cdot N_q$
137	$\mathbf{D}_{12} = -\mathbf{D}_{temp} \cdot \mathbf{D}_{22}$	$N_q \cdot N_q + 2 \cdot N_r \cdot N_q$
138	Write \mathbf{D}_{12} to file	$N_q \cdot N_q + 2 \cdot N_r \cdot N_q$
139	Delete \mathbf{D}_{22}	$2 \cdot N_r \cdot N_q$
140	%+++++Build D11	
141	$\mathbf{D}_{11} = -\mathbf{D}_{12} \cdot \mathbf{D}_{temp}^\dagger$ %build D11 part 1)	$2 \cdot N_r \cdot N_q + N_r \cdot N_r$
142	Delete \mathbf{D}_{12} \mathbf{D}_{temp}	$N_r \cdot N_r$
143	Read $(\mathbf{D}_{rr})^{-1}$ from file	$2 \cdot N_r \cdot N_r$
144	$\mathbf{D}_{11} = \mathbf{D}_{11} + (\mathbf{D}_{rr})^{-1}$ %build D11 part 2) (complete)	$2 \cdot N_r \cdot N_r$
145	Write \mathbf{D}_{11} to file	$2 \cdot N_r \cdot N_r$
146	Delete \mathbf{D}_{11} $(\mathbf{D}_{rr})^{-1}$	-

A situation in which the presented implementation has benefits is the special case in which there is no access to any high-performance computer cluster and the dimension of matrix \mathbf{D} exceeds the available memory of one local machine. The block-wise inversion shown in Table 5 lists peak memory requirements at line (125) as $2 \cdot N_r \cdot N_q + N_r \cdot N_r$ and also at line (129) as $2 \cdot N_r \cdot N_q + N_q \cdot N_q$ if the dimensions of the diagonal blocks \mathbf{D}_{rr} and \mathbf{D}_{qq} do not match. Building these two particular blocks in turn has peak memory requirements of $3 \cdot N_r \cdot N_r$ and $3 \cdot N_q \cdot N_q$ respectively, as can be seen at lines (78) and (96) in Appendix D. In conclusion, partitioning \mathbf{D} into four equally sized sub-matrices, i.e. $N_r = N_q$, is recommended. In many real world applications, however, system parameters far outnumber system responses and the dimension of the deviation matrix \mathbf{D} is not the largest data block that has to be hold in memory. As mentioned in [30], the multiplication between the sensitivity

matrix and the variance-covariance matrix can be a limiting factor for data assimilation as well. Which matrix operation during DA is the most time and/or memory consuming depends on the size of the system, particularly the ratio between numbers of responses N_r (N_q) to numbers of parameters N_α (N_β).

The example of the heat conduction chosen in this chapter in order to illustrate the partitioned DA has, for example, the location x_i as one of the system parameters and thus $N_r < N_\alpha$ is always true. Another example of a system for which $N_r < N_\alpha$ is true would be a transient system in which boundary conditions are considered as system parameters and consequently outnumber the responses, see e.g. [5]. Finally, neutron transport applications have neutron cross sections as parameters and these can easily outnumber the responses by several orders of magnitude, [27].

Based on the 1-dimensional heat conduction, large sets of synthetic data were created to compare the actual memory requirements to the theoretical values of Table 5 and Appendix D. The complete data set A comprises $N_r = 5000$ responses and $N_\alpha = 10000$ parameters. In this data set matrices with the dimension of parameters are expected to dominate the computational performance. The second complete data set B comprises $N_r = 10000$ responses and $N_\alpha = 10006$ parameters. In this case both the dimension of responses and the dimension of parameters are expected to have an impact on performance. The theoretical analysis above revealed that an even partition between subsystem I and II leads to minimal memory allocations. Thus, 4 particular cases of matrix partitioning were considered for both data sets A and B. The individual size of each subsystem is listed in Table 6.

Table 6: Cases for block-matrix partitioning of data set A and B

	“Half – Half”	“Full – Half”	“Half – Full”	“Full – Full”
Data set A	$N_r^{pDA} = 2500$	$N_r^{pDA} = 5000$	$N_r^{pDA} = 2500$	$N_r^{pDA} = 5000$
	$N_q^{pDA} = 2500$	$N_q^{pDA} = 0$	$N_q^{pDA} = 2500$	$N_q^{pDA} = 0$
	$N_\alpha^{pDA} = 5000$	$N_\alpha^{pDA} = 5000$	$N_\alpha^{pDA} = 10000$	$N_\alpha^{pDA} = 10000$
	$N_\beta^{pDA} = 5000$	$N_\beta^{pDA} = 5000$	$N_\beta^{pDA} = 0$	$N_\beta^{pDA} = 0$

	$N_r^{pDA} = 5000$	$N_r^{pDA} = 10000$	$N_r^{pDA} = 5000$	$N_r^{pDA} = 10000$
Data set B	$N_q^{pDA} = 5000$	$N_q^{pDA} = 0$	$N_q^{pDA} = 5000$	$N_q^{pDA} = 0$
	$N_\alpha^{pDA} = 5003$	$N_\alpha^{pDA} = 5003$	$N_\alpha^{pDA} = 10006$	$N_\alpha^{pDA} = 10006$
	$N_\beta^{pDA} = 5003$	$N_\beta^{pDA} = 5003$	$N_\beta^{pDA} = 0$	$N_\beta^{pDA} = 0$

The splitting into equally sized subsystems labeled “Half – Half” yields the smallest matrix-blocks in theory and the peak for allocated memory is indeed minimal as shown in Figure 4. The maximum memory shown in this figure is the average over 10 individual data assimilation runs. For all cases the reported peak in memory is larger than the theoretical value, i.e. converting the maximum number of matrix elements held in memory into GB. This is due to the fact that MATLAB in combination with Windows as operating system handles memory in a specific way that creates quite substantial overhead of allocated memory. The trend of increasing memory requirement with fewer matrix partitions is however not affected by this overhead. The partition labeled “Full-Full” leaves subsystem II empty and this case is mathematically equivalent to the non-partitioned DA. Figure 4 therefore clearly demonstrates the benefit in memory requirements for the partitioned DA. Note that the intermediate partitioning case “Full-Half” requires approximately as much memory as the non-partitioned DA if the complete system is dominated by the dimensionality of responses. This is due to the fact, that the presented data assimilation is formulated in response-space such that the computationally most expensive operations, namely computing the inverse of a matrix, have the dimensions of N_r .

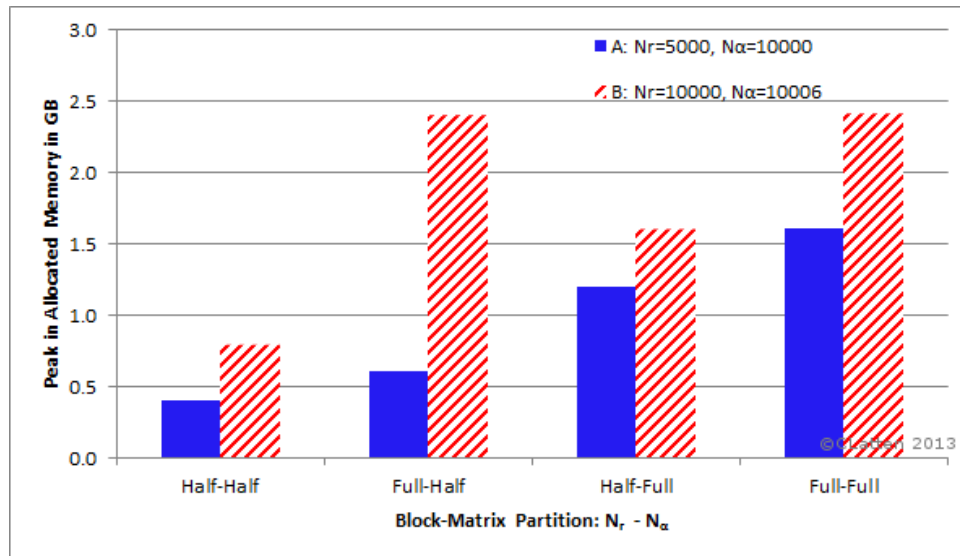


Figure 4: Average maximum in allocated memory of four different partitions for 2 sets of synthetic data

The implementation of the partitioned DA in MATLAB shows a significant decrease in peak memory requirement compared to the non-partitioned DA. Limitations of the presented algorithm are that the algorithms were compared in a serial environment using a scripting language. With the promising results shown in the present work, a parallel implementation in a programming language like C++ or FORTRAN would be the next step to further prove the positive performance of the suggested algorithm.

3.5 Evaluation Procedure to Identify least consistent Responses

The χ^2 metric, which was introduced shortly in Chapter 2.5, is a quantitative indicator to measure the mutual and joint consistency of the information available for model calibration, [9]. Eqs (2.60) - (2.63) clearly show that the partitioned DA offers three consistency indicators that can be computed separately, each measuring the agreement between the computed and experimental responses of the respective subsystem or matrix partition. A convenient form to compare the consistency of different systems is per degree of freedom, i.e. χ^2 normalized to the number of responses. In this case the closer χ^2/N_r is to unity the more likely it is that the experimental data is free of blunders and consistent with the assumptions. Here, assumptions would be the values of input parameters. In application to nuclear criticality benchmarks, assumptions are thus the cross section data in the respective nuclear data library. In general, even a single discrepant response can significantly worsen the set's overall consistency, particularly so in case the input parameters are assumed to follow a Gaussian distribution, [36] and [33]. It is therefore desirable to create an evaluation procedure that orders data in terms of least to most consistent. A method to do this was established in the 70s and is still accepted today, [36] and [9]. The following is a brief outline of this "consistency-wise optimal sequence", [36].

Starting from the complete set with N_r responses and the overall consistency χ^2 each response i is excluded once and $\chi_{N_r-1}^2(i)$ is re-evaluated. Next, the response on whose exclusion the value of $\chi_{N_r-1}^2$ decreases the most is identified as the least consistent one. After eliminating this least consistent response, N_{r-1} responses remain within the system and the new overall consistency indicator is $\chi_{N_r-1}^2$. In absence of the partitioned DA equations this requires computing the initial consistency indicator

$$\chi^2 = \underbrace{(\mathbf{r}_c - \mathbf{r}_m)^\dagger}_{(1 \times N_r)} \cdot \underbrace{\mathbf{D}^{-1}}_{(N_r \times N_r)} \cdot \underbrace{(\mathbf{r}_c - \mathbf{r}_m)}_{(N_r \times 1)} \quad (3.10)$$

once as well as computing the consistency indicator of each reduced system N_r times

$$\chi_{N_r-1}^2(i) = \underbrace{(\mathbf{r}_c - \mathbf{r}_m)^\dagger}_{(1 \times N_r-1)_{|_{i,i}}} \cdot \underbrace{\mathbf{D}^{-1}}_{(N_r-1 \times N_r-1)_{|_{i,i}}} \cdot \underbrace{(\mathbf{r}_c - \mathbf{r}_m)}_{(N_r-1 \times 1)_{|_{i,i}}} \quad (3.11)$$

The block matrix \mathbf{D} has been defined in Eq. (2.39). Values below the horizontal braces in Eqs (3.10) and (3.11) indicate the dimension of vectors and matrices. The procedure described so far is then applied repeatedly until only one response remains in the system. In total this would require $\frac{N_r \cdot (N_r + 1)}{2}$ computations of $\chi^2 = (\mathbf{r}_c - \mathbf{r}_m)^\dagger \mathbf{D}^{-1} (\mathbf{r}_c - \mathbf{r}_m)$ with changing vector and matrix dimensions. The re-evaluation of matrix \mathbf{D} as a first step and its inverse as a subsequent step is hereby implied. Depending on the size of the system this χ^2 evaluation procedure can become computationally expensive.

The partitioned DA comes with three individual consistency indicators, which can be used to reduce the computational cost of the consistency evaluation. The initial step of the evaluation procedure remains the same as in Eq. (3.10). Next, one response q is separated into subsystem II and the remaining $(N_r - 1)$ responses become subsystem I. Recall that the consistency indicators are correlated via

$$\chi^2 = \chi_{rr}^2 + \chi_{qq}^2 + \chi_{rq}^2 \quad (3.12)$$

Subsystem II consists of only one response and its consistency indicator can be readily obtained with the scalar operation

$$\begin{aligned} \chi_{qq}^2(i) &= \underbrace{(\mathbf{q}_c - \mathbf{q}_m)^\dagger}_{(1 \times 1)} \cdot \underbrace{\mathbf{D}_{22}}_{(1 \times 1)} \cdot \underbrace{(\mathbf{q}_c - \mathbf{q}_m)}_{1 \times 1} \\ &= \frac{(r_{c,i} - r_{m,i})^2}{D_{i,i}} \end{aligned} \quad (3.13)$$

The cross-term between subsystem I and II is a multiplication between vectors

$$\begin{aligned}
 \chi_{rq}^2(i) &= 2 \cdot \underbrace{(\mathbf{r}_c - \mathbf{r}_m)^\dagger}_{(1 \times N_r - 1)} \cdot \underbrace{\mathbf{D}_{12}}_{(N_r - 1 \times 1)} \cdot \underbrace{(\mathbf{q}_c - \mathbf{q}_m)}_{1 \times 1} \\
 &= 2 \cdot (r_{c,j} - r_{m,j})_{j \neq i}^\dagger \cdot \mathbf{D}_{12} \cdot (r_{c,i} - r_{m,i})
 \end{aligned} \tag{3.14}$$

The consistency indicator of the remaining, large subsystem I is then available via Eq. (3.12)

$$\chi_{rr}^2 = \chi^2 - \chi_{qq}^2 - \chi_{rq}^2. \tag{3.15}$$

Consequently, the partitioned DA identifies the optimal sequence with only computing \mathbf{D} and its inverse once per iteration step. The additional cost of multiplications between both scalars and vectors is negligible. This evaluation procedure is first illustrated with a small set of data based again on the 1-dimensional heat conduction of the previous chapter and the computational benefit is demonstrated with a larger data set next. Finally limitations of the new method are explained.

3.5.1 Small synthetic data set with $N_r = 10$ and $N_\alpha = 34$

Let a small sample set have $N_r = 10$ responses and $N = 10$ Fourier coefficients resulting in a total of $N_\alpha = 34$ parameters. The synthetic experimental and computed values with their respective uncertainty are chosen in a way that several responses are deliberately discrepant. This is visualized in Figure 5 by plotting the nominal response values with error bars of one standard deviation. The quantities appearing in the legend of Figure 5 have the same meaning as already explained in chapter 3.2. This figure shows that response r_1 , for instance, has a nominal computed value that is farther away from the nominal measured value than the sum of their respective standard deviations. This is equivalent with the error bars of one standard not overlapping for a particular response in Figure 5. Such a behavior can be an indicator of discrepant data. The complete system including all responses yields the following consistency indicator per degree of freedom

$$\frac{\chi^2}{N_r} = \frac{62.96}{10} = 6.296. \tag{3.16}$$

This normalized value is far from unity and indicates again the presence of inconsistent data. However, this single value does not identify which response(s) are the most discrepant.

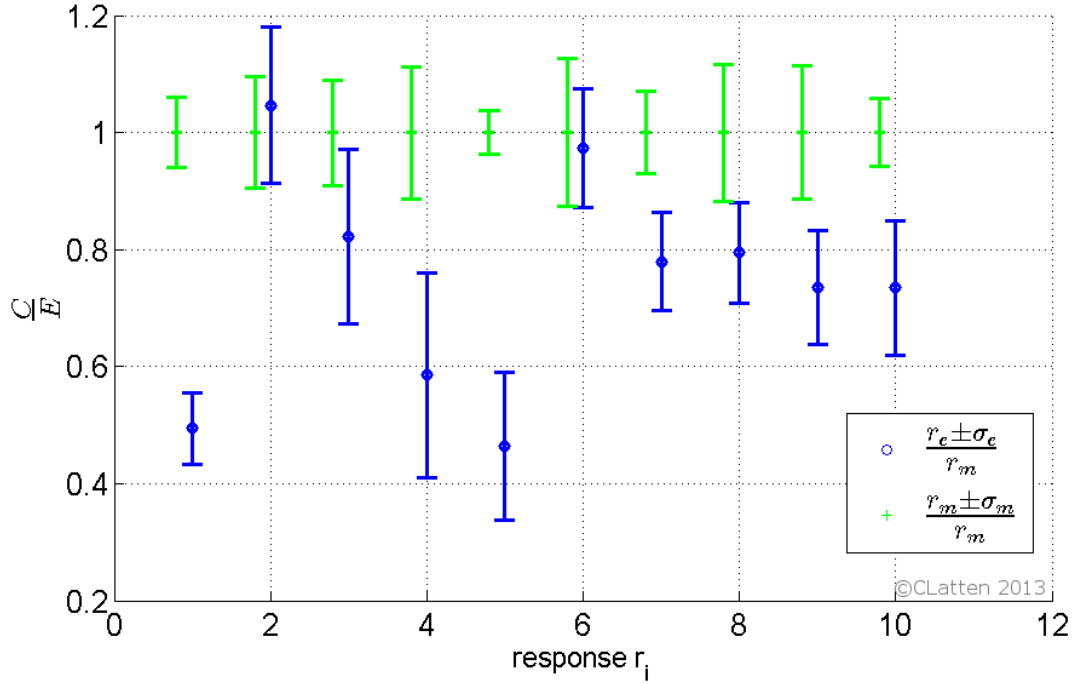


Figure 5: Measured and computed responses with one standard deviation normalized to the measured nominal value.

Starting the χ^2 evaluation procedure response r_{10} is excluded and thus assigned to subsystem II. The deviation matrix \mathbf{D} is therefore partitioned in the following way,

$$\mathbf{D}^{-1} = \left[\begin{array}{ccc|c} D_{1,1} & \cdots & D_{1,9} & D_{1,10} \\ \vdots & \ddots & \vdots & \vdots \\ D_{9,1} & \cdots & D_{9,9} & D_{9,10} \\ \hline D_{10,1} & \cdots & D_{10,9} & D_{10,10} \end{array} \right]^{-1} = \left[\begin{array}{c|c} \mathbf{D}_{11} & \mathbf{D}_{12} \\ \mathbf{D}_{12}^\dagger & \mathbf{D}_{22} \end{array} \right]. \quad (3.17)$$

The individual blocks in Eq. (3.17) are separated visually by vertical and horizontal lines. The partition \mathbf{D}_{11} represents subsystem I, the partition \mathbf{D}_{22} represents subsystem II and the off-diagonal partition \mathbf{D}_{12} represents coupling terms between subsystem I and subsystem II. Application of Eq. (3.13) yields the new consistency indicator $\chi_{rr}^2 = 64.009$ for subsystem I, which includes responses (r_1, \dots, r_9) . Eq. (3.14) gives the individual consistency of subsystem II, which includes only response r_{10} , as $\chi_{qq}^2 = 5.921$. And finally Eq. (3.15) yields the cross-term $\chi_{rq}^2 = -6.966$. Note that excluding response r_{10} from the data set does not change the consistency indicator of subsystem I much. As Figure 5 already indicated in a

qualitative way, response r_{10} is not the least consistent response and its exclusion improves the overall consistency only marginally. Next, response r_{10} is returned to the system and response r_9 is treated as subsystem II. This sequence is repeated for all responses in the set. And thus after this first iteration step one particular response can be identified which changes the overall consistency the most. Figure 6 shows the normalized consistency indicator of sub system I, $\chi_{rr}^2(i)$, for each excluded response r_i . The horizontal axis in this figure lists which response was shifted to subsystem II. The legend refers to the standard method, which excludes a response r_i completely, and the new partitioned DA method, which shifts a response r_i to subsystem II. Figure 6 displays a slight deviation between the new and the standard method. This deviation is addressed in chapter 3.5.2.

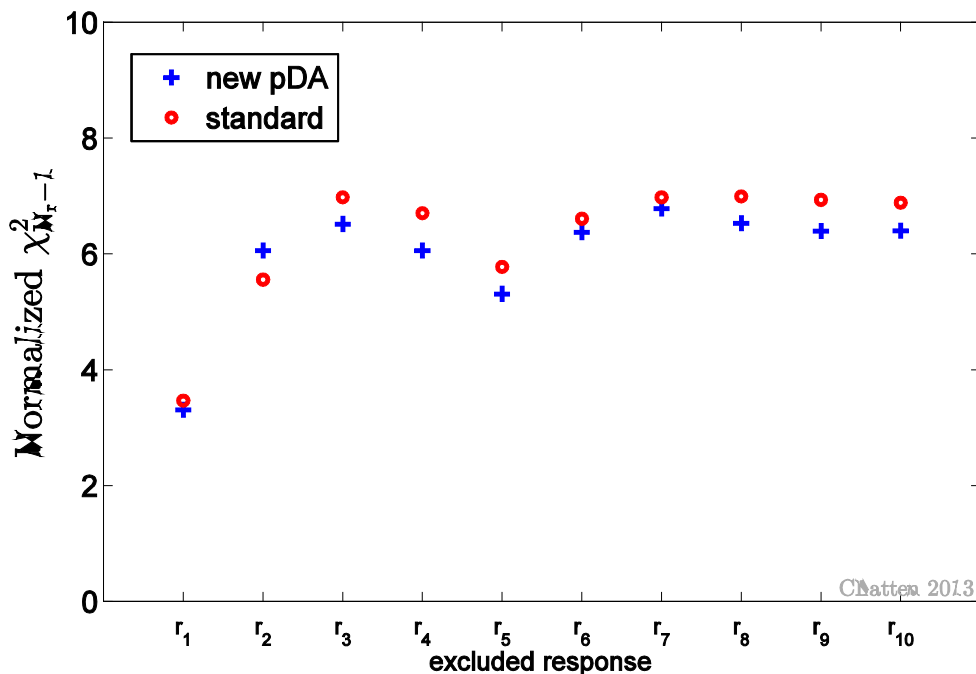


Figure 6: Normalized χ^2 of the remaining 9 responses computed with the standard and the new procedure

Figure 6 identifies response r_1 as least consistent. Excluding response r_1 from the system entails eliminating rows and/or columns from the vector of measured responses \mathbf{r}_m , the vector of computed responses \mathbf{r}_c , the variance-covariance matrix \mathbf{C}_{rr} for the measured responses, the sensitivity matrix $\mathbf{S}_{r\alpha}$ and finally the parameter-response uncertainty matrix $\mathbf{C}_{r\alpha}$. The matrix of deviations between computed and measured responses \mathbf{D} and its inverse have to be re-evaluated for the new, reduced system once. Next, each of the

remaining responses $\mathbf{r}^{N_r=9} = [r_2 \ r_3 \ r_4 \ r_5 \ r_6 \ r_7 \ r_8 \ r_9 \ r_{10}]$ is excluded once and the effect on the consistency indicator is again noted. This step identifies the second to least discrepant response and the procedure is repeated until only one response is left in the system. The complete sequence for χ^2 per degree of freedom is shown in Figure 7. The horizontal axis lists the progressively excluded responses starting with the least consistent one, namely the already mentioned response r_1 . The quantities in the legend refer to the consistency indicator of the complete system with $N_r = 10$ responses (compare to Eq. (3.16)), the consistency indicator of the reduced systems computed with the standard method and the consistency indicator of the reduced systems computed with the new partitioned DA procedure. Furthermore, the same figure shows the central 90% significance range depending on the remaining degrees of freedom. Excluding the two responses r_1 and r_5 brings the normalized χ^2 inside the central 90% significance range. Based on this confidence interval as criteria several reduced systems are identified as consistent. Deciding

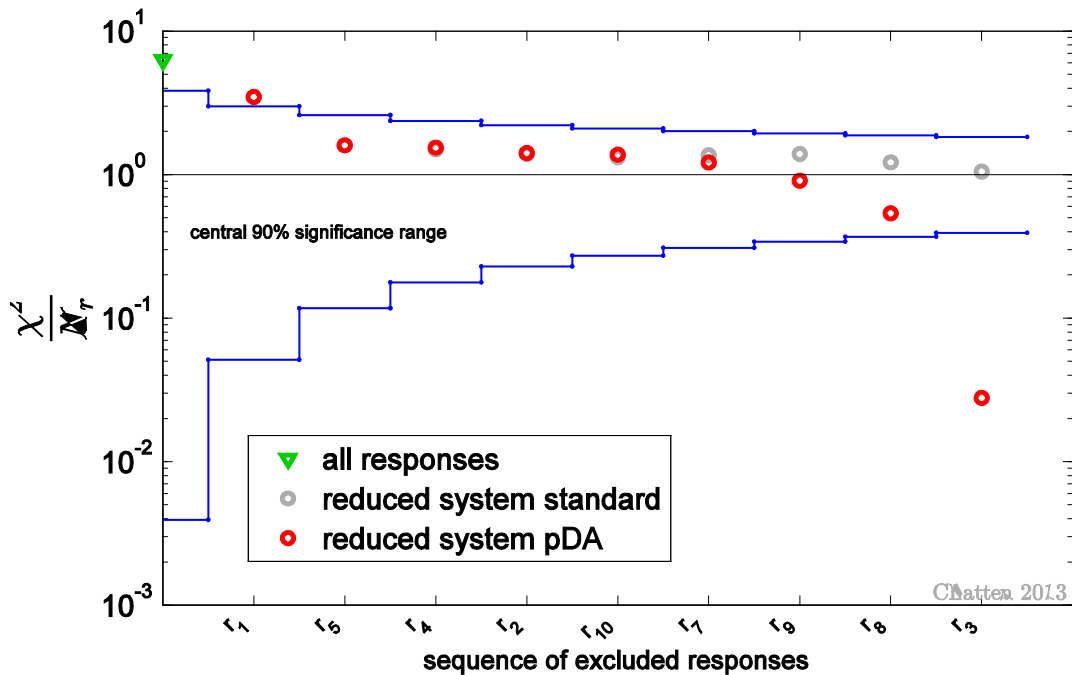


Figure 7: Normalized χ^2 for progressively excluded discrepant responses

which of these should be used for the subsequent data assimilation is a trade-off between less but consistent data compared to more but marginally discrepant data. The more consistent information is available for data assimilation the smaller become the best-estimate uncertainties. Finally, exclusion of response r_3 moves the normalized χ^2 outside the confidence range. This usually indicates that the uncertainties assigned to the model's

assumptions have been overestimated. However, in this case the remaining system consists of one single response, namely r_6 . With only one degree of freedom the χ^2 metric loses credibility. The reduction to the extreme case of one remaining response was demonstrated here for illustrative purposes only and is unlikely to occur in real-world applications. Figure 6 and Figure 7 both display a slight deviation between the new and the standard method. This deviation is addressed in chapter 3.5.2.

Best-estimate results of data assimilation depend strongly on the data used as input. The following section compares data assimilation applied to the complete data set, which contains deliberately discrepant data, to data assimilation applied to the first reduced system, which falls within the 90% significance range and excludes the two most discrepant responses. The complete system includes all $N_r = 10$ responses. The selected, reduced system includes $N_r = 8$ responses excluding the two least consistent responses, namely r_1 and r_5 . The calibrated responses for both cases are shown in Figure 8 together with the nominal measured and computed values. New symbols appearing in the legend of this figure have the following meanings: \mathbf{r}_{all}^{be} denotes the mean value for a best-estimate response resulting from the application of DA to the complete system and \mathbf{r}_8^{be} denotes the mean value for a best-estimate response resulting from the application of DA to the selected, reduced system with eight responses. Figure 8 illustrates that applying data assimilation to the complete system yields significantly different best-estimate results than applying it the reduced system. In this example, the mean best-estimate values of responses r_2 and r_6 vary considerably with the number of included responses. The corresponding best-estimate standard deviations vary only marginally. The impact of excluded responses on the calibration depends on the magnitude of discrepancy in the data set. This highlights the importance of a consistency evaluation procedure prior to data assimilation.

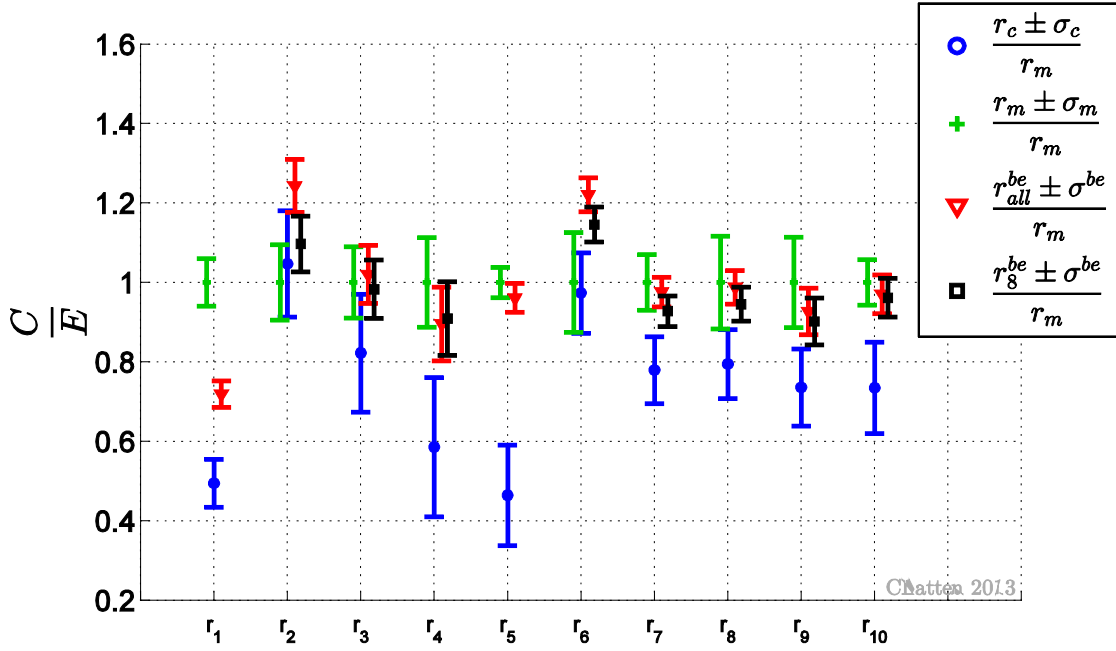


Figure 8: Normalized measured, computed and best-estimate responses with one standard deviation for the complete system with ten responses and a selected, reduced system with eight responses.

3.5.2 Large synthetic data sets

In order to compare computational performance of the χ^2 evaluation procedures large synthetic data sets, which range from 50 to 500 responses, were created. One representative data set with $N_r = 100$ responses and $N_\alpha = 124$ parameters is shown as example in Figure 9. The legend of this figure uses the already introduced symbols for the mean measured values \mathbf{r}_m and their corresponding standard deviation σ_m as well as the mean computed values \mathbf{r}_c and their corresponding standard deviation σ_c . All systems contain intentionally inconsistent data, which can qualitatively be seen in Figure 9 by particular responses with non-overlapping error bars. The created data sets contain discrepant data of varying degree and the consistency indicator χ^2 per degrees of freedom ranges from 2.2 to 9.3. The consistency procedure is applied with the limit to identify the 20 least consistent responses for each data set. This leaves a minimum of 30 responses in the smallest system, which has a total of $N_r = 50$ responses. In this way it is assured that sufficient degrees of freedom remain for the χ^2 metric to be reliable. The sequence of χ^2 per degrees of freedom is shown in Figure 10 for the data set with $N_r = 100$ as representative example. The consistency indicator for the complete system (green triangle) falls as expected outside the central 90% significance range, which is indicated with blue

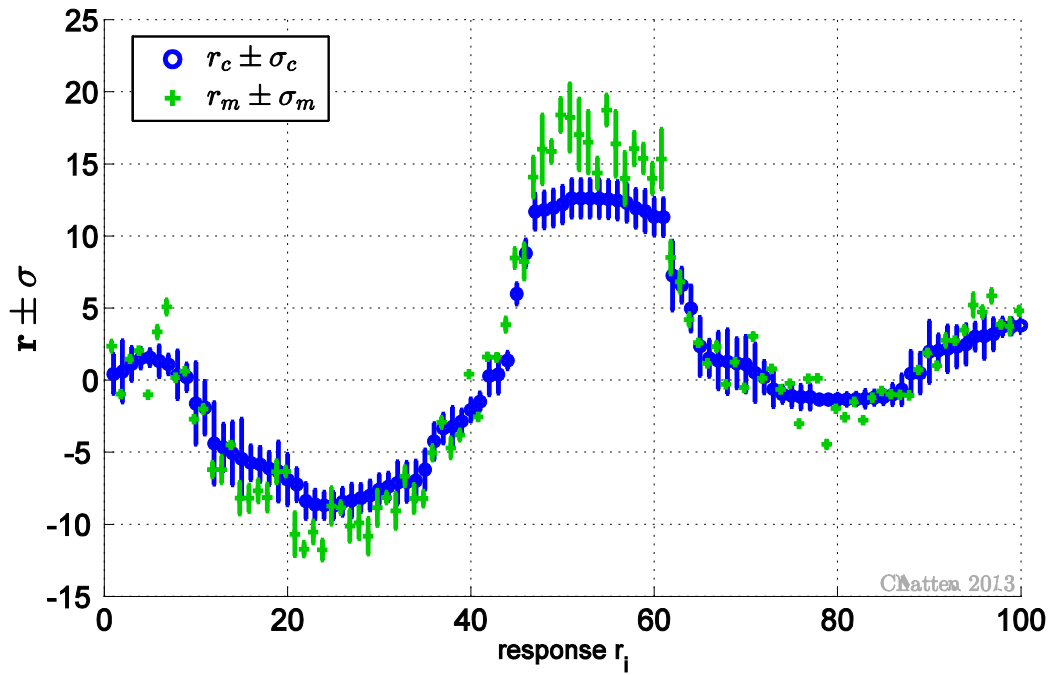


Figure 9: Measured and computed responses for synthetic data set with $N_r = 100$

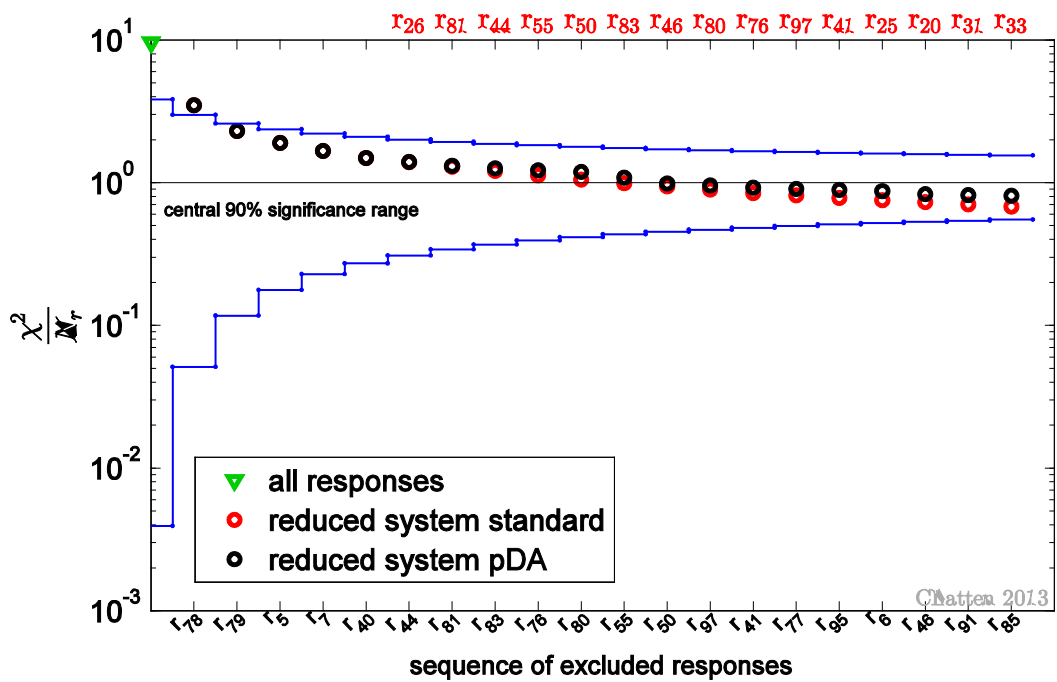


Figure 10: Normalized χ^2 for progressively excluded discrepant responses in case of the synthetic data set with $N_r = 100$

lines. The most discrepant response in this data set is response r_{78} . Exclusion of this response improves the overall consistency considerably, but the χ^2 metric remains outside the central 90% significance range. Only the additional exclusion of response r_{79} results in a consistency indicator that falls within the chosen significance range. Similar sequences are obtained for the other data sets.

The performance of Eqs. (3.13), (3.14) and (3.15), which are available through the partitioned DA method, compared to the standard non-partitioned method is measured as time on 1 CPU to identify and progressively exclude the 20 least consistent responses. The partitioned DA decreases the computational time by two orders of magnitude, see Figure 11.

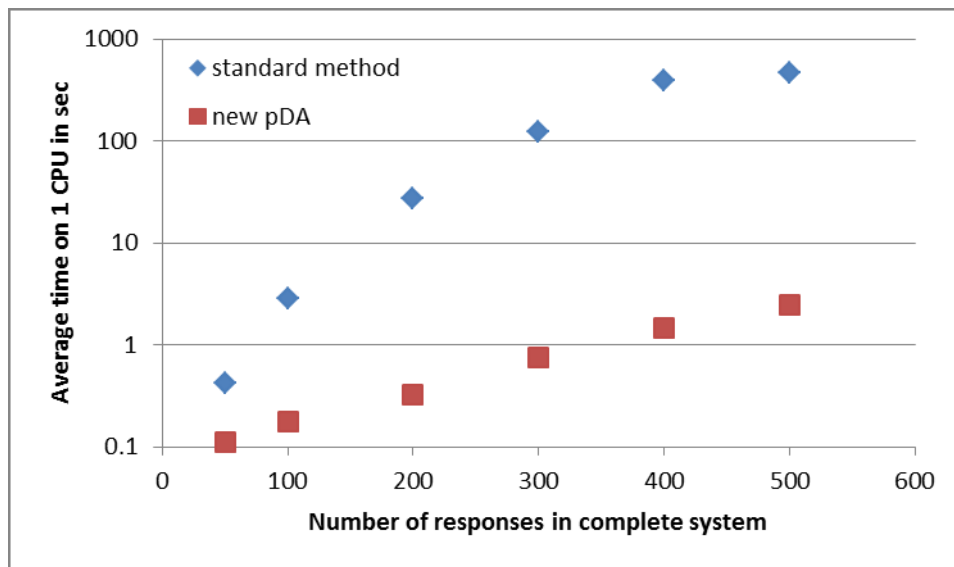


Figure 11: Average time on 1 CPU to identify the 20 least consistent responses using the new partitioned DA method compared to the standard method for several data sets

In order to gain this huge benefit in computational performance the new consistency evaluation procedure is not mathematically equivalent with the standard method. The slight deviation between methods could already be seen in Figure 6, Figure 7 and more notably so in Figure 10. The resulting sequence of excluded responses can differ between the two methods. Using again the data set with $N_r = 100$ as representative example, Figure 10 immediately shows that both procedures identify the 5 least consistent responses in the same order and the consistency indicator χ^2 falls well within the central 90% confidence range. However, as the sequence continues to identify marginally discrepant responses, the two procedures yield different answers, see Figure 10. This behaviour is theoretically possible, since the values are computed with mathematically non-equivalent equations. The

qualitative difference is that $\chi_{N_r-1}^2$ of the standard method is computed excluding one response completely, while $\chi_{rr}^{2,(pDA)}$ is computed including some interdependence between subsystem I and the “excluded” response in subsystem II. Another way of looking at it is that $\chi_{rr}^{2,(pDA)}$ reflects primarily the consistency of subsystem I, but keeps some aspects of the coupling to subsystem II (as the “excluded” response). This remaining interdependence to the response that is excluded becomes visible if responses that are only marginally discrepant are excluded. Since the deviation between methods only occurs after the 90% significance range is reached, the new procedure is advantageous if applied to find the most discrepant responses. To identify responses that are only marginally discrepant (i.e. the system is already within a certain confidence range) the standard procedure yields more reliable results at a high computational cost.

4. Application to Neutron Transport Benchmarks

The previous chapter served as illustrative introduction to data assimilation and demonstrated the functionality of the partitioned data assimilation method with synthetic data. In this chapter, partitioned DA is applied to several neutron transport benchmarks, namely the bare uranium sphere Godiva, the bare plutonium spheres Jezebel-239 and Jezebel-240 as well as the cylindrical assembly with mixed plutonium-uranium-oxide fuel and sodium ZPR-6/7, which has a thick depleted uranium reflector. Various combinations of these reactor physics criticality benchmarks are considered. Section 4.2 presents the fast critical assemblies Jezebel-239 and Jezebel-240. These two benchmarks have been selected primarily because they share plutonium as the major material component. Isotopes that both systems have in common lead to a strong coupling between benchmarks by means of cross-terms in the parameter variance-covariance matrix. Section 4.3 considers the critical assembly Godiva, which was chosen for the amount of available experimental data. Having $N_r = 17$ system responses in total is considered sufficient to in turn allow the χ^2 evaluation procedure, which has been illustrated with a heat conduction example in chapter 3.5, to be applied. This demonstrates how discrepant responses can be easily identified and excluded with the partitioned DA method. Also, there exists a weak coupling between Godiva and the Jezebel benchmarks through shared nuclear data. Complementary to the exclusion of responses, the three benchmarks are combined, which in turn demonstrates how systems can be added with the partitioned DA method. Lastly, section 4.4 presents one particular loading of the Zero Power Reactor 6 assembly 7, which was selected as large scale application.

4.1 Neutron Transport

The rate at which various nuclear reactions occur as well as the stability of the fission chain reaction is determined by the distribution of neutrons. This population of neutrons is modeled by means of the neutron transport equation. The time-dependent transport equation expressed in terms of the angular flux ψ reads

$$\frac{1}{v} \frac{\partial \psi}{\partial t} + \mathbf{\Omega} \cdot \vec{\nabla} \psi(\mathbf{r}, \mathbf{\Omega}, E, t) + \Sigma_t(\mathbf{r}, E) \psi(\mathbf{r}, \mathbf{\Omega}, E, t) = \int_{4\pi} d\mathbf{\Omega}' \int_0^\infty dE' \Sigma_s(\mathbf{r}, \mathbf{\Omega}' \rightarrow \mathbf{\Omega}, E' \rightarrow E) \psi(\mathbf{r}, \mathbf{\Omega}', E', t) + Q(\mathbf{r}, \mathbf{\Omega}, E, t), \quad (4.1)$$

also called linear Boltzmann equation. Criticality safety benchmarks consider systems where the neutron population reaches a time independent equilibrium in the absence of external neutron sources. The k-eigenvalue of the neutron transport equation has the form

$$\begin{aligned} \boldsymbol{\Omega} \cdot \bar{\nabla} \psi(\mathbf{r}, \boldsymbol{\Omega}, E) + \Sigma_t(\mathbf{r}, E) \psi(\mathbf{r}, \boldsymbol{\Omega}, E) = \\ \int_{4\pi} d\boldsymbol{\Omega}' \int_0^\infty dE' \Sigma_s(\mathbf{r}, \boldsymbol{\Omega}' \rightarrow \boldsymbol{\Omega}, E' \rightarrow E) \psi(\mathbf{r}, \boldsymbol{\Omega}', E') \\ + \frac{\chi(\mathbf{r}, E)}{4\pi k} \int_{4\pi} d\boldsymbol{\Omega}' \int_0^\infty dE' \nu_f(\mathbf{r}, E') \Sigma_f(\mathbf{r}, E') \psi(\mathbf{r}, \boldsymbol{\Omega}', E'). \end{aligned} \quad (4.2)$$

In order to solve the k-eigenvalue for realistic, multi-dimensional energy-dependent problems it is necessary to calculate numerical solutions. Research on computational methods for the Boltzmann transport equation has been actively pursued from the 1950's and continues in the present. Two fundamentally different approaches exist, namely stochastic and deterministic methods. Stochastic methods, also called Monte Carlo methods, are based on a probabilistic interpretation of the transport process; whereas deterministic methods are based on discretizing the Boltzmann transport equation in each of its independent variables. The standard method to discretize energy is called discrete ordinates method (S_N), in which energy is defined in groups on a discrete grid. A variety of spatial differencing methods exists, which can be classified as first or second order schemes and cell-balance or finite element schemes. Discretization of all independent variables results in a very large algebraic system of equations that is computationally expensive to solve. In the present work the three-dimensional deterministic neutron transport code Denovo was used. Denovo is part of the code package SCALE6.1 which is developed at ORNL, see [\[15\]](#).

Two different types of integral system responses are considered for data assimilation. They are the effective multiplication factor k_{eff} on the one hand and spectral indices on the other. A spectral index is a reaction rate ratio of the form

$$r_i = \frac{\langle \sigma_1, \phi \rangle}{\langle \sigma_2, \phi \rangle}. \quad (4.3)$$

Several reaction rate ratios are available as system responses for each benchmark. The brackets indicate the inner product

$$\langle \sigma_1, \phi \rangle = \int_{\Delta V} \int_{\Delta E} \sigma_1 \phi dE dV \quad (4.4)$$

where σ_1 denotes a neutron cross section and ϕ is the scalar neutron flux. Thus, a reaction rate ratio is defined as the ratio of isotope's 1 neutron reaction rate divided by isotope's 2 neutron reaction rate at a particular volume V . The reaction rates considered here are fission and radiative capture. The volume for all benchmarks is a thin foil placed at a particular location inside the critical assembly. Both Jezebel configurations and Godiva have experimentally measured spectral indices for foils placed in the center of the sphere. ZPR-6/7 has experimentally measured spectral indices for several locations throughout the core.

Input parameters of deterministic neutron transport models are usually comprised of microscopic multi-group neutron cross section data of major reaction types, the average prompt fission neutron multiplicity $\bar{\nu}$ and fission spectrum information. There are individual cross sections for each material, nuclide, reaction type and energy-group in turn, thus the total number of parameters is here defined as

$$N_{\alpha} = N_{\text{Material}} \cdot N_{\text{Nuclides}} \cdot N_{\text{Reaction Type}} \cdot N_{\text{Energy Groups}} \quad (4.5)$$

The number of responses and parameters in each benchmark defines the respective size of matrices used in the data assimilation and Table 7 gives an overview. Even though the Jezebel-240 benchmark contains more individual nuclides than the Jezebel-239 configuration the total number of parameters is larger in the latter, because this benchmark has more reaction rate measurements with external foils placed at the central location.

Table 7: Parameter and response space of benchmarks

	Jezebel-239	Jezebel-240	Godiva
N_r	8	3	17
N_{α}	2241	1458	2916
Nuclides in sphere	$^{69}\text{Ga}, ^{71}\text{Ga},$ $^{239}\text{Pu}, ^{240}\text{Pu}, ^{241}\text{Pu}.$	$^{69}\text{Ga}, ^{71}\text{Ga},$ $^{239}\text{Pu}, ^{240}\text{Pu}, ^{241}\text{Pu}, ^{242}\text{Pu}.$	$^{234}\text{U}, ^{235}\text{U}, ^{238}\text{U}.$
Nuclides in foils	$^{238}\text{U},$ $^{233}\text{U},$ $^{237}\text{Np},$ $^{239}\text{Pu},$ $^{55}\text{Mn},$ $^{93}\text{Nb},$ $^{63}\text{Cu}.$	$^{238}\text{U},$ $^{237}\text{Np}.$	$^{238}\text{U},$ $^{233}\text{U},$ $^{237}\text{Np},$ $^{239}\text{Pu},$ $^{55}\text{Mn},$ $^{93}\text{Nb},$ $^{63}\text{Cu},$ $^{79}\text{Br},$ $^{81}\text{Br},$ $^{107}\text{Ag},$ $^{197}\text{Au},$ $^{127}\text{I},$ $^{209}\text{Bi},$ $^{59}\text{Co},$ $^{103}\text{Rh},$ $^{115}\text{In}.$

As mentioned above, the experimental values for each benchmark are taken from the International Handbook of Evaluated Criticality Safety Benchmark Experiments, [19]. The input parameters stem from the ORNL code package SCALE6.1. Several modules in SCALE6.1 process the raw nuclear data, e.g. from ENDF files, into a problem specific neutron cross section library. The same code package also contains variance-covariance information for neutron cross sections, the number of neutrons emitted per fission $\bar{\nu}$ and the fission spectrum χ for fissionable nuclides. This covariance information is a comprehensive compilation of uncertainty data available to date, but nonetheless incomplete. The quality of any calibrated result depends on the quality of the covariance information that is used as input. For each nuclide listed in Table 7 there exists covariance data for some of the possible reaction types with correlations between some of the energy groups. Covariance data with cross-correlations between different nuclides only exist for the fission cross sections between plutonium and uranium isotopes. As a consequence, two particular benchmarks can not only be coupled by sharing the same nuclides either in its geometry or in external foils, but also through the cross-correlation between a particular plutonium isotope and a particular uranium isotope. The two Jezebel benchmarks are coupled through both shared nuclides in the spheres and shared nuclides in the external foils. A coupling between any Jezebel benchmark and Godiva is based on shared nuclides in the external foils and the cross-correlation in the covariance data of plutonium and uranium.

4.1.1 Renormalization of Fission Spectrum Covariance Matrix

The fission spectrum covariance information requires special treatment, since the underlying fission spectrum follows a probability density function that must satisfy the normalization to unity,

$$\sum_{i=1}^{N_E} \chi_i = 1 \quad (4.6)$$

where N_E is the number of energy groups. As suggested in [35] and [24] either the sensitivity coefficients can be constrained or the covariance matrix can be normalized to yield the correct uncertainty effect in the response. Here, the latter approach was used. For Eq. (4.6) to be satisfied, the sums of the elements in any row of the variance-covariance matrix must be zero, [13].

$$\sum_{i=1}^{N_E} \sigma_{ij}^2 = 0 \quad (4.7)$$

Due to the general symmetry requirement of any covariance matrix this holds also in any column. In case of unconstrained sensitivity coefficients the numerical precision of the zero-sum constraint needs to be very high, [24]. This can readily be achieved by way of a renormalization of the covariance matrix of the fission spectrum prior to data assimilation,

$$\tilde{\sigma}_{ij}^2 = \sum_k \sum_l (\delta_{ki} - \chi_i) \sigma_{kl}^2 (\delta_{lj} - \chi_j) \quad (4.8)$$

where δ_{ij} is the Kronecker delta. In anticipation of best-estimate results the effect of renormalization of the variance-covariance data on the fission spectrum is shown for the case of Godiva for the isotope ^{235}U in Figure 12. If the uncorrected variance-covariance data is used, the fission spectrum uncertainty is overestimated. This in turn causes the unrealistically large relative change in the best-estimate fission spectrum shown in Figure 12.

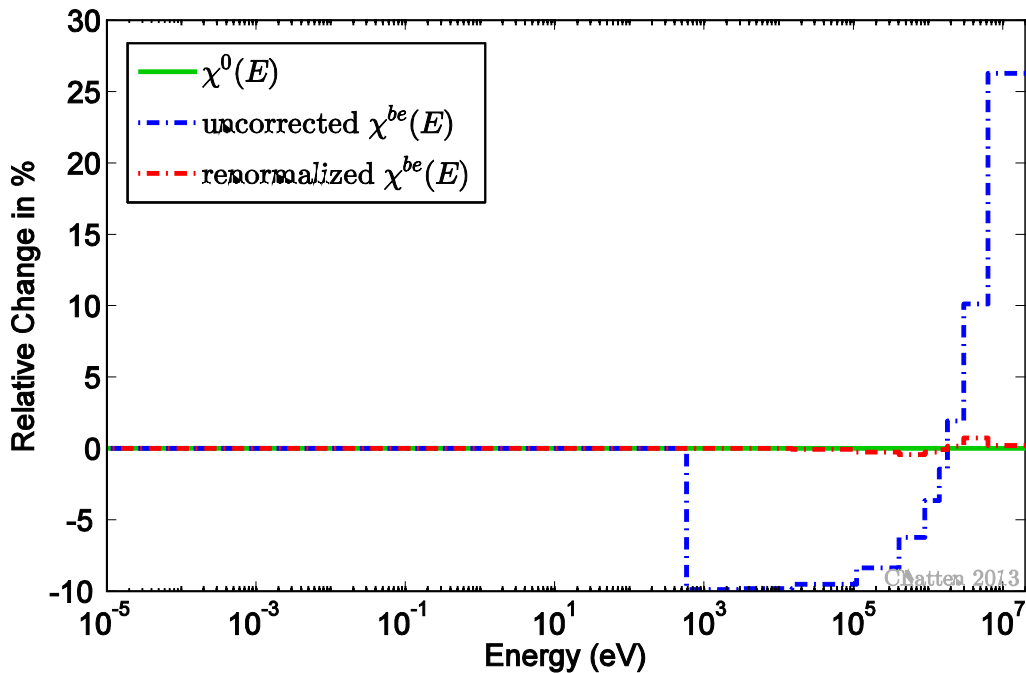


Figure 12: Relative change in best-estimate fission spectrum of ^{235}U prior (blue) and after (red) renormalization of the fission spectrum covariance data for Godiva.

The increase in numerical precision of the unity constraint for the probability distribution can be seen for selected fissionable nuclides in Table 8. This table clearly shows that the unity constraint for the best-estimate fission spectrum improves with increased precision. The overall effect of the renormalization on best-estimate integral responses is small for the applications considered here. However, including this step improves the numerical precision of the best-estimate fission spectrum considerably. Since the renormalization of an already

correctly normalized covariance matrix does not introduce any error, see [24], this renormalization procedure is applied to all covariance data of the fission spectrum of any fissionable isotope in the problem specific data sets prior to data assimilation.

Table 8: Unity constraint for the best-estimate fission spectrum of selected fissionable nuclides prior and after renormalization of the covariance data

Benchmark and selected fissionable nuclides		$\sum_{i=1}^{N_E} \chi_i$	$\left \sum_{i=1}^{N_E} \sigma_{ij}^2 \right _{\max}$
Jezebel-239: ^{239}Pu	Uncorrected	1.0014	5.0907e-005
	Renormalized	1.0000	8.9087e-007
Jezebel-240: ^{239}Pu	Uncorrected	1.0023	5.0907e-005
	Renormalized	1.0001	8.9087e-007
Godiva: ^{235}U	Uncorrected	0.9968	1.0117e-005
	Renormalized	0.9997	5.2671e-007

4.2 Data Assimilation on Jezebel-239 and Jezebel-240

During the 1950's and 1960's several critical assemblies were studied in detail at Los Alamos National Laboratory. Two unreflected plutonium spheres were considered acceptable as criticality benchmark and are referred to as Jezebel, [19]. Based on their isotopic abundance of plutonium, as shown in Table 9, one is denoted here as Jezebel-239 configuration and the other as Jezebel-240 configuration. The selection of these particular benchmarks illustrates the effect of systems that are coupled via shared isotopes. The average composition of the plutonium alloys as described in the respective benchmarks are listed in Table 10. The plutonium isotopes ^{239}Pu , ^{240}Pu and ^{241}Pu as well as the trace element gallium occur in both Jezebel configurations. All major reactions of these isotopes have been considered as parameters for the adjustment. Parameters that occur in both benchmarks lead to non-zero entries in the cross-term covariance matrix block $\mathbf{C}_{\alpha\beta}$ and thus couple Jezebel-239 to Jezebel-240. Eight responses were considered for Jezebel-239, as follows: the effective multiplication factor k_{eff} , the center core fission rates for ^{233}U , ^{238}U , ^{237}Np , and ^{239}Pu , as well as the center core radiative capture rates for ^{55}Mn , ^{93}Nb and ^{63}Cu . For Jezebel-240 the effective multiplication factor k_{eff} , along with the center core fission rates for ^{233}U and ^{237}Np were selected.

Table 9: Composition of the Plutonium in Jezebel-239 and Jezebel-240, [19]

	Jezebel-239 Radius: 6.3849cm	Jezebel-240 Radius:6.6595cm
Isotope	Abundance [at. %]	Abundance [at. %]
²³⁹ Pu	95.2	76.4
²⁴⁰ Pu	4.5	20.1
²⁴¹ Pu	0.3	3.1
²⁴² Pu	-	0.4

Table 10: Atom densities for the Jezebel-239 and Jezebel-240 benchmark, [19]

	Jezebel-239 Radius: 6.3849cm	Jezebel-240 Radius:6.6595cm
Nuclide	Atom Density [atoms / barn-cm]	Atom Density, [atoms / barn-cm]
Ga	$1.3752 \cdot 10^{-3}$	$1.3722 \cdot 10^{-3}$
²³⁹ Pu	$3.7047 \cdot 10^{-2}$	$2.9934 \cdot 10^{-2}$
²⁴⁰ Pu	$1.7512 \cdot 10^{-3}$	$7.8754 \cdot 10^{-3}$
²⁴¹ Pu	$1.1674 \cdot 10^{-4}$	$1.2146 \cdot 10^{-3}$
²⁴² Pu	-	$1.5672 \cdot 10^{-4}$

All experimental data stems from [19], which also contains a detailed description of the two benchmarks. The computational responses are results of numerical simulations using the neutron transport code Denovo with a weighted diamond-difference spatial discretization scheme. The spherical geometries of the Jezebel benchmarks are inherently symmetric so that computing an octant of each sphere is sufficient. The computational solutions are based on a $10 \times 10 \times 10$ Cartesian mesh and the ENDF/BVII.0 neutron cross section library with 27 energy groups. The boundaries of this energy group structure range from 10^{-5} eV to 20MeV. Integration of the computed scalar flux over the computational domain for each energy group yields a neutron flux spectrum, which is a characteristic quantity for any assembly. The normalized spectrum for both Jezebel configurations is shown in Figure 13. This figure illustrates that both Jezebel benchmarks are indeed fast assemblies, because the bulk of the spectrum is located at high energies in the intermediate and fast range. This is the expected behavior for bare plutonium spheres, which do not contain any neutron moderating materials. The neutron flux spectrum for lower energy ranges is vanishingly small. This includes in particular the resonance region and self-shielding can therefore be neglected in the computational model. Shape and magnitude of the spectrum of Jezebel-239 is very similar to the one of Jezebel-240.

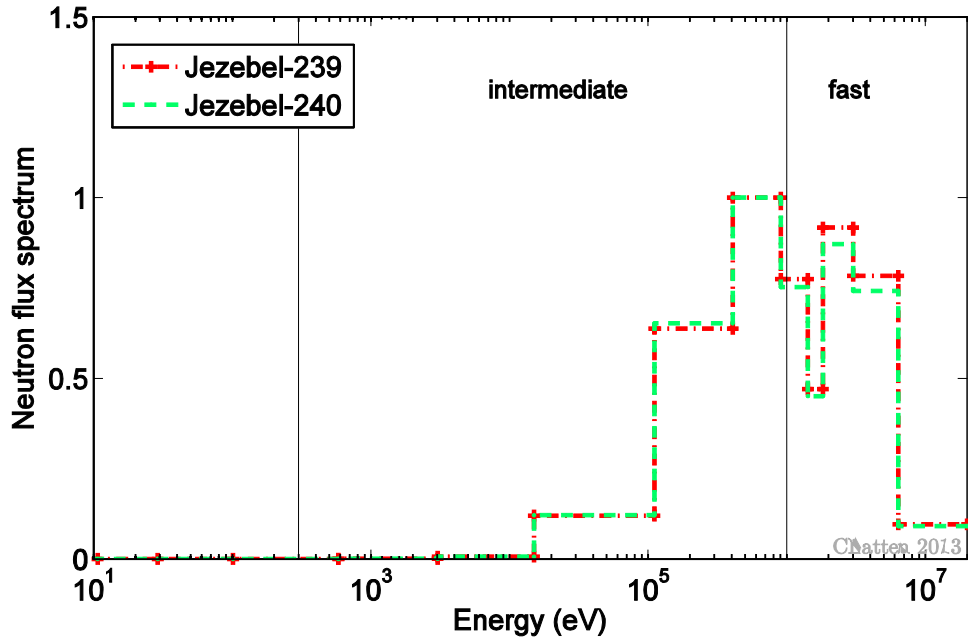


Figure 13: Spectrum of the neutron flux for Jezebel-239 and Jezebel-240

4.2.1 Sensitivity Analysis

Sensitivity coefficients of all system responses to all of the system parameters are essential quantities for data assimilation. Energy-dependent sensitivity profiles were computed via an adjoint sensitivity analysis procedure based on a customized addition to the standard adjoint capabilities of Denovo, [14]. The nuclear reactor community usually refers to the adjoint method, which obtains sensitivity coefficients, as perturbation method for the effective multiplication constant k_{eff} and as generalized perturbation method for reaction rate ratios.

Relative sensitivity coefficients are denoted here as

$$\left(\frac{\partial r_i}{\partial \alpha_j^x} \right)_{relative} = \frac{\partial r_i}{\partial \alpha_j^x} \cdot \frac{\alpha_j^x}{r_i} \quad (4.9)$$

where the response r in the nominator is either k_{eff} or a spectral index and the parameter α in the denominator is specified by the isotope j and the quantity x , which includes neutron cross sections to all major reaction types, the average prompt fission neutron multiplicity $\bar{\nu}$ and the fission spectrum χ . All figures in this section show relative sensitivities only and legend entries use thus the abbreviated form $\partial r_i / \partial \alpha_j^x$ to denote a relative sensitivity.

Recalling Table 7, which gave an overview of the parameter and response space of the benchmarks, it becomes clear that several thousand sensitivity coefficients have been computed. Grouping them into energy-dependent sensitivity profiles there remain 83 profiles for Jezebel-239 and 54 profiles for Jezebel-240. Representative sensitivity profiles have been selected and are discussed in the following; in particular the largest sensitivities for k_{eff} of Jezebel-239 and Jezebel-240 as well as the largest sensitivities for a fission reaction rate and a radiative capture reaction rate of Jezebel-239.

Energy-dependent profiles of relevant sensitivities of the effective multiplication constant k_{eff} are shown for Jezebel-239 in Figure 14 and for Jezebel-240 in Figure 15. The two largest sensitivity coefficients for the effective multiplication constant k_{eff} are observed in both Jezebel benchmarks for $\bar{\nu}$ and the fission cross section of ^{239}Pu . The sensitivity profiles ranked third and fourth most important differ for the two benchmarks. In case of Jezebel-240 the sensitivity coefficients for $\bar{\nu}$ and the fission cross section of ^{240}Pu are important, see Figure 15. The higher ^{240}Pu content in the Jezebel-240 configuration leads to significant sensitivity coefficients for this particular isotope. On the other hand, the fission spectrum χ is the third largest and the elastic scattering cross sections of ^{239}Pu is the fourth largest sensitivity profile for Jezebel-239, see Figure 14. Both benchmarks are fast assemblies and sensitivity coefficients at lower energies, which are not shown in Figure 14 or Figure 15, are vanishingly small.

The reaction rate ratios are grouped into two categories, namely *similar* and *dissimilar*. Spectral indices that have been measured in both Jezebel configurations are categorized as *similar*. For instance the fission rate of ^{238}U relative to the fission rate of ^{235}U has been measured in both Jezebel-239 and Jezebel-240. This *similar* response is denoted as

$$r_2 = \frac{\sigma_f(^{238}\text{U})}{\sigma_f(^{235}\text{U})}. \text{ A } \textit{dissimilar} \text{ response on the other hand is a spectral index, which is}$$

exclusively measured in one benchmark only. Sensitivity profiles to the most important cross sections of the respective nuclei for the *similar* response r_2 of Jezebel-239 are shown in Figure 16. The fission cross section of the isotopes ^{235}U and ^{238}U have the largest sensitivity coefficients. The response r_2 is thus most sensitive to changes in the cross sections and nuclides that make up the reaction ratio. This is the expected behavior for sensitivities of reaction rate ratios in general. To indicate that a particular parameter is associated with a foil, which is used in the experiments for reaction rate measurements,

those quantities have the additional index “foil” in their legend entries, see Figure 16. Note also that the sensitivity profile of the fission cross section of ^{235}U has a negative sign. This stems from the fact that $\sigma_f(^{235}\text{U})$ is the denominator of the reaction rate. Since all reaction rate ratios considered in the present work have the same denominator, namely $\sigma_f(^{235}\text{U})$, it follows that all responses associated with a specific benchmark have identical relative sensitivity profiles for the fission cross section of ^{235}U .

Figure 17 depicts the largest sensitivity profiles of the radiative capture reaction rate of ^{63}Cu normalized to the fission reaction rate of ^{235}U . This is a *dissimilar* response of Jezebel-239, which is denoted as $r_8 = \frac{\sigma_\gamma(^{63}\text{Cu})}{\sigma_f(^{235}\text{U})}$. Analogous to r_2 , the largest sensitivity coefficients of r_8

are the radiative capture cross section of ^{63}Cu and the fission cross section of ^{235}U . A comparison of the latter profile between Figure 17 and Figure 16 readily demonstrates that the energy-dependent sensitivities of the denominator $\sigma_f(^{235}\text{U})$ are indeed identical.

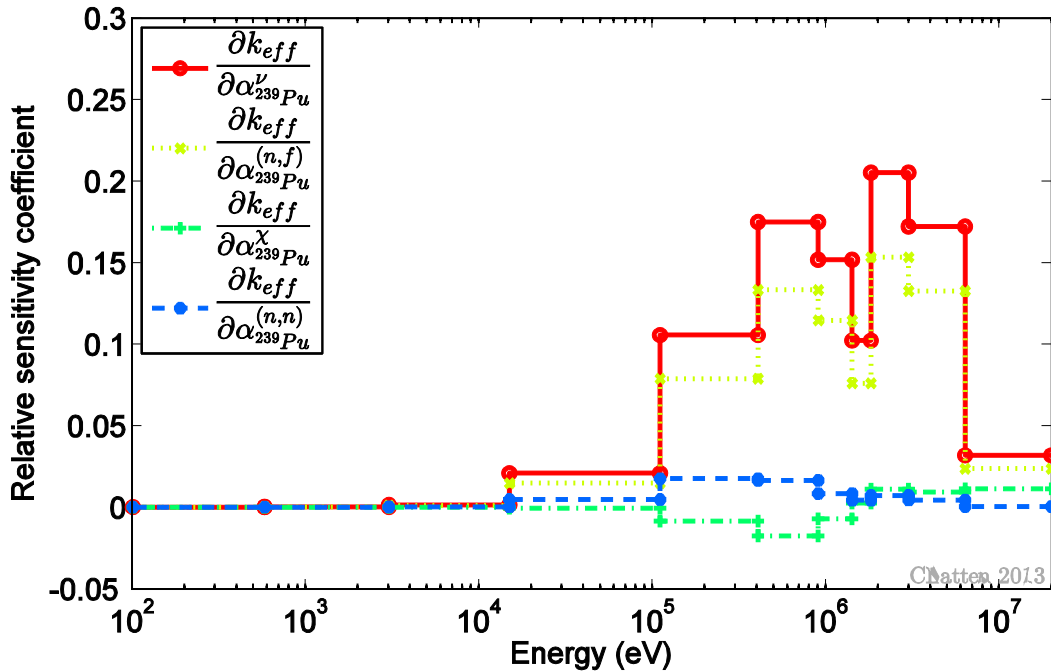


Figure 14: Sensitivity profile of k_{eff} to selected parameters for Jezebel-239

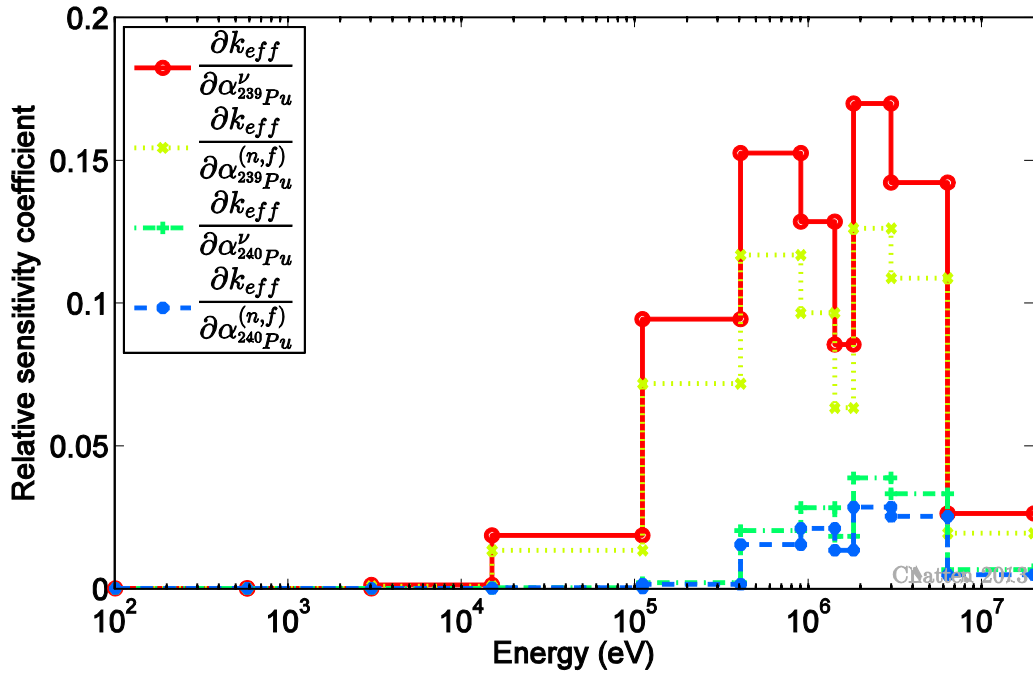


Figure 15: Sensitivity profile of k_{eff} to selected parameters for Jezebel-240

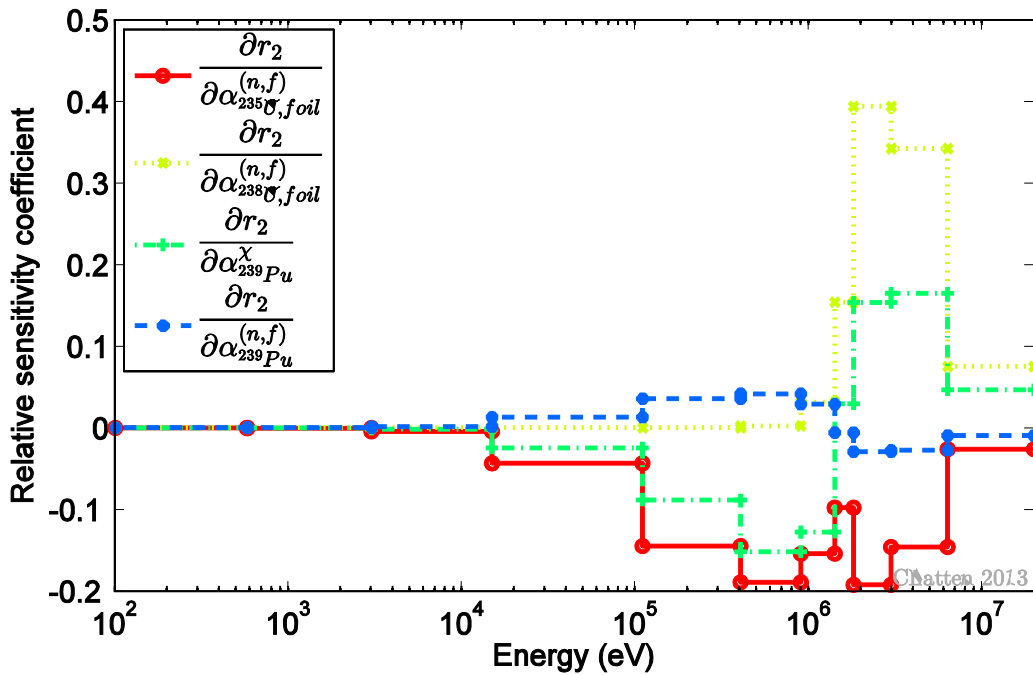


Figure 16: Sensitivity profile of $r_2 = \frac{\sigma_f(^{238}\text{U})}{\sigma_f(^{235}\text{U})}$ to selected parameters for Jezebel-239

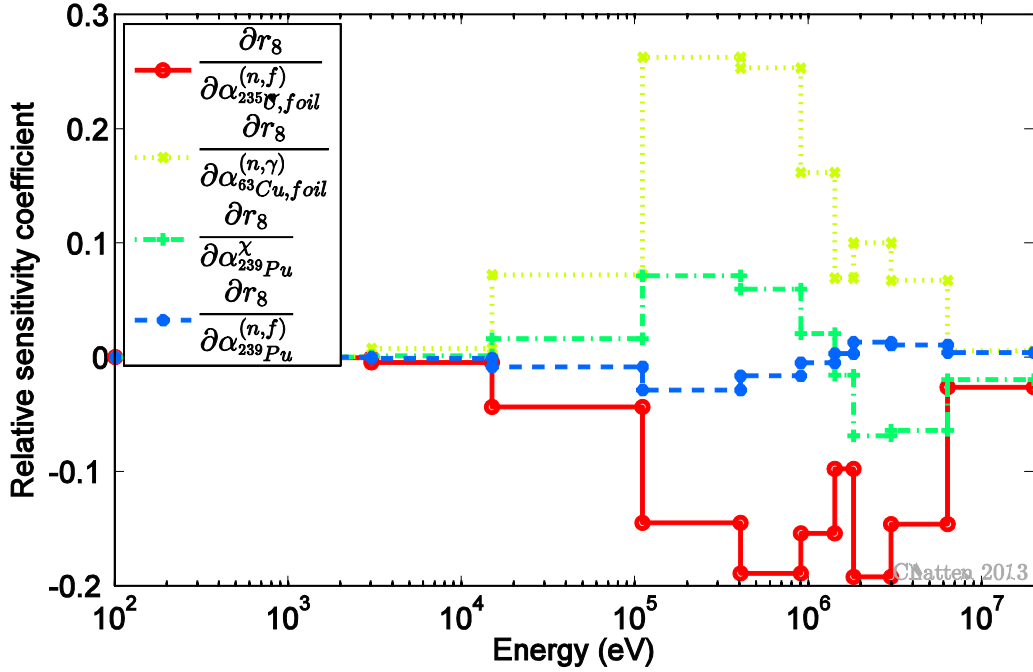


Figure 17: Sensitivity profile of $r_8 = \frac{\sigma_\gamma(^{63}\text{Cu})}{\sigma_f(^{235}\text{U})}$ to selected parameters for Jezebel-239

4.2.2 Uncertainty Quantification

Using the sensitivity coefficients above and available covariance data for the input parameters, the uncertainty of the parameters is propagated to the responses according to

$$\mathbf{C}_c^{(N_r+N_q) \times (N_r+N_q)} = \mathbf{S}^{(N_r+N_q) \times (N_\alpha+N_\beta)} \mathbf{C}_p^{(N_\alpha+N_\beta) \times (N_\alpha+N_\beta)} \left(\mathbf{S}^{(N_r+N_q) \times (N_\alpha+N_\beta)} \right)^\dagger. \quad (4.10)$$

Matrix dimensions are indicated in parenthesis. Eq. (4.10) is formulated in the most general form for a partitioned system, which includes the special case of a non-partitioned system if no additional parameters, i.e. $N_\beta = 0$, and no additional responses, i.e. $N_q = 0$ are present.

Let the relative uncertainty in a particular response r due to one or several particular processes be

$$\sigma_{r_i^x}^2 = S_{r,\alpha_i^x} \cdot \mathbf{C}_{\alpha_i^x \alpha_j^y} \cdot S_{r,\alpha_j^y} \quad (4.11)$$

where α_i^x denotes the nuclear data parameter of isotope i and reaction x . Eq. (4.11) can be defined for each energy group. Recall that parameters in neutron transport applications

are neutron cross sections, average number of neutrons per fission $\bar{\nu}$ and the fission spectrum χ . The summation of these entire group-wise relative covariances yields the uncertainty in response r due to a nuclide reaction pair. The top six uncertainty contributions for k_{eff} and $r_2 = \frac{\sigma_f(^{238}U)}{\sigma_f(^{235}U)}$ of Jezebel-239 are listed in Table 11. The largest uncertainty contribution in k_{eff} for the individual benchmark Jezebel-239 stems from $\bar{\nu}$ of the isotope ^{239}Pu , the largest uncertainty contribution in r_2 stems from inelastic scattering in ^{239}Pu . The fact that the largest uncertainty contribution does not necessarily correspond with the top ranked sensitivity coefficient can be explained by Eq. (4.11), which shows how the uncertainty in a response arises from matrix products of parameter (co)variances and sensitivities. A list of the six top ranked nuclide-quantity pairs varies therefore from the largest sensitivity profiles as shown in the previous chapter. Among the largest uncertainty contribution is only one covariance block, namely the uncertainty between elastic and inelastic scattering in the isotope ^{239}Pu . This value is negative, which corresponds with an expected anti-correlated behavior between elastic and inelastic scattering. The top six uncertainty contributions for k_{eff} and r_2 of Jezebel-240 are listed in Table 12. Order of magnitude and rank of the listed uncertainty contributions are similar to the ones of the Jezebel-239 configuration. Similar to the effects seen in the sensitivity coefficients, the higher abundance of the isotope ^{240}Pu in the Jezebel-240 configuration causes $\bar{\nu}$ in ^{240}Pu to be significant.

Table 11: Uncertainty contribution from Eq. (4.11) in k_{eff} and $r_2 = \frac{\sigma_f(^{238}U)}{\sigma_f(^{235}U)}$ for Jezebel-239

Nuclide Reaction Pair	Uncertainty in k_{eff} (%)	Nuclide Reaction Pair	Uncertainty in r_2 (%)
$^{239}Pu \bar{\nu}$ $^{239}Pu \bar{\nu}$	1.46E-02	$^{239}Pu(n, n')$ $^{239}Pu(n, n')$	9.55E-02
$^{239}Pu(n, n')$ $^{239}Pu(n, n')$	7.46E-03	$^{239}Pu(n, n)$ $^{239}Pu(n, n')$	-8.12E-03
$^{239}Pu(n, n)$ $^{239}Pu(n, n')$	-3.72E-03	$^{238}U(n, f)$ $^{238}U(n, f)$	2.68E-03
$^{239}Pu(n, n)$ $^{239}Pu(n, n)$	2.07E-03	$^{239}Pu(n, n)$ $^{239}Pu(n, n)$	1.82E-03
$^{239}Pu(n, f)$ $^{239}Pu(n, f)$	1.21E-03	$^{235}U(n, f)$ $^{235}U(n, f)$	1.68E-03
$^{239}Pu(n, \gamma)$ $^{239}Pu(n, \gamma)$	5.39E-05	$^{239}Pu \chi$ $^{239}Pu \chi$	1.32E-03

Table 12: Uncertainty contribution from Eq. (4.11) in k_{eff} and $r_2 = \frac{\sigma_f(^{238}U)}{\sigma_f(^{235}U)}$ for Jezebel-240

Nuclide Reaction Pair		Uncertainty in k_{eff} (%)	Nuclide Reaction Pair		Uncertainty in r_2 (%)
$^{239}Pu \bar{\nu}$	$^{239}Pu \bar{\nu}$	1.04E-02	$^{239}Pu(n, n')$	$^{239}Pu(n, n')$	7.01E-02
$^{239}Pu(n, n')$	$^{239}Pu(n, n')$	4.04E-03	$^{239}Pu(n, n)$	$^{239}Pu(n, n')$	-6.10E-03
$^{239}Pu(n, n)$	$^{239}Pu(n, n')$	-2.27E-03	$^{238}U(n, f)$	$^{238}U(n, f)$	2.68E-03
$^{239}Pu(n, n)$	$^{239}Pu(n, n)$	1.41E-03	$^{235}U(n, f)$	$^{235}U(n, f)$	1.68E-03
$^{240}Pu \bar{\nu}$	$^{240}Pu \bar{\nu}$	1.09E-03	$^{240}Pu(n, n')$	$^{240}Pu(n, n')$	1.64E-03
$^{239}Pu(n, f)$	$^{239}Pu(n, f)$	8.60E-04	$^{239}Pu(n, n)$	$^{239}Pu(n, n)$	1.35E-03

So far, only uncertainty contributions of each benchmark considered individually have been discussed. As already pointed out above, the two Jezebel configurations are coupled via the covariance block $C_{\alpha\beta}$ of shared isotopes. However, the blocks in the sensitivity matrix S , which contain cross-terms remain zero, e.g. $S_{r\beta} = \mathbf{0}$ and $S_{q\alpha} = \mathbf{0}$. This is a reasonable assumption, because a change in the parameters of Jezebel-239 does not affect the computed responses in Jezebel-240. The total uncertainty of a particular response is generally affected by these additional coupling contributions, but in the cases considered here the largest contributions stay unchanged. This means that both Table 11 and Table 12 are applicable either if the Jezebel configurations are considered individually or jointly. Depending on the magnitude of the interdependence between two subsystems it is in general possible that the coupling would create a significant or even the largest uncertainty contribution.

4.2.3 Cross-terms and Consistency Indicators

Two combinations of the Jezebel benchmarks are considered for the application of data assimilation. First, each of the benchmarks is considered as single model and data assimilation yields best-estimate values to each data set individually. Next, both Jezebel configurations are combined and data assimilation yields again best-estimate values to this coupled data set simultaneously. It has already been demonstrated in chapter 3 that both partitioned DA and non-partitioned DA yield the same results to numerical precision, i.e. the largest absolute deviation between any updated vector or matrix is here of the order of $O(10^{-13})$. The partitioned DA is applied to the coupled Jezebel configurations and the change in updated results compared to DA on each benchmark separately is observed.

Nuclides that are present in both Jezebels have already been pointed out, see Table 10. The cross section of such a nuclide is then a parameter in both subsystem I and II. For instance, the microscopic fission cross section $\sigma_{239Pu}^{(n,f)}$ in the isotope ^{239}Pu occurs in Jezebel-239 as well as in Jezebel-240. Cross sections information is stored in nuclear data libraries like ENDF/B-VII.0 as infinite dilution cross sections. However, this cross section information is modified into a problem specific nuclear data library in several modules in SCALE6.1 and the neutron transport computation in Denovo uses these problem-dependent cross sections. The modification in SCALE6.1 accounts for example for self-shielding, see [31]. One consequence is that the nominal value for the same parameter might differ in each subsystem. As a result there exists a parameter $\alpha_i = \sigma_{239Pu}^{(n,f)}$ in Jezebel-239 (subsystem I) and a parameter $\beta_j = \sigma_{239Pu}^{(n,f)}$ in Jezebel-240 (subsystem II) which are not identical. They are only approximately equal, i.e. $\sigma_{239Pu}^{(n,f)}(\text{Jezebel-239}) \cong \sigma_{239Pu}^{(n,f)}(\text{Jezebel-240})$ despite the fact that the corresponding infinite dilution cross section is the same. This distinction is made for all parameters. The parameter uncertainty information on the other hand is assumed to be universal and is not modified on a problem specific basis, [31]. Parameters, which are present in both Jezebel benchmarks, have an uncertainty correlation of unity as a result. In terms of the fission cross section example

$$\text{cov}(\alpha_i, \alpha_i) = \text{cov}(\beta_j, \beta_j) = \text{cov}(\alpha_i, \beta_j) \quad (4.12)$$

where $\alpha_i = \sigma_{239Pu}^{(n,f)}$ and $\beta_j = \sigma_{239Pu}^{(n,f)}$. The energy group structure of the cross sections has been omitted for ease of notation in this example.

The complete covariance information of cross-terms between the coupled Jezebel systems is expressed as the matrix $\mathbf{C}_{\alpha\beta}$ defined in Eq. (2.47). Note that the matrix $\mathbf{C}_{\alpha\beta}$ is not square, because the subsystems have different number of parameters, i.e. $N_\alpha \neq N_\beta$. The cross-terms contribute only one matrix block to the complete covariance matrix \mathbf{C}_p for all parameters, which is square and symmetric. The non-zero entries of this block matrix are shown in Figure 18. Since parameters that are present in both subsystems are assigned as separate parameters of the respective subsystem, the cross-terms in the sensitivity matrix are assumed to be zeroes, i.e. $\mathbf{S}_{r\beta} = \mathbf{0}$ and $\mathbf{S}_{q\alpha} = \mathbf{0}$.

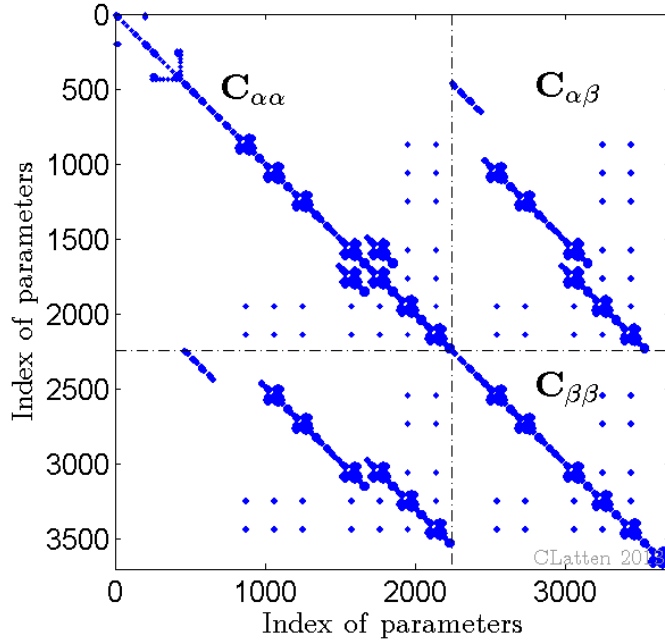


Figure 18: Non-zero elements in the covariance matrix C_p indicating parameters that are present in both Jezebel systems. $C_{\alpha\alpha}$ refers to Jezebel-239, $C_{\beta\beta}$ refers to Jezebel-240 and $C_{\alpha\beta}$ contains the cross-terms, which indicate the coupling between the two benchmarks.

Comparison of the consistency indicator χ^2 between the individual benchmarks and the coupled benchmarks shows in practice what Eqs. (2.58), (2.61) and (2.62) already indicated in theory. The overall consistency indicator $\chi^2(\text{pDA}) = 16.023$ for the coupled benchmarks cannot be compared to the consistency indicator of each Jezebel benchmark separately. The three individual parts that contribute to $\chi^2(\text{pDA})$, however, can readily be compared. A list of values can be found in Table 13. As expected, the values for the subsystems do not precisely match the values of the respective single model values. As soon as the systems are coupled it follows that some of the cross-terms, as for instance $C_{\alpha\beta}$, are non-zero and the subsystems affect each other as a result. For example, although χ_{rr}^2 indicates primarily the consistency for subsystem I (here Jezebel-239), it also reflects the interdependence to subsystem II (here Jezebel-240). Normalization to the respective degrees of freedom yields values that are approximately matching between the single model and the coupled model values. Thus, the partitioned DA allows conclusions about consistency for the combined system (here Jezebel-239 and Jezebel-240) as well as the individual systems.

Table 13: Comparison of consistency indicator χ^2 for benchmarks Jezebel-239 and Jezebel-240 regarded as single models separately and coupled models

	Single Model	Coupled Model
Jezebel-239	$\frac{\chi^2}{N_r} = \frac{9.032}{8} = 1.129$	$\frac{\chi_{rr}^2}{N_r^{pDA} + N_q^{pDA}} = \frac{12.523}{11} = 1.138$
Jezebel-240	$\frac{\chi^2}{N_r} = \frac{1.746}{3} = 0.582$	$\frac{\chi_{qq}^2}{N_r^{pDA} + N_q^{pDA}} = \frac{8.421}{11} = 0.766$
coupling term	-	$\frac{\chi_{rq}^2}{N_r^{pDA} + N_q^{pDA}} = \frac{-5.654}{11} = -0.514$

4.2.4 Partitioned and non-partitioned DA

Application of the partitioned DA on the combined system yields optimal values for each of the regarded eleven responses. Firstly, the response k_{eff} is discussed followed by *similar* responses and finally *dissimilar* responses are presented.

Figure 19 depicts the measured, computed and calibrated values for k_{eff} , all normalized to the nominal measured value. The error bars in this figure correspond with one standard deviation. The legend entries have the identical meaning as already introduced in chapter 3: \mathbf{r}_c and σ_c denote the mean value and corresponding standard deviation for a computed response, \mathbf{r}_m and σ_m denote the mean value and corresponding standard deviation for a measured response and lastly \mathbf{r}^{be} and σ^{be} denote the mean value and corresponding standard deviation for a best-estimate response resulting from the application of the non-partitioned data assimilation formulation to the benchmarks Jezebel-239 and Jezebel-240 individually. New quantities appearing in the legend are \mathbf{r}^{opt} and σ^{opt} , which denote the mean value and corresponding standard deviation for a calibrated (“optimal”) response resulting from the application of the partitioned data assimilation formulation to the benchmarks Jezebel-239 and Jezebel-240 considered jointly.

The computed value for k_{eff} is slightly super critical for both benchmarks. Also, the computed standard deviations are significantly larger than the measured standard deviations of the corresponding experiments. The relative values of the measured and computed standard

deviations indicate that the experimental nominal values are known more accurately than the computed ones. Applying data assimilation to each benchmark individually shifts the best-estimate mean values for k_{eff} closer to the respective experimentally measured nominal values, see Figure 19. Data assimilation inherently reduces the uncertainty of calibrated responses and the standard deviation for the best-estimate k_{eff} is thus, if only marginally here, smaller than the one of the measured k_{eff} . Partitioned data assimilation on both Jezebel configurations as coupled systems adjusts the mean k_{eff} value even closer to the measured mean value and simultaneously reduces the calibrated (“optimal”) standard deviation even more. The reason for this is simply that regarding Jezebel-239 and Jezebel-240 as a coupled systems provides more, consistent information and the uncertainty for the optimal k_{eff} is thus smaller than the best-estimate uncertainty for the individual benchmarks. The same information that is shown in Figure 19 is also compiled in Table 14.

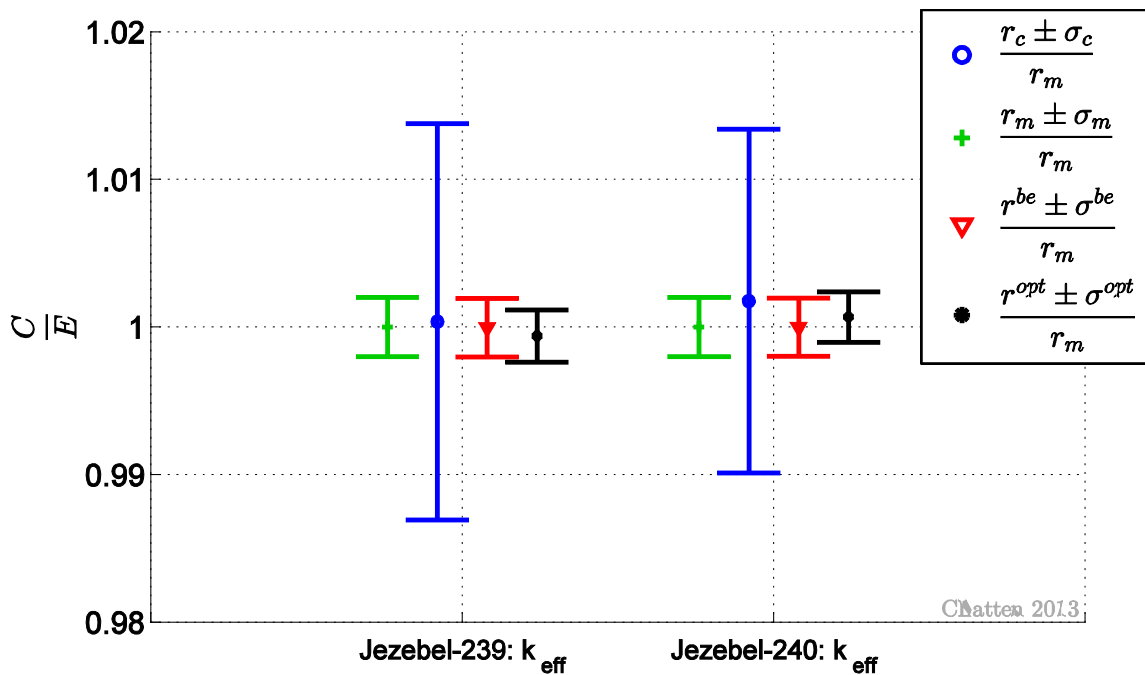


Figure 19: Jezebel-239 and Jezebel-240 – Measured, computed and best-estimate (single model) k_{eff} as well as optimal k_{eff} (coupled model) with one standard deviation normalized to the nominal measured value

Table 14: Jezebel-239 and Jezebel-240 measured and computed (Denovo) response values, as well as best-estimate and optimal values (based on partitioned DA) for k_{eff} .

Response	Type	Jezebel -239 ^{a)}		Jezebel – 240 ^{b)}	
		Value	± % rel. std.	Value	± % rel. std.
k_{eff}	Measured	1.000	0.2	1.000	0.2
	Computed	1.000355	1.342	1.001752	1.162
	Best-estimate (single model)	0.999958	0.197	0.999988	0.197
	Optimal (coupled model)	0.999391	0.178	1.000674	0.171

a) Jezebel-239 measured values are from [19] PU-MET-FAST-001 App. C Table D;

b) Jezebel-240 measured values are from [19] PU-MET-FAST-002 App. D Table D.

Figure 20 and Figure 21 present calibrated results for the reaction rate ratios responses. As before, these responses are grouped into two categories, namely *similar* responses and *dissimilar* responses. Recall that a *similar* response denotes a reaction rate ratio that was measured in Jezebel-239 as well as in Jezebel-240. A *dissimilar* response on the other hand was just measured in Jezebel-239.

The Jezebel benchmarks have two reaction rate ratios in common: the fission rates of ^{238}U and ^{237}Np . A comparison of these updated responses can be found in Table 15 and Figure 20. The computed fission rates of ^{238}U are both smaller than the experimentally measured ones, while the computed fission rates of ^{237}Np don't show a clear trend. Both calibrated values, i.e. best-estimate and optimal, fall in between the measured and the computed values, while reducing the respective calibrated standard deviations. The interdependence of *similar* responses is considerable. It is therefore not surprising that regarding both benchmarks jointly yields substantially different results from regarding Jezebel-239 and Jezebel-240 individually. As noted before, the availability of more, consistent data reduces the optimal standard deviations even further. Table 15 readily shows that the (relative) optimal standard deviation is always smaller than the corresponding (relative) best-estimate standard deviation.

Table 15: Jezebel-239 and Jezebel-240 measured and computed (Denovo) response values, as well as optimal values (based on partitioned DA) for *similar* reaction rate ratios.

Response	Jezebel -239			Jezebel - 240	
	Type	Value	± % rel. std.	Value	± % rel. std.
$\frac{\sigma_f(^{238}\text{U})}{\sigma_f(^{235}\text{U})}$	Measured	0.2133	1.1	0.2065	1.21
	Computed	0.206503	2.949	0.200878	2.580
	Best-est. (single model)	0.213349	0.978	0.205235	1.087
	Optimal (coupled model)	0.213307	0.809	0.206605	0.733
$\frac{\sigma_f(^{237}\text{Np})}{\sigma_f(^{235}\text{U})}$	Measured	0.9835	1.4	0.917	1.74
	Computed	0.977728	7.036	0.963701	6.960
	Best-est. (single model)	0.984273	1.392	0.920365	1.689
	Optimal (coupled model)	0.962971	1.091	0.946566	1.092

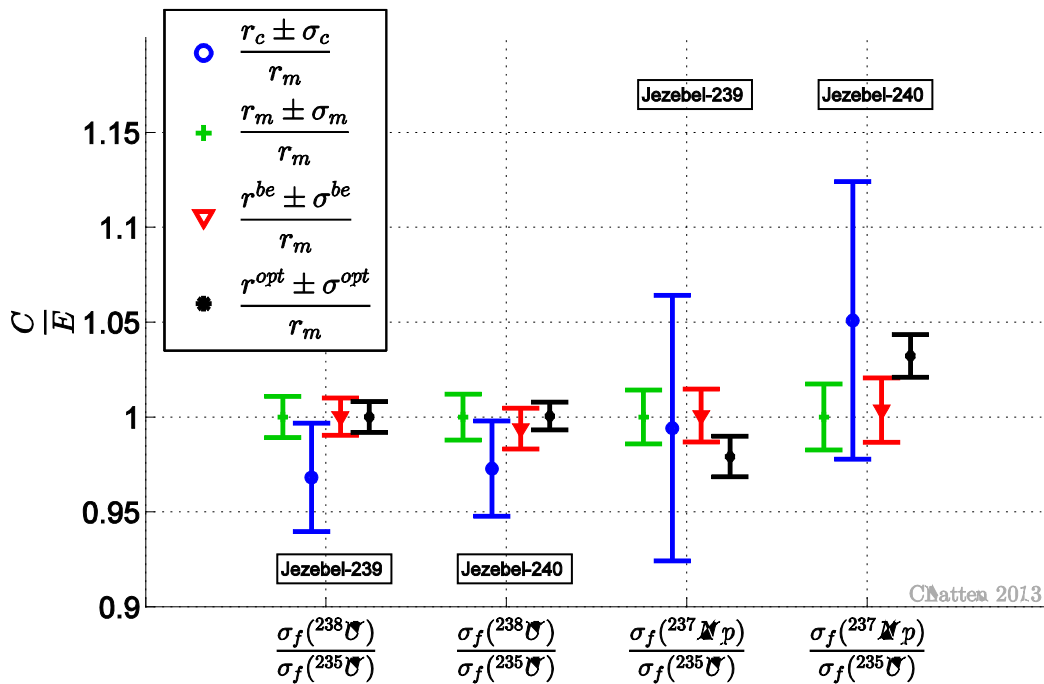


Figure 20: Jezebel-239 and Jezebel-240 – *Similar* measured, computed and best-estimate responses (single model) as well as optimal responses (coupled model) with one standard deviation normalized to the nominal measured value

Table 16 and Figure 21 present *dissimilar* reaction rate ratios, which includes both fission rate ratios and radiative capture rate ratios of Jezebel-239. The computed and experimentally measured standard deviations of the fission rate of ^{233}U and ^{239}Pu are

notably smaller than the standard deviations of the radiative capture ratios. Also, the fission rate of ^{239}Pu and the radiative capture rate of ^{93}Nb are discrepant. This is readily seen in Figure 21, since the difference between the computed and the experimentally measured nominal values is larger than the sum of one computed plus one experimentally measured standard deviation. Data assimilation yields in this case a calibrated nominal value and a calibrated standard deviation that reconcile the originally computed and measured discrepant values. The remaining consistent responses shown in Figure 21 have a calibrated value that falls in between the measured and the computed values while simultaneously reducing the respective calibrated standard deviation. In contradistinction to *similar* reaction rate ratios, *dissimilar* responses are only slightly affected by the coupling to the Jezebel-240 benchmark. The mean best-estimate values and the corresponding standard deviations, which stem from data assimilation applied to Jezebel-239 individually, are approximately identical to the optimal values, which stem from data assimilation applied to Jezebel-239 and Jezebel-240 as coupled system. A comparison of these updated responses can be found in Table 16. Note however, that if the calibrated standard deviations differ, the optimal (relative) standard deviation is always smaller than the respective best-estimate (relative) standard deviation.

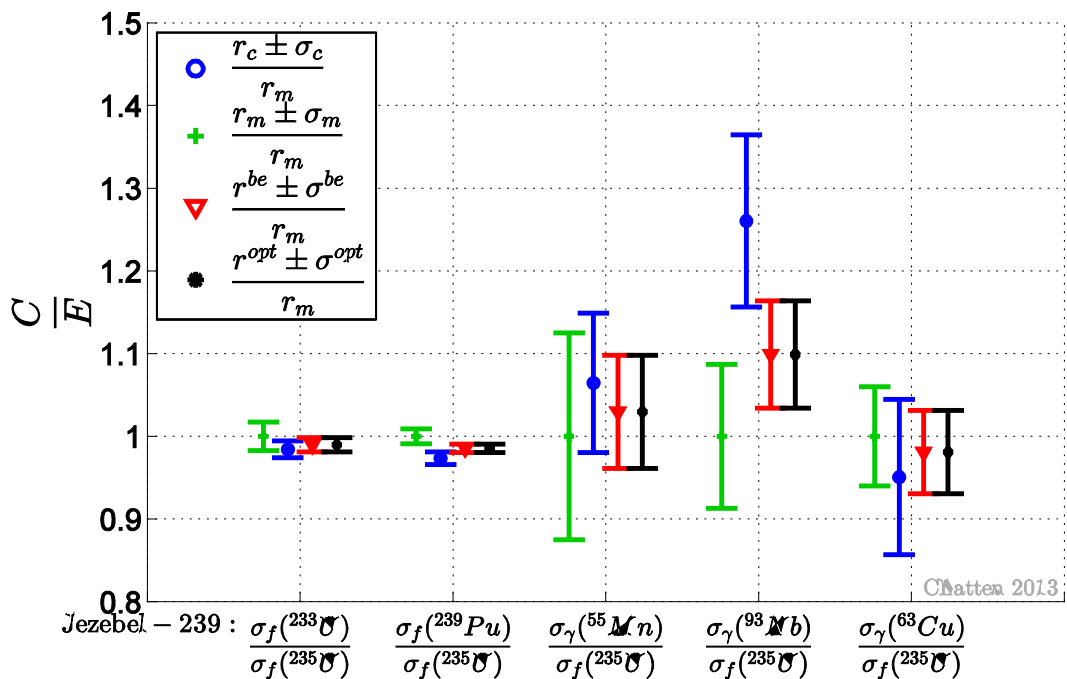


Figure 21: Jezebel-239 measured, computed and best-estimate responses (single model) as well as optimal responses (coupled model) for *dissimilar* reaction rate ratios with one standard deviation normalized to the nominal measured value

Table 16: Measured and computed (Denovo) response values as well as best-estimate and optimal values (based on partitioned DA) for *dissimilar* reaction rate ratios of Jezebel-239.

Response	Jezebel -239			Jezebel – 240	
	Type	Value	± % rel. std. dev.	Value	± % rel. std. dev.
$\frac{\sigma_f(^{233}\text{U})}{\sigma_f(^{235}\text{U})}$	Measured	1.578	1.7	-	-
	Computed	1.553310	1.030	-	-
	Best-est. (single model)	1.562141	0.875	-	-
	Optimal (coupled model)	1.562041	0.875	-	-
$\frac{\sigma_f(^{239}\text{Pu})}{\sigma_f(^{235}\text{U})}$	Measured	1.4609	0.9	-	-
	Computed	1.422123	0.781	-	-
	Best-est. (single model)	1.440020	0.511	-	-
	Optimal (coupled model)	1.439893	0.506	-	-
$\frac{\sigma_\gamma(^{55}\text{Mn})}{\sigma_f(^{235}\text{U})}$	Measured	0.0024	12.50	-	-
	Computed	0.002555	7.925	-	-
	Best-est. (single model)	0.002471	6.655	-	-
	Optimal (coupled model)	0.002471	6.650	-	-
$\frac{\sigma_\gamma(^{93}\text{Nb})}{\sigma_f(^{235}\text{U})}$	Measured	0.023	8.7	-	-
	Computed	0.028989	8.253	-	-
	Best-est. (single model)	0.025278	5.906	-	-
	Optimal (coupled model)	0.025277	5.899	-	-
$\frac{\sigma_\gamma(^{63}\text{Cu})}{\sigma_f(^{235}\text{U})}$	Measured	0.0100	6.00	-	-
	Computed	0.009507	9.871	-	-
	Best-est. (single model)	0.009810	5.136	-	-
	Optimal (coupled model)	0.009810	5.135	-	-

So far the calibrated responses and their respective uncertainty have been presented. However, data assimilation calibrates both responses and parameters simultaneously. Recall that there are thousands of parameters associated with the Jezebel-239 and Jezebel-240 benchmarks. It is thus not feasible to discuss the effects of calibration for each of them. Analogous to the sensitivity analysis in chapter 2.2.4 some particular parameters are selected here. ^{239}Pu is a major component of both Jezebel benchmarks and it serves furthermore as a fission rate ratio in Jezebel-239. Therefore several of this isotope's reactions are considered and serve as illustrative example. The obvious choice are parameters that are associated with large sensitivity coefficients for k_{eff} , which have been identified previously (see Figure 14 and Figure 15) as $\bar{\nu}$ and (n, f) of ^{239}Pu . Yet, the relative change

$$\frac{\alpha_{^{239}\text{Pu}}^{x, \text{calibrated}} - \alpha_{^{239}\text{Pu}}^{x, 0}}{\alpha_{^{239}\text{Pu}}^{x, 0}} \cdot 100 \quad \text{with } x: \{\text{cross section, } \bar{\nu}, \chi\}, \quad (4.13)$$

between the nominal and the calibrated values of these two parameters is marginally small. For instance, the maximum relative change in $\bar{\nu}$ of ^{239}Pu is 0.23% and the maximum relative change in the fission cross section (n, f) of ^{239}Pu is 0.6%. One explanation is, that the nominal values of these particular parameters are already known rather well, i.e. have small uncertainties. In contrast to this, the calibrated elastic scattering cross section (n, n) of ^{239}Pu differs by up to 12% from the nominal value, see Figure 22. The legend entries in this and subsequent figures have the following meaning: cross sections associated with Jezebel-239 are denoted " α " while cross sections associated with Jezebel-240 are denoted " β ". For instance, the nominal value of the elastic scattering cross section of ^{239}Pu in Jezebel-239 is denoted as $\alpha_{^{239}\text{Pu}}^{(n, n), 0}$, while the same elastic scattering cross section of ^{239}Pu in Jezebel-240 is denoted as $\beta_{^{239}\text{Pu}}^{(n, n), 0}$. Recall from the discussion earlier in this chapter, that these two nominal values are not identical. The code package SCALE6.1 processes the infinite dilution cross section to benchmark specific cross sections. These problem specific cross sections account for example for self-shielding effects. Since self-shielding effects in Jezebel-239 differ from self-shielding effects in Jezebel-240, the same infinite dilution cross section leads to two only approximately equal, i.e. $\alpha_{^{239}\text{Pu}}^{(n, n), 0} \cong \beta_{^{239}\text{Pu}}^{(n, n), 0}$, nominal cross sections in Jezebel-239 and Jezebel-240. The individually calibrated elastic scattering cross section of ^{239}Pu for Jezebel-239 is

denoted as $\alpha_{239 Pu}^{(n,n),be}$ while the same calibrated cross section for Jezebel-240 is labelled $\beta_{239 Pu}^{(n,n),be}$. Considering the two benchmarks as coupled yields the jointly calibrated elastic scattering cross section for Jezebel-239 and Jezebel-240, which are denoted as $\alpha_{239 Pu}^{(n,n),opt}$ and $\beta_{239 Pu}^{(n,n),opt}$ respectively. Note that the nominal and the optimal cross sections are approximately the same for both Jezebel benchmarks, i.e. $\alpha_{239 Pu}^{(n,n),0} \cong \beta_{239 Pu}^{(n,n),0}$ and $\alpha_{239 Pu}^{(n,n),opt} \cong \beta_{239 Pu}^{(n,n),opt}$ respectively. The relative change in a cross section caused by the data assimilation is orders of magnitude larger than the deviation of nominal values between benchmarks, because the self-shielding effects are small in fast assemblies such as the two benchmarks considered here. Figure 22 therefore presents only nominal and optimal values of Jezebel-239 and omits the nominal and optimal values of Jezebel-240. The relative change in the best-estimate value is over 12% when the Jezebel-239 benchmark is considered individually, but is smaller (up to 8%) when the Jezebel-240 benchmark is considered individually. The optimal cross section is approximately identical with the best-estimate cross section. This implies that Jezebel-239 dominates the parameter adjustment even when Jezebel-239 and Jezebel-240 are considered as coupled systems.

Figure 23 presents the calibrated relative standard deviations of the elastic scattering cross section of ^{239}Pu . The calibrated standard deviations for this particular cross section are always smaller than the nominal standard deviation. The optimal standard deviation, which results from considering Jezebel-239 and Jezebel-240 as coupled system, is smallest. This demonstrates again that including more, consistent data yields smaller uncertainties.

The data assimilation results for inelastic scattering cross section (n,n') of ^{239}Pu are presented in Figure 24 and Figure 25. Observations made for the elastic scattering cross section above can be made here analogously. The inelastic scattering cross section is anti-correlated to the elastic scattering cross section, recall Table 11 and Table 12. An increase in the calibrated elastic scattering cross section is therefore counterbalanced with a decrease in the calibrated inelastic scattering cross section. The relative change in the inelastic scattering cross section has a negative sign and reaches from 5% to up to 37%.

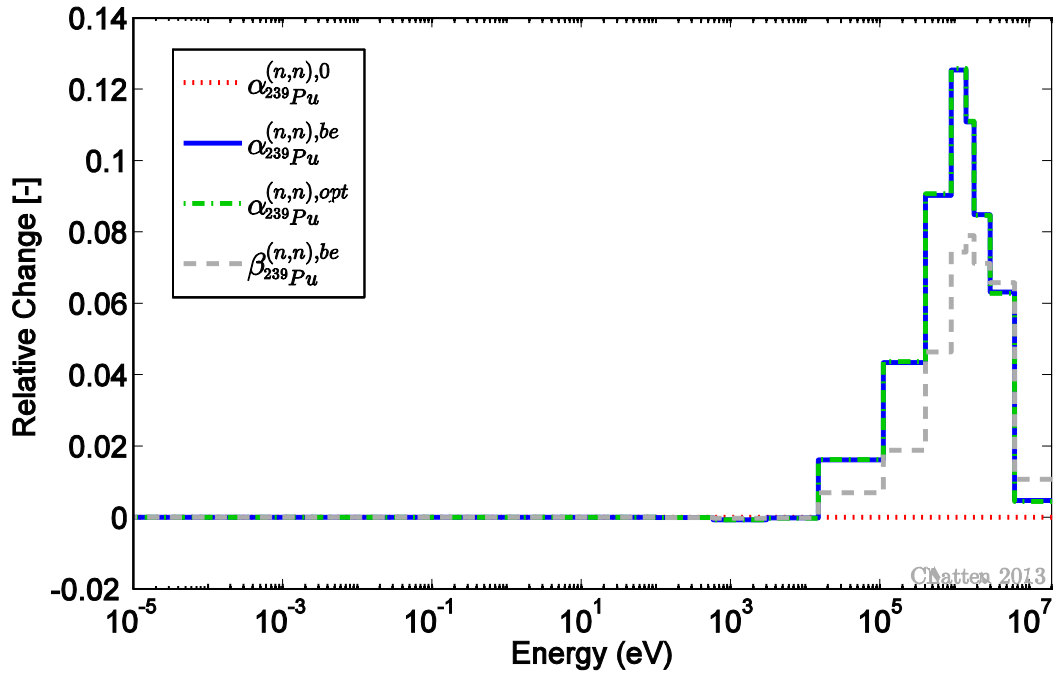


Figure 22: Relative change in individually and jointly adjusted elastic scattering cross section in ^{239}Pu for Jezebel-239 and Jezebel-240

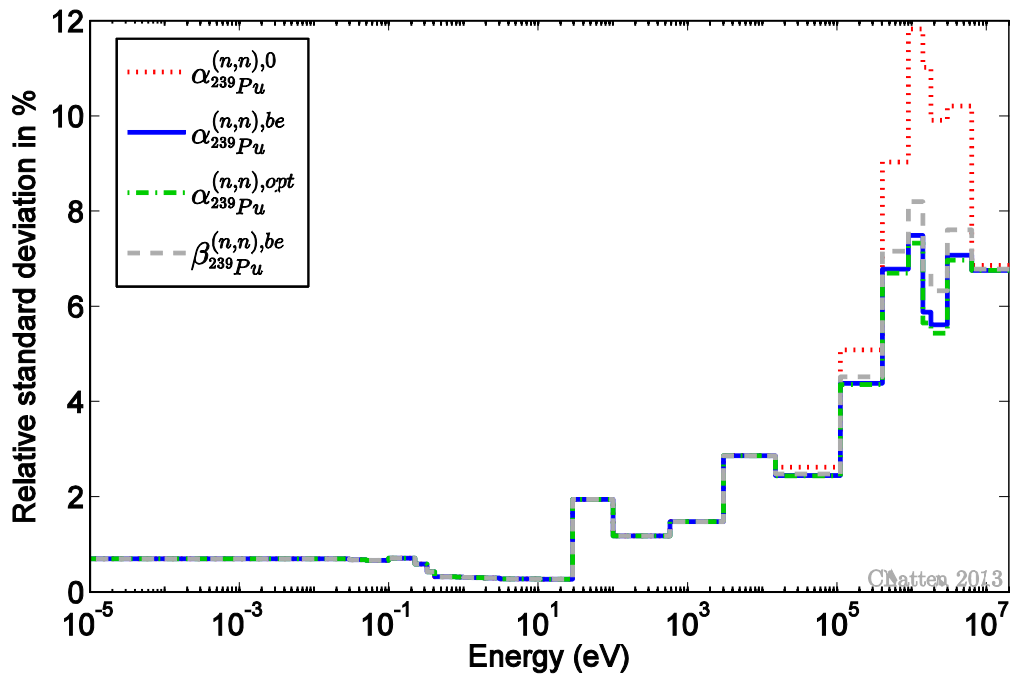


Figure 23: Nominal, individually and jointly adjusted relative standard deviation of the elastic scattering cross section in ^{239}Pu for Jezebel-239 and Jezebel-240

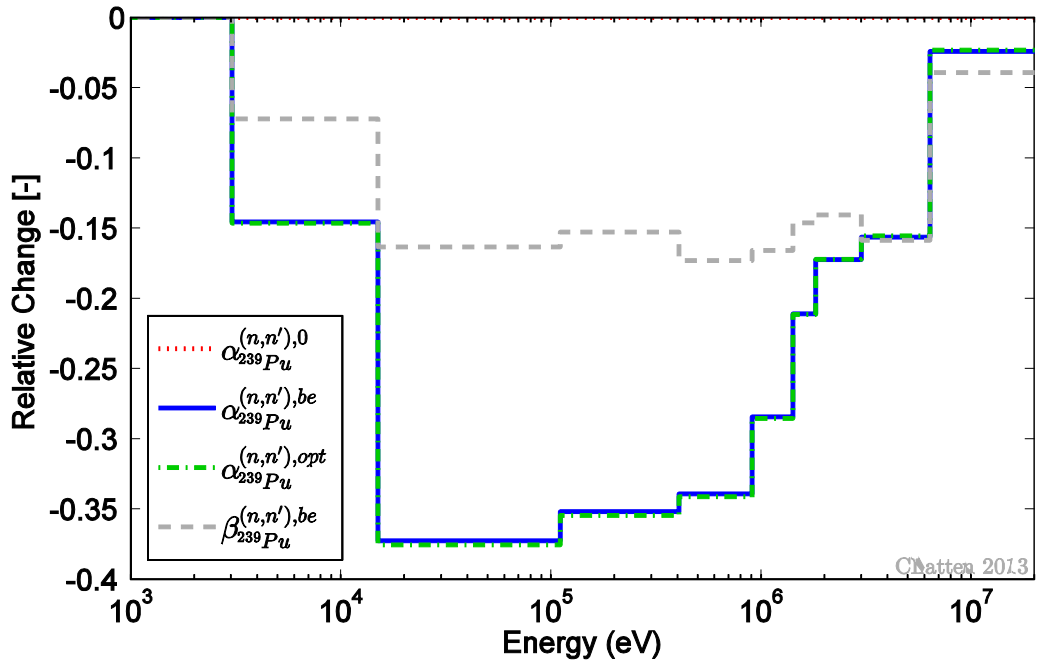


Figure 24: Relative change in individually and jointly adjusted inelastic scattering cross section in ^{239}Pu for Jezebel-239 and Jezebel-240

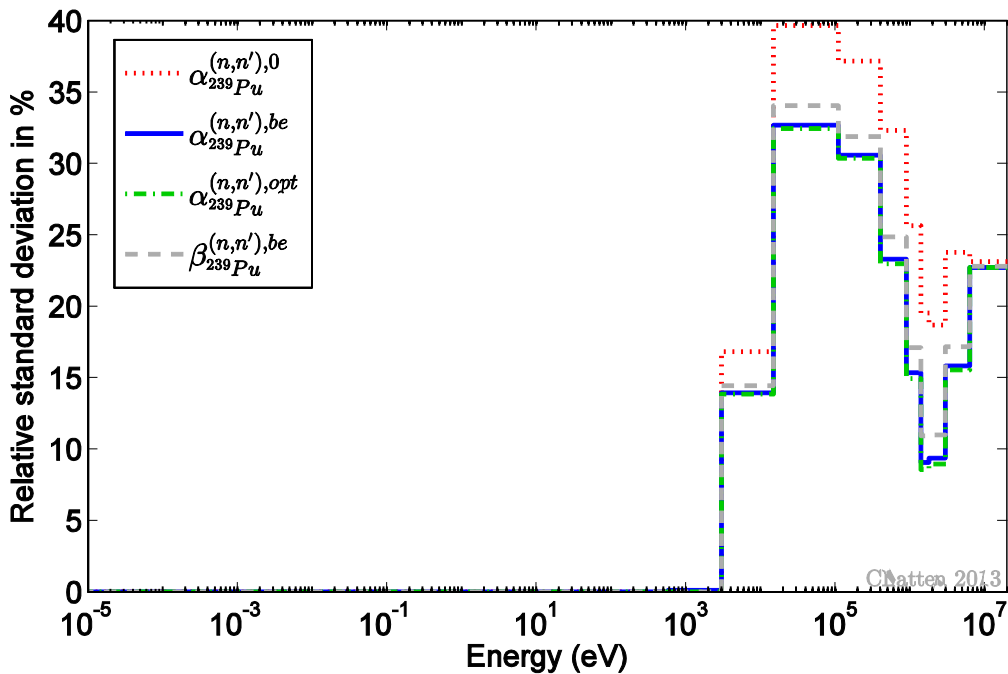


Figure 25: Nominal, individually and jointly adjusted relative standard deviation of the inelastic scattering cross section in ^{239}Pu for Jezebel-239 and Jezebel-240

The foils, which are placed in the center location to measure reaction rate ratios, allow calibrating parameters that aren't components of the Jezebel spheres. The fission rate of ^{237}Np is a *similar* response. Its best-estimate fission cross section (n, f) displays a larger decrease for Jezebel-240 than for Jezebel-239 in the energy range 0.5 MeV – 10 MeV, see Figure 26 and Figure 27. Adjusting both benchmarks jointly leads to yet another magnitude of decrease, which is in between the values of the individually calibrated cross sections. For this particular response the Jezebel-240 configuration is the dominating system, which causes the jointly calibrated parameter to be closer to the best-estimate value of the individually adjusted Jezebel-240. The calibrated standard deviations for energies $> 10^3$ eV are notably smaller than the nominal one.

Radiative capture in ^{93}Nb illustrates a parameter of a *dissimilar* response. As already observed for the response, calibrating both systems jointly has no significant effect on this cross section. The best-estimate parameter and the optimal parameter are thus identical; see Figure 28 and Figure 29.

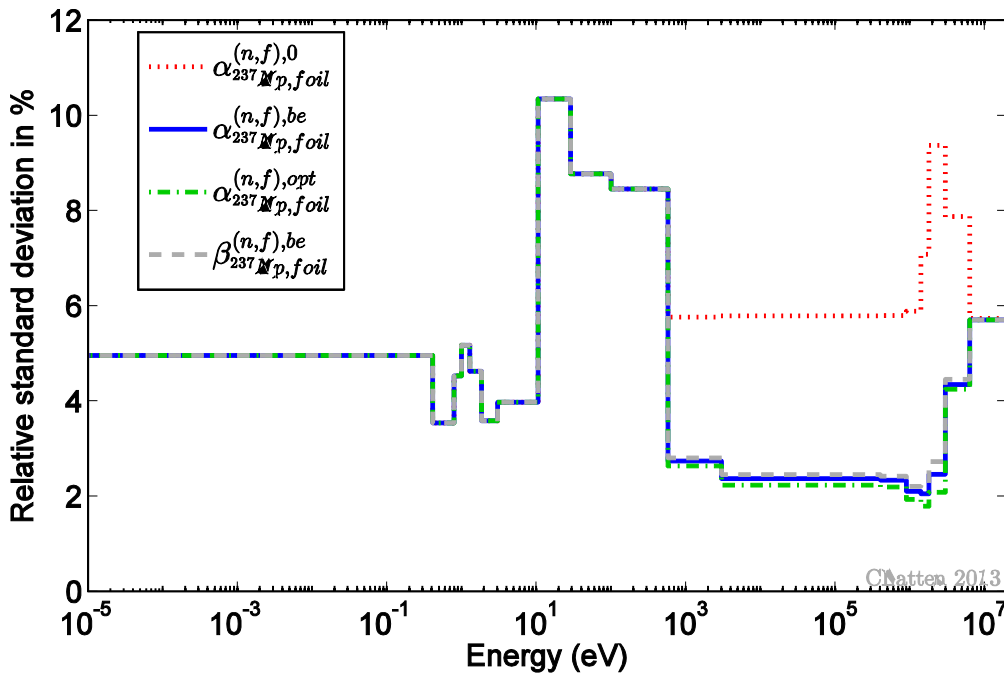


Figure 26: Nominal, individually and jointly adjusted fission cross section in ^{237}Np for Jezebel-239 and Jezebel-240

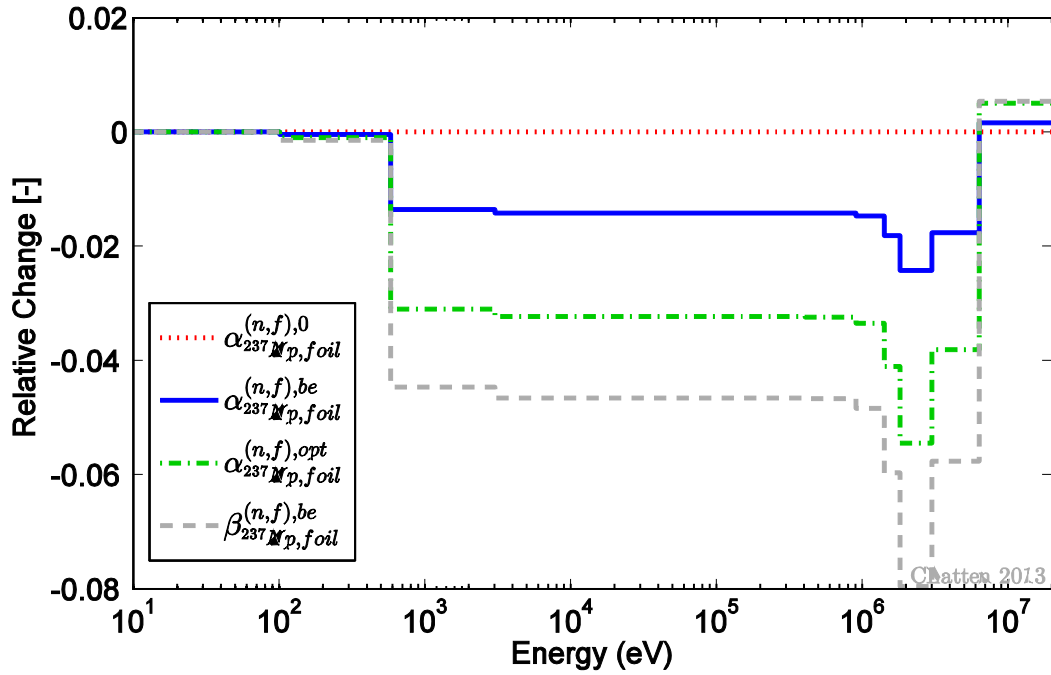


Figure 27: Relative change in individually and jointly adjusted fission cross section in ^{237}Np for Jezebel-239 and Jezebel-240

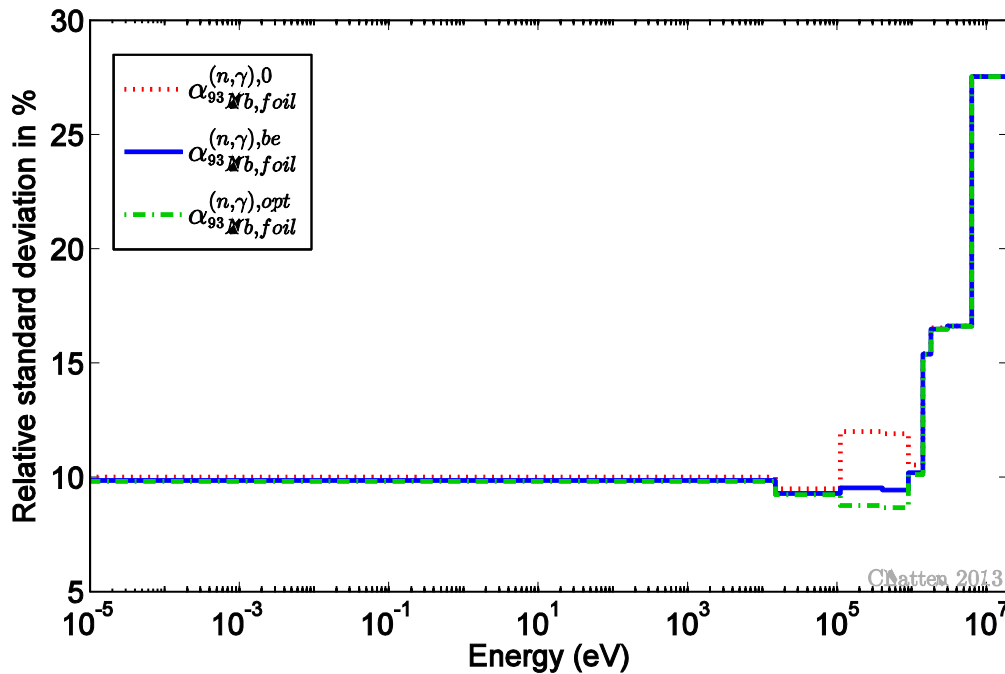


Figure 28: Nominal, individually and jointly adjusted relative standard deviation of the radiative capture cross section in ^{93}Nb for Jezebel-239

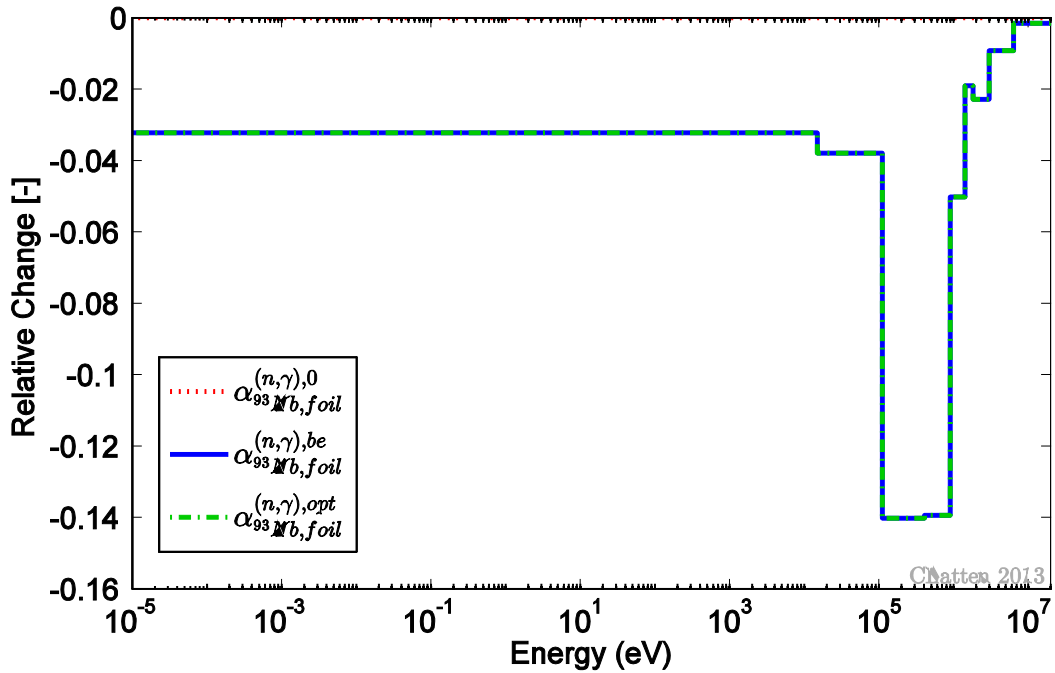


Figure 29: Relative change in individually and jointly adjusted radiative capture cross section in ^{93}Nb for Jezebel-239

4.2.5 Computational Requirement Considerations

Let Jezebel-239 be subsystem I with $N_r^{pDA} = 8$ responses, including k_{eff} and seven reaction rate ratios, and $N_\alpha^{pDA} = 2241$ parameters. Parameters include neutron cross sections, the average prompt fission multiplicity $\bar{\nu}$ and the fission spectrum χ . Jezebel-240 is then subsystem II accordingly with $N_q^{pDA} = 3$ responses and $N_\beta^{pDA} = 1458$ parameters. It turns out that the resulting matrix dimensions for these benchmarks are too small to have but a marginal effect on computational performance. Table 17 lists the average time on 1 CPU and the maximum memory requirement for the partitioned DA compared to the non-partitioned DA. Similar to the performance results in chapter 3.4 the partitioned DA requires less memory while the trade-off is an increase in elapsed time. The majority of the time is spent with I/O functions. The algorithm has to handle more but smaller data packages in case of the partitioned DA, whereas the non-partitioned DA has fewer, but larger data packages. This causes the larger execution time for the partitioned DA.

In general, the peak memory requirement is driven by the largest matrix of the system. In case the number of responses N_r of subsystem I or the number of responses N_q of

subsystem II dominates the combined system, the inverse of \mathbf{D}_{rr} or the inverse of the Schur complement $(\mathbf{D}_{qq} - \mathbf{D}_{rq}^\dagger \mathbf{D}_{rr}^{-1} \mathbf{D}_{rq})$ respectively becomes the most expensive operation. If on the other hand the number of parameters N_α of subsystem I or the number of parameters N_β of subsystem II dominates the combined system, any matrix multiplication involving $\mathbf{C}_{\alpha\alpha}$ or $\mathbf{C}_{\beta\beta}$ respectively becomes the most expensive operation. This is a direct consequence of the data assimilation being formulated in the response space. Here, the peak memory requirement is reached for both the partitioned DA and the non-partitioned DA while computing $\mathbf{C}_{\alpha\alpha}^{opt,(2241 \times 2241)}$ and $\mathbf{C}_{\alpha\alpha}^{be,(3699 \times 3699)}$ respectively. Since the number of parameters N_α in subsystem I is the largest dimension for any matrix in the algorithm this peak in memory mirrors the expected behavior. Considering both Jezebel configurations jointly with the non-partitioned DA increases the number of parameters by a factor of 1.6 compared to the partitioned DA on the same data. The peak memory required for the non-partitioned DA is 2.5 times larger than for the partitioned DA on the same data. An overview of this data can be found in Table 17.

Table 17: Performance for partitioned DA algorithm compared to non-partitioned DA. Results shown are average values over 10 individual runs on 1 CPU.

	Partitioned DA	Non-partitioned DA
	$N_r = 8, \quad N_q = 3$	$N_r = 11, \quad N_q = 0$
	$N_\alpha = 2241, \quad N_\beta = 1458$	$N_\alpha = 3699, \quad N_\beta = 0$
Time in sec	8.60	7.48
Peak memory in Mb	42.7	110.5

4.3 Data Assimilation on Godiva

The benchmark Godiva is a critical assembly of highly enriched uranium. The bare configuration consists just like the Jezebel benchmarks in the previous sections of an unreflected sphere. The composition of the sphere is listed in Table 18. All major reactions of the isotopes listed there have been considered as parameters for the adjustment. Godiva was chosen as a benchmark because a large number of fission and activation ratio measurements are available, [19] and [17]. Seventeen responses were considered for

Godiva, as follows: the effective multiplication factor k_{eff} , the center core fission rates for ^{233}U , ^{238}U , ^{237}Np , and ^{239}Pu , as well as the center core radiative capture rates for ^{55}Mn , ^{93}Nb , ^{63}Cu , ^{197}Au , ^{107}Ag , ^{209}Bi , ^{79}Br , ^{81}Br , ^{59}Co , ^{127}I , ^{115}In and ^{103}Rh . The number of responses $N_r = 17$ is deemed sufficiently large to demonstrate the χ^2 evaluation procedure.

Table 18: Atom densities for the Godiva benchmark, [19]

Godiva	
Radius:8.7407cm	
Nuclide	Atom Density [atoms / barn-cm]
^{234}U	$4.9184 \cdot 10^{-4}$
^{235}U	$4.4994 \cdot 10^{-2}$
^{238}U	$2.4984 \cdot 10^{-3}$

All experimental data stems from [19], which also contains a detailed description of the benchmark. The computational responses are results of numerical simulations in Denovo with a weighted diamond-difference as spatial discretization scheme. The spherical geometry of the Godiva benchmark is inherently symmetric so that computing an octant of the sphere is sufficient. The computational solutions are based on a $10 \times 10 \times 10$ Cartesian mesh and the ENDF/BVII.0 neutron cross section library with 27 energy groups. Recall that the boundaries of this energy group structure reach from 10^{-5} eV to 20 MeV. Figure 30 shows the normalized spectrum of the computed scalar flux of Godiva together with the normalized spectrum of Jezebel-239 and Jezebel-240 from Figure 13 for comparison. The figure illustrates that Godiva is a fast assembly just like the Jezebel configurations of the previous section, which entails that effects of the resonance region can be neglected. Beyond that, Godiva has its own characteristic spectrum, which differs from the plutonium benchmarks in shape and magnitude.

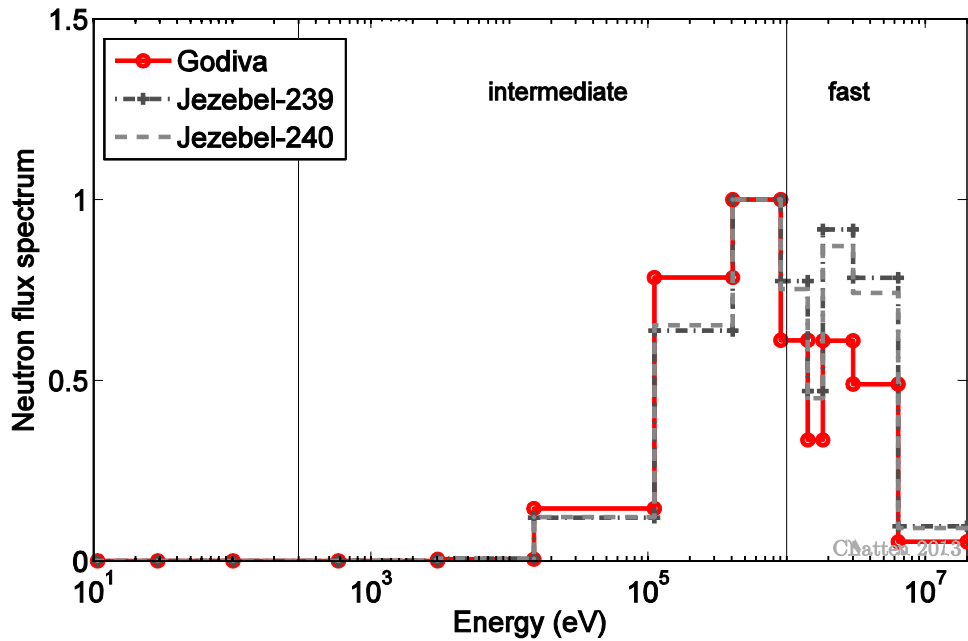


Figure 30: Spectrum of the neutron flux for Godiva and Jezebel configurations

4.3.1 Sensitivity Analysis

This chapter uses the same notation as introduced in chapter 4.2.1. Representative sensitivity profiles have been selected and are discussed in the following; in particular the largest sensitivities for the effective multiplication constant k_{eff} as well as the largest sensitivities for a fission reaction rate and a radiative capture reaction rate.

Energy-dependent profiles of relevant sensitivities of k_{eff} are shown in Figure 31. The largest sensitivity coefficients for the multiplication constant k_{eff} are observed for $\bar{\nu}$ and the fission cross section of ^{235}U . These match the top ranked quantities for both Jezebel configurations, but with Godiva being a uranium system they refer to the major component ^{235}U instead of plutonium ^{239}Pu . As a fast assembly the sensitivity profiles for lower energies are vanishingly small and Figure 31 only shows sensitivity coefficients for energies $>10^2$ eV. Elastic scattering in ^{235}U is the third largest sensitivity profile. Note, however, that the third most important profile is an order of magnitude smaller than the largest sensitivity profile.

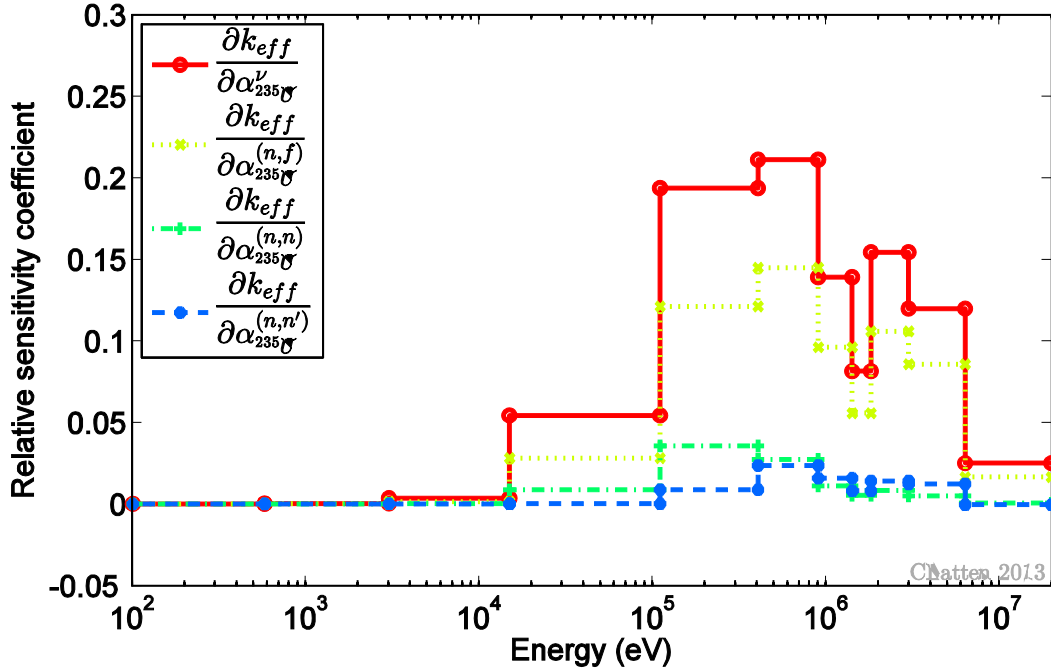


Figure 31: Sensitivity profile of k_{eff} to selected parameters for Godiva

Sensitivity profiles for the fission rate of ^{238}U relative to the fission rate of ^{235}U , denoted as

$r_2 = \frac{\sigma_f(^{238}\text{U})}{\sigma_f(^{235}\text{U})}$, are shown in Figure 32 and sensitivity profiles of the radiative capture rate of

^{55}Mn relative to the fission rate of ^{235}U , denoted as $r_6 = \frac{\sigma_\gamma(^{55}\text{Mn})}{\sigma_f(^{235}\text{U})}$ are shown in Figure 33.

These reaction rate ratios have been selected as representative examples of sensitivity profiles of spectral indices of Godiva. As already demonstrated in the previous section with the two Jezebel benchmarks, reaction rate ratio have the largest sensitivity coefficients for the cross sections and nuclides that make up the reaction ratio. Figure 32 for instance shows that the largest sensitivity profiles of r_2 are the fission cross section of ^{238}U and ^{235}U occurring within a foil. The isotope ^{235}U is not only associated with a foil, which is placed at the center location to obtain reaction ratios, but the same isotope is also the major component of the Godiva sphere itself. In this case there exist separate sensitivity coefficients to parameters of ^{235}U depending on location, i.e. foil or sphere. As can be seen in Figure 32 the sensitivity profile to the fission cross section of ^{235}U has a similar shape for both cases but opposing signs. The sensitivity coefficients for the foil are negative because ^{235}U appears as the denominator in the ratio. Since all reaction rate ratios considered in the

present work share the same denominator it follows that all responses of Godiva have identical sensitivity profiles for the fission cross section of ^{235}U .

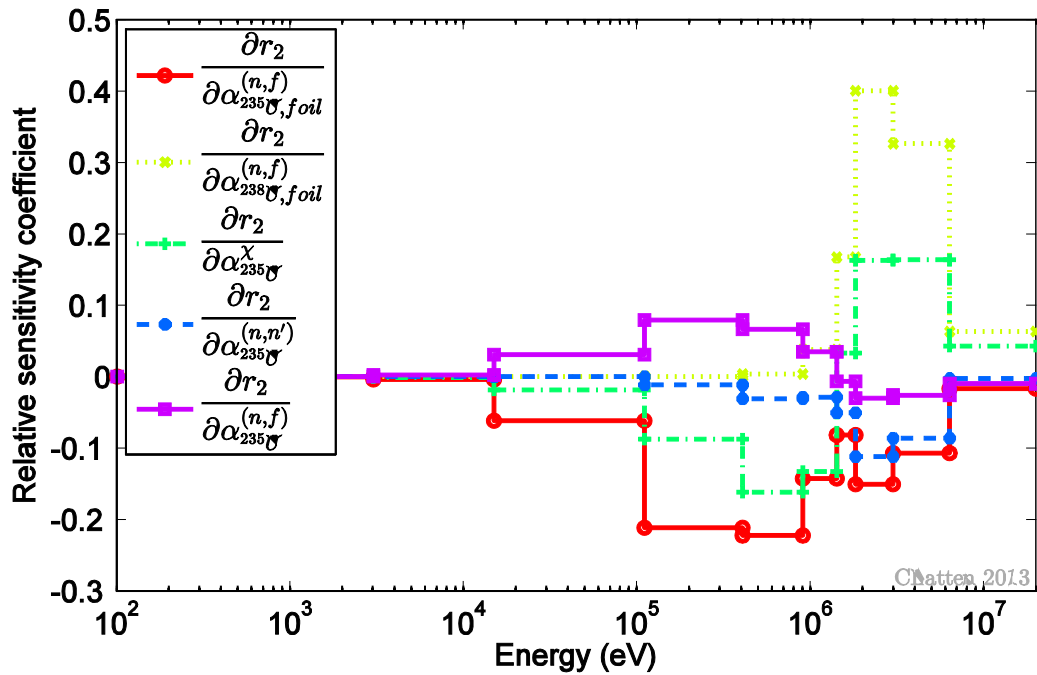


Figure 32: Sensitivity profile of $r_2 = \frac{\sigma_f(^{238}\text{U})}{\sigma_f(^{235}\text{U})}$ to selected parameters for Godiva

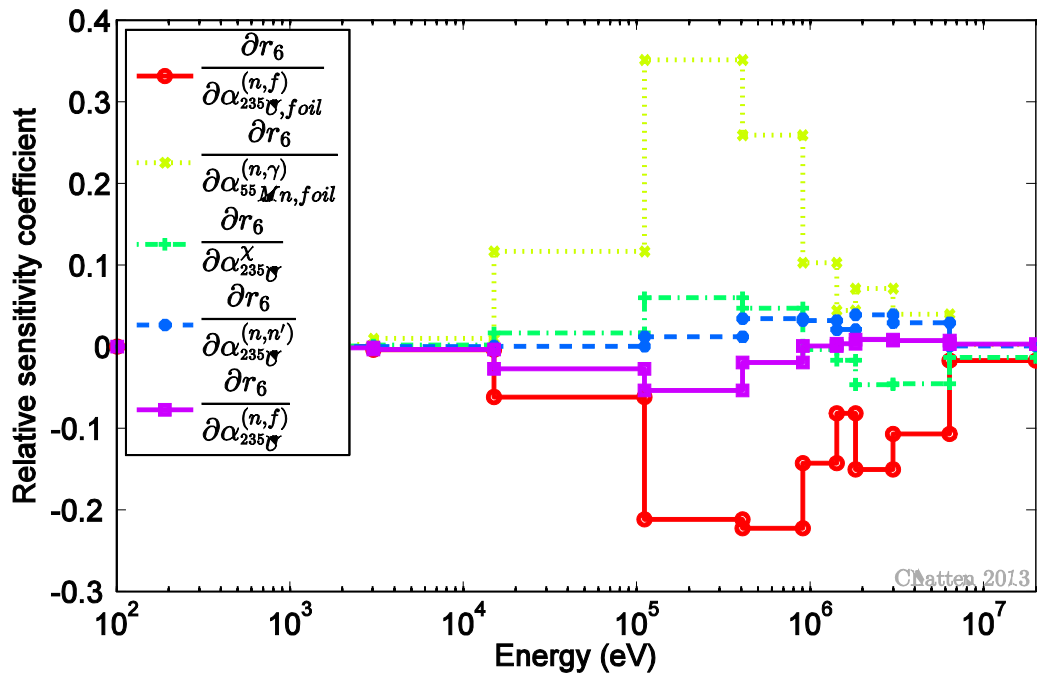


Figure 33: Sensitivity profile of $r_6 = \frac{\sigma_\gamma(^{55}\text{Mn})}{\sigma_f(^{235}\text{U})}$ to parameters for Godiva

4.3.2 Uncertainty Quantification

This section uses the same notation as introduced in section 4.2.2. Also, recall Eqs. (4.10) and (4.11) to propagate the uncertainty of input parameters to the computed responses. The

top six uncertainty contributions for k_{eff} and $r_2 = \frac{\sigma_f(^{238}U)}{\sigma_f(^{235}U)}$ of Godiva are listed in Table 19.

The largest uncertainty contribution in k_{eff} stems from the radiative capture cross section of the isotope ^{235}U , the largest uncertainty contribution in r_2 stems from the inelastic scattering cross section in ^{235}U . Among the listed uncertainty contribution is only one covariance block, namely the uncertainty between elastic and inelastic scattering in the isotope ^{235}U . This value is negative, which reflects the anti-correlation between elastic and inelastic scattering.

Table 19: Uncertainty contribution from Eq. (4.11) in k_{eff} and $r_2 = \frac{\sigma_f(^{238}U)}{\sigma_f(^{235}U)}$ of Godiva

Nuclide Reaction Pair		Uncertainty in k_{eff} (%)	Nuclide Reaction Pair		Uncertainty in r_2 (%)
$^{235}U(n,\gamma)$	$^{235}U(n,\gamma)$	7.10E-03	$^{235}U(n,n')$	$^{235}U(n,n')$	4.05E-02
$^{235}U(n,n')$	$^{235}U(n,n')$	3.57E-03	$^{235}U(n,\gamma)$	$^{235}U(n,\gamma)$	7.53E-03
$^{235}U(n,n)$	$^{235}U(n,n')$	-1.40E-03	$^{235}U(n,n)$	$^{235}U(n,n')$	-2.72E-03
$^{235}U(n,n)$	$^{235}U(n,n)$	8.28E-04	$^{238}U(n,f)$	$^{238}U(n,f)$	2.69E-03
$^{235}U(n,f)$	$^{235}U(n,f)$	7.23E-04	$^{238}U(n,n')$	$^{238}U(n,n')$	1.70E-03
$^{235}U(n,\gamma)$	$^{235}U(n,\gamma)$	5.70E-04	$^{235}U(n,f)$	$^{235}U(n,f)$	1.68E-03

4.3.3 Excluding Responses - Consistency Evaluation Procedure

The partitioned DA is applied to the benchmark Godiva including initially $N_r = 17$ responses. An overview of the measured, computed and optimal values for each response with one standard deviation is shown in Figure 34. Numerical values can be found in a table in Appendix E. The legend entries have the following meaning: \mathbf{r}_c and σ_c denote the mean value and corresponding standard deviation for a computed response, \mathbf{r}_m and σ_m denote the mean value and corresponding standard deviation for a measured response and lastly \mathbf{r}^{opt} and σ^{opt} denote the mean value and corresponding standard deviation for a calibrated (“optimal”) response resulting from the application of the partitioned data assimilation. The horizontal axis lists all seventeen responses, which are listed in Table 20.

Table 20: Godiva responses r_i and corresponding label

#1	#2	#3	#4	#5	#6	#7	#8	#9
k_{eff}	$\frac{\sigma_f(^{238}\text{U})}{\sigma_f(^{235}\text{U})}$	$\frac{\sigma_f(^{233}\text{U})}{\sigma_f(^{235}\text{U})}$	$\frac{\sigma_f(^{237}\text{Np})}{\sigma_f(^{235}\text{U})}$	$\frac{\sigma_f(^{239}\text{Pu})}{\sigma_f(^{235}\text{U})}$	$\frac{\sigma_\gamma(^{55}\text{Mn})}{\sigma_f(^{235}\text{U})}$	$\frac{\sigma_\gamma(^{93}\text{Nb})}{\sigma_f(^{235}\text{U})}$	$\frac{\sigma_\gamma(^{63}\text{Cu})}{\sigma_f(^{235}\text{U})}$	$\frac{\sigma_\gamma(^{197}\text{Au})}{\sigma_f(^{235}\text{U})}$
#10	#11	#12	#13	#14	#15	#16	#17	
$\frac{\sigma_\gamma(^{107}\text{Ag})}{\sigma_f(^{235}\text{U})}$	$\frac{\sigma_\gamma(^{209}\text{Bi})}{\sigma_f(^{235}\text{U})}$	$\frac{\sigma_\gamma(^{79}\text{Br})}{\sigma_f(^{238}\text{U})}$	$\frac{\sigma_\gamma(^{81}\text{Br})}{\sigma_f(^{235}\text{U})}$	$\frac{\sigma_\gamma(^{59}\text{Co})}{\sigma_f(^{238}\text{U})}$	$\frac{\sigma_\gamma(^{127}\text{I})}{\sigma_f(^{235}\text{U})}$	$\frac{\sigma_\gamma(^{115}\text{In})}{\sigma_f(^{238}\text{U})}$	$\frac{\sigma_\gamma(^{103}\text{Rh})}{\sigma_f(^{238}\text{U})}$	

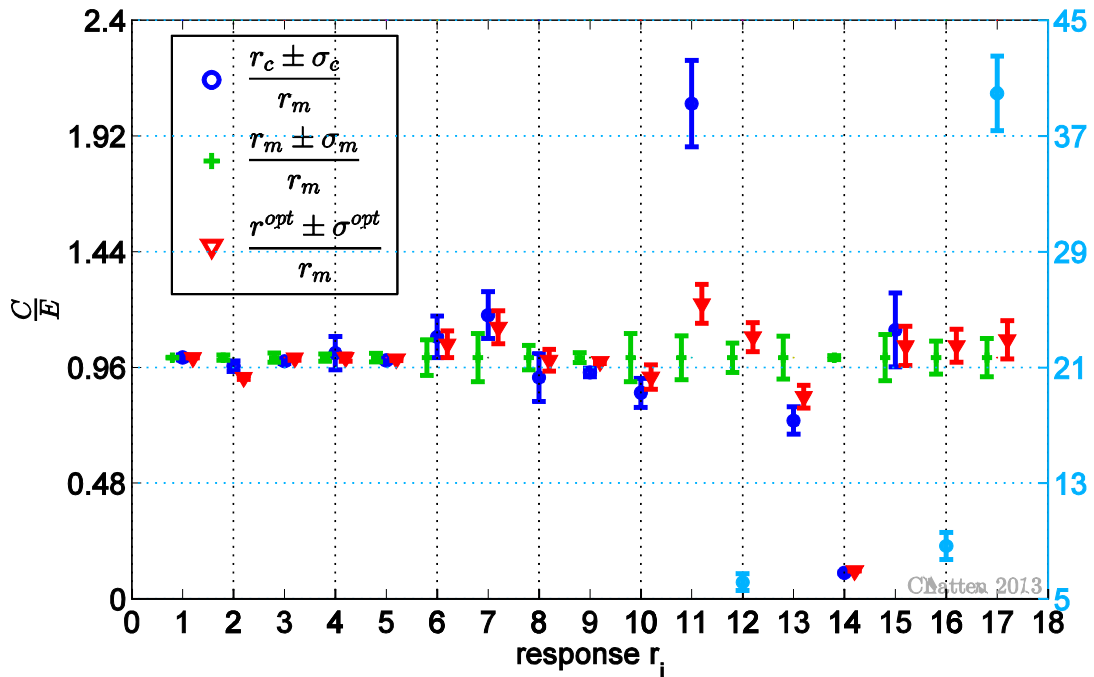


Figure 34: Measured (green), computed (blue) and optimal (red) values for all 17 responses of benchmark Godiva. Error bars correspond to one standard deviation. All values are normalized to the experimental value. Note that the computational value of response r_{12} , r_{16} and r_{17} scales according to the right hand side y-axis.

The values in this graph are normalized to the nominal experimental value of each response. For some of the responses the standard deviations of the measured and computed values do not overlap, i.e. those responses are possibly discrepant. Particularly the computed

activation ratios of $r_{12} = \frac{\sigma_\gamma(^{79}\text{Br})}{\sigma_f(^{238}\text{U})}$, $r_{16} = \frac{\sigma_\gamma(^{115}\text{In})}{\sigma_f(^{238}\text{U})}$ and $r_{17} = \frac{\sigma_\gamma(^{103}\text{Rh})}{\sigma_f(^{238}\text{U})}$ differ to such a

large extent from the measured values that for ease of representation a second vertical axis has been introduced in Figure 34. Similar to the previous applications of data assimilation,

the calibrated values fall in between the measured and the computed ones, while reducing the respective calibrated standard deviations. However, the calibration procedure cannot fully bridge the gap between the markedly discrepant computed and experimentally measured values pointed out above. The overall consistency indicator is $\chi^2/N_r=12803/17=753.16$. This large value also displays the huge discrepancy in the system since the 90% central confidence range is (0.5101, 1.6228). In terms of demonstrating the capabilities of the χ^2 evaluation procedure, this is an excellent starting point. Please refer to chapter 3.5 for a detailed explanation of the consistency evaluation procedure.

For the first iteration step each of the 17 responses is excluded once and the consistency indicator for the system of the remaining 16 responses is computed. To illustrate the χ^2 evaluation procedure further this intermediate step is shown in Figure 35. The response that by exclusion changes χ^2 the most towards a desired value is then labeled as the least consistent and excluded from the system. Figure 35 readily identifies this to be response

$$r_{14} = \frac{\sigma_\gamma(^{59}\text{Co})}{\sigma_f(^{238}\text{U})}. \text{ Comparing this with the initial visualization in Figure 34 it may come as a}$$

surprise that neither of the blatantly discrepant responses, i.e. r_{12} , r_{16} or r_{17} , is identified as the least consistent response in the very first iteration. This highlights the importance of a systematic χ^2 evaluation procedure, since identifying discrepant data points with a quantitative method yields different results than simply gaging them qualitatively from plots like Figure 34. It turns out that the matrix dimensions of Godiva are too small to represent a benchmark for computational performance. However, the overall benefit of the new consistency evaluation procedure compared to the standard method can still be demonstrated even on this small scale. The new procedure requires on average 0.5 seconds on 1 CPU to identify the complete consistency sequence, while the standard method requires 4.0 seconds. As already pointed out, the methods are not equivalent and can yield different results. As can be seen in Figure 35 the normalized χ^2 values differ between the methods within one iteration. However, both methods identify the same response, i.e. r_{14} , as the least consistent response of the first iteration step. This is also true for the subsequent iteration steps and thus both methods yield an identical consistency sequence of Godiva. Here, the procedure is taken to the extreme case with only one response remaining in the system. This way a sequence from least to most consistent response is created. Figure 36 shows each iteration's χ^2 normalized to the decreasing number of responses. Note the logarithmic scale on the y-axis and the change in order of magnitude for excluding the first 2 responses. Both

methods, the new procedure, which is based on the partitioned DA, and the standard one yield the same sequence.

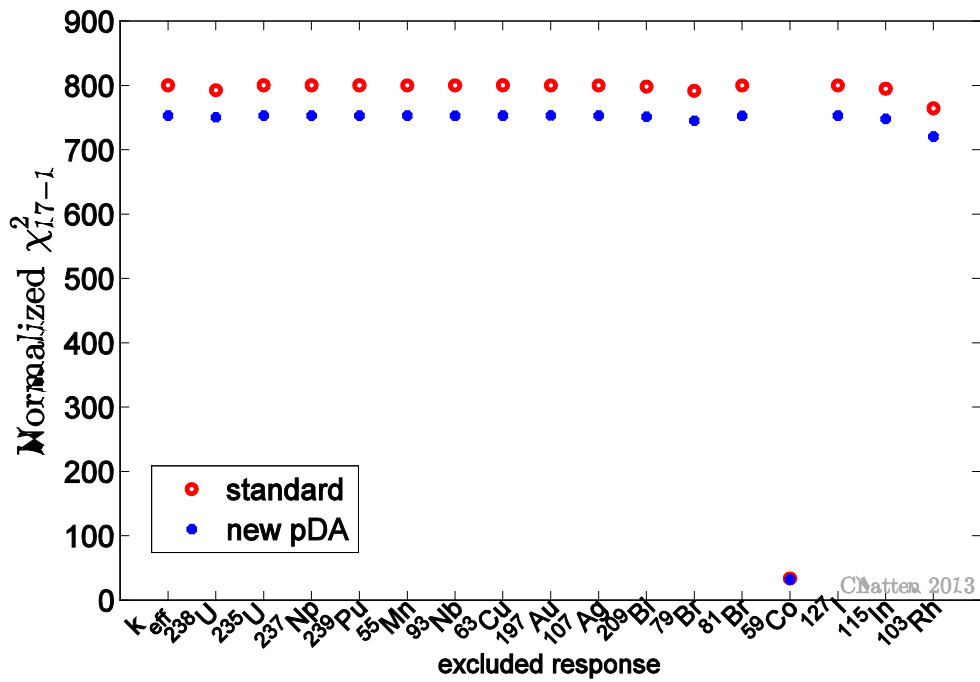


Figure 35: Normalized χ^2 for each excluded response at the first iteration

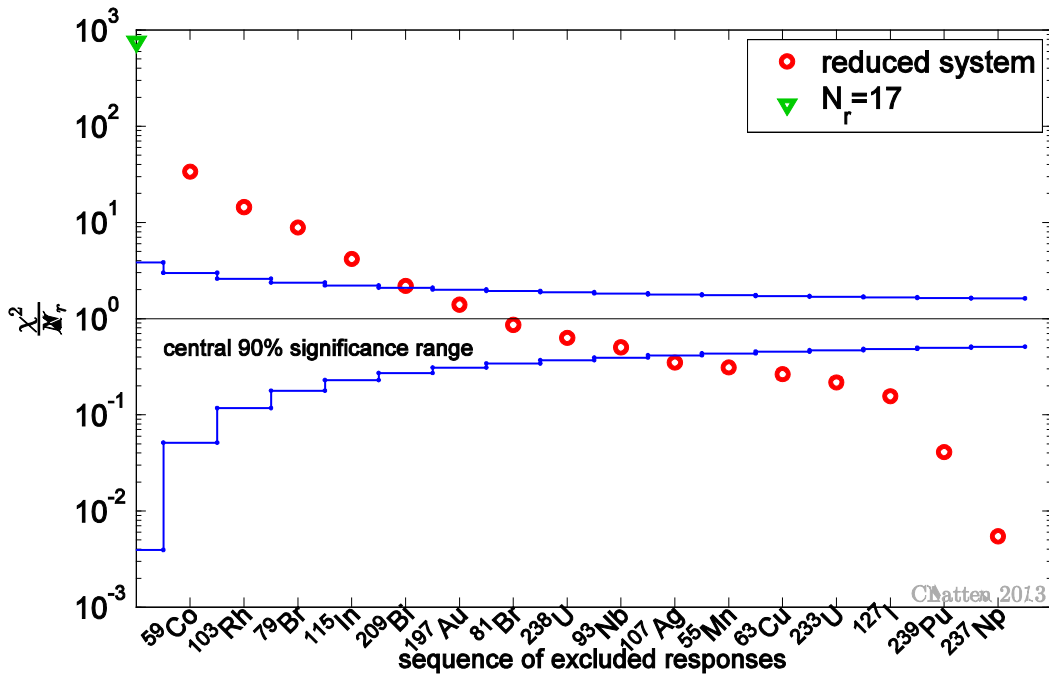


Figure 36: Normalized χ^2 for progressively excluded discrepant responses for Godiva

Considering merely the closeness of χ^2 per degree of freedom to unity as consistency indicator can be insufficient or even misleading, [36]. Thus, the central 90% significance range based on the inverse of the χ^2 probability distribution is shown in Figure 36 as well. Four different selections of responses fall within the chosen confidence level. If the normalized χ^2 is larger than the upper bound, the data is likely to be discrepant and the respective response should be excluded from the data assimilation. If the normalized χ^2 is smaller than the lower bound, the uncertainties for the assumptions of the model have been overestimated, [16]. Here, two sets of responses, which fall into the central 90% significance range, are selected. For the first set the seven least consistent responses according to Figure 36 were excluded. This leaves $N_r = 10$ responses in the system to which the data assimilation is then applied. The second set excludes the six least consistent responses according to Figure 36. This leaves $N_r = 11$ responses in the system and data assimilation is again applied. The first set with $N_r = 10$ responses yields a normalized consistency indicator that is closest to unity. The second set with $N_r = 11$ responses yields the first normalized consistency indicator that falls within the central 90% significance range. The additional response in the second set is radiative capture in bromine.

Table 21 lists the calibrated values together with the measured and computed responses of both sets. The second column of this table contains the experimentally measured values with their corresponding relative standard deviations, the computed mean values with their corresponding relative standard deviations and the calibrated (“optimal”) mean values with their calibrated relative standard deviations of the first set with $N_r = 10$. The third column of this table only contains the calibrated (“optimal”) mean values with their calibrated relative standard deviations of the second set with $N_r = 11$. The experimentally measured and computed values are not repeated in this column, but are of course identical. The same information is shown in Figure 37 for the first set and in Figure 38 for the second set. New quantities appearing in the legend of these figures are $\mathbf{r}^{opt,x}$ and $\sigma^{opt,x}$, which denote the mean value and corresponding standard deviation for a calibrated (“optimal”) response resulting from the application of the partitioned DA formulation to the Godiva benchmark including $N_r = x$ responses. The two selected sets now include only consistent responses, which can readily be seen by the overlapping error bars for $\mathbf{r}^{opt,10}$ and $\mathbf{r}^{opt,11}$. The calibrated values of these two consistent sets differ significantly from the corresponding optimal values

Table 21: Measured, computed and optimal values for 10 and 11 selected responses of Godiva

Response	Godiva $N_r = 10$			Godiva $N_r = 11$	
	Type	Value	\pm % rel. std. dev.	Value	\pm % rel. std. dev.
k_{eff}	Measured	1.000	0.1		
	Computed	1.000777	1.063		
	Optimal	0.999863	0.099	0.999873	0.099
$\frac{\sigma_f(^{238}\text{U})}{\sigma_f(^{235}\text{U})}$	Measured	0.1647	1.1		
	Computed	0.158868	3.178		
	Optimal	0.162914	0.902	0.162746	0.902
$\frac{\sigma_f(^{233}\text{U})}{\sigma_f(^{235}\text{U})}$	Measured	1.590	1.9		
	Computed	1.566506	1.053		
	Optimal	1.571671	0.910	1.572322	0.910
$\frac{\sigma_f(^{237}\text{Np})}{\sigma_f(^{235}\text{U})}$	Measured	0.837	1.6		
	Computed	0.852545	6.895		
	Optimal	0.838386	1.512	0.838349	1.512
$\frac{\sigma_f(^{239}\text{Pu})}{\sigma_f(^{235}\text{U})}$	Measured	1.402	1.8		
	Computed	1.385358	0.735		
	Optimal	1.391157	0.550	1.391393	0.550
$\frac{\sigma_\gamma(^{55}\text{Mn})}{\sigma_f(^{235}\text{U})}$	Measured	0.0027	7.4		
	Computed	0.002932	7.970		
	Optimal	0.002786	5.421	0.002788	5.417
$\frac{\sigma_\gamma(^{93}\text{Nb})}{\sigma_f(^{235}\text{U})}$	Measured	0.03	10.0		
	Computed	0.035280	8.336		
	Optimal	0.032482	6.354	0.032528	6.345
$\frac{\sigma_\gamma(^{63}\text{Cu})}{\sigma_f(^{235}\text{U})}$	Measure ^d	0.0117	5.1		
	Computed	0.010738	10.851		
	Optimal	0.011476	4.644	0.011479	4.642
$\frac{\sigma_\gamma(^{107}\text{Ag})}{\sigma_f(^{235}\text{U})}$	Measure ^l	0.1440	10.0		
	Computed	0.123043	7.074		
	Optimal	0.127060	5.743	0.1272503	5.734
$\frac{\sigma_\gamma(^{127}\text{I})}{\sigma_f(^{235}\text{U})}$	Measured	0.0832	9.6		
	Computed	0.092771	13.812		
	Optimal	0.085486	7.911	0.08555343	7.905
$\frac{\sigma_\gamma(^{81}\text{Br})}{\sigma_f(^{235}\text{U})}$	Measured	-	-	0.036	8.89
	Computed	-	-	0.026618	7.725
	Optimal	-	-	0.02894927	5.875

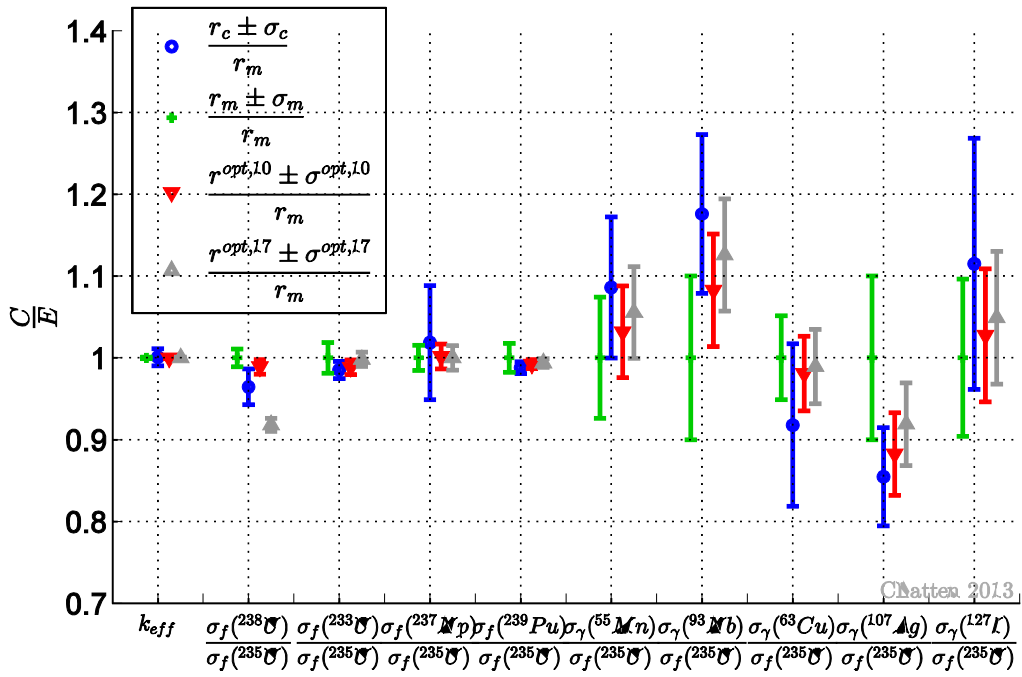


Figure 37: Measured, computed and optimal values for $N_r = 10$ responses with one standard deviation normalized to the nominal measured value.

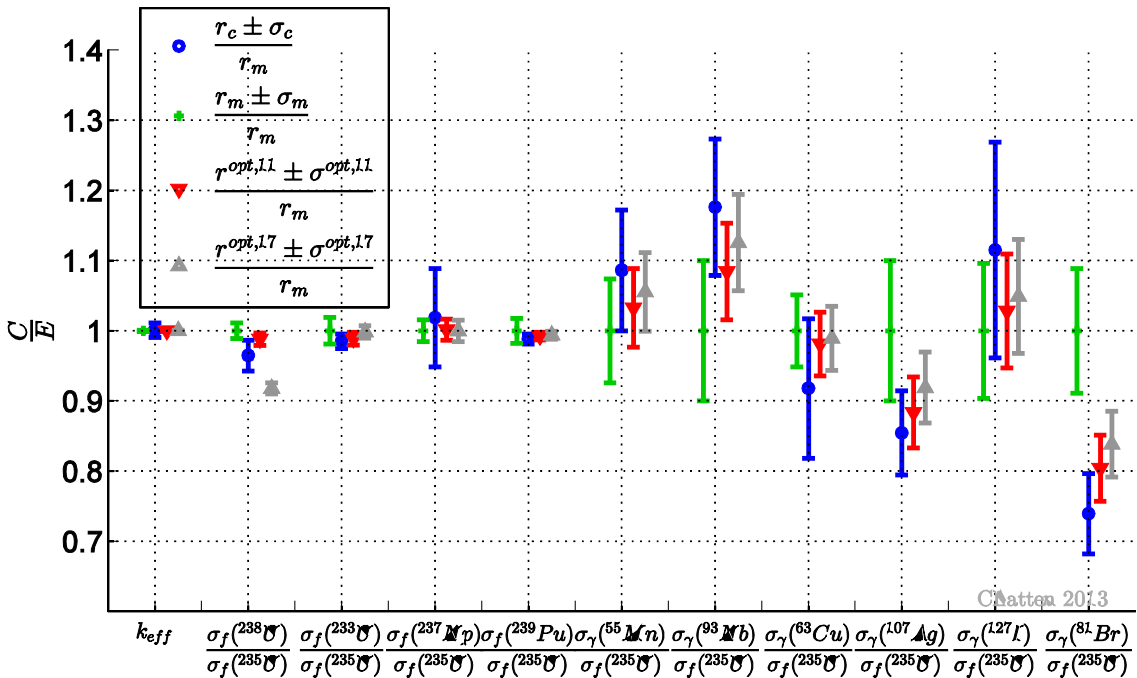


Figure 38: Measured, computed and optimal values for $N_r = 11$ responses with one standard deviation normalized to the nominal measured value.

$\mathbf{r}^{opt,17}$, which include all $N_r = 17$ responses and are repeated here from Figure 34 for comparison. The change in the mean calibrated values between the two consistent sets is negligibly small. All three variations of calibrated values have almost identical standard deviations. It has already been demonstrated in chapter 4.2 that inclusion of more, consistent data reduces the calibrated standard deviation. However, this is not the case for inclusion of discrepant data. In conclusion, identifying discrepant data points and excluding them from the assimilation process is important. The new evaluation procedure provides a consistency sequence, which is computationally beneficial compared to the standard method.

Analogous to the effects observed for responses, the calibrated values of parameters change considerably based on which responses are included in the data assimilation. The same three sets as selected previously are considered: namely including all $N_r = 17$ responses, excluding the six most discrepant responses, which yields the first χ^2 value inside the central 90% confidence range, and lastly a set of $N_r = 10$ responses with a normalized χ^2 closest to unity, recall Figure 36. Elastic and inelastic scattering in ^{235}U as well as radiative capture in the ^{55}Mn foil were selected as illustrative examples from the large number of parameters in the Godiva benchmark. Figure 39 to Figure 44 show both the relative change in cross section values and the corresponding relative standard deviation. The optimal cross sections are labelled with the number of responses that were used for the calibration, e.g. “opt,17” refers to the complete set of responses with $N_r = 17$. Otherwise, the same notation is used as already introduced with the Jezebel benchmarks in chapter 4.2.

Scattering in ^{235}U , both elastic and inelastic, is an important reaction, which can be seen by the large sensitivity coefficients and uncertainty contributions presented in the previous sections. Figure 39 shows the relative change in the elastic scattering cross section of ^{235}U caused by data assimilation. If all seventeen responses are included in the calibration process, the optimal cross section is reduced by up to 11%. In case of the consistent sets with either $N_r = 10$ or $N_r = 11$ responses, the relative change is smaller (up to 5%) and has a positive sign. The optimal cross section $\alpha_{^{235}\text{U}}^{(n,n),opt,10}$, which stems from the calibration with ten responses, is similar to the optimal cross section $\alpha_{^{235}\text{U}}^{(n,n),opt,11}$, which stems from the calibration with eleven responses. The partitioned data assimilation method reduces the uncertainties in parameters and Figure 40 depicts that each of the three calibrated standard deviations is significantly smaller than the nominal standard deviation of the elastic scattering cross section of ^{235}U .

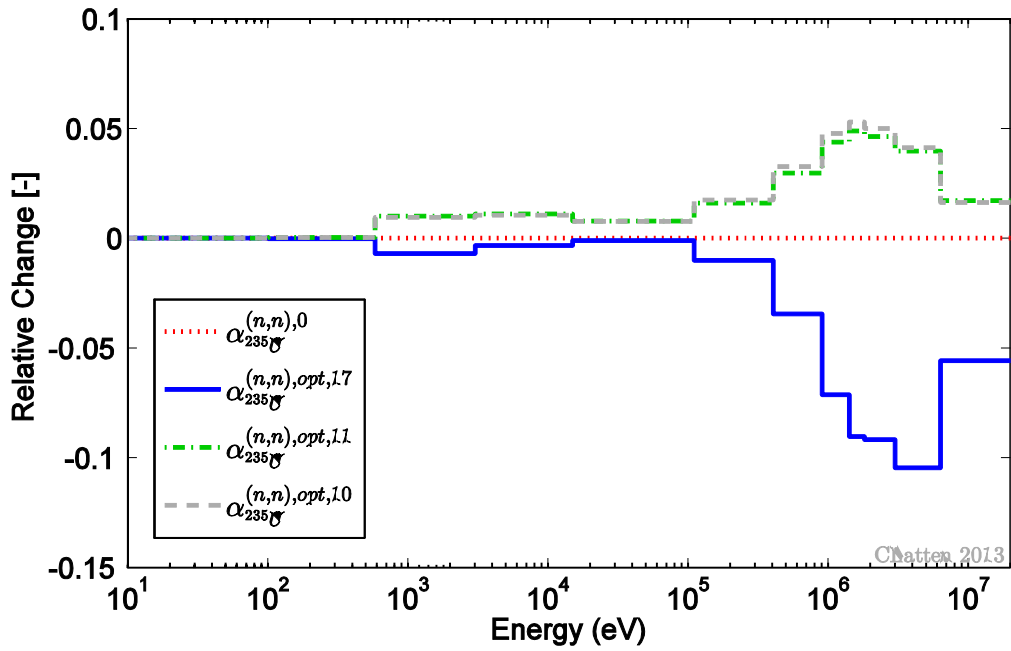


Figure 39: Relative change in the adjusted elastic scattering cross section of ^{235}U for particular sets of responses for Godiva

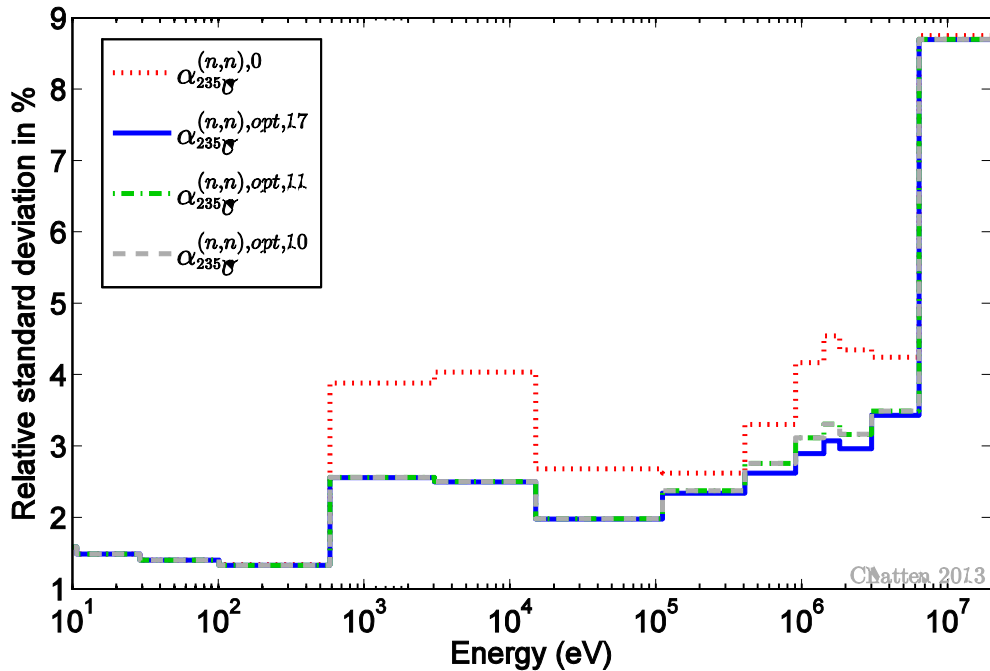


Figure 40: Nominal and adjusted relative standard deviation of the elastic scattering cross section of ^{235}U for particular sets of responses for Godiva

Figure 41 presents the relative change in the inelastic scattering cross section of ^{235}U . The two types of scattering are anti-correlated and a decrease in the calibrated elastic scattering cross sections leads to an increase in the calibrated inelastic scattering cross section and vice versa. The relative change in the inelastic scattering cross section is larger if all seventeen responses are included. The corresponding calibrated standard deviations are shown in Figure 42. All three calibrated standard deviations are smaller than the nominal standard deviation of $\alpha_{235\text{U}}^{(n,n'),0}$. Notably, the nominal standard deviation is very large and reaches up to 50%. This indicates that the inelastic scattering cross section is only known inaccurately in this particular energy range. Data assimilation reduces the uncertainty in this parameter, but the largest standard deviation, i.e. 50%, is not affected. One explanation for this is that the Godiva benchmark doesn't provide enough information to adjust the standard deviation of the inelastic scattering cross section. Data assimilation on Godiva coupled to additional benchmarks or DA on a different benchmark altogether could in theory alleviate this.

Figure 43 presents the relative change in the calibrated radiative capture cross section of ^{55}Mn . The corresponding standard deviations are shown in Figure 44.

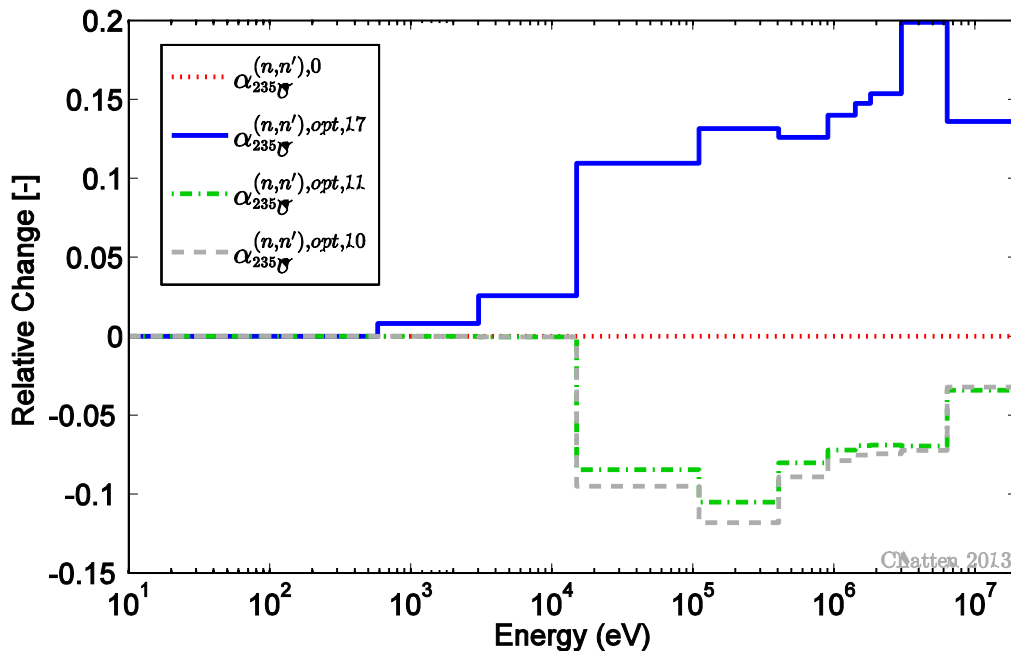


Figure 41: Relative change in the adjusted inelastic scattering cross section of ^{235}U for particular sets of responses for Godiva

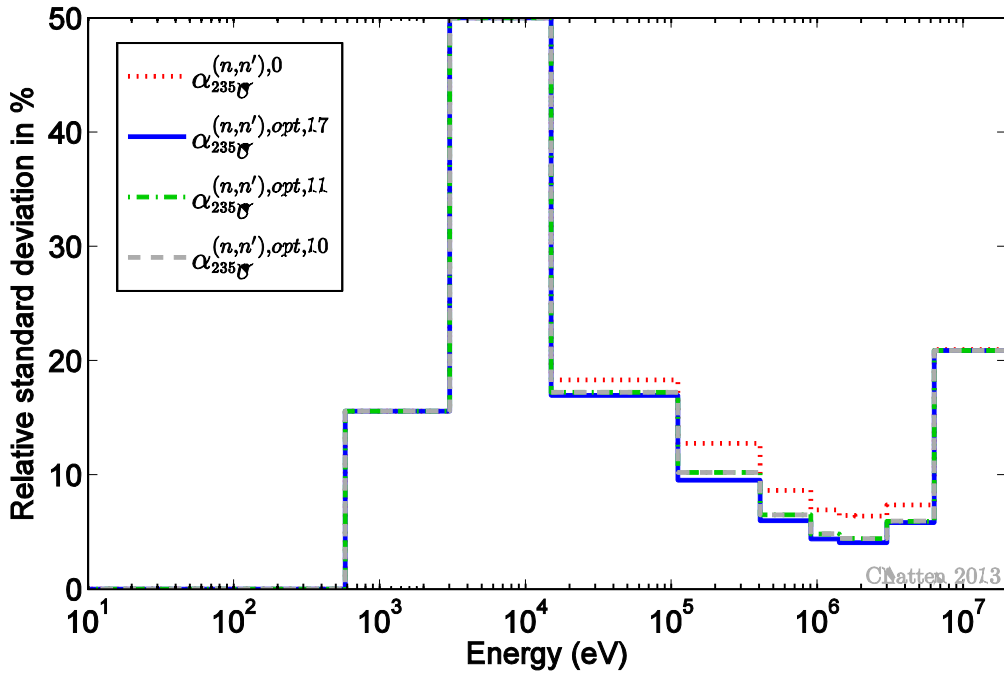


Figure 42: Nominal and adjusted relative standard deviation of the inelastic scattering cross section of ^{235}U for particular sets of responses for Godiva

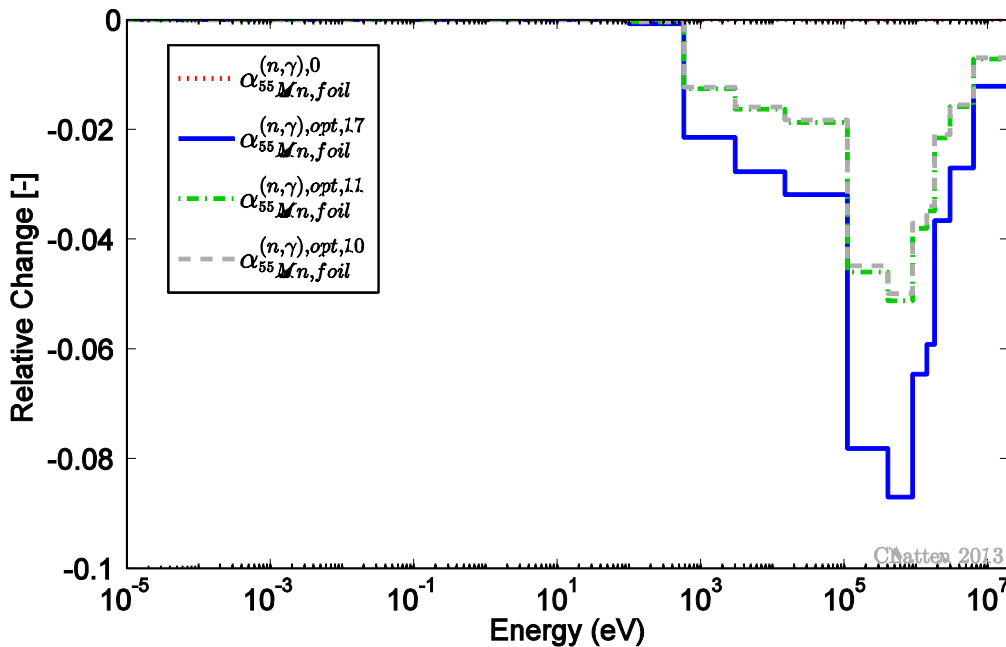


Figure 43: Relative change in the adjusted radiative capture cross section of ^{55}Mn for particular sets of responses for Godiva

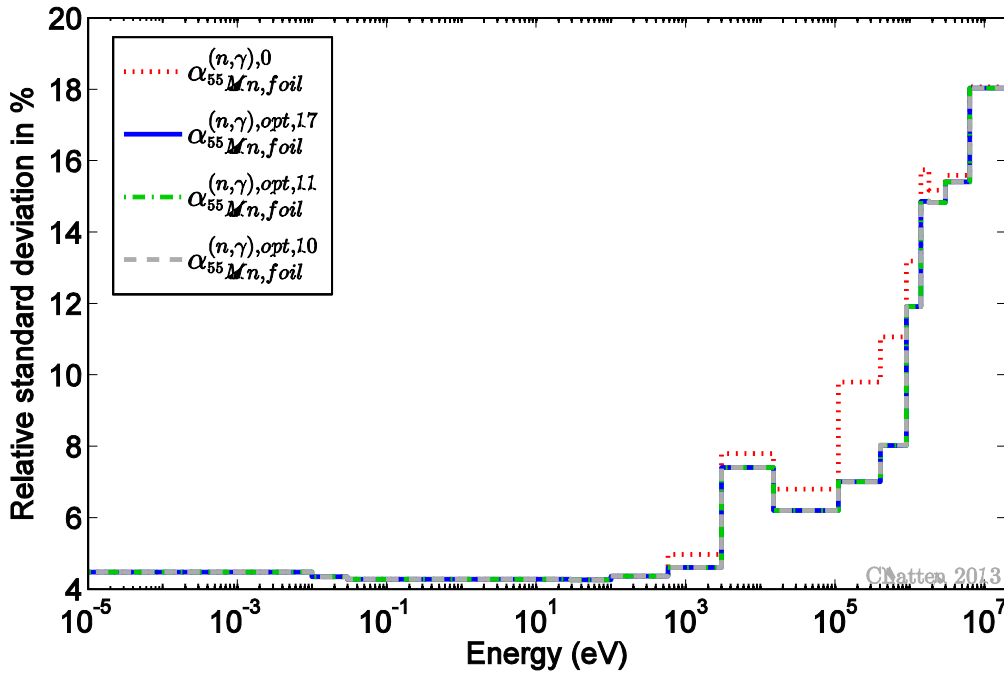


Figure 44: Nominal and adjusted relative standard deviation of the radiative capture cross section of ^{235}U for particular sets of responses for Godiva

4.3.4 Adding Benchmarks

The previous chapter illustrated how the new consistency evaluation procedure efficiently identifies and excludes discrepant responses from the considered system, i.e. Godiva. In this chapter the opposite procedure is illustrated, namely combining Godiva with additional systems. Godiva is combined with the two Jezebel benchmarks, which have already been presented in chapter 4.2. Jezebel-239 which has eight responses and Jezebel-240 which has three responses comprises subsystem I. Subsystem II consists of Godiva with eleven consistent responses, which have been identified in the previous section. Using partitioned DA these systems can be considered sequentially rather than simultaneously, while preserving exactly the same results as if the systems were treated simultaneously. Recall that the Jezebel benchmarks are bare plutonium spheres, while Godiva is a bare uranium sphere. The two subsystems are coupled via shared isotopes and correlations between the fission cross section in plutonium and uranium. Note that the Godiva sphere doesn't have any isotopes in common with either of the Jezebel spheres. However, the isotopes ^{238}U , ^{235}U and ^{237}Np appear in similar foils, which are used to measure the corresponding reaction rate, in each of the three benchmarks. And the isotopes ^{233}U , ^{239}Pu , ^{55}Mn , ^{93}Nb and ^{63}Cu appear in similar foils in Jezebel-239 and Godiva. Figure 45 visualizes the extent

of the coupling between Jezebel-239, Jezebel-240 and Godiva by presenting the non-zero elements in the variance-covariance matrix \mathbf{C}_p of all parameters. In this figure, all model parameters of subsystem I (Jezebel-239 and Jezebel-240) denoted as α . The matrix block $\mathbf{C}_{\alpha\alpha}$, which is outlined in Figure 45 by a dotted line, is thus identical to the variance-covariance matrix \mathbf{C}_p shown in Figure 18. The matrix block denoted as $\mathbf{C}_{\beta\beta}$ refers to Godiva with eleven consistent responses and the matrix block $\mathbf{C}_{\alpha\beta}$ contains the cross-terms, which indicate the coupling between the two Jezebels and Godiva.

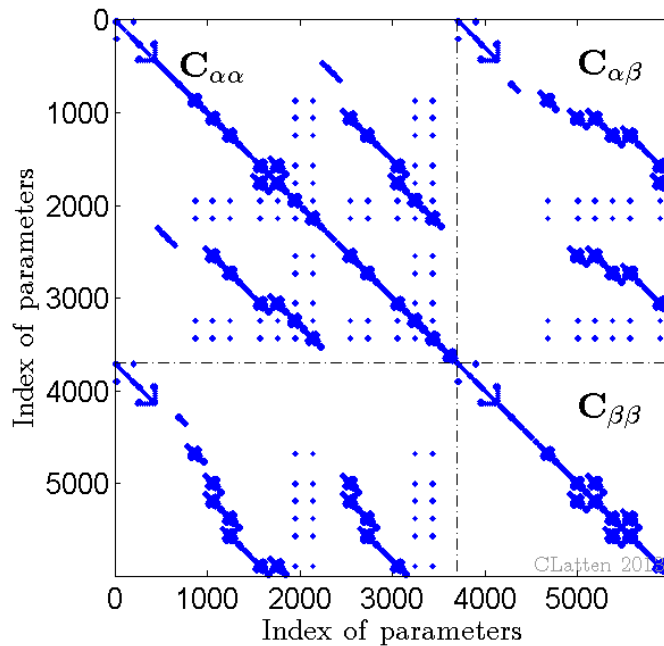


Figure 45: Non-zero elements in the covariance matrix \mathbf{C}_p of parameters. $\mathbf{C}_{\alpha\alpha}$ refers to the combined Jezebel systems, $\mathbf{C}_{\beta\beta}$ refers to Godiva and $\mathbf{C}_{\alpha\beta}$ contains the cross-terms, which indicate the coupling between the benchmarks.

Data assimilation is applied to several combinations of the benchmarks Jezebel-239, Jezebel-240 and Godiva and the results are compared. Each of the benchmarks has already been considered individually as a stand-alone system and the calibrated results are referred to as best-estimate values with corresponding best-estimate standard deviations. These quantities are labelled with the superscript “be” in the figures below. Next, the two Jezebel benchmarks have already been considered as coupled system and the calibrated results are included in the figures for comparison. Quantities based on DA of Jezebel-239 and Jezebel-240 calibrated jointly are denoted with the superscript “opt,1”. Finally, the Godiva benchmark is coupled to the Jezebel benchmarks in this section and DA is applied to all three benchmarks jointly. These quantities are labelled with the superscript “opt,2”.

Figure 46 depicts the measured, computed and calibrated values for k_{eff} , along with one standard deviation, all normalized to the nominal measured value, for the combinations of benchmarks described above. The calibrated results of considering Godiva jointly with the already coupled Jezebel benchmarks are new, while all other results have already been discussed in previous sections and are included for comparison only. Applying data assimilation to all three benchmarks simultaneously has little additional effect on the calibrated (“opt,2”) mean value of the multiplication factor. This can be expected from the weak coupling between the two plutonium benchmarks to the uranium benchmark.

Figure 47 presents calibrated results for selected reaction rate ratios. Recall that a spectral index, which was measured in several benchmarks, is called a *similar* response. The effects of coupling benchmarks are strongest for *similar* responses. Notably, all three computed fission rates of ^{238}U are smaller than the experimentally measured ones, while the computed fission rates of ^{237}Np don't have a strong trend. In all cases, the data assimilation method adjusts the respective response to calibrated values which fall in between the measured and the computed values, while reducing the corresponding calibrated standard deviations. The additional adjustment of the calibrated mean value and a further reduction of the calibrated standard deviation can be seen for the fission reaction ratio of ^{237}Np to ^{235}U .

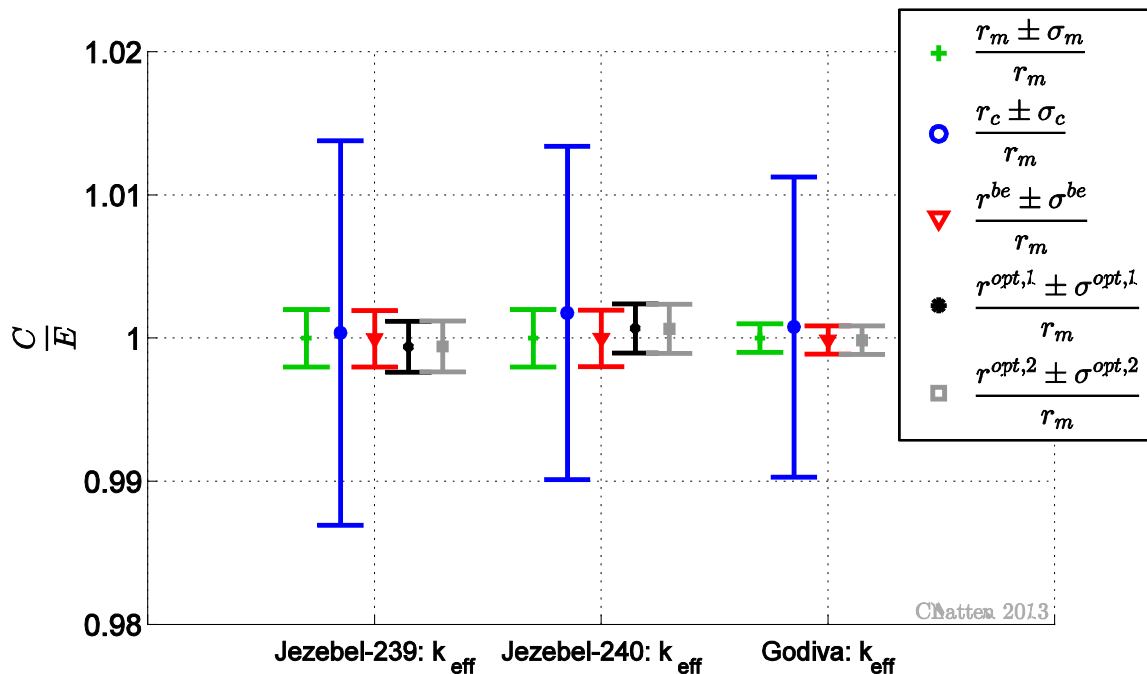


Figure 46: Measured, computed and adjusted values for k_{eff} and one standard deviation for individual benchmarks (“be”), couple Jezebel benchmarks (“opt,1”) and coupled Jezebel benchmarks and Godiva (“opt,2”)

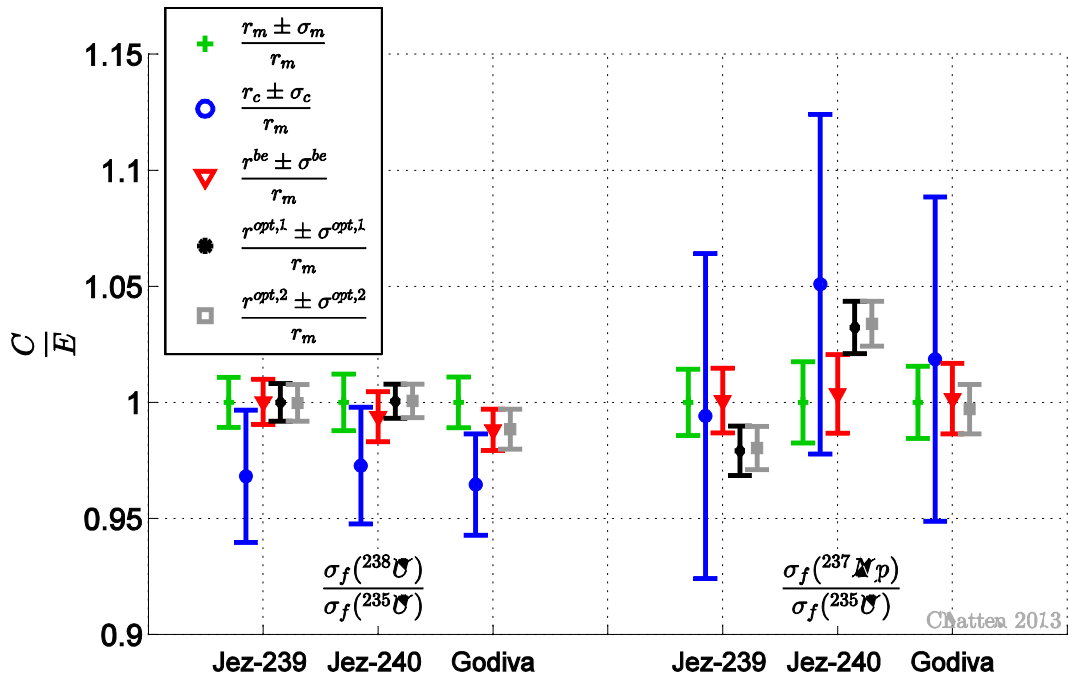


Figure 47: Measured, computed and adjusted values for *similar* responses and one standard deviation for individual benchmarks (“be”), couple Jezebel benchmarks (“opt,1”) and coupled Jezebel benchmarks and Godiva (“opt,2”)

The partitioned data assimilation methodology, as introduced in chapter 2, provides a convenient and computationally efficient way to exclude discrepant responses as well as include additional benchmarks. Depending on how strong or weak the coupling between the selected benchmarks is, the joint calibration can have a significant or marginal effect on the results. In case of Godiva and the two Jezebel benchmarks, the coupling is weak and the additional adjustment is small.

4.4 Data Assimilation on ZPR

Argonne National Laboratory (ANL) operated more than a hundred Zero Power Reactor (ZPR) assemblies over a period of three decades. Each facility was a fast critical assembly. Here the particular benchmark ZPR-6 assembly 7 was selected. ZPR-6/7 was a physics benchmark operational in 1970 and 1971. It was designed to test fast reactor physics data and its geometry and composition was kept as simple as possible, [19]. A description of the ZPR-6 facility quoted from [19] follows.

“[...]he fast critical facility was a horizontal split-table type machine consisting of a large, cast-steel bed supporting two tables, one stationary and the other moveable. [...]. During loading operations, the tables were separated by 1.5 meters. In operation, the moveable half

was driven against the stationary table with a nut and lead screw mechanism. Stainless steel square tubes [...] were [...] stacked horizontally on both tables to form a 45-row and 45-column square ‘honeycomb’ matrix. A matrix position is specified by three parameters: matrix half (S or M), row number (starting from the top) and column number (starting from the left looking from the moveable half towards the stationary half). “

Each matrix position could be filled with a drawer, which in turn contained rectangular plates of different materials. Specifying the plate-loading pattern of each drawer and then again specifying the matrix position of each drawer defines the average composition and is referred to as a particular loading of ZPR-6/7. In the present work two loadings were considered, namely Loading 12 as reference loading for the criticality safety benchmark and Loading 41 as reference loading for reaction rates. Both loadings are described in [19] in detail, Loading 12 has the identifier MIX-COMP-FAST-001 and Loading 41 has the identifier ZPR-LMFR-EXP-001.

4.4.1 ZPR-6/7 Benchmark Model

The ZPR-6/7 benchmark was initially modeled in full detail for ANL’s continuous energy neutron transport code VIM. Based on this as-built model a transformation was derived and the simplified, homogenous benchmark-model was created. Input decks for both the as-built as well as the benchmark-model are provided for Loading 12 in [19]. VIM is a Monte Carlo type neutron transport solver which can handle detailed three-dimensional geometry, [20]. The as-built model has been successfully ported into Los Alamos National Laboratory’s Monte Carlo transport code called MCNP5, [34]. Reference [18] compared the as-built model in MCNP5 with a custom-built model for a deterministic neutron transport tool. This custom-build model uses a 15 few group structure and homogenizes each drawer spatially. The effect of progressively increasing the heterogeneity of a custom-build model of a different loading of the ZPR-6/7 assembly was analyzed with a deterministic transport tool in [32]. To the best of the author’s knowledge, the ZPR-6/7 Loading 41 benchmark has never been built in full detail for a three-dimensional deterministic neutron transport solver like Denovo. The as-built model created for the present work is based on the information available in [19] and models each plate in each drawer separately. The cladding of fuel plates and the steel cans of sodium plates are also included. A central position of the drawers inside a matrix position was assumed and air gaps are consequently distributed evenly to the left and right of each drawer. A typical input listing is included in Appendix F. From here on the term “as-built” model refers to an input listing similar to the one shown in the appendix, the term benchmark-model refers to the homogenized R-Z model, to which input listings are provided in [19]. Figure 48 and Figure 49 show schematics of the R-Z- model.

The fuel for ZPR-6/7 consisted of plutonium and uranium plates. For instance, the fissile inventory of Loading 12 was 15.4kg of ^{235}U and 1118.1kg of isotopes ^{239}Pu and ^{241}Pu . ZPR-6/7 is thus regarded as a typical mixed plutonium-uranium oxide (MOX) fuelled fast reactor, [29]. The axial and radial blanket regions were composed of depleted uranium plates. The fuel composition tables for Loading 41 in [19] list masses corresponding to January 1st, 1977. According to [4], the reference day for the ZPR-6/7 facility is September 15th 1971 and the masses of ^{241}Pu and ^{241}Am are decay-corrected to this date. For the decay calculation the following assumptions were made:

- ^{241}Pu decays to 99.998% to ^{241}Am with a half-life of $\lambda = 14.290$ years;
- The decay branch of ^{241}Pu to ^{237}U is neglected;
- The daughters of ^{241}Am are neglected.

Based on these assumptions the number of nuclei on 15/9/1971 is

$$N_{Pu}^0 = \frac{N_{Pu}}{e^{-\lambda t}} \quad (4.14)$$

$$N_{Am}^0 = N_{Am} - N_{Pu}^0 (1 - e^{-\lambda t}) \quad (4.15)$$

with $t = 1935$ days and $\lambda = 14.290$ years.

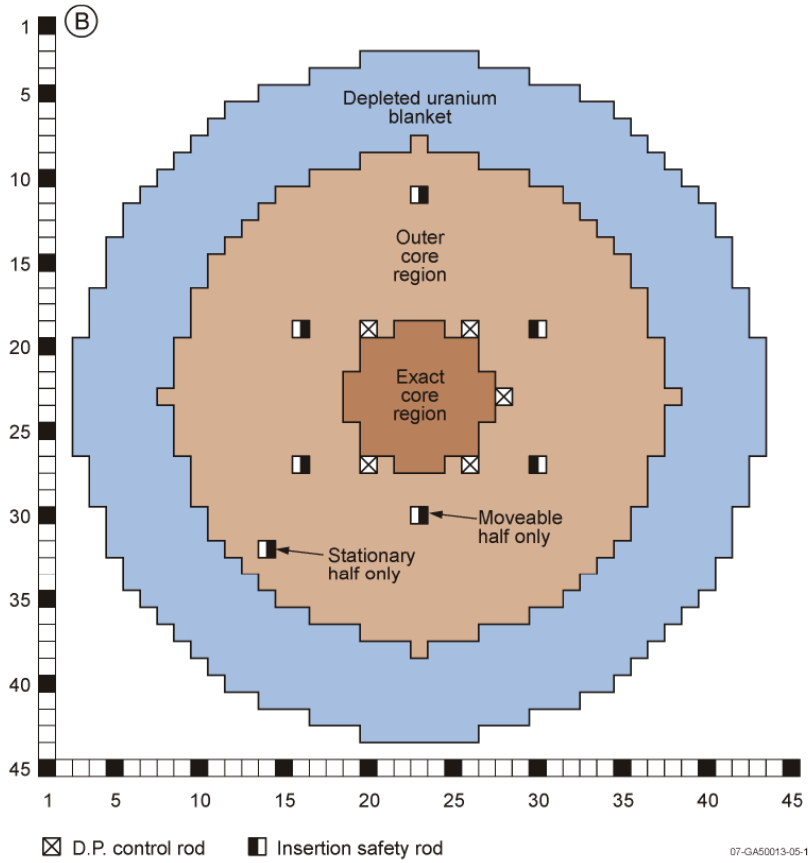


Figure 48: XY view of benchmark model for ZPR-6/7 Loading 41, [19].

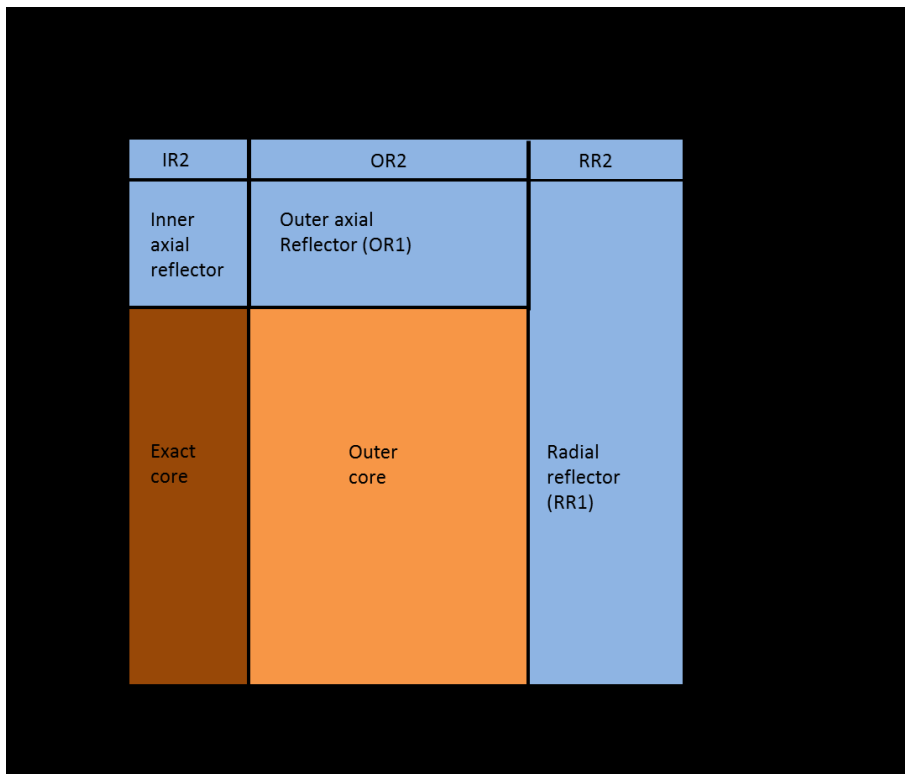


Figure 49: Axial dimensions in cm for the ZPR-6/7 Loading 41 benchmark R-Z model, [19]

4.4.2 Model Comparison with Monte Carlo Module KENOVI

ORNL's SCALE6.1 code package comes with its own flavor of Monte Carlo code called MONACO/MAVRIC. The multiplication constant k_{eff} is calculated for the newly created as-built model and the homogeneous R-Z model using several ENDF/B libraries. All calculations were done for 650 generations with 100 000 particles per generation skipping the first 50 generations. An overview of the results is listed in Table 22 and the same information is also shown in Figure 50. Note that the uncertainty for k_{eff} included in Table 22 represents merely the statistical standard deviations of the Monte Carlo computation. This statistical standard deviation cannot be compared to the uncertainties for computed responses, which data assimilation provides. The quantities in the legend of Figure 50 have the following meaning: Loading 12, which is the reference loading of the multiplication constant k_{eff} , is denoted as "L12", Loading 41, which is the reference loading for spectral indices, is denoted as "L41" and the entry "benchmark results" refer to illustrative computational results given in [19].

The model comparison with Monte Carlo calculations yields several conclusions. Firstly, the computed k_{eff} for Loading 12 and Loading 41 differ less than 61pcm. This clearly indicates that the change in criticality between Loading 12 and Loading 41 is vanishingly small and can be neglected. Based on this observation, only Loading 41 is modelled as-built in Denovo and the multiplication constant k_{eff} of Loading 12 is used as an additional response for Loading 41. Secondly, a significant change in k_{eff} depending on the version of the nuclear data library is observed. The multiplication constant of the same loading and model decreases ~400pcm between version 5 and version 7 for a continuous energy structure and increases ~800pcm for a 238 group energy structure. The ENDF/B libraries are labelled chronologically and later version include more nuclides. ENDF/B-VII is the latest nuclear data library available in SCALE6.1 and presents thus the newest and most complete information of the included libraries, [31]. Thirdly, the dependence of k_{eff} on energy groups is even stronger than the dependence on a particular library version, for instance collapsing 238 groups to 27 groups within library version 7 changes k_{eff} by up to 7000pcm.

The results of the as-built model correspond closest with the results of the homogenized R-Z model for point wise continuous energy libraries. The as-built model, which accounts for heterogeneities, consistently yields a higher multiplication constant than the respective R-Z model. The difference between the as-built and the R-Z model becomes larger with fewer energy groups. This trend persists over the available library versions and this behaviour is most likely attributed to energy self-shielding of the ZPR-6/7 assembly. Using the latest and

most detailed information available, i.e. the as-built model with the ENDF/B-VII library and point wise continuous energy, yields a computed k_{eff} that matches the experimentally measured value best, see Figure 50.

Table 22: k_{eff} for the homogeneous R-Z benchmark model as well as the as-built model computed using SCALE6.1 KENOVI with 650 generations, 100 000 particles per generation and the first 50 generations skipped

	R-Z model Loading 12	R-Z model Loading 41	As-built model Loading 41 (L12)
ENDF/B-V 238 groups	0.987403 ± 0.000085	0.986890 ± 0.000080	1.019330 ± 0.000092
ENDF/B-V 44 groups	1.008683 ± 0.000085	1.008166 ± 0.000070	1.043307 ± 0.000096
ENDF/B-VI CE	0.99380 ± 0.00011	0.993484 ± 0.000090	1.005230 ± 0.000093
ENDF/B-VII CE	0.989355 ± 0.000085	0.988971 ± 0.000095	1.001107 ± 0.000093
ENDF/B-VII 238 groups	0.995062 ± 0.000073	0.994452 ± 0.000088	1.02837 ± 0.000088
ENDF/B-VII 27 groups	1.068209 ± 0.000080	1.067948 ± 0.000073	1.095311 ± 0.000080
SCALE 4.4 ENDF/B-V 238 groups, [19]	0.9949 ± 0.0004		
VIM ENDF/B-VI CE, [19]	(0.9891 ± 0.0005)		

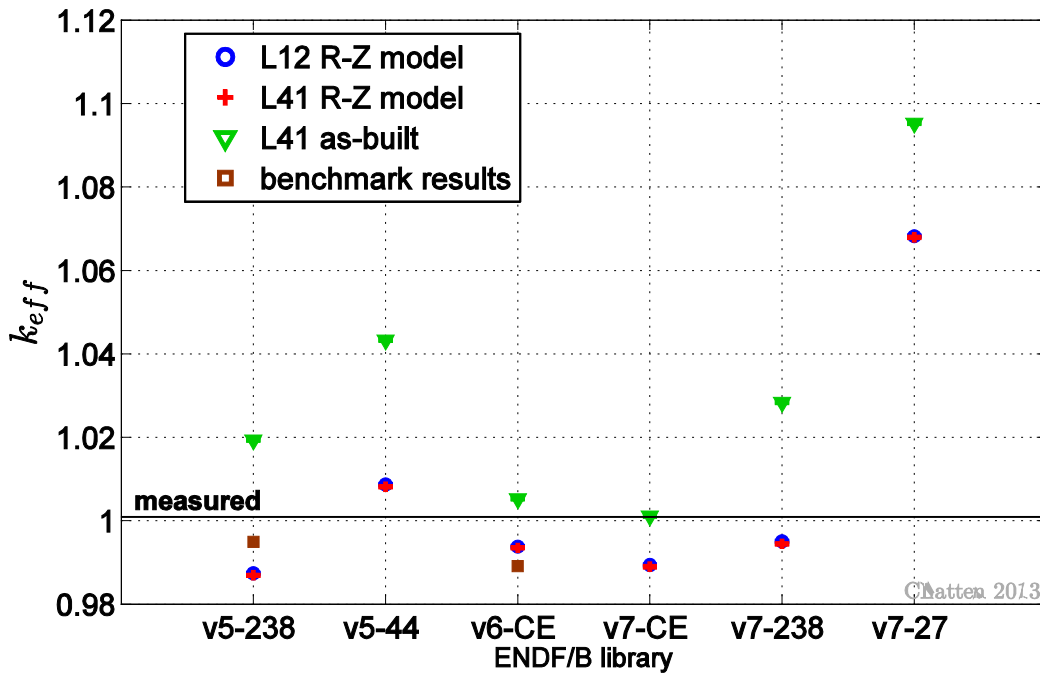


Figure 50: KENOVI results for several ENDF/B libraries computed with both the R-Z model and the benchmark-model of the ZPR-6/7 assembly Loadings 12 and 41.

4.4.3 Model Comparison with Denovo

The deterministic neutron transport solver Denovo does not support a continuous energy structure. Given the time and computational resources available for the present work, the ENDF/B-VII library with 27 energy groups was chosen. Since Figure 50 clearly indicates a significant dependence on energy group structure, future work could entail different nuclear data libraries with a customized number of energy groups and/or customized energy boundaries. The ZPR-6/7 assembly features some small asymmetries. Computational tests demonstrated that these asymmetries have no effect on the computational solutions of k_{eff} or the selected spectral indices. From here on, ZPR-6/7 always refers to the ZPR-6/7 assembly Loading 41. All numerical simulations in the present work are based on a $71 \times 71 \times 37$ Cartesian mesh of an octant of the ZPR-6/7 assembly and step characteristics as spatial discretization scheme. The spectrum of the neutron flux of the as-built model agrees very well with the R-Z model, see Figure 51. The previous two sections presented results of the fast critical assemblies Jezebel and Godiva. A comparison between their spectra, recall Figure 30, reveals that the spectrum of ZPR6/7 reaches further into the intermediate energy range.

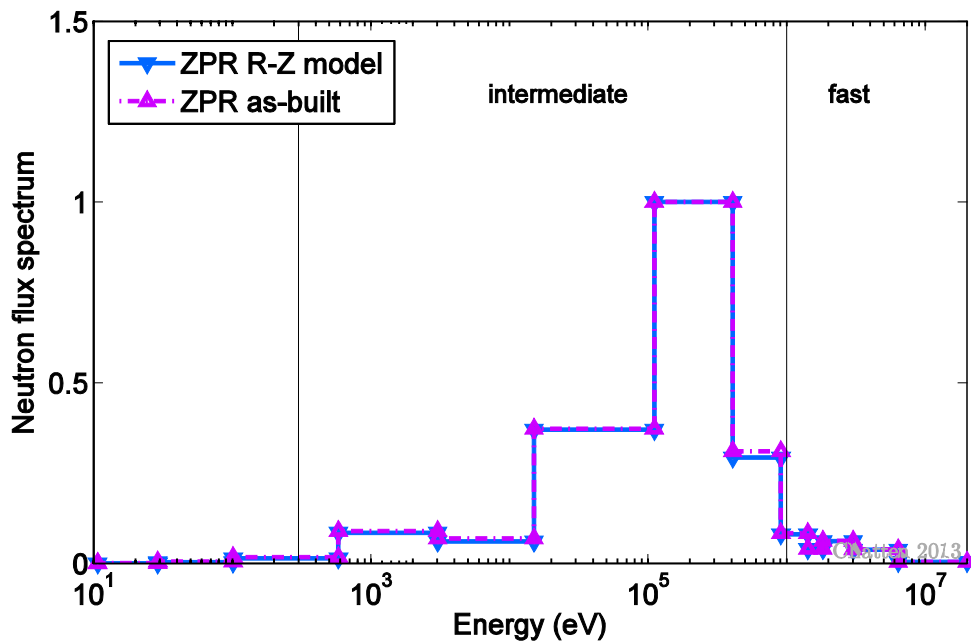


Figure 51: Denovo computations of the spectrum of the neutron flux for ZPR-6/7 Loading 41

Loading 41 is the reference loading for spectral index measurements. Experimental data of fission and capture reaction rate ratios for isotopes ^{235}U , ^{238}U and ^{239}Pu at various locations throughout the core and blanket region of ZPR-6/7 is listed in [19]. Four locations in

the stationary (S) half of the assembly were selected as system responses: the central matrix position S-23/23 at $Z = 0$ in, the right most core matrix position S-23/37 at $Z = 0$ in, which is adjacent to the radial blanket region, and both these matrix position at $Z = 28$ in, which is adjacent to the axial blanket region. All four matrix positions lie physically within the octant of the assembly that is computed. This assures that slight asymmetries in the assembly do not affect the chosen reaction rate ratios. The coordinate system is chosen in such a way that the interface between the stationary and the moveable half of the assembly coincides with the origin of the z-axis. Figure 52 shows the scalar neutron fast flux computed with the R-Z model (left) and the as-built model (right) at the interface, i.e. $Z=0$. As expected, the as-built model reveals a higher level of detail. The pattern in the scalar flux of the as-built model represents individual drawers and the outline of the core matches the schematic in Figure 48. Figure 52 also indicates the approximate location of two of the selected spectral indices measurements. The homogeneous R-Z model is based on a transformation and simplification of a detailed model, [19]. This transformation includes a specific correction factor for k_{eff} .

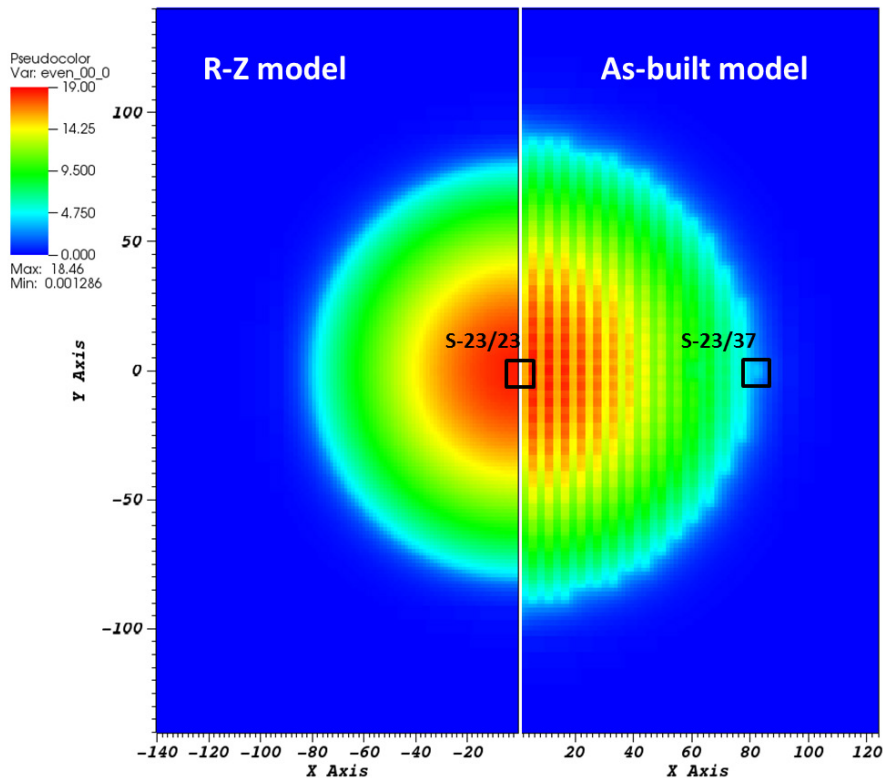


Figure 52: Fast scalar flux of ZPR-6/7 at $Z=0$ cm. Left half is computed with the R-Z model, right half is computed with the as-built model. Matrix positions which contain measurement foils are highlighted (not to scale).

Not surprisingly, the R-Z model therefore yields a computed k_{eff} value that is closer to the measured multiplication constant than the as-built model, see Figure 53. This figure presents experimentally measured values with corresponding standard deviations, computed mean values based on the R-Z model with corresponding standard deviations and computed mean values based on the as-built model with corresponding standard deviations. The notation used here is similar to the one already introduced in chapter 4.2: $r_{c,R-Z}$ and $\sigma_{c,R-Z}$ denote the mean value and corresponding standard deviation for a computed response, which is computed with the R-Z model; $r_{c,as-built}$ and $\sigma_{c,as-built}$ denote the mean value and corresponding standard deviation for a computed response, which is computed with the as-built model. Three fission reaction rate ratios and three radiative capture reaction rate ratios at the central location S-23/23 Z=0-2in are shown. These reaction rate ratios are representative for all locations. With the exception of k_{eff} mentioned above, the computed values based on the as-built model agree better with the measured values than the computed values based on the R-Z model. Notably, all three radiative capture ratios are discrepant. The standard deviation of computed responses is similar for both models.

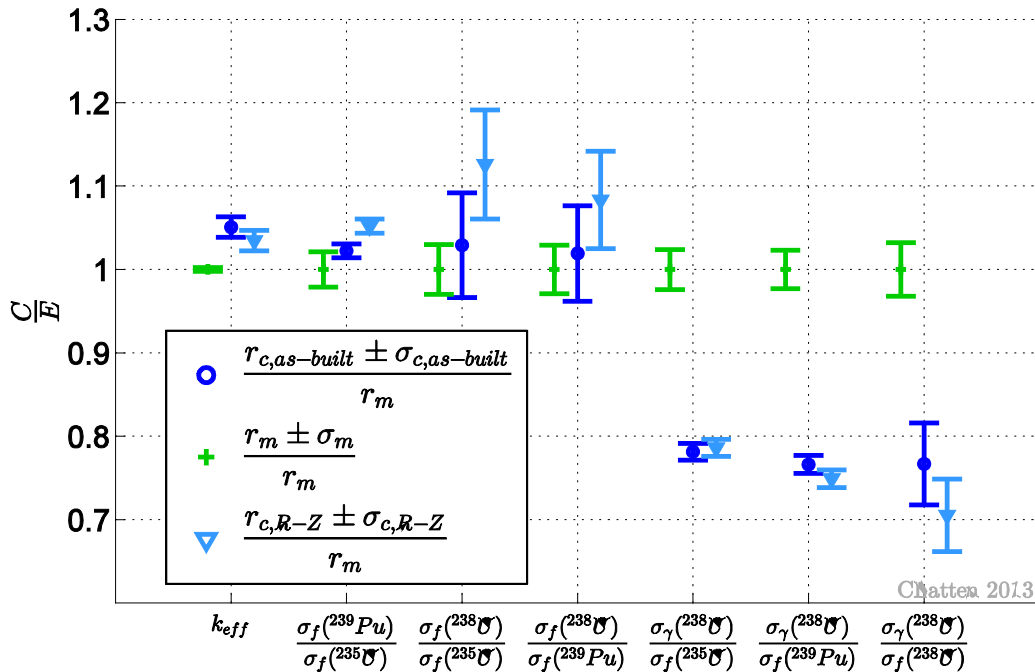


Figure 53: Measured and computed (Denovo) k_{eff} and spectral indices at S-23/23 Z=0-2in. Error bars represent one standard deviation.

4.4.4 Sensitivity Analysis

This chapter uses the same notation as introduced in chapter 4.2.1. The ZPR-6/7 assembly has a more complex geometry than Godiva or Jezebel and additional subscripts are introduced to identify the location of particular parameters.

Relevant sensitivity profiles of k_{eff} are shown in Figure 54 for the R-Z model and in Figure 55 for the as-built model. Both models are most sensitive to a change in $\bar{\nu}$ in the isotope ^{239}Pu . The R-Z model simplifies the core into two cylindrical regions, which are labeled as inner core (“IC1”) and outer core (“OC1”). These labels stem from the schematic of the ZPR-6/7 assembly, recall Figure 49. Each region is assigned a homogenized material, which leads to two problem dependent parameters for each cross section. For example, the sensitivity analysis yields separate coefficients for fission in ^{239}Pu in the inner core and fission in ^{239}Pu in the outer core. Interestingly this particular parameter displays a larger sensitivity in the outer core than the one of the inner core. The as-built model preserves the heterogeneous plate pattern of the assembly, which results for instance in ten problem dependent parameters for each cross section associated with fuel plates. Since one particular type of fuel plate is spread throughout the core, a clear spatial dependency of sensitivity profiles cannot be determined. Instead the sensitivity coefficients of similar parameters are summed for ease of representation and comparison in Figure 55. The shape and magnitude of sensitivity profiles agree very well between the two models. The sensitivity profile of radiative capture in ^{238}U has negative values, which confirms that this parameter acts as a neutron sink. The as-built model offers additional insight, since the uranium component of the MOX fuel plates can be distinguished from the depleted uranium oxide plates (DUO_2) that are present in each drawer and make up the blanket region. The major contribution to the sensitivity profile stems from the depleted uranium oxide.

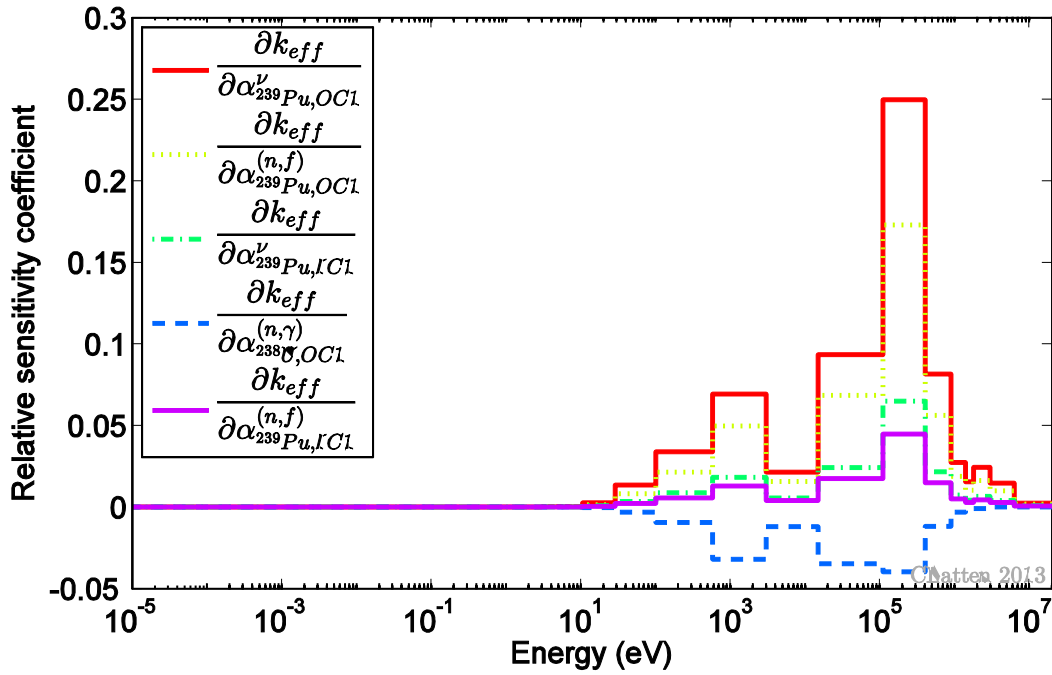


Figure 54: Sensitivity profile of k_{eff} to selected parameters for ZPR-6/7 based on the R-Z model

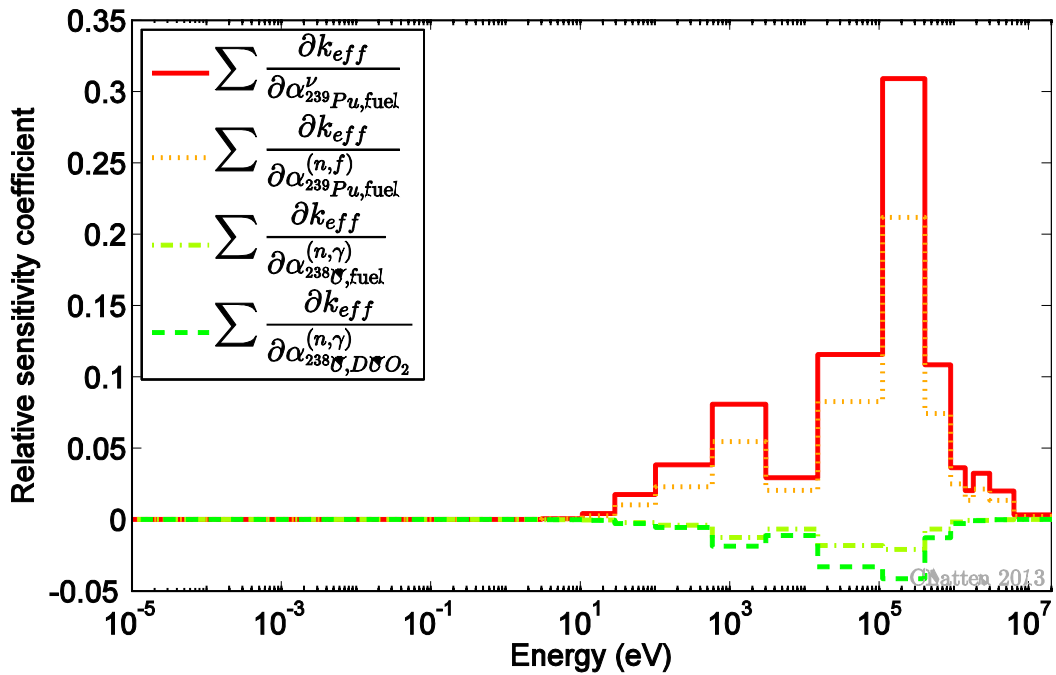


Figure 55: Sensitivity profile of k_{eff} to selected parameters for ZPR-6/7 based on the as-built model

4.4.5 Data Assimilation

The previous sections highlight the benefits of the as-built model, which preserves the heterogeneous drawer structure of the ZPR-6/7 assembly and allows a deeper insight into the underlying physics. This section presents calibrated results for Loading 41 based on the as-built model. Data assimilation is applied to this large-scale system with twenty-five responses and approximately $1.6 \cdot 10^5$ parameters. The responses include the effective multiplication constant k_{eff} and reaction rate ratios at four different locations in the core. Each location has the same six reaction rate ratios associated with it; namely the fission reaction rate of ^{239}Pu normalized to the fission reaction rate of ^{235}U , the fission reaction rate of ^{238}U normalized to the fission reaction rate of ^{235}U , the fission reaction rate of ^{238}U normalized to the fission reaction rate of ^{239}Pu , the radiative capture reaction rate of ^{238}U normalized separately to the fission reaction rate of ^{235}U , ^{239}Pu and ^{238}U . The figures below use the same notation as introduced in chapter 4.2. The normalized consistency indicator of this system is $\chi^2/25 = 12.2$ with a central 90% confidence interval of (0.58 – 1.50).

Figures 56 to 58 depict the measured, computed and calibrated values of k_{eff} and the selected twenty-four reaction rate ratios. The computed value of k_{eff} is super critical and larger than the experimentally measured value. Also, the computed standard deviation of k_{eff} is significantly larger than the experimentally measured one. Applying data assimilation shifts the best-estimate mean value of k_{eff} closer to the experimentally measured nominal value, since this value is more accurately known. The best-estimate standard deviation is simultaneously slightly reduced.

The computed mean values of all fission reaction rate ratios are larger than the corresponding experimentally measured ones, while the computed mean values of all radiative capture reaction rate ratios are significantly smaller than the experimentally measured ones. Furthermore, the latter ratios are discrepant at all four locations. The best-estimate mean value of these discrepant responses lies in between the nominal measured and the nominal computed value. The respective best-estimate standard deviations are reduced and cannot bridge the gap between computational values and experimentally measured values. The level of discrepancy is smallest at the central location, i.e. S-23/23 Z=0-2in. Locations adjacent to the radial blanket, which are indicated with the matrix position S-23/37, and locations adjacent to the axial blanket, which are indicated with the axial position Z=28-30in, display larger deviations between computed and measured nominal

values. A possible explanation is that the underlying computational mesh is too coarse to resolve rapid changes between the core and the blanket region. Here, the mesh size was limited by the available computer resources.

The best-estimate mean values of several fission reaction rate ratios aren't calibrated to a value that falls in between the nominal computed value and experimentally measured one. One example is the fission rate of ^{238}U normalized to the fission rate of ^{235}U at location S-23/23 Z=0-2in, which is shown in Figure 56. This unexpected behaviour has been observed for Godiva as well and stems from the inclusion of discrepant data in the calibration procedure. Identifying and excluding the most discrepant responses has shifted the best-estimate value to its expected value in case of Godiva. A similar behaviour is anticipated for ZPR-6/7. However, here the focus lies on the successful application of partitioned data assimilation on a large-scale system.

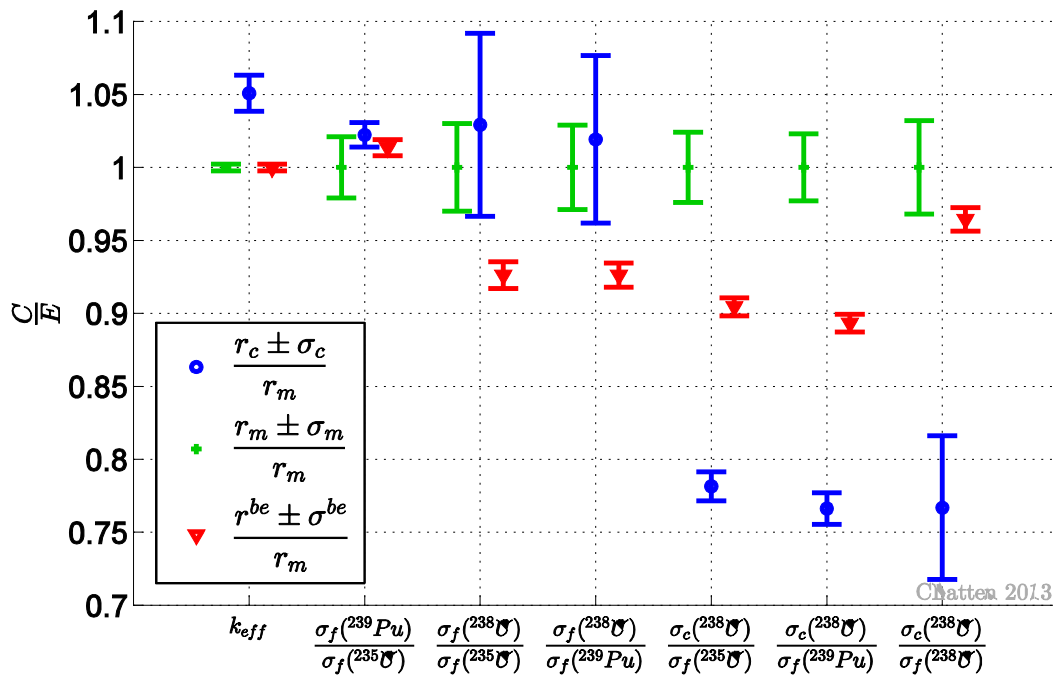


Figure 56: ZPR-6/7 measured, computed and best-estimate k_{eff} and spectral indices at location S-23/23 Z=0-2in. Error bars correspond with one standard deviation.

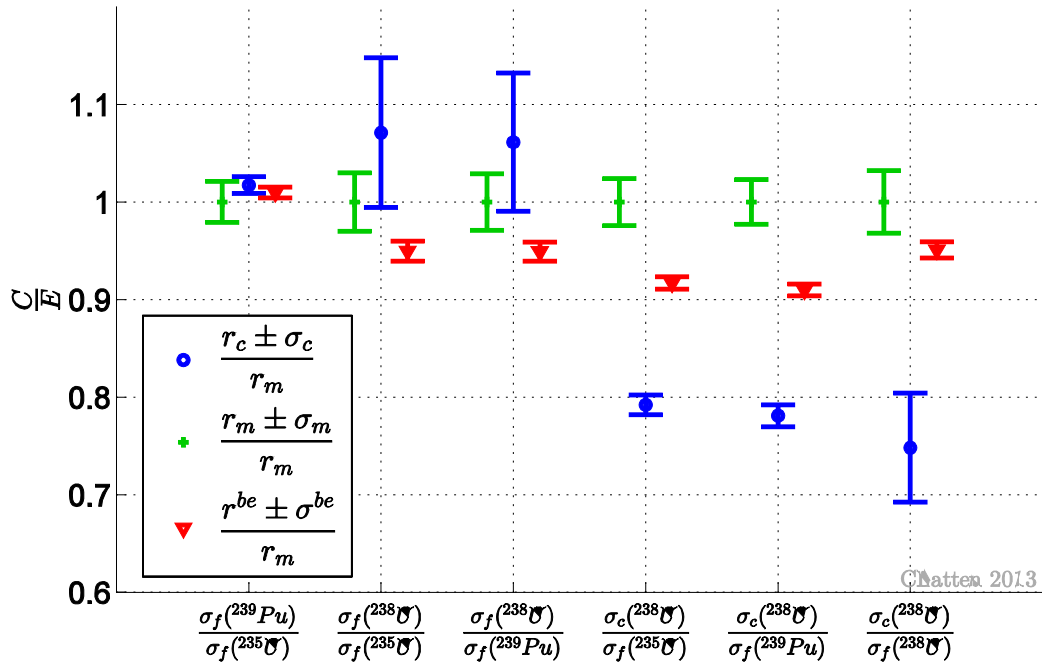


Figure 57: ZPR-6/7 measured, computed and best-estimate responses at location S-23/23 Z=28-30in. Error bars correspond with one standard deviation.

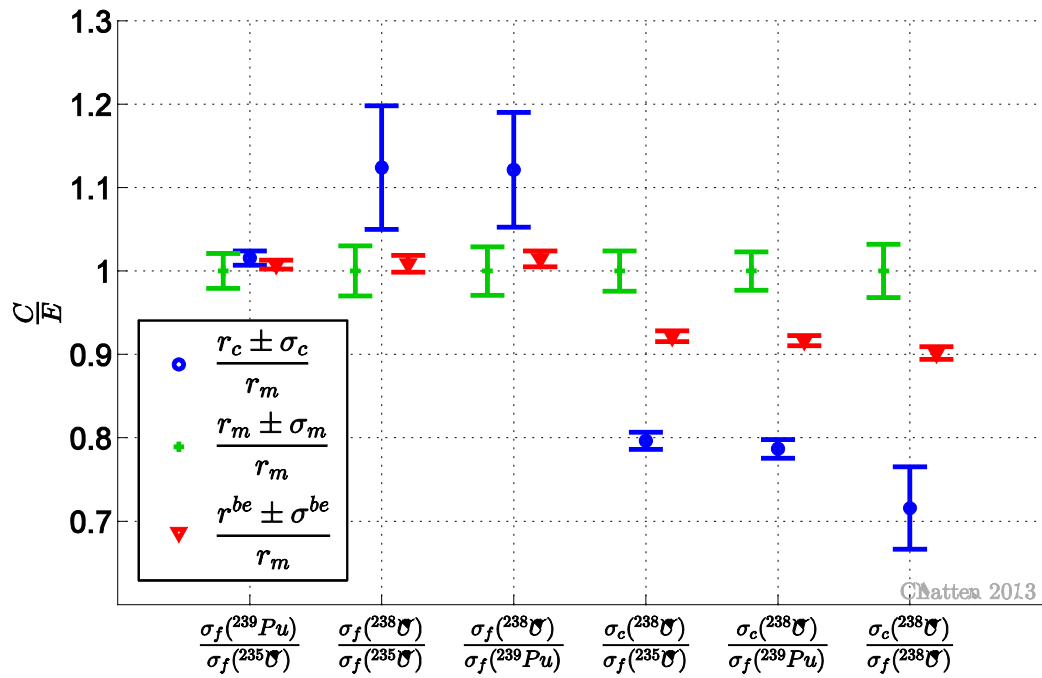


Figure 58: ZPR-6/7 measured, computed and best-estimate responses at location S-23/37 Z=0-2in. Error bars correspond with one standard deviation.

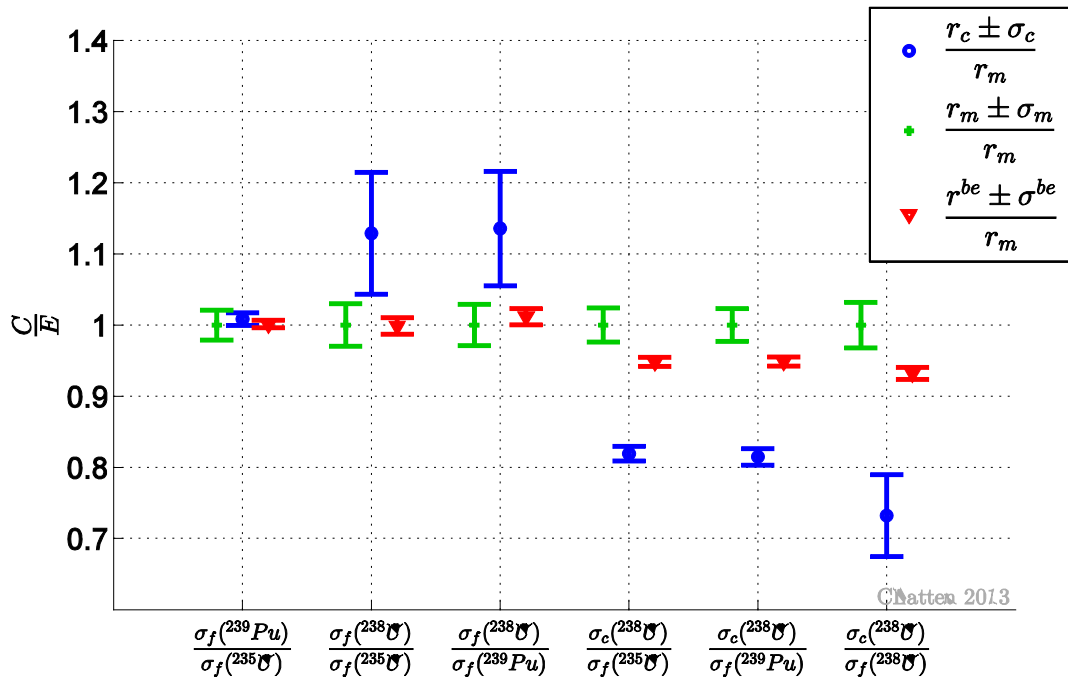


Figure 59: ZPR-6/7 measured, computed and best-estimate responses at location S-23/37 Z=28-30in. Error bars correspond with one standard deviation.

5. Summary and Conclusion

In the present work a general mathematical methodology for predictive modeling of coupled multi-physics systems, formulated by [10], is implemented. The new formulation is denoted here as partitioned data assimilation (DA). In this work the method of [10] has been applied without change to an illustrative heat conduction example and reactor physics benchmarks. Application of the partitioned DA yields optimal values of system parameters and responses, while simultaneously reducing the corresponding uncertainties in parameters and responses. This methodology also provides quantitative indicators constructed from sensitivity and covariance matrices for determining the consistency among the a priori computational and experimental data. Standard formulations of data assimilation methods treat all of the available computational and experimental information simultaneously. In case of very large systems, this simultaneous approach can become computationally expensive. In particular, the memory requirement can exceed available computational resources. The new partitioned data assimilation is constructed in a way that an implementation can consider parts of the available information sequentially rather than all information simultaneously, while preserving exactly the same results.

The same mathematical framework can be implemented into a multitude of different algorithms, each targeted at opposing goals like performance, stability, range of use, complexity of the implementation etc. For the present work an implementation of the partitioned DA was created that requires the least memory in a serial environment disregarding any trade-offs with regard to execution time. Furthermore, a consistency evaluation procedure based on the partitioned DA formulas is suggested. Both, the implementation and the consistency evaluation procedure are thoroughly tested with several examples and benchmarks.

The first application is an illustrative heat conduction example with synthetic data. 1-dimensional time-dependent heat conduction in an infinite medium has an analytic solution, which makes sensitivity coefficients readily available. Synthetic data is advantageous because on the one hand data sets, which are tailored to specific problems, can be created and on the other hand a wider variety of systems can be analyzed than is available as real-world benchmarks. Paradigm data sets have clearly demonstrated the above characteristics of the new partitioned DA: calibrated results of the new method, which partitions one data set into two subsystems, match best-estimate results of the non-partitioned data assimilation, which is the standard formulation see e.g. [30], to machine precision. Large paradigm data sets have also demonstrated the reduced memory requirement of the implementation.

However, further analysis of the performance of the algorithm also shows that the minimal memory requirement comes at a high cost of execution time. The sequential approach of the partitioned data assimilation increases data transfer operations, which consume most of the time. Testing of various synthetic data sets also reveals that the computational performance of the algorithm depends on the matrix dimensions dictated by the number of responses and parameters. For this reason, it would be possible to design customized implementations that are optimized to a particular application in the future, while making use of the flexibility of the partitioned data assimilation formulas.

In addition, the heat conduction problem based on synthetic data is also used to feature a new consistency evaluation procedure. The degree of consistency, which describes the agreement or disagreement between computed and experimentally measured values, is easily varied for synthetic data sets. The established method to obtain a “consistency-wise optimal sequence”, [36], is modified making use of the new partitioned data assimilation formulas. The suggested new consistency evaluation procedure identifies a sequence from least to most consistent system responses in substantially less time than the standard method. Large systems, for which the computational effort of the standard method has been too high, can now be analyzed and a consistency sequence can be identified. Once this sequence is identified, a user-defined criterion decides which responses are included and which ones are excluded from the data set. For the present work, the rejection criterion is the central 90% significance range. Starting from a complete data set with all responses, discrepant responses are gradually excluded. As soon as the consistency indicator of the system, which is step by step reduced, falls inside the selected confidence range the remaining responses of the system are considered to be consistent. Inclusion and exclusion of discrepant responses has a significant impact on the calibrated results of data assimilation. Data assimilation applied to a consistent data set yields best-estimate mean values that fall usually in between the computed nominal value and the experimentally measured one while the corresponding best-estimate standard deviation is reduced. In the presence of marginally discrepant data, data assimilation also yields best-estimate mean values that fall in between the computed nominal value and the experimentally measured one while the corresponding best-estimate standard deviation usually bridges the gap between the discrepant computed and measured values. If the system includes significant discrepancies, data assimilation can yield unexpected best-estimate mean values. Tests based on synthetic data demonstrated that a single discrepant response can have a considerable effect on the consistency indicator of the system. At the same time, the consistency indicator of systems with a deliberately large degree of discrepancy usually falls inside the central 90% confidence range with the exclusion of only a few responses. This is an important observation, because the computationally beneficial, new consistency

evaluation procedure is not mathematically equivalent with the standard method. For this reason, it is possible that the two methods do not yield exactly the same sequence of discrepant responses. However, a deviation between the two methods has only been observed in case marginally discrepant responses of a system that already complies with the chosen confidence criterion are identified. This situation arises rarely in practical applications, where one aims to include as much of the available information as possible and only identify and then possibly exclude blatantly discrepant data points.

Several neutron transport benchmarks of the International Handbook of Evaluated Criticality Safety Benchmark Experiments [19] are considered as applications. The benchmarks' parameters included individual cross sections for each material, nuclide, reaction type and energy-group, fission spectra, and average number of prompt neutrons emitted per fission, while the responses included the respective benchmarks' effective multiplication constants, various fission rate ratios and various radiative capture rate ratios. The deterministic neutron transport code Denovo developed at Oak Ridge National Laboratory (ORNL) is used for the numerical computations in the present work. Sensitivity coefficients, which are essential quantities for data assimilation, are computed via an adjoint sensitivity analysis tool that was added to the standard capabilities of Denovo in [14]. This customized sensitivity analysis tool provides energy-dependent sensitivity coefficients of the effective multiplication constant and spectral indices to all parameters in the system. Only the fission spectrum requires special treatment. This parameter follows a probability density function that must satisfy the normalization to unity. To guarantee that the best-estimate fission spectrum still satisfies this requirement to a high numerical precision, even if unconstrained sensitivity coefficients are used, the a priori variance-covariance information of the fission spectrum is renormalized.

The first reactor physics applications are the two plutonium spheres Jezebel-239 and Jezebel-240. Shared isotopes that occur in the composition of both benchmarks couple Jezebel-239 to Jezebel-240. Partitioned data assimilation was applied to each benchmark individually as well as to the two Jezebel benchmarks considered as a coupled system. The new method yielded in both cases calibrated response and parameter values with reduced calibrated uncertainties. The results obtained indicate that *similar* responses, which were measured in both benchmarks, are affected more by the joint data assimilation than *dissimilar* responses, which were measured in only a single benchmark. The reason for this is that *similar* responses display a stronger interdependence. More generally, the consideration of the complete information, including couplings, provided jointly by Jezebel-239 and Jezebel-240 leads to more accurate best-estimate values for responses and model parameters and also yields larger reductions in the best-estimate uncertainties that accompany the predicted mean values of responses and model parameters. As can be

expected from principles of information theory, the inclusion of more consistent information reduces the uncertainty in best-estimate responses and model parameters more.

The next benchmark is the uranium sphere called Godiva. The overall consistency indicator of this benchmark, which included seventeen selected responses, indicated the presence of substantially discrepant data. The new consistency evaluation procedure was used to identify two distinct sets of responses that comply with the central 90% significance range. The first set, which represents the first selection of responses that are consistent in terms of the chosen confidence range, includes eleven responses and the second set, which has a normalized consistency indicator closest to unity, includes only ten responses. Application of data assimilation to all three sets individually confirms all conclusions drawn for the heat conduction examples based on synthetic data: exclusion of the most discrepant responses dramatically improves the overall consistency and quality of the best-estimate results. As soon as those few, discrepant responses are excluded the further exclusion of a marginally discrepant response does not significantly affect best-estimate results. Since only a few considerably discrepant responses are excluded, the sequence identified of the new consistency evaluation procedure matches the sequence of the standard method perfectly. Finally, the Godiva is also calibrated jointly with Jezebel-239 and Jezebel-240. This demonstrates the ability of the partitioned data assimilation to not only easily reduce a system but also to efficiently combine coupled systems. Godiva is weakly coupled to the two Jezebel benchmarks via cross-correlations between the uncertainties of uranium and plutonium as well as *similar* responses.

The Zero Power Reactor 6 assembly 7 represents with over one hundred thousand parameters and twenty-five responses are large-scale application. A detailed as-built model of Loading 41 was created as input deck for two neutron transport codes. A comparison of the homogenized, cylindrical benchmark model to this as-built model with the Monte Carlo code MAVRIC, which is part of ORNL's SCALE6.1 code package, showed that the as-built model matches the experimentally measured value of the effective multiplication constant better, if the ENDF/B VII continuous energy library is used. The as-built model, which does without the simplifications and transformations that are included in the benchmark model, represents reality in more detail. The capabilities of Denovo as well as the availability of computer resources limited the simulations to a coarse energy-group structure and coarse spatial mesh. Nonetheless, the as-built model yielded computed reaction rate ratios that agreed better with the experimentally measured values than the benchmark model. Application of the partitioned data assimilation confirmed that the implementation can indeed handle large-scale data sets.

The present work presents some features of the partitioned data assimilation and demonstrates the applicability to coupled systems. The flexibility and plethora of information and results offered by this new methodology is expected to be fully utilized by multi-physics applications possibly larger than the reactor physics applications presented in this work. The partitioned data assimilation formulas take into account only first-order sensitivities and predict only mean values and covariances for the system responses and parameters. Although first-order sensitivities provided sufficient accuracy for the reactor physics benchmarks considered here, they may not suffice to ensure the needed accuracy when dealing with problems significantly more nonlinear than neutron transport. Ongoing research, therefore, aims at alleviating the methodology's current restrictions, and extending it to include higher-order sensitivities and distribution moments.

Also, the presented algorithm is limited by the usage of the scripting language MATLAB and a serial environment. With the promising results shown in the present work, a parallel implementation in a programming language like C++ or FORTRAN would be the next step to further prove the positive performance of the suggested algorithm.

Appendix

A Derivation of Eqs. (2.10) and (2.34)

To minimize the exponent of Eq. (2.31) under the constraint of the first order Taylor-series the following steps are necessary to obtain a useful form.

Non-partitioned DA based on [9]

$$\mathbf{r} = \mathbf{r}_c(\boldsymbol{\alpha}^0) + \mathbf{S}_{r\alpha}(\boldsymbol{\alpha}^0)(\boldsymbol{\alpha} - \boldsymbol{\alpha}^0)$$

$$0 = \mathbf{r}_c(\boldsymbol{\alpha}^0) + \mathbf{S}_{r\alpha}(\boldsymbol{\alpha}^0)(\boldsymbol{\alpha} - \boldsymbol{\alpha}^0) - \mathbf{r}$$

$$0 = \mathbf{r}_c(\boldsymbol{\alpha}^0) + \mathbf{S}_{r\alpha}(\boldsymbol{\alpha}^0)(\boldsymbol{\alpha} - \boldsymbol{\alpha}^0) - (\mathbf{r} - \mathbf{r}_m) - \mathbf{r}_m$$

$$0 = \mathbf{r}_c(\boldsymbol{\alpha}^0) + (\mathbf{S}_{r\alpha} \quad -\mathbf{I}) \begin{pmatrix} \boldsymbol{\alpha} - \boldsymbol{\alpha}^0 \\ \mathbf{r} - \mathbf{r}_m \end{pmatrix} - \mathbf{r}_m$$

$$0 = \mathbf{r}_c(\boldsymbol{\alpha}^0) + (\mathbf{S}_{r\alpha} \quad -\mathbf{I}) \mathbf{z} - \mathbf{r}_m$$

$$0 = (\mathbf{S}_{r\alpha} \quad -\mathbf{I}) \mathbf{z} + \mathbf{d}$$

$$0 = \mathbf{Z}(\boldsymbol{\alpha}^0) \mathbf{z} + \mathbf{d}$$

partitioned DA, [10]

$$\mathbf{r}_A = \mathbf{r}_{Ac}(\boldsymbol{\alpha}^0, \boldsymbol{\beta}^0) + \mathbf{S}(\boldsymbol{\alpha}^0, \boldsymbol{\beta}^0) \begin{pmatrix} \boldsymbol{\alpha} - \boldsymbol{\alpha}^0 \\ \boldsymbol{\beta} - \boldsymbol{\beta}^0 \end{pmatrix}$$

$$0 = \begin{pmatrix} \mathbf{r}_c(\boldsymbol{\alpha}^0) \\ \mathbf{q}_c(\boldsymbol{\beta}^0) \end{pmatrix} + \mathbf{S}(\boldsymbol{\alpha}^0, \boldsymbol{\beta}^0) \begin{pmatrix} \boldsymbol{\alpha} - \boldsymbol{\alpha}^0 \\ \boldsymbol{\beta} - \boldsymbol{\beta}^0 \end{pmatrix} - \begin{pmatrix} \mathbf{r} \\ \mathbf{q} \end{pmatrix}$$

$$0 = \begin{pmatrix} \mathbf{r}_c(\boldsymbol{\alpha}^0) \\ \mathbf{q}_c(\boldsymbol{\beta}^0) \end{pmatrix} + \mathbf{S}(\boldsymbol{\alpha}^0, \boldsymbol{\beta}^0) \begin{pmatrix} \boldsymbol{\alpha} - \boldsymbol{\alpha}^0 \\ \boldsymbol{\beta} - \boldsymbol{\beta}^0 \end{pmatrix} - \left(\begin{pmatrix} \mathbf{r} - \mathbf{r}_m \\ \mathbf{q} - \mathbf{q}_m \end{pmatrix} \right) - \begin{pmatrix} \mathbf{r}_m \\ \mathbf{q}_m \end{pmatrix}$$

$$0 = \begin{pmatrix} \mathbf{r}_c(\boldsymbol{\alpha}^0) \\ \mathbf{q}_c(\boldsymbol{\beta}^0) \end{pmatrix} + (\mathbf{S} \quad -\mathbf{I}) \begin{pmatrix} \boldsymbol{\alpha} - \boldsymbol{\alpha}^0 \\ \boldsymbol{\beta} - \boldsymbol{\beta}^0 \\ \mathbf{r} - \mathbf{r}_m \\ \mathbf{q} - \mathbf{q}_m \end{pmatrix} - \begin{pmatrix} \mathbf{r}_m \\ \mathbf{q}_m \end{pmatrix}$$

$$0 = \begin{pmatrix} \mathbf{r}_c(\boldsymbol{\alpha}^0) \\ \mathbf{q}_c(\boldsymbol{\beta}^0) \end{pmatrix} + (\mathbf{S} \quad -\mathbf{I}) \mathbf{z}_A - \begin{pmatrix} \mathbf{r}_m \\ \mathbf{q}_m \end{pmatrix}$$

$$0 = (\mathbf{S} \quad -\mathbf{I}) \mathbf{z}_A + \begin{pmatrix} \mathbf{r}^d \\ \mathbf{q}^d \end{pmatrix}$$

B Derivation of Optimal Predicted Values

A detailed solution of the constrained minimization problem expressed in Eq. (2.36) as presented in [10] follows.

The as of yet unknown blocks of the inverse of \mathbf{C} are denoted the following way:

$$\mathbf{C}^{-1} = \begin{pmatrix} \mathbf{C}_{\alpha\alpha} & \mathbf{C}_{\alpha\beta} & \mathbf{C}_{\alpha r} & \mathbf{C}_{\alpha q} \\ \mathbf{C}_{\beta\alpha} & \mathbf{C}_{\beta\beta} & \mathbf{C}_{\beta r} & \mathbf{C}_{\beta q} \\ \mathbf{C}_{r\alpha} & \mathbf{C}_{r\beta} & \mathbf{C}_{rr} & \mathbf{C}_{rq} \\ \mathbf{C}_{q\alpha} & \mathbf{C}_{q\beta} & \mathbf{C}_{qr} & \mathbf{C}_{qq} \end{pmatrix}^{-1} = \begin{pmatrix} \mathbf{X}_{11} & \mathbf{X}_{12} & \mathbf{X}_{13} & \mathbf{X}_{14} \\ \mathbf{X}_{12}^\dagger & \mathbf{X}_{22} & \mathbf{X}_{23} & \mathbf{X}_{24} \\ \mathbf{X}_{13}^\dagger & \mathbf{X}_{23}^\dagger & \mathbf{X}_{33} & \mathbf{X}_{34} \\ \mathbf{X}_{14}^\dagger & \mathbf{X}_{24}^\dagger & \mathbf{X}_{34}^\dagger & \mathbf{X}_{44} \end{pmatrix} \quad (\text{B.1})$$

Inserting this into the constrained minimization problem results in

$$\begin{aligned} P(\mathbf{z}, \boldsymbol{\lambda}) = & (\boldsymbol{\alpha} - \boldsymbol{\alpha}^0, \boldsymbol{\beta} - \boldsymbol{\beta}^0, \mathbf{r} - \mathbf{r}^m, \mathbf{q} - \mathbf{q}^m) \begin{pmatrix} \mathbf{X}_{11} & \mathbf{X}_{12} & \mathbf{X}_{13} & \mathbf{X}_{14} \\ \mathbf{X}_{12}^\dagger & \mathbf{X}_{22} & \mathbf{X}_{23} & \mathbf{X}_{24} \\ \mathbf{X}_{13}^\dagger & \mathbf{X}_{23}^\dagger & \mathbf{X}_{33} & \mathbf{X}_{34} \\ \mathbf{X}_{14}^\dagger & \mathbf{X}_{24}^\dagger & \mathbf{X}_{34}^\dagger & \mathbf{X}_{44} \end{pmatrix} \begin{pmatrix} \boldsymbol{\alpha} - \boldsymbol{\alpha}^0 \\ \boldsymbol{\beta} - \boldsymbol{\beta}^0 \\ \mathbf{r} - \mathbf{r}^m \\ \mathbf{q} - \mathbf{q}^m \end{pmatrix} \\ & + \boldsymbol{\lambda}_r^\dagger (\mathbf{r} - \mathbf{r}^c(\boldsymbol{\alpha}, \boldsymbol{\beta})) + \boldsymbol{\lambda}_q^\dagger (\mathbf{q} - \mathbf{q}^c(\boldsymbol{\alpha}, \boldsymbol{\beta})). \end{aligned} \quad (\text{B.2})$$

Next, performing the matrix product leads to

$$\begin{aligned} P(\boldsymbol{\alpha}, \boldsymbol{\beta}, \mathbf{r}, \mathbf{q}, \boldsymbol{\lambda}) = & -\frac{1}{2}(\boldsymbol{\alpha} - \boldsymbol{\alpha}^0)^\dagger [\mathbf{X}_{11}(\boldsymbol{\alpha} - \boldsymbol{\alpha}^0) + \mathbf{X}_{12}(\boldsymbol{\beta} - \boldsymbol{\beta}^0) + \mathbf{X}_{13}(\mathbf{r} - \mathbf{r}^m) + \mathbf{X}_{14}(\mathbf{q} - \mathbf{q}^m)] + \\ & -\frac{1}{2}(\boldsymbol{\beta} - \boldsymbol{\beta}^0)^\dagger [\mathbf{X}_{12}^\dagger(\boldsymbol{\alpha} - \boldsymbol{\alpha}^0) + \mathbf{X}_{22}(\boldsymbol{\beta} - \boldsymbol{\beta}^0) + \mathbf{X}_{23}(\mathbf{r} - \mathbf{r}^m) + \mathbf{X}_{24}(\mathbf{q} - \mathbf{q}^m)] + \\ & -\frac{1}{2}(\mathbf{r} - \mathbf{r}^m)^\dagger [\mathbf{X}_{13}^\dagger(\boldsymbol{\alpha} - \boldsymbol{\alpha}^0) + \mathbf{X}_{23}^\dagger(\boldsymbol{\beta} - \boldsymbol{\beta}^0) + \mathbf{X}_{33}(\mathbf{r} - \mathbf{r}^m) + \mathbf{X}_{34}(\mathbf{q} - \mathbf{q}^m)] + \\ & -\frac{1}{2}(\mathbf{q} - \mathbf{q}^m)^\dagger [\mathbf{X}_{14}^\dagger(\boldsymbol{\alpha} - \boldsymbol{\alpha}^0) + \mathbf{X}_{24}^\dagger(\boldsymbol{\beta} - \boldsymbol{\beta}^0) + \mathbf{X}_{34}^\dagger(\mathbf{r} - \mathbf{r}^m) + \mathbf{X}_{44}(\mathbf{q} - \mathbf{q}^m)] + \\ & \boldsymbol{\lambda}_r^\dagger [\mathbf{r} - \mathbf{r}^c(\boldsymbol{\alpha}, \boldsymbol{\beta})] + \boldsymbol{\lambda}_q^\dagger [\mathbf{q} - \mathbf{q}^c(\boldsymbol{\alpha}, \boldsymbol{\beta})]. \end{aligned} \quad (\text{B.3})$$

From this equation all the partial derivatives with respect to the dependent variables can be easily found.

$$\begin{aligned}
 \nabla_{\alpha} \mathbf{P} &= -\mathbf{X}_{11}(\boldsymbol{\alpha} - \boldsymbol{\alpha}^0) - \frac{1}{2} \mathbf{X}_{12}(\boldsymbol{\beta} - \boldsymbol{\beta}^0) - \frac{1}{2} \mathbf{X}_{13}(\mathbf{r} - \mathbf{r}^m) - \frac{1}{2} \mathbf{X}_{14}(\mathbf{q} - \mathbf{q}^m) \\
 &\quad - \frac{1}{2}(\boldsymbol{\beta} - \boldsymbol{\beta}^0)^{\dagger} \mathbf{X}_{12}^{\dagger} - \frac{1}{2}(\mathbf{r} - \mathbf{r}^m)^{\dagger} \mathbf{X}_{13}^{\dagger} - \frac{1}{2}(\mathbf{q} - \mathbf{q}^m)^{\dagger} \mathbf{X}_{14}^{\dagger} - \mathbf{S}_{r\alpha}^{\dagger} \boldsymbol{\lambda}_r - \mathbf{S}_{q\alpha}^{\dagger} \boldsymbol{\lambda}_q \\
 &= -\mathbf{X}_{11}(\boldsymbol{\alpha} - \boldsymbol{\alpha}^0) - \mathbf{X}_{12}(\boldsymbol{\beta} - \boldsymbol{\beta}^0) - \mathbf{X}_{13}(\mathbf{r} - \mathbf{r}^m) - \mathbf{X}_{14}(\mathbf{q} - \mathbf{q}^m) - \mathbf{S}_{r\alpha}^{\dagger} \boldsymbol{\lambda}_r - \mathbf{S}_{q\alpha}^{\dagger} \boldsymbol{\lambda}_q
 \end{aligned} \tag{B.4}$$

$$\begin{aligned}
 \nabla_{\beta} \mathbf{P} &= -\frac{1}{2}(\boldsymbol{\alpha} - \boldsymbol{\alpha}^0)^{\dagger} \mathbf{X}_{12} - \frac{1}{2} \mathbf{X}_{12}^{\dagger}(\boldsymbol{\alpha} - \boldsymbol{\alpha}^0) - \mathbf{X}_{22}(\boldsymbol{\beta} - \boldsymbol{\beta}^0) - \frac{1}{2} \mathbf{X}_{23}(\mathbf{r} - \mathbf{r}^m) \\
 &\quad - \frac{1}{2} \mathbf{X}_{24}(\mathbf{q} - \mathbf{q}^m) - \frac{1}{2} \mathbf{X}_{23}(\mathbf{r} - \mathbf{r}^m) - \frac{1}{2} \mathbf{X}_{24}(\mathbf{q} - \mathbf{q}^m) - \mathbf{S}_{r\beta}^{\dagger} \boldsymbol{\lambda}_r - \mathbf{S}_{q\beta}^{\dagger} \boldsymbol{\lambda}_q \\
 &= -\mathbf{X}_{12}^{\dagger}(\boldsymbol{\alpha} - \boldsymbol{\alpha}^0) - \mathbf{X}_{22}(\boldsymbol{\beta} - \boldsymbol{\beta}^0) - \mathbf{X}_{23}(\mathbf{r} - \mathbf{r}^m) - \mathbf{X}_{24}(\mathbf{q} - \mathbf{q}^m) - \mathbf{S}_{r\beta}^{\dagger} \boldsymbol{\lambda}_r - \mathbf{S}_{q\beta}^{\dagger} \boldsymbol{\lambda}_q
 \end{aligned} \tag{B.5}$$

$$\begin{aligned}
 \nabla_r \mathbf{P} &= -\frac{1}{2} \mathbf{X}_{13}^{\dagger}(\boldsymbol{\alpha} - \boldsymbol{\alpha}^0) - \frac{1}{2} \mathbf{X}_{23}^{\dagger}(\boldsymbol{\beta} - \boldsymbol{\beta}^0) - \frac{1}{2} \mathbf{X}_{13}^{\dagger}(\boldsymbol{\alpha} - \boldsymbol{\alpha}^0) - \frac{1}{2} \mathbf{X}_{23}^{\dagger}(\boldsymbol{\beta} - \boldsymbol{\beta}^0) \\
 &\quad - \mathbf{X}_{33}(\mathbf{r} - \mathbf{r}^m) - \frac{1}{2} \mathbf{X}_{34}(\mathbf{q} - \mathbf{q}^m) - \frac{1}{2} \mathbf{X}_{34}(\mathbf{q} - \mathbf{q}^m) + \boldsymbol{\lambda}_r \\
 &= -\mathbf{X}_{13}^{\dagger}(\boldsymbol{\alpha} - \boldsymbol{\alpha}^0) - \mathbf{X}_{23}^{\dagger}(\boldsymbol{\beta} - \boldsymbol{\beta}^0) - \mathbf{X}_{33}(\mathbf{r} - \mathbf{r}^m) - \mathbf{X}_{34}(\mathbf{q} - \mathbf{q}^m) + \boldsymbol{\lambda}_r
 \end{aligned} \tag{B.6}$$

$$\begin{aligned}
 \nabla_q \mathbf{P} &= -\frac{1}{2} \mathbf{X}_{14}^{\dagger}(\boldsymbol{\alpha} - \boldsymbol{\alpha}^0) - \frac{1}{2} \mathbf{X}_{24}^{\dagger}(\boldsymbol{\beta} - \boldsymbol{\beta}^0) - \frac{1}{2} \mathbf{X}_{34}^{\dagger}(\mathbf{r} - \mathbf{r}^m) - \frac{1}{2} \mathbf{X}_{14}^{\dagger}(\boldsymbol{\alpha} - \boldsymbol{\alpha}^0) \\
 &\quad - \frac{1}{2} \mathbf{X}_{24}^{\dagger}(\boldsymbol{\beta} - \boldsymbol{\beta}^0) - \frac{1}{2} \mathbf{X}_{34}^{\dagger}(\mathbf{r} - \mathbf{r}^m) - \mathbf{X}_{44}(\mathbf{q} - \mathbf{q}^m) + \boldsymbol{\lambda}_q \\
 &= -\mathbf{X}_{14}^{\dagger}(\boldsymbol{\alpha} - \boldsymbol{\alpha}^0) - \mathbf{X}_{24}^{\dagger}(\boldsymbol{\beta} - \boldsymbol{\beta}^0) - \mathbf{X}_{34}^{\dagger}(\mathbf{r} - \mathbf{r}^m) - \mathbf{X}_{44}(\mathbf{q} - \mathbf{q}^m) + \boldsymbol{\lambda}_q
 \end{aligned} \tag{B.7}$$

The partial derivatives with respect to the Lagrange multipliers simply return the imposed minimization constraints $\nabla_{\lambda_r} \mathbf{P} = \mathbf{r} - \mathbf{r}^c(\boldsymbol{\alpha}, \boldsymbol{\beta}) = 0$; $\nabla_{\lambda_q} \mathbf{P} = \mathbf{q} - \mathbf{q}^c(\boldsymbol{\alpha}, \boldsymbol{\beta}) = 0$.

At the minimum, i.e. $\nabla_{\xi} \mathbf{P} = 0$ for $\xi = \{\alpha, \beta, r, q\}$, the variables reach their optimal value. In matrix-form this results in the following equations

$$\underbrace{\begin{pmatrix} \mathbf{X}_{11} & \mathbf{X}_{12} & \mathbf{X}_{13} & \mathbf{X}_{14} \\ \mathbf{X}_{12}^{\dagger} & \mathbf{X}_{22} & \mathbf{X}_{23} & \mathbf{X}_{24} \\ \mathbf{X}_{13}^{\dagger} & \mathbf{X}_{23}^{\dagger} & \mathbf{X}_{33} & \mathbf{X}_{34} \\ \mathbf{X}_{14}^{\dagger} & \mathbf{X}_{23}^{\dagger} & \mathbf{X}_{34}^{\dagger} & \mathbf{X}_{44} \end{pmatrix}}_{\mathbf{C}^{-1}} \begin{pmatrix} \boldsymbol{\alpha}^{opt} - \boldsymbol{\alpha}^0 \\ \boldsymbol{\beta}^{opt} - \boldsymbol{\beta}^0 \\ \mathbf{r}^{opt} - \mathbf{r}^m \\ \mathbf{q}^{opt} - \mathbf{q}^m \end{pmatrix} + \begin{pmatrix} -\mathbf{S}_{r\alpha}^{\dagger} \boldsymbol{\lambda}_r - \mathbf{S}_{q\alpha}^{\dagger} \boldsymbol{\lambda}_q \\ -\mathbf{S}_{r\beta}^{\dagger} \boldsymbol{\lambda}_r - \mathbf{S}_{q\beta}^{\dagger} \boldsymbol{\lambda}_q \\ \boldsymbol{\lambda}_r \\ \boldsymbol{\lambda}_q \end{pmatrix} = \begin{pmatrix} 0 \\ 0 \\ 0 \\ 0 \end{pmatrix}. \tag{B.8}$$

Rewriting Eq. (B.8) to isolate the optimal parameters yields

$$\begin{aligned}
 \begin{pmatrix} \boldsymbol{\alpha}^{opt} - \boldsymbol{\alpha}^0 \\ \boldsymbol{\beta}^{opt} - \boldsymbol{\beta}^0 \\ \mathbf{r}^{opt} - \mathbf{r}^m \\ \mathbf{q}^{opt} - \mathbf{q}^m \end{pmatrix} &= \mathbf{C} \begin{pmatrix} -\mathbf{S}_{r\alpha}^\dagger \boldsymbol{\lambda}_r - \mathbf{S}_{q\alpha}^\dagger \boldsymbol{\lambda}_q \\ -\mathbf{S}_{r\beta}^\dagger \boldsymbol{\lambda}_r - \mathbf{S}_{q\beta}^\dagger \boldsymbol{\lambda}_q \\ \boldsymbol{\lambda}_r \\ \boldsymbol{\lambda}_q \end{pmatrix} \\
 &= \begin{pmatrix} \mathbf{C}_{\alpha\alpha} & \mathbf{C}_{\alpha\beta} & \mathbf{C}_{\alpha r} & \mathbf{C}_{\alpha q} \\ \mathbf{C}_{\alpha\beta}^\dagger & \mathbf{C}_{\beta\beta} & \mathbf{C}_{\beta r} & \mathbf{C}_{\beta q} \\ \mathbf{C}_{\alpha r}^\dagger & \mathbf{C}_{\beta r}^\dagger & \mathbf{C}_{rr} & \mathbf{C}_{rq} \\ \mathbf{C}_{\alpha q}^\dagger & \mathbf{C}_{\beta q}^\dagger & \mathbf{C}_{rq}^\dagger & \mathbf{C}_{qq} \end{pmatrix} \begin{pmatrix} -\mathbf{S}_{r\alpha}^\dagger \boldsymbol{\lambda}_r - \mathbf{S}_{q\alpha}^\dagger \boldsymbol{\lambda}_q \\ -\mathbf{S}_{r\beta}^\dagger \boldsymbol{\lambda}_r - \mathbf{S}_{q\beta}^\dagger \boldsymbol{\lambda}_q \\ \boldsymbol{\lambda}_r \\ \boldsymbol{\lambda}_q \end{pmatrix}.
 \end{aligned} \tag{B.9}$$

Explicitly written for each component, Eq. (B.9) is then

$$(\boldsymbol{\alpha}^{opt} - \boldsymbol{\alpha}^0) = -\mathbf{C}_{\alpha\alpha} (\mathbf{S}_{r\alpha}^\dagger \boldsymbol{\lambda}_r + \mathbf{S}_{q\alpha}^\dagger \boldsymbol{\lambda}_q) - \mathbf{C}_{\alpha\beta} (\mathbf{S}_{r\beta}^\dagger \boldsymbol{\lambda}_r + \mathbf{S}_{q\beta}^\dagger \boldsymbol{\lambda}_q) + \mathbf{C}_{\alpha r} \boldsymbol{\lambda}_r + \mathbf{C}_{\alpha q} \boldsymbol{\lambda}_q \tag{B.10}$$

$$(\boldsymbol{\beta}^{opt} - \boldsymbol{\beta}^0) = -\mathbf{C}_{\alpha\beta}^\dagger (\mathbf{S}_{r\alpha}^\dagger \boldsymbol{\lambda}_r + \mathbf{S}_{q\alpha}^\dagger \boldsymbol{\lambda}_q) - \mathbf{C}_{\beta\beta} (\mathbf{S}_{r\beta}^\dagger \boldsymbol{\lambda}_r + \mathbf{S}_{q\beta}^\dagger \boldsymbol{\lambda}_q) + \mathbf{C}_{\beta r} \boldsymbol{\lambda}_r + \mathbf{C}_{\beta q} \boldsymbol{\lambda}_q \tag{B.11}$$

$$(\mathbf{r}^{opt} - \mathbf{r}^0) = -\mathbf{C}_{\alpha r}^\dagger (\mathbf{S}_{r\alpha}^\dagger \boldsymbol{\lambda}_r + \mathbf{S}_{q\alpha}^\dagger \boldsymbol{\lambda}_q) - \mathbf{C}_{\beta r}^\dagger (\mathbf{S}_{r\beta}^\dagger \boldsymbol{\lambda}_r + \mathbf{S}_{q\beta}^\dagger \boldsymbol{\lambda}_q) + \mathbf{C}_{rr} \boldsymbol{\lambda}_r + \mathbf{C}_{rq} \boldsymbol{\lambda}_q \tag{B.12}$$

$$(\mathbf{q}^{opt} - \mathbf{q}^0) = -\mathbf{C}_{\alpha q}^\dagger (\mathbf{S}_{r\alpha}^\dagger \boldsymbol{\lambda}_r + \mathbf{S}_{q\alpha}^\dagger \boldsymbol{\lambda}_q) - \mathbf{C}_{\beta q}^\dagger (\mathbf{S}_{r\beta}^\dagger \boldsymbol{\lambda}_r + \mathbf{S}_{q\beta}^\dagger \boldsymbol{\lambda}_q) + \mathbf{C}_{rq} \boldsymbol{\lambda}_r + \mathbf{C}_{qq} \boldsymbol{\lambda}_q \tag{B.13}$$

The goal is now to solve this set of equations for the Lagrange multipliers, thus all terms are sorted towards this end.

$$(\boldsymbol{\alpha}^{opt} - \boldsymbol{\alpha}^0) = (-\mathbf{C}_{\alpha\alpha} \mathbf{S}_{r\alpha}^\dagger - \mathbf{C}_{\alpha\beta} \mathbf{S}_{r\beta}^\dagger + \mathbf{C}_{\alpha r}) \boldsymbol{\lambda}_r + (-\mathbf{C}_{\alpha\alpha} \mathbf{S}_{q\alpha}^\dagger - \mathbf{C}_{\alpha\beta} \mathbf{S}_{q\beta}^\dagger + \mathbf{C}_{\alpha q}) \boldsymbol{\lambda}_q \tag{B.14}$$

$$(\boldsymbol{\beta}^{opt} - \boldsymbol{\beta}^0) = (-\mathbf{C}_{\alpha\beta}^\dagger \mathbf{S}_{r\alpha}^\dagger - \mathbf{C}_{\beta\beta} \mathbf{S}_{r\beta}^\dagger + \mathbf{C}_{\beta r}) \boldsymbol{\lambda}_r + (-\mathbf{C}_{\alpha\beta}^\dagger \mathbf{S}_{q\alpha}^\dagger - \mathbf{C}_{\beta\beta} \mathbf{S}_{q\beta}^\dagger + \mathbf{C}_{\beta q}) \boldsymbol{\lambda}_q \tag{B.15}$$

$$(\mathbf{r}^{opt} - \mathbf{r}^0) = (-\mathbf{C}_{\alpha r}^\dagger \mathbf{S}_{r\alpha}^\dagger - \mathbf{C}_{\beta r}^\dagger \mathbf{S}_{r\beta}^\dagger + \mathbf{C}_{rr}) \boldsymbol{\lambda}_r + (-\mathbf{C}_{\alpha r}^\dagger \mathbf{S}_{q\alpha}^\dagger - \mathbf{C}_{\beta r}^\dagger \mathbf{S}_{q\beta}^\dagger + \mathbf{C}_{rq}) \boldsymbol{\lambda}_q \tag{B.16}$$

$$(\mathbf{q}^{opt} - \mathbf{q}^0) = (-\mathbf{C}_{\alpha q}^\dagger \mathbf{S}_{r\alpha}^\dagger - \mathbf{C}_{\beta q}^\dagger \mathbf{S}_{r\beta}^\dagger + \mathbf{C}_{rq}) \boldsymbol{\lambda}_r + (-\mathbf{C}_{\alpha q}^\dagger \mathbf{S}_{q\alpha}^\dagger - \mathbf{C}_{\beta q}^\dagger \mathbf{S}_{q\beta}^\dagger + \mathbf{C}_{qq}) \boldsymbol{\lambda}_q \tag{B.17}$$

Since there are 6 unknown vectors $(\boldsymbol{\alpha}, \boldsymbol{\beta}, \mathbf{r}, \mathbf{q}, \boldsymbol{\lambda}_r, \boldsymbol{\lambda}_q)$, the two equations from the model – assuming a first-order Taylor-series expansion – are needed as well as the four equations above.

$$\begin{aligned}
 \mathbf{r}^{opt} &= \mathbf{r}^c(\boldsymbol{\alpha}^0, \boldsymbol{\beta}^0) + \mathbf{S}_{r\alpha} (\boldsymbol{\alpha}^{opt} - \boldsymbol{\alpha}^0) + \mathbf{S}_{r\beta} (\boldsymbol{\beta}^{opt} - \boldsymbol{\beta}^0) \\
 &\text{or} \\
 \mathbf{r}^{opt} - \mathbf{r}^c(\boldsymbol{\alpha}^0, \boldsymbol{\beta}^0) &= \mathbf{S}_{r\alpha} (\boldsymbol{\alpha}^{opt} - \boldsymbol{\alpha}^0) + \mathbf{S}_{r\beta} (\boldsymbol{\beta}^{opt} - \boldsymbol{\beta}^0)
 \end{aligned} \tag{B.18}$$

$$\begin{aligned}
 \mathbf{q}^{opt} &= \mathbf{q}^c(\boldsymbol{\alpha}^0, \boldsymbol{\beta}^0) + \mathbf{S}_{q\alpha}(\boldsymbol{\alpha}^{opt} - \boldsymbol{\alpha}^0) + \mathbf{S}_{q\beta}(\boldsymbol{\beta}^{opt} - \boldsymbol{\beta}^0) \\
 &\text{or} \\
 \mathbf{q}^{opt} - \mathbf{q}^c(\boldsymbol{\alpha}^0, \boldsymbol{\beta}^0) &= \mathbf{S}_{q\alpha}(\boldsymbol{\alpha}^{opt} - \boldsymbol{\alpha}^0) + \mathbf{S}_{q\beta}(\boldsymbol{\beta}^{opt} - \boldsymbol{\beta}^0)
 \end{aligned} \tag{B.19}$$

Eqs. (B.18) and (B.19) are used to eliminate \mathbf{r} and \mathbf{q} in the equations (B.14 – B.17) to obtain a 4x4 system in the variables $(\boldsymbol{\alpha}, \boldsymbol{\beta}, \boldsymbol{\lambda}_r, \boldsymbol{\lambda}_q)$

$$\begin{aligned}
 (\boldsymbol{\alpha}^{opt} - \boldsymbol{\alpha}^0) &= (-\mathbf{C}_{\alpha\alpha}\mathbf{S}_{r\alpha}^\dagger - \mathbf{C}_{\alpha\beta}\mathbf{S}_{r\beta}^\dagger + \mathbf{C}_{\alpha r})\boldsymbol{\lambda}_r + (-\mathbf{C}_{\alpha\alpha}\mathbf{S}_{q\alpha}^\dagger - \mathbf{C}_{\alpha\beta}\mathbf{S}_{q\beta}^\dagger + \mathbf{C}_{\alpha q})\boldsymbol{\lambda}_q \\
 (\boldsymbol{\beta}^{opt} - \boldsymbol{\beta}^0) &= (-\mathbf{C}_{\alpha\beta}^\dagger\mathbf{S}_{r\alpha}^\dagger - \mathbf{C}_{\beta\beta}\mathbf{S}_{r\beta}^\dagger + \mathbf{C}_{\beta r})\boldsymbol{\lambda}_r + (-\mathbf{C}_{\alpha\beta}^\dagger\mathbf{S}_{q\alpha}^\dagger - \mathbf{C}_{\beta\beta}\mathbf{S}_{q\beta}^\dagger + \mathbf{C}_{\beta q})\boldsymbol{\lambda}_q \\
 (\mathbf{r}^c - \mathbf{r}^m) &= -\mathbf{S}_{r\alpha}(\boldsymbol{\alpha}^{opt} - \boldsymbol{\alpha}^0) - \mathbf{S}_{r\beta}(\boldsymbol{\beta}^{opt} - \boldsymbol{\beta}^0) + (-\mathbf{C}_{\alpha r}^\dagger\mathbf{S}_{r\alpha}^\dagger - \mathbf{C}_{\beta r}^\dagger\mathbf{S}_{r\beta}^\dagger + \mathbf{C}_{rr})\boldsymbol{\lambda}_r + (-\mathbf{C}_{\alpha r}^\dagger\mathbf{S}_{q\alpha}^\dagger - \mathbf{C}_{\beta r}^\dagger\mathbf{S}_{q\beta}^\dagger + \mathbf{C}_{rq})\boldsymbol{\lambda}_q \\
 (\mathbf{q}^c - \mathbf{q}^m) &= -\mathbf{S}_{q\alpha}(\boldsymbol{\alpha}^{opt} - \boldsymbol{\alpha}^0) - \mathbf{S}_{q\beta}(\boldsymbol{\beta}^{opt} - \boldsymbol{\beta}^0) + (-\mathbf{C}_{\alpha q}^\dagger\mathbf{S}_{r\alpha}^\dagger - \mathbf{C}_{\beta q}^\dagger\mathbf{S}_{r\beta}^\dagger + \mathbf{C}_{rq})\boldsymbol{\lambda}_r + (-\mathbf{C}_{\alpha q}^\dagger\mathbf{S}_{q\alpha}^\dagger - \mathbf{C}_{\beta q}^\dagger\mathbf{S}_{q\beta}^\dagger + \mathbf{C}_{qq})\boldsymbol{\lambda}_q
 \end{aligned}$$

The next step is to replace $(\boldsymbol{\alpha}^{opt} - \boldsymbol{\alpha}^0)$ and $(\boldsymbol{\beta}^{opt} - \boldsymbol{\beta}^0)$ to reduce this to a 2x2 system in the variables $(\boldsymbol{\lambda}_r, \boldsymbol{\lambda}_q)$ only

$$\begin{aligned}
 (\mathbf{r}^c - \mathbf{r}^m) &= -\mathbf{S}_{r\alpha} \left[(-\mathbf{C}_{\alpha\alpha}\mathbf{S}_{r\alpha}^\dagger - \mathbf{C}_{\alpha\beta}\mathbf{S}_{r\beta}^\dagger + \mathbf{C}_{\alpha r})\boldsymbol{\lambda}_r + (-\mathbf{C}_{\alpha\alpha}\mathbf{S}_{q\alpha}^\dagger - \mathbf{C}_{\alpha\beta}\mathbf{S}_{q\beta}^\dagger + \mathbf{C}_{\alpha q})\boldsymbol{\lambda}_q \right] \\
 &\quad - \mathbf{S}_{r\beta} \left[(-\mathbf{C}_{\alpha\beta}^\dagger\mathbf{S}_{r\alpha}^\dagger - \mathbf{C}_{\beta\beta}\mathbf{S}_{r\beta}^\dagger + \mathbf{C}_{\beta r})\boldsymbol{\lambda}_r + (-\mathbf{C}_{\alpha\beta}^\dagger\mathbf{S}_{q\alpha}^\dagger - \mathbf{C}_{\beta\beta}\mathbf{S}_{q\beta}^\dagger + \mathbf{C}_{\beta q})\boldsymbol{\lambda}_q \right] \\
 &\quad + (-\mathbf{C}_{\alpha r}^\dagger\mathbf{S}_{r\alpha}^\dagger - \mathbf{C}_{\beta r}^\dagger\mathbf{S}_{r\beta}^\dagger + \mathbf{C}_{rr})\boldsymbol{\lambda}_r + (-\mathbf{C}_{\alpha r}^\dagger\mathbf{S}_{q\alpha}^\dagger - \mathbf{C}_{\beta r}^\dagger\mathbf{S}_{q\beta}^\dagger + \mathbf{C}_{rq})\boldsymbol{\lambda}_q
 \end{aligned} \tag{B.20}$$

$$\begin{aligned}
 (\mathbf{q}^c - \mathbf{q}^m) &= -\mathbf{S}_{q\alpha} \left[(-\mathbf{C}_{\alpha\alpha}\mathbf{S}_{r\alpha}^\dagger - \mathbf{C}_{\alpha\beta}\mathbf{S}_{r\beta}^\dagger + \mathbf{C}_{\alpha r})\boldsymbol{\lambda}_r + (-\mathbf{C}_{\alpha\alpha}\mathbf{S}_{q\alpha}^\dagger - \mathbf{C}_{\alpha\beta}\mathbf{S}_{q\beta}^\dagger + \mathbf{C}_{\alpha q})\boldsymbol{\lambda}_q \right] \\
 &\quad - \mathbf{S}_{q\beta} \left[(-\mathbf{C}_{\alpha\beta}^\dagger\mathbf{S}_{r\alpha}^\dagger - \mathbf{C}_{\beta\beta}\mathbf{S}_{r\beta}^\dagger + \mathbf{C}_{\beta r})\boldsymbol{\lambda}_r + (-\mathbf{C}_{\alpha\beta}^\dagger\mathbf{S}_{q\alpha}^\dagger - \mathbf{C}_{\beta\beta}\mathbf{S}_{q\beta}^\dagger + \mathbf{C}_{\beta q})\boldsymbol{\lambda}_q \right] \\
 &\quad + (-\mathbf{C}_{\alpha q}^\dagger\mathbf{S}_{r\alpha}^\dagger - \mathbf{C}_{\beta q}^\dagger\mathbf{S}_{r\beta}^\dagger + \mathbf{C}_{rq})\boldsymbol{\lambda}_r + (-\mathbf{C}_{\alpha q}^\dagger\mathbf{S}_{q\alpha}^\dagger - \mathbf{C}_{\beta q}^\dagger\mathbf{S}_{q\beta}^\dagger + \mathbf{C}_{qq})\boldsymbol{\lambda}_q
 \end{aligned} \tag{B.21}$$

Again, in block matrix form, equations (B.20) and (B.21) can be written as

$$\begin{pmatrix} \mathbf{r}^c - \mathbf{r}^m \\ \mathbf{q}^c - \mathbf{q}^m \end{pmatrix} = \begin{pmatrix} \mathbf{D}_{rr} & \mathbf{D}_{rq} \\ \mathbf{D}_{qr} & \mathbf{D}_{qq} \end{pmatrix} \begin{pmatrix} \boldsymbol{\lambda}_r \\ \boldsymbol{\lambda}_q \end{pmatrix} \tag{B.22}$$

The individual blocks are defined as

$$\begin{aligned}
 \mathbf{D}_{rr} &= \\
 &\mathbf{S}_{r\alpha} (\mathbf{C}_{\alpha\alpha}\mathbf{S}_{r\alpha}^\dagger + \mathbf{C}_{\alpha\beta}\mathbf{S}_{r\beta}^\dagger - \mathbf{C}_{\alpha r}) + \mathbf{S}_{r\beta} (\mathbf{C}_{\alpha\beta}^\dagger\mathbf{S}_{r\alpha}^\dagger + \mathbf{C}_{\beta\beta}\mathbf{S}_{r\beta}^\dagger - \mathbf{C}_{\beta r}) - \mathbf{C}_{\alpha r}^\dagger\mathbf{S}_{r\alpha}^\dagger - \mathbf{C}_{\beta r}^\dagger\mathbf{S}_{r\beta}^\dagger + \mathbf{C}_{rr}
 \end{aligned} \tag{B.23}$$

$$\mathbf{D}_{rq} = \mathbf{S}_{r\alpha} \left(\mathbf{C}_{\alpha\alpha} \mathbf{S}_{q\alpha}^\dagger + \mathbf{C}_{\alpha\beta} \mathbf{S}_{q\beta}^\dagger - \mathbf{C}_{\alpha q} \right) + \mathbf{S}_{r\beta} \left(\mathbf{C}_{\alpha\beta}^\dagger \mathbf{S}_{q\alpha}^\dagger + \mathbf{C}_{\beta\beta} \mathbf{S}_{q\beta}^\dagger - \mathbf{C}_{\beta q} \right) - \mathbf{C}_{\alpha r}^\dagger \mathbf{S}_{q\alpha}^\dagger - \mathbf{C}_{\beta r}^\dagger \mathbf{S}_{q\beta}^\dagger + \mathbf{C}_{rq} \quad (\text{B.24})$$

$$\begin{aligned} \mathbf{D}_{qr} &= \mathbf{S}_{q\alpha} \left(\mathbf{C}_{\alpha\alpha} \mathbf{S}_{r\alpha}^\dagger + \mathbf{C}_{\alpha\beta} \mathbf{S}_{r\beta}^\dagger - \mathbf{C}_{\alpha r} \right) + \mathbf{S}_{q\beta} \left(\mathbf{C}_{\alpha\beta}^\dagger \mathbf{S}_{r\alpha}^\dagger + \mathbf{C}_{\beta\beta} \mathbf{S}_{r\beta}^\dagger - \mathbf{C}_{\beta r} \right) - \mathbf{C}_{\alpha q}^\dagger \mathbf{S}_{r\alpha}^\dagger - \mathbf{C}_{\beta q}^\dagger \mathbf{S}_{r\beta}^\dagger + \mathbf{C}_{rq}^\dagger \\ &= \mathbf{D}_{rq}^\dagger \end{aligned} \quad (\text{B.25})$$

$$\mathbf{D}_{qq} = \mathbf{S}_{q\alpha} \left(\mathbf{C}_{\alpha\alpha} \mathbf{S}_{q\alpha}^\dagger + \mathbf{C}_{\alpha\beta} \mathbf{S}_{q\beta}^\dagger - \mathbf{C}_{\alpha q} \right) + \mathbf{S}_{q\beta} \left(\mathbf{C}_{\alpha\beta}^\dagger \mathbf{S}_{q\alpha}^\dagger + \mathbf{C}_{\beta\beta} \mathbf{S}_{q\beta}^\dagger - \mathbf{C}_{\beta q} \right) - \mathbf{C}_{\alpha q}^\dagger \mathbf{S}_{q\alpha}^\dagger - \mathbf{C}_{\beta q}^\dagger \mathbf{S}_{q\beta}^\dagger + \mathbf{C}_{qq} \quad (\text{B.26})$$

The symmetry of the particular block in Eq. (B.25) can readily be shown

$$\begin{aligned} (\mathbf{D}_{rq})^\dagger &= \left[\mathbf{S}_{r\alpha} \left(\mathbf{C}_{\alpha\alpha} \mathbf{S}_{q\alpha}^\dagger + \mathbf{C}_{\alpha\beta} \mathbf{S}_{q\beta}^\dagger - \mathbf{C}_{\alpha q} \right) + \mathbf{S}_{r\beta} \left(\mathbf{C}_{\alpha\beta}^\dagger \mathbf{S}_{q\alpha}^\dagger + \mathbf{C}_{\beta\beta} \mathbf{S}_{q\beta}^\dagger - \mathbf{C}_{\beta q} \right) - \mathbf{C}_{\alpha r}^\dagger \mathbf{S}_{q\alpha}^\dagger - \mathbf{C}_{\beta r}^\dagger \mathbf{S}_{q\beta}^\dagger + \mathbf{C}_{rq} \right]^\dagger \\ &= \left(\mathbf{C}_{\alpha\alpha} \mathbf{S}_{q\alpha}^\dagger + \mathbf{C}_{\alpha\beta} \mathbf{S}_{q\beta}^\dagger - \mathbf{C}_{\alpha q} \right)^\dagger \mathbf{S}_{r\alpha}^\dagger + \left(\mathbf{C}_{\alpha\beta}^\dagger \mathbf{S}_{q\alpha}^\dagger + \mathbf{C}_{\beta\beta} \mathbf{S}_{q\beta}^\dagger - \mathbf{C}_{\beta q} \right)^\dagger \mathbf{S}_{r\beta}^\dagger - \mathbf{S}_{q\alpha} \mathbf{C}_{\alpha r} - \mathbf{S}_{q\beta} \mathbf{C}_{\beta r} + \mathbf{C}_{rq}^\dagger \\ &= \mathbf{S}_{q\alpha} \left(\mathbf{C}_{\alpha\alpha} \mathbf{S}_{r\alpha}^\dagger + \mathbf{C}_{\alpha\beta} \mathbf{S}_{r\beta}^\dagger - \mathbf{C}_{\alpha r} \right) + \mathbf{S}_{q\beta} \left(\mathbf{C}_{\alpha\beta}^\dagger \mathbf{S}_{r\alpha}^\dagger + \mathbf{C}_{\beta\beta} \mathbf{S}_{r\beta}^\dagger - \mathbf{C}_{\beta r} \right) - \mathbf{C}_{\alpha q}^\dagger \mathbf{S}_{r\alpha}^\dagger - \mathbf{C}_{\beta q}^\dagger \mathbf{S}_{r\beta}^\dagger + \mathbf{C}_{rq}^\dagger \\ &= \mathbf{D}_{qr} \end{aligned}$$

And it follows that

$$\begin{pmatrix} \mathbf{D}_{rr} & \mathbf{D}_{rq} \\ \mathbf{D}_{qr} & \mathbf{D}_{qq} \end{pmatrix} = \begin{pmatrix} \mathbf{D}_{rr} & \mathbf{D}_{rq} \\ \mathbf{D}_{rq}^\dagger & \mathbf{D}_{qq} \end{pmatrix} \quad (\text{B.27})$$

with dimensions:

$$\mathbf{D}_{rr} = (N_r \times N_r) ; \mathbf{D}_{rq} = (N_r \times N_q) ; \mathbf{D}_{qr} = \mathbf{D}_{rq}^\dagger = (N_q \times N_r) ; \mathbf{D}_{qq} = (N_q \times N_q)$$

We are still looking for the particular Lagrange multipliers that minimize the constrained problem. Recall Eq. (B.22) and solve for (λ_r, λ_q)

$$\begin{aligned} \begin{pmatrix} \mathbf{r}^c - \mathbf{r}^m \\ \mathbf{q}^c - \mathbf{q}^m \end{pmatrix} &= \begin{pmatrix} \mathbf{D}_{rr} & \mathbf{D}_{rq} \\ \mathbf{D}_{rq}^\dagger & \mathbf{D}_{qq} \end{pmatrix} \begin{pmatrix} \lambda_r^{opt} \\ \lambda_q^{opt} \end{pmatrix} \\ \begin{pmatrix} \lambda_r^{opt} \\ \lambda_q^{opt} \end{pmatrix} &= \underbrace{\begin{pmatrix} \mathbf{D}_{rr} & \mathbf{D}_{rq} \\ \mathbf{D}_{rq}^\dagger & \mathbf{D}_{qq} \end{pmatrix}^{-1}}_{\mathbf{D}} \begin{pmatrix} \mathbf{r}^c - \mathbf{r}^m \\ \mathbf{q}^c - \mathbf{q}^m \end{pmatrix} \\ &= \mathbf{D}^{-1} \begin{pmatrix} \mathbf{r}^c - \mathbf{r}^m \\ \mathbf{q}^c - \mathbf{q}^m \end{pmatrix} \end{aligned} \quad (\text{B.28})$$

Thus, we can now replace the multipliers (λ_r, λ_q) in the original set of equations (B.14–B.17).

C Synthetic Data

Synthetic data for 1-D time-dependent heat conduction in infinite medium used in Chapter 3.

Input parameters:

$k \left[\frac{W}{m K} \right]$	$\rho \left[\frac{kg}{m^3} \right]$	$c_p \left[\frac{J}{kg K} \right]$	$t_j [s]$
$0.59 \pm 2.95 \cdot 10^{-2} (\pm 5\%)$	$2040 \pm 204 (\pm 10\%)$	$1.84 \cdot 10^3 \pm 36.8 (\pm 2\%)$	$10 \pm 0.1 (\pm 1\%)$

#	Location x_i		Fourier coefficient a_n		Fourier coefficient b_n	
1	-0.3955	± 10.236	0.3581	± 5.0136	0.8563	± 8.3808
2	-0.2907	± 7.9882	0.4890	± 5.0309	0.5842	± 13.595
3	-0.2701	± 12.040	0.2560	± 5.8747	0.3736	± 8.4048
4	-0.2401	± 8.8161	0.9292	± 7.6073	0.2217	± 6.3812
5	0.0344	± 10.677	0.4668	± 5.2280	0.2190	± 10.078
6	0.0859	± 13.879	0.2540	± 9.2408	0.5222	± 13.567
7	0.1439	± 13.429	0.4312	± 8.4106	0.4334	± 8.8431
8	0.2118	± 13.988	0.7025	± 10.414	0.7413	± 11.957
9	0.2172	± 14.390	0.4023	± 14.262	0.0704	± 11.279
10	0.2867	± 13.154	0.1818	± 7.9850	0.8473	± 9.5039

The sensitivity matrix has the following elements

$$\mathbf{S}_{r\alpha} = \begin{bmatrix} \frac{\partial r_1}{\partial k} & \frac{\partial r_1}{\partial \rho} & \frac{\partial r_1}{\partial c_p} & \frac{\partial r_1}{\partial t} & \frac{\partial r_1}{\partial x_1} & \dots & \frac{\partial r_1}{\partial x_{10}} & \frac{\partial r_1}{\partial a_1} & \dots & \frac{\partial r_1}{\partial a_{10}} & \frac{\partial r_1}{\partial b_1} & \dots & \frac{\partial r_1}{\partial b_{10}} \\ \vdots & & & & & & \ddots & & & & & & \vdots \\ \frac{\partial r_{10}}{\partial k} & \frac{\partial r_{10}}{\partial \rho} & \frac{\partial r_{10}}{\partial c_p} & \frac{\partial r_{10}}{\partial t} & \frac{\partial r_{10}}{\partial x_1} & \dots & \frac{\partial r_{10}}{\partial x_{10}} & \frac{\partial r_{10}}{\partial a_1} & \dots & \frac{\partial r_{10}}{\partial a_{10}} & \frac{\partial r_{10}}{\partial b_1} & \dots & \frac{\partial r_{10}}{\partial b_{10}} \end{bmatrix}$$

and the analytically computed relative sensitivities of the form

Appendix

$$S_{r_i \alpha_j}^{rel} = S_{r_i \alpha_j} \cdot \frac{\alpha_j}{r_i} = \frac{\partial r_i}{\partial \alpha_j} \cdot \frac{\alpha_j}{r_i}$$

follow in the tables below.

$\frac{\partial r_i}{\partial k} \frac{k}{r_i} \cdot 10^{-3}$	$\frac{\partial r_i}{\partial \rho} \frac{\rho}{r_i} \cdot 10^{-3}$	$\frac{\partial r_i}{\partial c_p} \frac{c_p}{r_i} \cdot 10^{-3}$	$\frac{\partial r_i}{\partial t} \frac{t}{r_i}$
-0.0520	0.0520	0.0520	-10
-0.1017	0.1017	0.1017	-10
-0.1113	0.1113	0.1113	-10
-0.1283	0.1283	0.1283	-10
-0.0613	0.0613	0.0613	-10
-0.0651	0.0651	0.0651	-10
-0.0636	0.0636	0.0636	-10
-0.0533	0.0533	0.0533	-10
-0.0519	0.0519	0.0519	-10
-0.0190	0.0190	0.0190	-10

Only non-zero sensitivity coefficients for each location x_j are listed below.

$\frac{\partial r_1}{\partial x_1} \frac{x_1}{r_1}$	$\frac{\partial r_2}{\partial x_2} \frac{x_2}{r_2}$	$\frac{\partial r_3}{\partial x_3} \frac{x_3}{r_3}$	$\frac{\partial r_4}{\partial x_4} \frac{x_4}{r_4}$	$\frac{\partial r_5}{\partial x_5} \frac{x_5}{r_5}$	$\frac{\partial r_6}{\partial x_6} \frac{x_6}{r_6}$	$\frac{\partial r_7}{\partial x_7} \frac{x_7}{r_7}$	$\frac{\partial r_8}{\partial x_8} \frac{x_8}{r_8}$	$\frac{\partial r_9}{\partial x_9} \frac{x_9}{r_9}$	$\frac{\partial r_{10}}{\partial x_{10}} \frac{x_{10}}{r_{10}}$
-1.4061	0.5852	0.9629	1.5875	0.1309	0.1169	-0.1527	-0.8721	-0.9542	-2.6406

$\frac{\partial r_i}{\partial a_1} \frac{a_1}{r_i}$	$\frac{\partial r_i}{\partial a_2} \frac{a_2}{r_i}$	$\frac{\partial r_i}{\partial a_3} \frac{a_3}{r_i}$	$\frac{\partial r_i}{\partial a_4} \frac{a_4}{r_i}$	$\frac{\partial r_i}{\partial a_5} \frac{a_5}{r_i}$	$\frac{\partial r_i}{\partial a_6} \frac{a_6}{r_i}$	$\frac{\partial r_i}{\partial a_7} \frac{a_7}{r_i}$	$\frac{\partial r_i}{\partial a_8} \frac{a_8}{r_i}$	$\frac{\partial r_i}{\partial a_9} \frac{a_9}{r_i}$	$\frac{\partial r_i}{\partial a_{10}} \frac{a_{10}}{r_i}$
0.0954	0.1303	0.0682	0.2476	0.1244	0.0677	0.1149	0.1872	0.1072	0.0485
0.1222	0.1668	0.0873	0.3170	0.1592	0.0866	0.1471	0.2397	0.1372	0.0620
0.1203	-0.1642	0.0860	0.3121	0.1568	0.0853	0.1448	0.2359	0.1351	0.0611
0.1140	0.1557	0.0815	0.2958	0.1486	0.0809	0.1373	0.2236	0.1281	0.0579
0.0639	0.0873	0.0457	0.1658	0.0833	0.0453	0.0770	0.1254	0.0718	0.0324
0.0389	0.0532	0.0278	0.1010	0.0507	0.0276	0.0469	0.0764	0.0437	0.0198

Appendix

0.0078	0.0106	0.0055	0.0201	0.0101	0.0055	0.0093	0.0152	0.0087	0.0039
-0.0366	-0.0499	-0.0261	-0.0948	-0.0476	-0.0259	-0.0440	-0.0717	-0.0411	-0.0186
-0.0406	-0.0555	-0.0290	-0.1054	-0.0529	-0.0288	-0.0489	-0.0797	-0.0456	-0.0206
-0.1091	-0.1489	-0.0780	-0.2830	-0.1422	-0.0774	-0.1313	-0.2140	-0.1225	-0.0554

$\frac{\partial r_i b_1}{\partial b_1 r_i}$	$\frac{\partial r_i b_2}{\partial b_2 r_i}$	$\frac{\partial r_i b_3}{\partial b_3 r_i}$	$\frac{\partial r_i b_4}{\partial b_4 r_i}$	$\frac{\partial r_i b_5}{\partial b_5 r_i}$	$\frac{\partial r_i b_6}{\partial b_6 r_i}$	$\frac{\partial r_i b_7}{\partial b_7 r_i}$	$\frac{\partial r_i b_8}{\partial b_8 r_i}$	$\frac{\partial r_i b_9}{\partial b_9 r_i}$	$\frac{\partial r_i b_{10}}{\partial b_{10} r_i}$
-0.2412	-0.1646	-0.1052	-0.0625	-0.0617	-0.1471	-0.1221	-0.2088	-0.0198	-0.2387
0.0699	0.0477	0.0305	0.0181	0.0179	0.0426	0.0354	0.0605	0.0057	0.0691
0.1355	0.0924	0.0591	0.0351	0.0346	0.0826	0.0686	0.1173	0.0111	0.1340
0.2490	0.1699	0.1086	0.0645	0.0637	0.1519	0.1260	0.2156	0.0205	0.2464
0.0548	0.0374	0.0239	0.0142	0.0140	0.0334	0.0277	0.0474	0.0045	0.0542
0.1078	0.0736	0.0471	0.0279	0.0276	0.0658	0.0546	0.0934	0.0089	0.1067
0.1401	0.0956	0.0611	0.0363	0.0358	0.0854	0.0709	0.1213	0.0115	0.1386
0.1433	0.0978	0.0625	0.0371	0.0367	0.0874	0.0726	0.1241	0.0118	0.1418
0.1416	0.0966	0.0618	0.0367	0.0362	0.0864	0.0717	0.1226	0.0117	0.1402
0.0734	0.0501	0.0320	0.0190	0.0188	0.0448	0.0372	0.0635	0.0060	0.0726

D Implementation of partitioned DA

Pseudo-Code for the algorithm of partitioned data assimilation is listed below. The first column consists of line numbers of executed lines (“%” initiates comments in MATLAB) and the right-most column keeps track of the number of elements in memory. The actual algorithm used in this work was implemented in the scripting language MATLAB, however, it is written here as pseudo-code applicable to any language.

	%+++++Build Xalpha	In memory
1	Read from file \mathbf{C}_{aa}	$N_\alpha \cdot N_\alpha$
2	Read from file \mathbf{S}_{ra}	$N_\alpha \cdot N_\alpha + N_r \cdot N_\alpha$
3	$\mathbf{X}_\alpha = \mathbf{C}_{aa} \cdot \mathbf{S}_{ra}^\dagger$ %build Xalpha step 1)	$N_\alpha \cdot N_\alpha + 2 \cdot N_r \cdot N_\alpha$
4	Delete \mathbf{C}_{aa} \mathbf{S}_{ra}	$N_r \cdot N_\alpha$
5	Read from file $\mathbf{C}_{a\beta}$	$N_r \cdot N_\alpha + N_\alpha \cdot N_\beta$
6	Read from file $\mathbf{S}_{r\beta}$	$N_r \cdot N_\alpha + N_\alpha \cdot N_\beta + N_r \cdot N_\beta$
7	$\mathbf{X}_\alpha = \mathbf{X}_\alpha + \mathbf{C}_{a\beta} \cdot \mathbf{S}_{r\beta}^\dagger$ %build Xalpha step 2)	$N_r \cdot N_\alpha + N_\alpha \cdot N_\beta + N_r \cdot N_\beta$
8	Delete $\mathbf{C}_{a\beta}$ $\mathbf{S}_{r\beta}$	$N_r \cdot N_\alpha$
9	Build \mathbf{C}_{ar}	$2 \cdot N_r \cdot N_\alpha$
10	$\mathbf{X}_\alpha = \mathbf{X}_\alpha - \mathbf{C}_{ar}$ %build Xalpha step 3) (complete)	$2 \cdot N_r \cdot N_\alpha$
11	Write \mathbf{X}_α to file	$2 \cdot N_r \cdot N_\alpha$
12	Delete \mathbf{C}_{ar} \mathbf{X}_α	-
	%+++++Build Xbeta	
13	Read from file $\mathbf{C}_{\beta\beta}$	$N_\beta \cdot N_\beta$
14	Read from file $\mathbf{S}_{r\beta}$	$N_\beta \cdot N_\beta + N_r \cdot N_\beta$
15	$\mathbf{X}_\beta = \mathbf{C}_{\beta\beta} \cdot \mathbf{S}_{r\beta}^\dagger$ %build Xbeta step 1)	$N_\beta \cdot N_\beta + 2 \cdot N_r \cdot N_\beta$
16	Delete $\mathbf{C}_{\beta\beta}$ $\mathbf{S}_{r\beta}$	$N_r \cdot N_\beta$
17	Read from file $\mathbf{C}_{a\beta}$	$N_r \cdot N_\beta + N_\alpha \cdot N_\beta$
18	Read from file \mathbf{S}_{ra}	$N_r \cdot N_\beta + N_\alpha \cdot N_\beta + N_r \cdot N_\beta$
19	$\mathbf{X}_\beta = \mathbf{X}_\beta + \mathbf{C}_{a\beta} \cdot \mathbf{S}_{ra}^\dagger$ %build Xbeta step 2)	$2 \cdot N_r \cdot N_\beta + N_\alpha \cdot N_\beta$
20	Delete $\mathbf{C}_{a\beta}$ \mathbf{S}_{ra}	$N_r \cdot N_\beta$
21	Build $\mathbf{C}_{\beta r}$	$2 \cdot N_r \cdot N_\beta$

22	$\mathbf{X}_\beta = \mathbf{X}_\beta - \mathbf{C}_{\beta r}$ %build Xbeta step 3) (complete)	$2 \cdot N_r \cdot N_\beta$
23	Write \mathbf{X}_β to file	$2 \cdot N_r \cdot N_\beta$
24	Delete $\mathbf{C}_{\beta r}$ %+++++Build Crc11	$N_r \cdot N_\beta$
25	Read from file $\mathbf{S}_{r\beta}$	$2 \cdot N_r \cdot N_\beta$
26	$\mathbf{C}_{rc,11} = \mathbf{S}_{r\beta} \cdot \mathbf{X}_\beta$ %build Crc11 step 1)	$2 \cdot N_r \cdot N_\beta + N_r \cdot N_r$
27	Delete $\mathbf{S}_{r\beta}$ \mathbf{X}_β	$N_r \cdot N_r$
28	Read from file \mathbf{S}_{ra}	$N_r \cdot N_r + N_r \cdot N_\alpha$
29	Read from file \mathbf{X}_α	$N_r \cdot N_r + 2 \cdot N_r \cdot N_\alpha$
30	$\mathbf{C}_{rc,11} = \mathbf{S}_{ra} \cdot \mathbf{X}_\alpha + \mathbf{C}_{rc,11}$ %build Crc11 step 2)	$N_r \cdot N_r + 2 \cdot N_r \cdot N_\alpha$
31	Write $\mathbf{C}_{rc,11}$ to file	$N_r \cdot N_r + 2 \cdot N_r \cdot N_\alpha$
32	Delete \mathbf{S}_{ra} \mathbf{X}_α $\mathbf{C}_{rc,11}$ %+++++Build Yalpha	-
33	Read from file $\mathbf{C}_{\alpha\alpha}$	$N_\alpha \cdot N_\alpha$
34	Read from file $\mathbf{S}_{q\alpha}$	$N_\alpha \cdot N_\alpha + N_q \cdot N_\alpha$
35	$\mathbf{Y}_\alpha = \mathbf{C}_{\alpha\alpha} \cdot \mathbf{S}_{q\alpha}^\dagger$ %build Yalpha step 1)	$N_\alpha \cdot N_\alpha + 2 \cdot N_q \cdot N_\alpha$
36	Delete $\mathbf{C}_{\alpha\alpha}$ $\mathbf{S}_{q\alpha}$	$N_q \cdot N_\alpha$
37	Read from file $\mathbf{C}_{\alpha\beta}$	$N_q \cdot N_\alpha + N_\alpha \cdot N_\beta$
38	Read from file $\mathbf{S}_{q\beta}$	$N_q \cdot N_\alpha + N_\alpha \cdot N_\beta + N_q \cdot N_\beta$
39	$\mathbf{Y}_\alpha = \mathbf{Y}_\alpha + \mathbf{C}_{\alpha\beta} \cdot \mathbf{S}_{q\beta}^\dagger$ %build Yalpha step 2)	$N_q \cdot N_\alpha + N_\alpha \cdot N_\beta + N_q \cdot N_\beta$
40	Delete $\mathbf{C}_{\alpha\beta}$ $\mathbf{S}_{q\beta}$	$N_q \cdot N_\alpha$
41	Build $\mathbf{C}_{\alpha q}$	$2 \cdot N_q \cdot N_\alpha$
42	$\mathbf{Y}_\alpha = \mathbf{Y}_\alpha - \mathbf{C}_{\alpha q}$ %build Yalpha step 3) (complete)	$2 \cdot N_q \cdot N_\alpha$
43	Write \mathbf{Y}_α to file	$2 \cdot N_q \cdot N_\alpha$
44	Delete $\mathbf{C}_{\alpha q}$ \mathbf{Y}_α %+++++Build Ybeta	-
45	Read from file $\mathbf{C}_{\beta\beta}$	$N_\beta \cdot N_\beta$
46	Read from file $\mathbf{S}_{q\beta}$	$N_\beta \cdot N_\beta + N_q \cdot N_\beta$
47	$\mathbf{Y}_\beta = \mathbf{C}_{\beta\beta} \cdot \mathbf{S}_{q\beta}^\dagger$ %build Ybeta step 1)	$N_\beta \cdot N_\beta + 2 \cdot N_q \cdot N_\beta$
48	Delete $\mathbf{C}_{\beta\beta}$ $\mathbf{S}_{q\beta}$	$N_q \cdot N_\beta$

49	Read from file $\mathbf{C}_{\alpha\beta}$	$N_q \cdot N_\beta + N_\alpha \cdot N_\beta$
50	Read from file $\mathbf{S}_{q\alpha}$	$N_q \cdot N_\beta + N_\alpha \cdot N_\beta + N_q \cdot N_\alpha$
51	$\mathbf{Y}_\beta = \mathbf{Y}_\beta + \mathbf{C}_{\alpha\beta}^\dagger \cdot \mathbf{S}_{q\alpha}^\dagger$ %build Ybeta step 2)	$N_q \cdot N_\beta + N_\alpha \cdot N_\beta + N_q \cdot N_\alpha$
52	Delete $\mathbf{C}_{\alpha\beta}$ $\mathbf{S}_{q\alpha}$	$N_q \cdot N_\beta$
53	Build $\mathbf{C}_{\beta q}$	$2 \cdot N_q \cdot N_\beta$
54	$\mathbf{Y}_\beta = \mathbf{Y}_\beta - \mathbf{C}_{\beta q}$ %build Ybeta step 3) (complete)	$2 \cdot N_q \cdot N_\beta$
55	Write \mathbf{Y}_β to file	$2 \cdot N_q \cdot N_\beta$
56	Delete $\mathbf{C}_{\alpha q}$ %+++++Build Cqc22	$N_q \cdot N_\beta$
57	Read from file $\mathbf{S}_{q\beta}$	$2 \cdot N_q \cdot N_\beta$
58	$\mathbf{C}_{qc,22} = \mathbf{S}_{q\beta} \cdot \mathbf{Y}_\beta$ %build Cqc22 step 1)	$2 \cdot N_q \cdot N_\beta + N_q \cdot N_q$
59	Delete $\mathbf{S}_{q\beta}$ \mathbf{Y}_β	$N_q \cdot N_q$
60	Read from file $\mathbf{S}_{q\alpha}$	$N_q \cdot N_q + N_q \cdot N_\alpha$
61	Read from file \mathbf{Y}_α	$N_q \cdot N_q + 2 \cdot N_q \cdot N_\alpha$
62	$\mathbf{C}_{qc,22} = \mathbf{S}_{q\alpha} \cdot \mathbf{Y}_\alpha + \mathbf{C}_{qc,22}$ %build Cqc22 step 2)	$N_q \cdot N_q + 2 \cdot N_q \cdot N_\alpha$
63	Write $\mathbf{C}_{qc,22}$ to file	$N_q \cdot N_q + 2 \cdot N_q \cdot N_\alpha$
64	Delete $\mathbf{S}_{q\alpha}$ \mathbf{Y}_α $\mathbf{C}_{qc,22}$ %+++++Build X_r	-
65	Build \mathbf{C}_{ar}	$N_\alpha \cdot N_r$
66	Read from file $\mathbf{S}_{r\alpha}$	$2 \cdot N_\alpha \cdot N_r$
67	$\mathbf{X}_r = \mathbf{C}_{ar}^\dagger \cdot \mathbf{S}_{r\alpha}^\dagger$ %build X_r step 1)	$2 \cdot N_\alpha \cdot N_r + N_r \cdot N_r$
68	Delete \mathbf{C}_{ar} $\mathbf{S}_{r\alpha}$	$N_r \cdot N_r$
69	Build $\mathbf{C}_{\beta r}$	$N_r \cdot N_r + N_r \cdot N_\beta$
70	Read from file $\mathbf{S}_{r\beta}$	$N_r \cdot N_r + 2 \cdot N_r \cdot N_\beta$
71	$\mathbf{X}_r = \mathbf{X}_r + \mathbf{C}_{\beta r}^\dagger \cdot \mathbf{S}_{r\beta}^\dagger$ %build X_r step 2)	$N_r \cdot N_r + 2 \cdot N_r \cdot N_\beta$
72	Delete $\mathbf{C}_{\beta r}$ $\mathbf{S}_{r\beta}$	$N_r \cdot N_r$
73	Read from file \mathbf{C}_{rr}	$2 \cdot N_r \cdot N_r$
74	$\mathbf{X}_r = \mathbf{X}_r - \mathbf{C}_{rr}$ %build X_r step 3) (complete)	$2 \cdot N_r \cdot N_r$
75	Write \mathbf{X}_r to file	$2 \cdot N_r \cdot N_r$

76	Delete \mathbf{C}_{rr}	$N_r \cdot N_r$
	%+++++Build Drr and Inverse inv(D_rr)	
77	Read from file $\mathbf{C}_{rc,11}$	$2 \cdot N_r \cdot N_r$
78	$\mathbf{D}_{rr} = \mathbf{C}_{rc,11} - \mathbf{X}_r$	$3 \cdot N_r \cdot N_r$
79	Delete $\mathbf{C}_{rc,11}$ \mathbf{X}_r	$N_r \cdot N_r$
80	Compute Inverse $(\mathbf{D}_{rr})^{-1}$	$2 \cdot N_r \cdot N_r$
81	Write $(\mathbf{D}_{rr})^{-1}$ to file	$2 \cdot N_r \cdot N_r$
82	Delete $(\mathbf{D}_{rr})^{-1}$ \mathbf{D}_{rr}	-
	%+++++Build Y_q	
83	Build $\mathbf{C}_{\alpha q}$	$N_\alpha \cdot N_q$
84	Read from file $\mathbf{S}_{q\alpha}$	$2 \cdot N_\alpha \cdot N_q$
85	$\mathbf{Y}_q = \mathbf{C}_{\alpha q}^\dagger \cdot \mathbf{S}_{q\alpha}^\dagger$ %build Y_q step 1)	$2 \cdot N_\alpha \cdot N_q + N_q \cdot N_q$
86	Delete $\mathbf{C}_{\alpha q}$ $\mathbf{S}_{q\alpha}$	$N_q \cdot N_q$
87	Build $\mathbf{C}_{\beta q}$	$N_q \cdot N_q + N_\beta \cdot N_q$
88	Read from file $\mathbf{S}_{q\beta}$	$N_q \cdot N_q + 2 \cdot N_\beta \cdot N_q$
89	$\mathbf{Y}_q = \mathbf{Y}_q + \mathbf{C}_{\beta q}^\dagger \cdot \mathbf{S}_{q\beta}^\dagger$ %build Y_q step 2)	$N_q \cdot N_q + 2 \cdot N_\beta \cdot N_q$
90	Delete $\mathbf{C}_{\beta q}$ $\mathbf{S}_{q\beta}$	$N_q \cdot N_q$
91	Read from file \mathbf{C}_{qq}	$2 \cdot N_q \cdot N_q$
92	$\mathbf{Y}_q = \mathbf{Y}_q - \mathbf{C}_{qq}$ %build Y_q step 3) (complete)	$2 \cdot N_q \cdot N_q$
93	Write \mathbf{Y}_q to file	$2 \cdot N_q \cdot N_q$
94	Delete \mathbf{C}_{qq}	$N_q \cdot N_q$
	%+++++Build Dqq	
95	Read from file $\mathbf{C}_{qc,22}$	$2 \cdot N_q \cdot N_q$
96	$\mathbf{D}_{qq} = \mathbf{C}_{qc,22} - \mathbf{Y}_q$	$3 \cdot N_q \cdot N_q$
97	Delete $\mathbf{C}_{qc,22}$ \mathbf{Y}_q	$N_q \cdot N_q$
98	Write \mathbf{D}_{qq} to file	$N_q \cdot N_q$
99	Delete \mathbf{D}_{qq}	-
	%+++++Build Y_r	
100	Build \mathbf{C}_{ar}	$N_\alpha \cdot N_r$

101	Read from file $\mathbf{S}_{q\alpha}$	$N_\alpha \cdot N_q + N_\alpha \cdot N_r$
102	$\mathbf{Y}_r = \mathbf{C}_{\alpha r}^\dagger \cdot \mathbf{S}_{q\alpha}^\dagger$ %build \mathbf{Y}_r step 1)	$N_\alpha \cdot N_q + N_\alpha \cdot N_r + N_r \cdot N_q$
103	Delete $\mathbf{C}_{\alpha q}$ $\mathbf{S}_{q\alpha}$	$N_r \cdot N_q$
104	Build $\mathbf{C}_{\beta r}$	$N_r \cdot N_q + N_\beta \cdot N_r$
105	Read from file $\mathbf{S}_{q\beta}$	$N_r \cdot N_q + 2 \cdot N_\beta \cdot N_r$
106	$\mathbf{Y}_r = \mathbf{Y}_r + \mathbf{C}_{\beta r}^\dagger \cdot \mathbf{S}_{q\beta}^\dagger$ %build \mathbf{Y}_r step 2)	$N_r \cdot N_q + 2 \cdot N_\beta \cdot N_r$
107	Delete $\mathbf{C}_{\beta r}$ $\mathbf{S}_{q\beta}$	$N_r \cdot N_q$
108	Read from file \mathbf{C}_{rq}	$2 \cdot N_r \cdot N_q$
109	$\mathbf{Y}_r = \mathbf{Y}_r - \mathbf{C}_{rq}$ %build \mathbf{Y}_r step 3) (complete)	$2 \cdot N_r \cdot N_q$
110	Write \mathbf{Y}_r to file	$2 \cdot N_r \cdot N_q$
111	Delete \mathbf{C}_{rq} %+++++Build Drq	$N_r \cdot N_q$
112	$\mathbf{D}_{rq} = -\mathbf{Y}_r$ %build Drq step 1)	$N_r \cdot N_q$
113	Delete \mathbf{Y}_r	$N_r \cdot N_q$
114	Read from file $\mathbf{S}_{r\alpha}$	$N_r \cdot N_q + N_r \cdot N_\alpha$
115	Read from file \mathbf{Y}_α	$N_r \cdot N_q + N_r \cdot N_\alpha + N_\alpha \cdot N_q$
116	$\mathbf{D}_{rq} = \mathbf{D}_{rq} + \mathbf{S}_{r\alpha} \cdot \mathbf{Y}_\alpha$ %build Drq step 2)	$N_r \cdot N_q + N_r \cdot N_\alpha + N_\alpha \cdot N_q$
117	Delete $\mathbf{S}_{r\alpha}$ \mathbf{Y}_α	$N_r \cdot N_q$
118	Read from file $\mathbf{S}_{r\beta}$	$N_r \cdot N_q + N_r \cdot N_\beta$
119	Read from file \mathbf{Y}_β	$N_r \cdot N_q + N_r \cdot N_\beta + N_\beta \cdot N_q$
120	$\mathbf{D}_{rq} = \mathbf{D}_{rq} + \mathbf{S}_{r\beta} \cdot \mathbf{Y}_\beta$ %build Drq step 3) (complete)	$N_r \cdot N_q + N_r \cdot N_\beta + N_\beta \cdot N_q$
121	Write \mathbf{D}_{rq} to file	$N_r \cdot N_q + N_r \cdot N_\beta + N_\beta \cdot N_q$
122	Delete $\mathbf{S}_{r\beta}$ \mathbf{Y}_β %+++++Build the Schur complement D22	$N_r \cdot N_q$
123	Read from file $(\mathbf{D}_{rr})^{-1}$	$N_r \cdot N_q + N_r \cdot N_r$
124	$\mathbf{D}_{temp} = (\mathbf{D}_{rr})^{-1} \cdot \mathbf{D}_{rq}$ %build temporary variable	$2 \cdot N_r \cdot N_q + N_r \cdot N_r$
125	Write \mathbf{D}_{temp} to file	$2 \cdot N_r \cdot N_q + N_r \cdot N_r$
126	$\mathbf{D}_{22} = \mathbf{D}_{temp}$ %build D22 step 1)	$2 \cdot N_r \cdot N_q + N_r \cdot N_r$

127	Delete \mathbf{D}_{temp} $(\mathbf{D}_{rr})^{-1}$	$2 \cdot N_r \cdot N_q$
128	$\mathbf{D}_{22} = \mathbf{D}_{rq}^\dagger \cdot \mathbf{D}_{22}$ %build D22 step 2*)	$N_r \cdot N_q + N_q \cdot N_q$
129	*allocation mismatch if $N_r \neq N_q$ causes temporary memory requirement of	$2 \cdot N_r \cdot N_q + N_q \cdot N_q$
130	Delete \mathbf{D}_{rq}	$N_q \cdot N_q$
131	Read \mathbf{D}_{qq} from file	$2 \cdot N_q \cdot N_q$
132	$\mathbf{D}_{22} = \mathbf{D}_{qq} - \mathbf{D}_{22}$ %build D22 step 3)	$2 \cdot N_q \cdot N_q$
133	Delete \mathbf{D}_{qq}	$N_q \cdot N_q$
134	Compute Inverse of \mathbf{D}_{22} %build D22 step 4) (complete)	$N_q \cdot N_q$
135	Write \mathbf{D}_{22} to file %+++++Build D12	$N_q \cdot N_q$
136	Read \mathbf{D}_{temp} from file	$N_q \cdot N_q + N_r \cdot N_q$
137	$\mathbf{D}_{12} = -\mathbf{D}_{temp} \cdot \mathbf{D}_{22}$	$N_q \cdot N_q + 2 \cdot N_r \cdot N_q$
138	Write \mathbf{D}_{12} to file	$N_q \cdot N_q + 2 \cdot N_r \cdot N_q$
139	Delete \mathbf{D}_{22}	$2 \cdot N_r \cdot N_q$
140	%+++++Build D11	
141	$\mathbf{D}_{11} = -\mathbf{D}_{12} \cdot \mathbf{D}_{temp}^\dagger$ %build D11 part 1)	$2 \cdot N_r \cdot N_q + N_r \cdot N_r$
142	Delete \mathbf{D}_{12} \mathbf{D}_{temp}	$N_r \cdot N_r$
143	Read $(\mathbf{D}_{rr})^{-1}$ from file	$2 \cdot N_r \cdot N_r$
144	$\mathbf{D}_{11} = \mathbf{D}_{11} + (\mathbf{D}_{rr})^{-1}$ %build D11 part 2) (complete)	$2 \cdot N_r \cdot N_r$
145	Write \mathbf{D}_{11} to file	$2 \cdot N_r \cdot N_r$
146	Delete \mathbf{D}_{11} $(\mathbf{D}_{rr})^{-1}$	-
147	%+++++Build X_q	
148	Build $\mathbf{C}_{\alpha q}$	$N_\alpha \cdot N_q$
149	Read \mathbf{S}_{ra} from file	$N_\alpha \cdot N_q + N_r \cdot N_\alpha$
150	$\mathbf{X}_q = \mathbf{C}_{\alpha q}^\dagger \cdot \mathbf{S}_{ra}^\dagger$ %build X_q step 1)	$N_\alpha \cdot N_q + N_r \cdot N_\alpha + N_r \cdot N_q$
151	Delete $\mathbf{C}_{\alpha q}$ \mathbf{S}_{ra}	$N_r \cdot N_q$
152	Build $\mathbf{C}_{\beta q}$	$N_r \cdot N_q + N_\beta \cdot N_q$

153	Read from file $\mathbf{S}_{r\beta}$	$N_r \cdot N_q + N_\beta \cdot N_q + N_r \cdot N_\beta$
154	$\mathbf{X}_q = \mathbf{X}_q + \mathbf{C}_{\beta q}^\dagger \cdot \mathbf{S}_{r\beta}^\dagger$ %build X_q step 2)	$N_r \cdot N_q + N_\beta \cdot N_q + N_r \cdot N_\beta$
155	Delete $\mathbf{C}_{\beta q}$ $\mathbf{S}_{r\beta}$	$N_r \cdot N_q$
156	Read from file \mathbf{C}_{rq}	$2 \cdot N_r \cdot N_q$
157	$\mathbf{X}_q = \mathbf{X}_q - \mathbf{C}_{rq}^\dagger$ %build X_q step 3) (complete)	$2 \cdot N_r \cdot N_q$
158	Write \mathbf{X}_q to file	$2 \cdot N_r \cdot N_q$
159	Delete \mathbf{C}_{rq} \mathbf{X}_q %+++++Build XalphaD11_YalphaD12	-
160	Read \mathbf{X}_α from file	$N_\alpha \cdot N_r$
161	Read \mathbf{D}_{11} from file	$N_\alpha \cdot N_r + N_r \cdot N_r$
162	$\mathbf{X}_\alpha \mathbf{D}_{11} - \mathbf{Y}_\alpha \mathbf{D}_{12} = \mathbf{X}_\alpha \cdot \mathbf{D}_{11}$ %build step 1)	$2 \cdot N_\alpha \cdot N_r + N_r \cdot N_r$
163	Delete \mathbf{X}_α \mathbf{D}_{11}	$N_\alpha \cdot N_r$
164	Read \mathbf{Y}_α from file	$N_\alpha \cdot N_r + N_\alpha \cdot N_q$
165	Read \mathbf{D}_{12} from file	$N_\alpha \cdot N_r + N_\alpha \cdot N_q + N_r \cdot N_q$
166	$\mathbf{X}_\alpha \mathbf{D}_{11} - \mathbf{Y}_\alpha \mathbf{D}_{12} = \mathbf{X}_\alpha \mathbf{D}_{11} - \mathbf{Y}_\alpha \mathbf{D}_{12} + \mathbf{Y}_\alpha \cdot \mathbf{D}_{12}^\dagger$ %build step 2)	$N_\alpha \cdot N_r + N_\alpha \cdot N_q + N_r \cdot N_q$
167	Write $\mathbf{X}_\alpha \mathbf{D}_{11} - \mathbf{Y}_\alpha \mathbf{D}_{12}$ to file	$N_\alpha \cdot N_r + N_\alpha \cdot N_q + N_r \cdot N_q$
168	Delete \mathbf{Y}_α $\mathbf{X}_\alpha \mathbf{D}_{11} - \mathbf{Y}_\alpha \mathbf{D}_{12}$ %+++++Build XalphaD12_YalphaD22	$N_r \cdot N_q$
169	Read \mathbf{X}_α from file	$N_r \cdot N_q + N_\alpha \cdot N_r$
170	$\mathbf{X}_\alpha \mathbf{D}_{12} - \mathbf{Y}_\alpha \mathbf{D}_{22} = \mathbf{X}_\alpha \cdot \mathbf{D}_{12}$ %build step 1)	$N_r \cdot N_q + N_\alpha \cdot N_r + N_\alpha \cdot N_q$
171	Delete \mathbf{X}_α \mathbf{D}_{12}	$N_\alpha \cdot N_q$
172	Read \mathbf{Y}_α from file	$2 \cdot N_\alpha \cdot N_q$
173	Read \mathbf{D}_{22} from file	$2 \cdot N_\alpha \cdot N_q + N_q \cdot N_q$
174	$\mathbf{X}_\alpha \mathbf{D}_{12} - \mathbf{Y}_\alpha \mathbf{D}_{22} = \mathbf{X}_\alpha \mathbf{D}_{12} - \mathbf{Y}_\alpha \mathbf{D}_{22} + \mathbf{Y}_\alpha \cdot \mathbf{D}_{22}$ %build step 2)	$2 \cdot N_\alpha \cdot N_q + N_q \cdot N_q$
175	Write $\mathbf{X}_\alpha \mathbf{D}_{12} - \mathbf{Y}_\alpha \mathbf{D}_{22}$ to file	$2 \cdot N_\alpha \cdot N_q + N_q \cdot N_q$
176	Delete \mathbf{Y}_α $\mathbf{X}_\alpha \mathbf{D}_{12} - \mathbf{Y}_\alpha \mathbf{D}_{22}$ %+++++Build XbetaD12_YbetaD22	$N_q \cdot N_q$
177	Read \mathbf{Y}_β from file	$N_q \cdot N_q + N_\beta \cdot N_q$

178	$\mathbf{X}_\beta \mathbf{D}_{12} - \mathbf{Y}_\beta \mathbf{D}_{22} = \mathbf{Y}_\beta \cdot \mathbf{D}_{22}$ %build step 1)	$N_q \cdot N_q + 2 \cdot N_\beta \cdot N_q$
179	Delete \mathbf{D}_{22} \mathbf{Y}_β	$N_\beta \cdot N_q$
180	Read \mathbf{X}_β from file	$N_\beta \cdot N_q + N_\beta \cdot N_r$
181	Read \mathbf{D}_{12} from file	$N_\beta \cdot N_q + N_\beta \cdot N_r + N_r \cdot N_q$
182	$\mathbf{X}_\beta \mathbf{D}_{12} - \mathbf{Y}_\beta \mathbf{D}_{22} = \mathbf{X}_\beta \mathbf{D}_{12} - \mathbf{Y}_\beta \mathbf{D}_{22} + \mathbf{X}_\beta \cdot \mathbf{D}_{12}$ %build step 2)	$N_\beta \cdot N_q + N_\beta \cdot N_r + N_r \cdot N_q$
183	Write $\mathbf{X}_\beta \mathbf{D}_{12} - \mathbf{Y}_\beta \mathbf{D}_{22}$ to file	$N_\beta \cdot N_q + N_\beta \cdot N_r + N_r \cdot N_q$
184	Delete \mathbf{X}_β $\mathbf{X}_\beta \mathbf{D}_{12} - \mathbf{Y}_\beta \mathbf{D}_{22}$ %+++++Build XbetaD11_YbetaD12	$N_r \cdot N_q$
185	Read \mathbf{Y}_β from file	$N_r \cdot N_q + N_\beta \cdot N_q$
186	$\mathbf{X}_\beta \mathbf{D}_{11} - \mathbf{Y}_\beta \mathbf{D}_{12} = \mathbf{Y}_\beta \cdot \mathbf{D}_{12}^\dagger$ %build step 1)	$N_r \cdot N_q + 2 \cdot N_\beta \cdot N_q$
187	Delete \mathbf{D}_{12} \mathbf{Y}_β	$N_\beta \cdot N_q$
188	Read \mathbf{X}_β from file	$N_\beta \cdot N_q + N_\beta \cdot N_r$
189	Read \mathbf{D}_{11} from file	$N_\beta \cdot N_q + N_\beta \cdot N_r + N_r \cdot N_r$
190	$\mathbf{X}_\beta \mathbf{D}_{11} - \mathbf{Y}_\beta \mathbf{D}_{12} = \mathbf{X}_\beta \mathbf{D}_{11} - \mathbf{Y}_\beta \mathbf{D}_{12} + \mathbf{X}_\beta \cdot \mathbf{D}_{11}$ %build step 2)	$N_\beta \cdot N_q + N_\beta \cdot N_r + N_r \cdot N_r$
191	Write $\mathbf{X}_\beta \mathbf{D}_{11} - \mathbf{Y}_\beta \mathbf{D}_{12}$ to file	$N_\beta \cdot N_q + N_\beta \cdot N_r + N_r \cdot N_r$
192	Delete $\mathbf{X}_\beta \mathbf{D}_{11} - \mathbf{Y}_\beta \mathbf{D}_{12}$ \mathbf{X}_β %+++++Build XrD11_YrD12	$N_r \cdot N_r$
193	Read \mathbf{X}_r from file	$N_r \cdot N_r + N_r \cdot N_r$
194	$\mathbf{X}_r \mathbf{D}_{11} - \mathbf{Y}_r \mathbf{D}_{12} = \mathbf{X}_r \cdot \mathbf{D}_{11}$ %build step 1)	$3 \cdot N_r \cdot N_r$
195	Delete \mathbf{X}_r \mathbf{D}_{11}	$N_r \cdot N_r$
196	Read \mathbf{Y}_r from file	$N_r \cdot N_r + N_r \cdot N_q$
197	Read \mathbf{D}_{12} from file	$N_r \cdot N_r + 2 \cdot N_r \cdot N_q$
198	$\mathbf{X}_r \mathbf{D}_{11} - \mathbf{Y}_r \mathbf{D}_{12} = \mathbf{X}_r \mathbf{D}_{11} - \mathbf{Y}_r \mathbf{D}_{12} + \mathbf{Y}_r \cdot \mathbf{D}_{12}^\dagger$ %build step 2)	$N_r \cdot N_r + 2 \cdot N_r \cdot N_q$
199	Write $\mathbf{X}_r \mathbf{D}_{11} - \mathbf{Y}_r \mathbf{D}_{12}$ to file	$N_r \cdot N_r + 2 \cdot N_r \cdot N_q$
200	Delete $\mathbf{X}_r \mathbf{D}_{11} - \mathbf{Y}_r \mathbf{D}_{12}$ \mathbf{Y}_r %+++++Build XrD12_YrD22	$N_r \cdot N_q$
201	Read \mathbf{X}_r from file	$N_r \cdot N_q + N_r \cdot N_r$

202	$\mathbf{X}_r \mathbf{D}_{12} - \mathbf{Y}_r \mathbf{D}_{22} = \mathbf{X}_r \cdot \mathbf{D}_{12}$ %build step 1)	$2 \cdot N_r \cdot N_q + N_r \cdot N_r$
203	Delete \mathbf{D}_{12} \mathbf{X}_r	$N_r \cdot N_q$
204	Read \mathbf{Y}_r from file	$2 \cdot N_r \cdot N_q$
205	Read \mathbf{D}_{22} from file	$2 \cdot N_r \cdot N_q + N_q \cdot N_q$
206	$\mathbf{X}_r \mathbf{D}_{12} - \mathbf{Y}_r \mathbf{D}_{22} = \mathbf{X}_r \mathbf{D}_{12} - \mathbf{Y}_r \mathbf{D}_{22} + \mathbf{Y}_r \cdot \mathbf{D}_{22}$ %build step 2)	$2 \cdot N_r \cdot N_q + N_q \cdot N_q$
207	Write $\mathbf{X}_r \mathbf{D}_{12} - \mathbf{Y}_r \mathbf{D}_{22}$ to file	$2 \cdot N_r \cdot N_q + N_q \cdot N_q$
208	Delete \mathbf{Y}_r $\mathbf{X}_r \mathbf{D}_{12} - \mathbf{Y}_r \mathbf{D}_{22}$ %+++++Build XqD12_YqD22	$N_q \cdot N_q$
209	Read \mathbf{Y}_q from file	$2 \cdot N_q \cdot N_q$
210	$\mathbf{X}_q \mathbf{D}_{12} - \mathbf{Y}_q \mathbf{D}_{22} = \mathbf{Y}_q \cdot \mathbf{D}_{22}$ %build step 1)	$3 \cdot N_q \cdot N_q$
211	Delete \mathbf{Y}_q \mathbf{D}_{22}	$N_q \cdot N_q$
212	Read \mathbf{X}_q from file	$N_q \cdot N_q + N_r \cdot N_q$
213	Read \mathbf{D}_{12} from file	$N_q \cdot N_q + 2 \cdot N_r \cdot N_q$
214	$\mathbf{X}_q \mathbf{D}_{12} - \mathbf{Y}_q \mathbf{D}_{22} = \mathbf{X}_q \mathbf{D}_{12} - \mathbf{Y}_q \mathbf{D}_{22} + \mathbf{X}_q \cdot \mathbf{D}_{12}$ %build step 2)	$N_q \cdot N_q + 2 \cdot N_r \cdot N_q$
215	Write $\mathbf{X}_q \mathbf{D}_{12} - \mathbf{Y}_q \mathbf{D}_{22}$ to file	$N_q \cdot N_q + 2 \cdot N_r \cdot N_q$
216	Delete \mathbf{X}_q $\mathbf{X}_q \mathbf{D}_{12} - \mathbf{Y}_q \mathbf{D}_{22}$ %+++++Build XqD11_YqD12	$N_r \cdot N_q$
217	Read \mathbf{Y}_q from file	$N_r \cdot N_q + N_q \cdot N_q$
218	$\mathbf{X}_q \mathbf{D}_{11} - \mathbf{Y}_q \mathbf{D}_{12} = \mathbf{Y}_q \cdot \mathbf{D}_{12}^\dagger$ %build step 1)	$2 \cdot N_r \cdot N_q + N_q \cdot N_q$
219	Delete \mathbf{Y}_q \mathbf{D}_{12}	$N_r \cdot N_q$
220	Read \mathbf{X}_q from file	$2 \cdot N_r \cdot N_q$
221	Read \mathbf{D}_{11} from file	$2 \cdot N_r \cdot N_q + N_r \cdot N_r$
222	$\mathbf{X}_q \mathbf{D}_{11} - \mathbf{Y}_q \mathbf{D}_{12} = \mathbf{X}_q \mathbf{D}_{11} - \mathbf{Y}_q \mathbf{D}_{12} + \mathbf{X}_q \cdot \mathbf{D}_{11}$ %build step 2)	$2 \cdot N_r \cdot N_q + N_r \cdot N_r$
223	Write $\mathbf{X}_q \mathbf{D}_{11} - \mathbf{Y}_q \mathbf{D}_{12}$ to file	$2 \cdot N_r \cdot N_q + N_r \cdot N_r$
224	Delete \mathbf{D}_{11} \mathbf{X}_q $\mathbf{X}_q \mathbf{D}_{11} - \mathbf{Y}_q \mathbf{D}_{12}$ %+++++Build r_cBE	-
225	Read \mathbf{r}_c from file	N_r

226	Read \mathbf{q}_c from file	$N_r + N_q$
227	Read \mathbf{r}_m from file	$2 \cdot N_r + N_q$
228	Read \mathbf{q}_m from file	$2 \cdot N_r + 2 \cdot N_q$
229	$\mathbf{d}_{\mathbf{r}_m} = \mathbf{r}_c - \mathbf{r}_m$	$3 \cdot N_r + 2 \cdot N_q$
230	$\mathbf{d}_{\mathbf{q}_m} = \mathbf{q}_c - \mathbf{q}_m$	$3 \cdot N_r + 3 \cdot N_q$
231	Delete \mathbf{r}_c \mathbf{q}_c	$2 \cdot N_r + 2 \cdot N_q$
232	Read $\mathbf{X}_r \mathbf{D}_{11} - \mathbf{Y}_r \mathbf{D}_{12}$ from file	$2 \cdot N_r + 2 \cdot N_q + N_r \cdot N_r$
233	$\mathbf{r}_c^{opt} = \mathbf{r}_m - \mathbf{X}_r \mathbf{D}_{11} - \mathbf{Y}_r \mathbf{D}_{12} \cdot \mathbf{d}_{\mathbf{r}_m}$ %build step 1)	$3 \cdot N_r + 2 \cdot N_q + N_r \cdot N_r$
234	Delete $\mathbf{X}_r \mathbf{D}_{11} - \mathbf{Y}_r \mathbf{D}_{12}$ \mathbf{r}_m	$2 \cdot N_r + 2 \cdot N_q$
235	Read $\mathbf{X}_r \mathbf{D}_{12} - \mathbf{Y}_r \mathbf{D}_{22}$ from file	$2 \cdot N_r + 2 \cdot N_q + N_r \cdot N_q$
236	$\mathbf{r}_c^{opt} = \mathbf{r}_c^{opt} - \mathbf{X}_r \mathbf{D}_{12} - \mathbf{Y}_r \mathbf{D}_{22} \cdot \mathbf{d}_{\mathbf{q}_m}$ %build step 2)	$2 \cdot N_r + 2 \cdot N_q + N_r \cdot N_q$
237	Write \mathbf{r}_c^{opt} to file	$2 \cdot N_r + 2 \cdot N_q + N_r \cdot N_q$
238	Delete $\mathbf{X}_r \mathbf{D}_{12} - \mathbf{Y}_r \mathbf{D}_{22}$ \mathbf{r}_c^{opt} %++++Build q_cBE	$N_r + 2 \cdot N_q$
239	Read $\mathbf{X}_q \mathbf{D}_{11} - \mathbf{Y}_q \mathbf{D}_{12}$ from file	$N_r + 2 \cdot N_q + N_r \cdot N_q$
240	$\mathbf{q}_c^{opt} = \mathbf{q}_m - \mathbf{X}_q \mathbf{D}_{11} - \mathbf{Y}_q \mathbf{D}_{12} \cdot \mathbf{d}_{\mathbf{r}_m}$ %build step 1)	$N_r + 3 \cdot N_q + N_r \cdot N_q$
241	Delete $\mathbf{X}_q \mathbf{D}_{11} - \mathbf{Y}_q \mathbf{D}_{12}$ \mathbf{q}_m	$N_r + 2 \cdot N_q$
242	Read $\mathbf{X}_q \mathbf{D}_{12} - \mathbf{Y}_q \mathbf{D}_{22}$ from file	$N_r + 2 \cdot N_q + N_q \cdot N_q$
243	$\mathbf{q}_c^{opt} = \mathbf{q}_c^{opt} - \mathbf{X}_q \mathbf{D}_{12} - \mathbf{Y}_q \mathbf{D}_{22} \cdot \mathbf{d}_{\mathbf{q}_m}$ %build step 2)	$N_r + 2 \cdot N_q + N_q \cdot N_q$
244	Write \mathbf{q}_c^{opt} to file	$N_r + 2 \cdot N_q + N_q \cdot N_q$
245	Delete $\mathbf{X}_q \mathbf{D}_{12} - \mathbf{Y}_q \mathbf{D}_{22}$ \mathbf{q}_c^{opt} %++++Build alpha_BE	$N_r + N_q$
246	Read α^0 from file	$N_r + N_q + N_\alpha$
247	Read $\mathbf{X}_\alpha \mathbf{D}_{11} - \mathbf{Y}_\alpha \mathbf{D}_{12}$ from file	$N_r + N_q + N_\alpha + N_\alpha \cdot N_r$
248	$\alpha^{opt} = \alpha^0 - \mathbf{X}_\alpha \mathbf{D}_{11} - \mathbf{Y}_\alpha \mathbf{D}_{12} \cdot \mathbf{d}_{\mathbf{r}_m}$ %build step 1)	$N_r + N_q + 2 \cdot N_\alpha + N_\alpha \cdot N_r$
249	Delete $\mathbf{X}_\alpha \mathbf{D}_{11} - \mathbf{Y}_\alpha \mathbf{D}_{12}$ α^0	$N_r + N_q + N_\alpha$
250	Read $\mathbf{X}_\alpha \mathbf{D}_{12} - \mathbf{Y}_\alpha \mathbf{D}_{22}$ from file	$N_r + N_q + N_\alpha + N_\alpha \cdot N_q$
251	$\alpha^{opt} = \alpha^{opt} - \mathbf{X}_\alpha \mathbf{D}_{12} - \mathbf{Y}_\alpha \mathbf{D}_{22} \cdot \mathbf{d}_{\mathbf{q}_m}$ %build step 2)	$N_r + N_q + N_\alpha + N_\alpha \cdot N_q$
252	Write α^{opt} to file	$N_r + N_q + N_\alpha + N_\alpha \cdot N_q$
253	Delete $\mathbf{X}_\alpha \mathbf{D}_{12} - \mathbf{Y}_\alpha \mathbf{D}_{22}$ α^{opt}	$N_r + N_q$

	%+++++Build beta_BE	
254	Read β^0 from file	$N_r + N_q + N_\beta$
255	Read $\mathbf{X}_\beta \mathbf{D}_{11} - \mathbf{Y}_\beta \mathbf{D}_{12}$ from file	$N_r + N_q + N_\beta + N_\beta \cdot N_r$
256	$\beta^{opt} = \beta^0 - \mathbf{X}_\beta \mathbf{D}_{11} - \mathbf{Y}_\beta \mathbf{D}_{12} \cdot \mathbf{d}_{r_m}$ %build step 1)	$N_r + N_q + 2 \cdot N_\beta + N_\beta \cdot N_r$
257	Delete β^0 $\mathbf{X}_\beta \mathbf{D}_{11} - \mathbf{Y}_\beta \mathbf{D}_{12}$	$N_r + N_q + N_\beta$
258	Read $\mathbf{X}_\beta \mathbf{D}_{12} - \mathbf{Y}_\beta \mathbf{D}_{22}$ from file	$N_r + N_q + N_\beta + N_\beta \cdot N_q$
259	$\beta^{opt} = \beta^{opt} - \mathbf{X}_\beta \mathbf{D}_{12} - \mathbf{Y}_\beta \mathbf{D}_{22} \cdot \mathbf{d}_{q_m}$ %build part 2)	$N_r + N_q + N_\beta + N_\beta \cdot N_q$
260	Write β^{opt} to file	$N_r + N_q + N_\beta + N_\beta \cdot N_q$
261	Delete $\mathbf{X}_\beta \mathbf{D}_{12} - \mathbf{Y}_\beta \mathbf{D}_{22}$ β^{opt}	$N_r + N_q$
	%+++++Build Chi2	
262	Read \mathbf{D}_{11} from file	$N_r + N_q + N_r \cdot N_r$
263	$\chi_{rr}^2 = \mathbf{d}_{r_m}^\dagger \mathbf{D}_{11} \mathbf{d}_{r_m}$	$N_r + N_q + N_r \cdot N_r$
264	Delete \mathbf{D}_{11}	$N_r + N_q$
265	Read \mathbf{D}_{12} from file	$N_r + N_q + N_r \cdot N_q$
266	$\chi_{rq}^2 = 2 \cdot \mathbf{d}_{r_m}^\dagger \cdot \mathbf{D}_{12} \cdot \mathbf{d}_{q_m}$	$N_r + N_q + N_r \cdot N_q$
267	Delete \mathbf{D}_{12}	$N_r + N_q$
268	Read \mathbf{D}_{22} from file	$N_r + N_q + N_q \cdot N_q$
269	$\chi_{qq}^2 = \mathbf{d}_{q_m}^\dagger \cdot \mathbf{D}_{22} \cdot \mathbf{d}_{q_m}$	$N_r + N_q + N_q \cdot N_q$
270	Delete \mathbf{D}_{22} \mathbf{d}_{r_m} \mathbf{d}_{q_m}	-
	%+++++C_alphaBE	
271	Read $\mathbf{C}_{\alpha\alpha}$ from file	$N_\alpha \cdot N_\alpha$
272	$\mathbf{C}_{\alpha\alpha}^{opt} = \mathbf{C}_{\alpha\alpha}$ %build step 1)	$N_\alpha \cdot N_\alpha$
273	Delete $\mathbf{C}_{\alpha\alpha}$	$N_\alpha \cdot N_\alpha$
274	Read $\mathbf{X}_\alpha \mathbf{D}_{11} - \mathbf{Y}_\alpha \mathbf{D}_{12}$ from file	$N_\alpha \cdot N_\alpha + N_\alpha \cdot N_r$
276	Read \mathbf{X}_α	$N_\alpha \cdot N_\alpha + 2 \cdot N_\alpha \cdot N_r$
277	$\mathbf{C}_{\alpha\alpha}^{opt} = \mathbf{C}_{\alpha\alpha}^{opt} - \mathbf{X}_\alpha \mathbf{D}_{11} - \mathbf{Y}_\alpha \mathbf{D}_{12} \cdot \mathbf{X}_\alpha^\dagger$ %build step 2)	$N_\alpha \cdot N_\alpha + 2 \cdot N_\alpha \cdot N_r$
278	Delete $\mathbf{X}_\alpha \mathbf{D}_{11} - \mathbf{Y}_\alpha \mathbf{D}_{12}$ \mathbf{X}_α	$N_\alpha \cdot N_\alpha$
279	Read $\mathbf{X}_\alpha \mathbf{D}_{12} - \mathbf{Y}_\alpha \mathbf{D}_{22}$ from file	$N_\alpha \cdot N_\alpha + N_\alpha \cdot N_q$
280	Read \mathbf{Y}_α from file	$N_\alpha \cdot N_\alpha + 2 \cdot N_\alpha \cdot N_q$
281	$\mathbf{C}_{\alpha\alpha}^{opt} = \mathbf{C}_{\alpha\alpha}^{opt} - \mathbf{X}_\alpha \mathbf{D}_{12} - \mathbf{Y}_\alpha \mathbf{D}_{22} \cdot \mathbf{Y}_\alpha^\dagger$ %build step 3)	$N_\alpha \cdot N_\alpha + 2 \cdot N_\alpha \cdot N_q$

282	Write $\mathbf{C}_{\alpha\alpha}^{opt}$ to file	$N_\alpha \cdot N_\alpha + 2 \cdot N_\alpha \cdot N_q$
283	Delete $\mathbf{C}_{\alpha\alpha}^{opt}$ $\mathbf{X}_\alpha \mathbf{D}_{12}$ $\mathbf{Y}_\alpha \mathbf{D}_{22}$ \mathbf{Y}_α %+++++C_betaBE	-
284	Read $\mathbf{C}_{\beta\beta}$ from file	$N_\beta \cdot N_\beta$
285	$\mathbf{C}_{\beta\beta}^{opt} = \mathbf{C}_{\beta\beta}$ %build step 1)	$N_\beta \cdot N_\beta$
286	Delete $\mathbf{C}_{\beta\beta}$	$N_\beta \cdot N_\beta$
287	Read $\mathbf{X}_\beta \mathbf{D}_{11}$ $\mathbf{Y}_\beta \mathbf{D}_{12}$ from file	$N_\beta \cdot N_\beta + N_\beta \cdot N_r$
288	Read \mathbf{X}_β	$N_\beta \cdot N_\beta + 2 \cdot N_\beta \cdot N_r$
289	$\mathbf{C}_{\beta\beta}^{opt} = \mathbf{C}_{\beta\beta}^{opt} - \mathbf{X}_\beta \mathbf{D}_{11} - \mathbf{Y}_\beta \mathbf{D}_{12} \cdot \mathbf{X}_\beta^\dagger$ %build step 2)	$N_\beta \cdot N_\beta + 2 \cdot N_\beta \cdot N_r$
290	Delete $\mathbf{X}_\beta \mathbf{D}_{11}$ $\mathbf{Y}_\beta \mathbf{D}_{12}$ \mathbf{X}_β	$N_\beta \cdot N_\beta$
291	Read $\mathbf{X}_\beta \mathbf{D}_{12}$ $\mathbf{Y}_\beta \mathbf{D}_{22}$ from file	$N_\beta \cdot N_\beta + N_\beta \cdot N_q$
292	Read \mathbf{Y}_β from file	$N_\beta \cdot N_\beta + 2 \cdot N_\beta \cdot N_q$
293	$\mathbf{C}_{\beta\beta}^{opt} = \mathbf{C}_{\beta\beta}^{opt} - \mathbf{X}_\beta \mathbf{D}_{12} - \mathbf{Y}_\beta \mathbf{D}_{22} \cdot \mathbf{Y}_\beta^\dagger$ %build step 3)	$N_\beta \cdot N_\beta + 2 \cdot N_\beta \cdot N_q$
294	Write $\mathbf{C}_{\beta\beta}^{opt}$ to file	$N_\beta \cdot N_\beta + 2 \cdot N_\beta \cdot N_q$
295	Delete $\mathbf{C}_{\beta\beta}^{opt}$ $\mathbf{X}_\beta \mathbf{D}_{12}$ $\mathbf{Y}_\beta \mathbf{D}_{22}$ \mathbf{Y}_β %++++Build C_alphabetaBE	-
296	Read $\mathbf{C}_{\alpha\beta}$ from file	$N_\alpha \cdot N_\beta$
297	$\mathbf{C}_{\alpha\beta}^{opt} = \mathbf{C}_{\alpha\beta}$ %build step 1)	$N_\alpha \cdot N_\beta$
298	Delete $\mathbf{C}_{\alpha\beta}$	$N_\alpha \cdot N_\beta$
299	Read $\mathbf{X}_\alpha \mathbf{D}_{11}$ $\mathbf{Y}_\alpha \mathbf{D}_{12}$ from file	$N_\alpha \cdot N_\beta + N_\alpha \cdot N_r$
300	Read \mathbf{X}_β	$N_\alpha \cdot N_\beta + N_\alpha \cdot N_r + N_\beta \cdot N_r$
301	$\mathbf{C}_{\alpha\beta}^{opt} = \mathbf{C}_{\alpha\beta}^{opt} - \mathbf{X}_\alpha \mathbf{D}_{11} - \mathbf{Y}_\alpha \mathbf{D}_{12} \cdot \mathbf{X}_\beta^\dagger$ %build step 2)	$N_\alpha \cdot N_\beta + N_\alpha \cdot N_r + N_\beta \cdot N_r$
302	Delete $\mathbf{X}_\alpha \mathbf{D}_{11}$ $\mathbf{Y}_\alpha \mathbf{D}_{12}$ \mathbf{X}_β	$N_\alpha \cdot N_\beta$
303	Read $\mathbf{X}_\alpha \mathbf{D}_{12}$ $\mathbf{Y}_\alpha \mathbf{D}_{22}$ from file	$N_\alpha \cdot N_\beta + N_\alpha \cdot N_q$
304	Read \mathbf{Y}_β from file	$N_\alpha \cdot N_\beta + N_\alpha \cdot N_q + N_\beta \cdot N_q$
305	$\mathbf{C}_{\alpha\beta}^{opt} = \mathbf{C}_{\alpha\beta}^{opt} - \mathbf{X}_\alpha \mathbf{D}_{12} - \mathbf{Y}_\alpha \mathbf{D}_{22} \cdot \mathbf{Y}_\beta^\dagger$ %build step 3)	$N_\alpha \cdot N_\beta + N_\alpha \cdot N_q + N_\beta \cdot N_q$
306	Write $\mathbf{C}_{\alpha\beta}^{opt}$ to file	$N_\alpha \cdot N_\beta + N_\alpha \cdot N_q + N_\beta \cdot N_q$
307	Delete $\mathbf{C}_{\alpha\beta}^{opt}$ $\mathbf{X}_\alpha \mathbf{D}_{12}$ $\mathbf{Y}_\alpha \mathbf{D}_{22}$ \mathbf{Y}_β %++++Build C_rrBE	-
308	Read \mathbf{C}_{rr} from file	$N_r \cdot N_r$

309	$\mathbf{C}_{rr}^{opt} = \mathbf{C}_{rr}$ %build step 1)	$N_r \cdot N_r$
310	Delete \mathbf{C}_{rr}	$N_r \cdot N_r$
311	Read $\mathbf{X}_r \mathbf{D}_{11} - \mathbf{Y}_r \mathbf{D}_{12}$ from file	$2 \cdot N_r \cdot N_r$
312	Read \mathbf{X}_r	$3 \cdot N_r \cdot N_r$
313	$\mathbf{C}_{rr}^{opt} = \mathbf{C}_{rr}^{opt} - \mathbf{X}_r \mathbf{D}_{11} - \mathbf{Y}_r \mathbf{D}_{12} \cdot \mathbf{X}_r^\dagger$ %build step 2)	$3 \cdot N_r \cdot N_r$
314	Delete $\mathbf{X}_r \mathbf{D}_{11} - \mathbf{Y}_r \mathbf{D}_{12}$ \mathbf{X}_r	$N_r \cdot N_r$
315	Read $\mathbf{X}_r \mathbf{D}_{12} - \mathbf{Y}_r \mathbf{D}_{22}$ from file	$N_r \cdot N_r + N_r \cdot N_q$
316	Read \mathbf{Y}_r from file	$N_r \cdot N_r + 2 \cdot N_r \cdot N_q$
317	$\mathbf{C}_{rr}^{opt} = \mathbf{C}_{rr}^{opt} - \mathbf{X}_r \mathbf{D}_{12} - \mathbf{Y}_r \mathbf{D}_{22} \cdot \mathbf{Y}_r^\dagger$ %build step 3)	$N_r \cdot N_r + 2 \cdot N_r \cdot N_q$
318	Write \mathbf{C}_{rr}^{opt} to file	$N_r \cdot N_r + 2 \cdot N_r \cdot N_q$
319	Delete \mathbf{C}_{rr}^{opt} $\mathbf{X}_r \mathbf{D}_{12} - \mathbf{Y}_r \mathbf{D}_{22}$ \mathbf{Y}_r %++++Build C_qqBE	-
320	Read \mathbf{C}_{qq} from file	$N_q \cdot N_q$
321	$\mathbf{C}_{qq}^{opt} = \mathbf{C}_{qq}$ %build step 1)	$N_q \cdot N_q$
322	Delete \mathbf{C}_{qq}	$N_q \cdot N_q$
323	Read $\mathbf{X}_q \mathbf{D}_{11} - \mathbf{Y}_q \mathbf{D}_{12}$ from file	$N_q \cdot N_q + N_r \cdot N_q$
324	Read \mathbf{X}_q	$N_q \cdot N_q + 2 \cdot N_r \cdot N_q$
325	$\mathbf{C}_{qq}^{opt} = \mathbf{C}_{qq}^{opt} - \mathbf{X}_q \mathbf{D}_{11} - \mathbf{Y}_q \mathbf{D}_{12} \cdot \mathbf{X}_q^\dagger$ %build step 2)	$N_q \cdot N_q + 2 \cdot N_r \cdot N_q$
326	Delete $\mathbf{X}_q \mathbf{D}_{11} - \mathbf{Y}_q \mathbf{D}_{12}$ \mathbf{X}_q	$N_q \cdot N_q$
327	Read $\mathbf{X}_q \mathbf{D}_{12} - \mathbf{Y}_q \mathbf{D}_{22}$ from file	$2 \cdot N_q \cdot N_q$
328	Read \mathbf{Y}_q from file	$3 \cdot N_q \cdot N_q$
329	$\mathbf{C}_{qq}^{opt} = \mathbf{C}_{qq}^{opt} - \mathbf{X}_q \mathbf{D}_{12} - \mathbf{Y}_q \mathbf{D}_{22} \cdot \mathbf{Y}_q^\dagger$ %build step 3)	$3 \cdot N_q \cdot N_q$
330	Write \mathbf{C}_{qq}^{opt} to file	$3 \cdot N_q \cdot N_q$
331	Delete $\mathbf{X}_q \mathbf{D}_{12} - \mathbf{Y}_q \mathbf{D}_{22}$ \mathbf{Y}_q \mathbf{C}_{qq}^{opt} %++++Build C_rqBE	-
332	Read \mathbf{C}_{rq} from file	$N_r \cdot N_q$
333	$\mathbf{C}_{rq}^{opt} = \mathbf{C}_{rq}$ %build step 1)	$N_r \cdot N_q$
334	Delete \mathbf{C}_{rq}	$N_r \cdot N_q$
335	Read $\mathbf{X}_r \mathbf{D}_{11} - \mathbf{Y}_r \mathbf{D}_{12}$ from file	$N_r \cdot N_q + N_r \cdot N_r$
336	Read \mathbf{X}_q	$2 \cdot N_r \cdot N_q + N_r \cdot N_r$

337	$\mathbf{C}_{rq}^{opt} = \mathbf{C}_{rq}^{opt} - \mathbf{X}_r \mathbf{D}_{11} - \mathbf{Y}_r \mathbf{D}_{12} \cdot \mathbf{X}_q^\dagger$ %build step 2)	$2 \cdot N_r \cdot N_q + N_r \cdot N_r$
338	Delete $\mathbf{X}_r \mathbf{D}_{11} - \mathbf{Y}_r \mathbf{D}_{12} \quad \mathbf{X}_q$	$N_r \cdot N_q$
339	Read $\mathbf{X}_r \mathbf{D}_{12} - \mathbf{Y}_r \mathbf{D}_{22}$ from file	$2 \cdot N_r \cdot N_q$
340	Read \mathbf{Y}_q from file	$3 \cdot N_r \cdot N_q$
341	$\mathbf{C}_{rq}^{opt} = \mathbf{C}_{rq}^{opt} - \mathbf{X}_r \mathbf{D}_{12} - \mathbf{Y}_r \mathbf{D}_{22} \cdot \mathbf{Y}_q^\dagger$ %build step 3)	$3 \cdot N_r \cdot N_q$
342	Write \mathbf{C}_{rq}^{opt} to file	$3 \cdot N_r \cdot N_q$
343	Delete $\mathbf{X}_r \mathbf{D}_{12} - \mathbf{Y}_r \mathbf{D}_{22} \quad \mathbf{Y}_q \quad \mathbf{C}_{rq}^{opt}$ %++++Build C_alpharBE	-
344	Build \mathbf{C}_{ar}	$N_r \cdot N_\alpha$
345	$\mathbf{C}_{ar}^{opt} = \mathbf{C}_{ar}$ %build step 1)	$N_r \cdot N_\alpha$
346	Delete \mathbf{C}_{ar}	$N_r \cdot N_\alpha$
347	Read $\mathbf{X}_\alpha \mathbf{D}_{11} - \mathbf{Y}_\alpha \mathbf{D}_{12}$ from file	$2 \cdot N_r \cdot N_\alpha$
348	Read \mathbf{X}_r	$2 \cdot N_r \cdot N_\alpha + N_r \cdot N_r$
349	$\mathbf{C}_{ar}^{opt} = \mathbf{C}_{ar}^{opt} - \mathbf{X}_\alpha \mathbf{D}_{11} - \mathbf{Y}_\alpha \mathbf{D}_{12} \cdot \mathbf{X}_r^\dagger$ %build step 2)	$2 \cdot N_r \cdot N_\alpha + N_r \cdot N_r$
350	Delete $\mathbf{X}_\alpha \mathbf{D}_{11} - \mathbf{Y}_\alpha \mathbf{D}_{12} \quad \mathbf{X}_r$	$N_r \cdot N_\alpha$
351	Read $\mathbf{X}_\alpha \mathbf{D}_{12} - \mathbf{Y}_\alpha \mathbf{D}_{22}$ from file	$N_r \cdot N_\alpha + N_\alpha \cdot N_q$
352	Read \mathbf{Y}_r from file	$N_r \cdot N_\alpha + N_\alpha \cdot N_q + N_r \cdot N_q$
353	$\mathbf{C}_{ar}^{opt} = \mathbf{C}_{ar}^{opt} - \mathbf{X}_\alpha \mathbf{D}_{12} - \mathbf{Y}_\alpha \mathbf{D}_{22} \cdot \mathbf{Y}_r^\dagger$ %build step 3)	$N_r \cdot N_\alpha + N_\alpha \cdot N_q + N_r \cdot N_q$
354	Write \mathbf{C}_{ar}^{opt} to file	$N_r \cdot N_\alpha + N_\alpha \cdot N_q + N_r \cdot N_q$
355	Delete $\mathbf{X}_\alpha \mathbf{D}_{12} - \mathbf{Y}_\alpha \mathbf{D}_{22} \quad \mathbf{Y}_r \quad \mathbf{C}_{ar}^{opt}$ %++++Build C_alphaqBE	-
356	Build \mathbf{C}_{aq}	$N_q \cdot N_\alpha$
357	$\mathbf{C}_{aq}^{opt} = \mathbf{C}_{aq}$ %build step 1)	$N_q \cdot N_\alpha$
358	Delete \mathbf{C}_{aq}	$N_q \cdot N_\alpha$
359	Read $\mathbf{X}_\alpha \mathbf{D}_{11} - \mathbf{Y}_\alpha \mathbf{D}_{12}$ from file	$2 \cdot N_q \cdot N_\alpha$
360	Read \mathbf{X}_q	$2 \cdot N_\alpha \cdot N_q + N_r \cdot N_q$
361	$\mathbf{C}_{aq}^{opt} = \mathbf{C}_{aq}^{opt} - \mathbf{X}_\alpha \mathbf{D}_{11} - \mathbf{Y}_\alpha \mathbf{D}_{12} \cdot \mathbf{X}_q^\dagger$ %build step 2)	$2 \cdot N_\alpha \cdot N_q + N_r \cdot N_q$
362	Delete $\mathbf{X}_\alpha \mathbf{D}_{11} - \mathbf{Y}_\alpha \mathbf{D}_{12} \quad \mathbf{X}_q$	$N_q \cdot N_\alpha$
363	Read $\mathbf{X}_\alpha \mathbf{D}_{12} - \mathbf{Y}_\alpha \mathbf{D}_{22}$ from file	$2 \cdot N_q \cdot N_\alpha$
364	Read \mathbf{Y}_q from file	$2 \cdot N_q \cdot N_\alpha + N_q \cdot N_q$

365	$\mathbf{C}_{\alpha q}^{opt} = \mathbf{C}_{\alpha q}^{opt} - \mathbf{X}_\alpha \mathbf{D}_{12} - \mathbf{Y}_\alpha \mathbf{D}_{22} \cdot \mathbf{Y}_q^\dagger$ %build step 3)	$2 \cdot N_q \cdot N_\alpha + N_q \cdot N_q$
366	Write $\mathbf{C}_{\alpha q}^{opt}$ to file	$2 \cdot N_q \cdot N_\alpha + N_q \cdot N_q$
367	Delete $\mathbf{X}_\alpha \mathbf{D}_{12} - \mathbf{Y}_\alpha \mathbf{D}_{22} \quad \mathbf{Y}_q \quad \mathbf{C}_{\alpha q}^{opt}$ %++++Build C_betarBE	-
368	Build $\mathbf{C}_{\beta r}$	$N_r \cdot N_\beta$
369	$\mathbf{C}_{\beta r}^{opt} = \mathbf{C}_{\beta r}$ %build step 1)	$N_r \cdot N_\beta$
370	Delete $\mathbf{C}_{\beta r}$	$N_r \cdot N_\beta$
371	Read $\mathbf{X}_\beta \mathbf{D}_{11} - \mathbf{Y}_\beta \mathbf{D}_{12}$ from file	$2 \cdot N_r \cdot N_\beta$
372	Read \mathbf{X}_r	$2 \cdot N_r \cdot N_\beta + N_r \cdot N_r$
373	$\mathbf{C}_{\beta r}^{opt} = \mathbf{C}_{\beta r}^{opt} - \mathbf{X}_\beta \mathbf{D}_{11} - \mathbf{Y}_\beta \mathbf{D}_{12} \cdot \mathbf{X}_r^\dagger$ %build step 2)	$2 \cdot N_r \cdot N_\beta + N_r \cdot N_r$
374	Delete $\mathbf{X}_\beta \mathbf{D}_{11} - \mathbf{Y}_\beta \mathbf{D}_{12} \quad \mathbf{X}_r$	$N_r \cdot N_\beta$
375	Read $\mathbf{X}_\beta \mathbf{D}_{12} - \mathbf{Y}_\beta \mathbf{D}_{22}$ from file	$2 \cdot N_r \cdot N_\beta$
376	Read \mathbf{Y}_r from file	$2 \cdot N_r \cdot N_\beta + N_r \cdot N_q$
377	$\mathbf{C}_{\beta r}^{opt} = \mathbf{C}_{\beta r}^{opt} - \mathbf{X}_\beta \mathbf{D}_{12} - \mathbf{Y}_\beta \mathbf{D}_{22} \cdot \mathbf{Y}_r^\dagger$ %build step 3)	$2 \cdot N_r \cdot N_\beta + N_r \cdot N_q$
378	Write $\mathbf{C}_{\beta r}^{opt}$ to file	$2 \cdot N_r \cdot N_\beta + N_r \cdot N_q$
379	Delete $\mathbf{X}_\beta \mathbf{D}_{12} - \mathbf{Y}_\beta \mathbf{D}_{22} \quad \mathbf{Y}_r \quad \mathbf{C}_{\beta r}^{opt}$ %++++Build C_betaqBE	-
380	Build $\mathbf{C}_{\beta q}$	$N_q \cdot N_\beta$
381	$\mathbf{C}_{\beta q}^{opt} = \mathbf{C}_{\beta q}$ %build step 1)	$N_q \cdot N_\beta$
382	Delete $\mathbf{C}_{\beta q}$	$N_q \cdot N_\beta$
383	Read $\mathbf{X}_\beta \mathbf{D}_{11} - \mathbf{Y}_\beta \mathbf{D}_{12}$ from file	$N_q \cdot N_\beta + N_r \cdot N_\beta$
384	Read \mathbf{X}_q	$N_q \cdot N_\beta + N_r \cdot N_\beta + N_r \cdot N_q$
385	$\mathbf{C}_{\beta q}^{opt} = \mathbf{C}_{\beta q}^{opt} - \mathbf{X}_\beta \mathbf{D}_{11} - \mathbf{Y}_\beta \mathbf{D}_{12} \cdot \mathbf{X}_q^\dagger$ %build step 2)	$N_q \cdot N_\beta + N_r \cdot N_\beta + N_r \cdot N_q$
386	Delete $\mathbf{X}_\beta \mathbf{D}_{11} - \mathbf{Y}_\beta \mathbf{D}_{12} \quad \mathbf{X}_q$	$N_q \cdot N_\beta$
387	Read $\mathbf{X}_\beta \mathbf{D}_{12} - \mathbf{Y}_\beta \mathbf{D}_{22}$ from file	$2 \cdot N_q \cdot N_\beta$
388	Read \mathbf{Y}_q from file	$3 \cdot N_q \cdot N_\beta$
389	$\mathbf{C}_{\beta q}^{opt} = \mathbf{C}_{\beta q}^{opt} - \mathbf{X}_\beta \mathbf{D}_{12} - \mathbf{Y}_\beta \mathbf{D}_{22} \cdot \mathbf{Y}_q^\dagger$ %build step 3)	$3 \cdot N_q \cdot N_\beta$
390	Write $\mathbf{C}_{\beta q}^{opt}$ to file	$3 \cdot N_q \cdot N_\beta$
391	Delete $\mathbf{X}_\beta \mathbf{D}_{12} - \mathbf{Y}_\beta \mathbf{D}_{22} \quad \mathbf{Y}_q \quad \mathbf{C}_{\beta q}^{opt}$	-

E Optimal Results for Godiva

#	Response	Godiva N _r =17			Godiva N _r =10	
		Type	Value	± % rel. std. dev.	Value	± % rel. std. dev.
1	k _{eff}	Measured ^{a)}	1.000	0.1	0.999894	0.099
		Computed	1.000777	1.048		
		Optimal	1.000008	0.099		
2	$\frac{\sigma_f(^{238}\text{U})}{\sigma_f(^{235}\text{U})}$	Measured ^{b)}	0.1647	1.1	0.162922	0.902
		Computed	0.158868	2.264		
		Optimal	0.151209	0.876		
3	$\frac{\sigma_f(^{233}\text{U})}{\sigma_f(^{235}\text{U})}$	Measured ^{b)}	1.590	1.9	1.572148	0.908
		Computed	1.566506	1.050		
		Optimal	1.587218	0.895		
4	$\frac{\sigma_f(^{237}\text{Np})}{\sigma_f(^{235}\text{U})}$	Measured ^{b)}	0.837	1.6	0.838380	1.512
		Computed	0.852545	6.858		
		Optimal	0.836947	1.515		
5	$\frac{\sigma_f(^{239}\text{Pu})}{\sigma_f(^{235}\text{U})}$	Measured ^{b)}	1.402	1.8	1.391574	0.544
		Computed	1.385358	0.727		
		Optimal	1.393197	0.548		
6	$\frac{\sigma_\gamma(^{55}\text{Mn})}{\sigma_f(^{235}\text{U})}$	Measured ^{a)}	0.0027	7.4	0.002787	5.420
		Computed	0.002932	7.934		
		Optimal	0.002850	5.296		
7	$\frac{\sigma_\gamma(^{93}\text{Nb})}{\sigma_f(^{235}\text{U})}$	Measured ^{b)}	0.03	10.0	0.032479	6.352
		Computed	0.035280	8.271		
		Optimal	0.033772	6.100		
8	$\frac{\sigma_\gamma(^{63}\text{Cu})}{\sigma_f(^{235}\text{U})}$	Measured ^{c)}	0.0117	5.1	0.011477	4.643
		Computed	0.010738	10.828		
		Optimal	0.011575	4.603		
9	$\frac{\sigma_\gamma(^{197}\text{Au})}{\sigma_f(^{235}\text{U})}$	Measured ^{c)}	0.1	2.0		
		Computed	0.093857	1.951		
		Optimal	0.098326	0.857		

Appendix

#	Response	Godiva Nr=17			Godiva Nr=10	
		Type	Value	± % rel. std. dev.	Value	± % rel. std. dev.
10	$\frac{\sigma_\gamma(^{107}\text{Ag})}{\sigma_f(^{235}\text{U})}$	Measured ^{c)}	0.1440	10.0	0.127101	5.739
		Computed	0.123043	7.022		
		Optimal	0.132341	5.500		
11	$\frac{\sigma_\gamma(^{209}\text{Bi})}{\sigma_f(^{235}\text{U})}$	Measured ^{c)}	0.0011	9.1		
		Computed	0.002259	8.715		
		Optimal	0.001345	6.627		
12	$\frac{\sigma_\gamma(^{79}\text{Br})}{\sigma_f(^{238}\text{U})}$	Measured ^{c)}	0.0706	6.1		
		Computed	0.433933	9.414		
		Optimal	0.076642	5.572		
13	$\frac{\sigma_\gamma(^{81}\text{Br})}{\sigma_f(^{235}\text{U})}$	Measured ^{c)}	0.0360	8.9		
		Computed	0.026618	7.725		
		Optimal	0.030183	5.620		
14	$\frac{\sigma_\gamma(^{59}\text{Co})}{\sigma_f(^{238}\text{U})}$	Measured ^{c)}	0.297	0.8		
		Computed	0.031922	3.219		
		Optimal	0.034608	1.105		
15	$\frac{\sigma_\gamma(^{127}\text{I})}{\sigma_f(^{235}\text{U})}$	Measured ^{c)}	0.0832	9.6	0.085483	7.910
		Computed	0.092771	13.776		
		Optimal	0.087280	7.745		
16	$\frac{\sigma_\gamma(^{115}\text{In})}{\sigma_f(^{238}\text{U})}$	Measured ^{c)}	0.1168	6.8		
		Computed	1.010555	10.727		
		Optimal	0.122521	6.511		
17	$\frac{\sigma_\gamma(^{103}\text{Rh})}{\sigma_f(^{238}\text{U})}$	Measured ^{c)}	0.0152	7.9		
		Computed	0.607013	6.448		
		Optimal	0.016329	7.343		

- a) Values from HEU-MET-FAST-001 Appendix D Table D, [\[19\]](#)
- b) Values from HEU-MET-FAST-001 Appendix D Table F, [\[19\]](#)
- c) Values from Table 7, [\[17\]](#)

F KENOVI Input Listings for as-built Model

The embedded txt-file contains an example of a KENOVI input listing for the as-built model.

Bibliography

- [1] R.V. Abramov, An improved algorithm for the multidimensional moment-constrained maximum entropy problem, *Journal of Computational Physics*, 226, pp. 621-644, 2007
- [2] E. Arslan, Prädiktive Einschätzungen bestmöglicher Modellkalibrierungen und Datenerhebungen auf Basis kerntechnischer Experimente, Dissertation, Karlsruher Institut für Technologie (KIT) Fakultät für Maschinenbau, 2011
- [3] E. Arslan, D. G. Cacuci, Predictive modeling of liquid-sodium thermal–hydraulics experiments and computations, *Annals of Nuclear Energy*, Vol. 63 pp. 355–370, 2014
- [4] R. Avery et al., Applied Physics Division, Annual Report, July 1, 1970, to June 30, 1971, ANL-7910, January 1972
- [5] A.F. Badea, D.G. Cacuci, Uncertainty reduction in coupled neutron-kinetics/ thermal-hydraulics computational predictions following assimilation of BWR-TT benchmark experimental data, The International Topical Meeting on Nuclear Reactor Thermal-Hydraulics, NURETH-15, Pisa May 2013
- [6] M.C. Badea, Best-Estimate predictions through consistent experimental data assimilation: Methodology and paradigm reactor physics applications, Dissertation, Karlsruher Institut für Technologie (KIT) Fakultät für Maschinenbau, 2011
- [7] A. Bejan, *Heat Transfer*, John Wiley & Sons, Inc. New York, 1993
- [8] D.G. Cacuci, *Sensitivity and Uncertainty Analysis: Theory*, Chapman and Hall/ CRC, Boca Raton, FL, 2003
- [9] D.G. Cacuci, M. Ionescu-Bujor, “Best-estimate model calibration and prediction through experimental data assimilation – I: Mathematical Framework”, *Nuclear Science and Engineering*, 165, pp. 18-44, 2010
- [10] D.G. Cacuci, Predictive modeling of coupled multi-physics systems: I. Theory, *Annals of Nuclear Energy*, v70, pp. 266-278, 2014
- [11] T.H. Cormen, *Introduction to Algorithms* (3rd Edition), MIT Press,

- [12] J. Dongarra, D. Walker, The Design of Linear Algebra Libraries for High Performance Computers, LAPACK Working Note 58, 1993
- [13] Cross Section Evaluation Working Group, ENDF-6 Formats Manual - Data formats and procedures for the Evaluated Nuclear Data File, ENDF-102, National Nuclear Data Center, Brookhaven National Laboratory (2009)
- [14] R.T. Evans, D.G. Cacuci, A parallel Krylov-based adjoint sensitivity analysis procedure, Nuclear Science and Engineering, 172, pp. 216-222, 2012
- [15] T.M. Evans, A.S. Stafford, R.N. Slaybaugh and K.T. Clarno, "Denovo: A new three-dimensional parallel discrete ordinates code in SCALE", Nuclear Technology, 171, pp. 171-200, 2010
- [16] P. Fornasini, The Uncertainty in Physical Measurements: An Introduction to Data Analysis in the Physics Laboratory, Springer, Berlin, 2008
- [17] S. C. Frankle, J. F. Briesmeister, Spectral Measurements in Critical Assemblies: MCNP Specifications and Calculated Results, LA-13675, Los Alamos National Laboratory (1999)
- [18] M. Iqbal , H. Abdel-Khalik and P. Turinsky, A comparative study of ZPR-6/7 with MCNP/5 and MC2-2/REBUS, Annals of Nuclear Energy 36, pp. 995–997, 2009
- [19] International Handbook of Evaluated Criticality Safety Benchmark Experiments (ICSBEP), NEA/NSC/DOC(95)03, September 2010 Edition
- [20] B. L. Kirk, Overview of Monte Carlo radiation transport codes, Radiation Measurements 45, pp. 1318-1322, 2010
- [21] W. Lahoz, B. Khattatov and R. Ménard (Editors), Data Assimilation – Making sense of observations, Springer-Verlag, Berlin, Germany 2010
- [22] C. Latten, Mathematical framework and illustrative examples of multi-physics data assimilation, Master of Nuclear Engineering unpublished report, North Carolina State University, 2012
- [23] The Math Works Inc. MATLAB 7.13 (R2011b). The Math Works Inc., 2011

- [24] Y. Nagaya, I. Kodeli, G. Chiba and M. Ishikawa, Evaluation of sensitivity coefficients of effective multiplication factor with respect to prompt fission neutron spectrum, *Nuclear Instruments and Methods in Physics Research A*, 603 (2009) pages 485 – 490.
- [25] S.K. Park, L. Xiu (Editors), *Data Assimilation for Atmospheric, Oceanic and Hydrologic Applications*, Springer-Verlag, Berlin, Germany, 2009
- [26] A. Petruzzi, D.G: Cacuci, F. D’Auria, Best-Estimate model calibration and prediction through experimental data assimilation – II: Application to a blowdown benchmark experiment, *Nuclear Science and Engineering*, 165, pp. 45-100, 2010
- [27] W.C. Proctor, *Elements of High-Order Predictive Model Calibration Algorithms with Applications to Large-Scale Reactor Physics Systems*, Dissertation, NCSU Department of Nuclear Engineering, 2012
- [28] Y. Ronen (editor), *CRC Handbook of Nuclear Reactors Calculations, Volume III*, CRC Press, Boca Raton, Fla. 1986
- [29] J. L. Rowlands, Accuracy of criticality calculations made using current nuclear data libraries for MOX fuelled fast critical assemblies, *Annals of Nuclear Energy Vol. 37*, pp. 1666–1673, 2010
- [30] M. Salvatores et. al., Methods and Issues for the combined use of integral experiments and covariance data: Results of a NEA International Collaborative Study, *Nuclear Data Sheets*, publication pending, preliminary version August 2013
- [31] Scale: A comprehensive modeling and simulation suite for nuclear safety analysis and design, ORNL/TM-2005/39, Version 6.1, June 2011. Available from Radiation Safety Information Computational Center at Oak Ridge National Laboratory as CCC-785
- [32] M. A. Smith et al., Zero Power Fast Reactor Deterministic Modeling with Heterogeneous Geometry, *ANS Transactions Vol. 104*, pp. 827-828, 2011
- [33] A. Tarantola, *Inverse Problem Theory and Methods for Model Parameter Estimation*, Society of Industrial and Applied Mathematics (SIAM) 2005
- [34] A. Varuttamaseni and John C. Lee, Simulation of ZPR-6 Assembly 7 with MCNP5, *ANS Transactions; Vol. 95* pp.734-735, 2006

- [35] W.S. Yang, G. Aliberti, R.D. McKnight and I. Kodeli, Fission Spectrum Covariance Matrix and Sensitivity Coefficients for Response Parameter Uncertainty Estimation, Nuclear Data Sheets 109 (2008) pages 2852 – 2857
- [36] Y.Yeivin, J.J. Wagschal, J.H. Marable and C.R. Weisbin, Relative consistency of ENDF/B-IV and –V with fast-reactor benchmarks, in Proc. of the Int. Conf. on Nuclear Cross Section for Technology, J.L. Fowler and C.H. Johnson, C.D. Bowman (editors), NBS Special Publication 594, 1980
- [37] Assessment of Existing Nuclear Data Adjustment Methodologies, International Evaluation Co-operation, Intermediate Report of Subgroup 33, NEA/NSC/WPEC/DOC(2010)429, OECD/NEA, Paris 2011

Eigenständigkeitserklärung

Ich erkläre hiermit, die vorliegende Arbeit selbstständig angefertigt zu haben. Es wurden dabei keine unerlaubten Hilfsmittel verwendet. Wortlaute oder dem Sinne aus anderen Werken entnommene Inhalte sind durch die angegebenen Quellen verdeutlicht.

Karlsruhe, April 2014

Christine Latten

Lebenslauf

Name	Christine Latten
Geburtsdatum	08.02.1985
Geburtsort	Göppingen
Staatsangehörigkeit	deutsch

Schulausbildung

Juni 2004	Allgemeine Hochschulreife Hohenstaufen-Gymnasium, Göppingen
-----------	--

Studium

Dezember 2010	Diplomprüfung Verfahrenstechnik Universität Stuttgart
Dezember 2012	Master of Nuclear Engineering North Carolina State University, Raleigh